Technische Universität München

Max-Planck-Institut für Astrophysik

Numerical Studies of the Magnetorotational Instability in Core Collapse Supernovae

Tomasz Piotr Rembiasz

MAX-PLANCK-GESELLSCHAFT

TECHNISCHE
UNIVERSITÄT
MÜNCHEN

Technische Universität München

Max-Planck-Institut für Astrophysik

Numerical Studies of the Magnetorotational Instability in Core Collapse Supernovae

Tomasz Piotr Rembiasz

Vollständiger Abdruck der von der Fakultät für Physik der Technischen Universität München zur Erlangung des akademischen Grades eines

Doktors der Naturwissenschaften (Dr. rer. nat.)

genehmigten Dissertation.

Vorsitzender: Univ.-Prof. Dr. A. Bausch

Prüfer der Dissertation:

1. Priv.-Doz. Dr. E. Müller
2. Univ.-Prof. Dr. B. Garbrecht

Die Dissertation wurde am 27 November 2013 bei der Technischen Universität München eingereicht und durch die Fakultät für Physik am 13 Dezember 2013 angenommen.

AN EXPERT IS A PERSON WHO HAS FOUND OUT BY HIS OWN PAINFUL EXPERIENCE ALL THE MISTAKES THAT ONE CAN MAKE IN A VERY NARROW FIELD.

Niels Bohr

Contents

Chapter 1

Introduction

I AM NOT YOUNG ENOUGH TO KNOW EVERYTHING.

J. M. Barrie, *The Admirable Crichton*

1.1 Explosion mechanisms of core-collapse supernovae

Core-collapse supernovae (CC-SNe) are one of the most fascinating and complex astrophysical phenomena. Almost all branches of physics, from particle physics to general relativity, are relevant for the explosion mechanism. Even though this very complex process has been studied for over six decades, there are still many questions which remain open. Discussing all the subtleties of this problem would be beyond the scope of this introduction. An excellent review by Bethe (1990) already had 66 pages and in over 20 years since then, because of ever increasing computational power and effort of many scientists, tremendous progress has been made. As a good introduction to the topic, we recommend review articles by Woosley et al. (2002), Janka et al. (2007), Janka (2012), Janka et al. (2012) and Burrows (2013). In this section, we are going to explain briefly presently discussed CC-SN mechanisms.

Evolution of massive stars

The fate of a newly born star is mostly determined by its initial mass and chemical composition. Massive stars ($M \gtrsim 8\ M_\odot$, where $M_\odot = 1.989 \times 10^{33}$g is the solar mass), as all stars, spend most of their lifetime on the main sequence (MS) burning the central hydrogen. This process releases energy and provides the necessary pressure gradient to balance the gravitational force and keep the star in the hydrostatic equilibrium. After millions to tens of millions of years, the hydrogen in the stellar core is exhausted (i.e. it is converted to helium) and the star leaves the main sequence. The core contracts, the central temperature and density rise and the burning of innermost helium layers sets in. Each time the star runs out of the central fuel, its core contracts again so that even heavier nuclei (which were produced in the preceding stages) can be burned in the subsequent phases: first carbon and then neon, oxygen and silicon.[1] The fusion of heavier elements can sustain the

[1] Not every star undergoes all these phases. Which nuclear burning stage will be reached for a given star, depends on its initial mass and chemical composition. For example, the Sun, like other stars with an initial mass $M \lesssim 8\ M_\odot$ will not reach the carbon burning stage. For massive starts with an initial mass $8\ M_\odot \lesssim M \lesssim 11\ M_\odot$ the central neon ignition

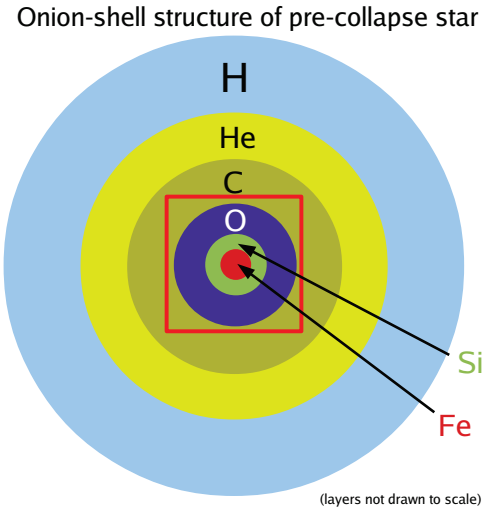

Figure 1.1: Chemical composition of a supernova progenitor shortly before core-collapse. The figure is not in scale: the biggest, hydrogen, shell is of order 10^7 km, and the smallest, iron core, has the radius of order of 10^3 km. The red square indicates the central region, whose zoom is presented in Fig. 1.2. The figure is reproduced with permission from Janka et al. (2012).

hydrostatic equilibrium for a much shorter time (order of 10^6 years) for two reasons. Firstly, it is energetically less efficient than hydrogen burning. Secondly, because of the higher central temperature, neutrino-antineutrino pairs can be created, which carry away a part of the energy from the star. Finally, as the end product of silicon fusion, an iron core[2] is formed in the centre, surrounded by concentric shells of ashes from the previous nuclear burning stages: the heavier the element, the closer to the centre. This onion-like structure is schematically presented in Fig. 1.1. Iron, as the element with the lowest nuclear binding energy, is the final stage of the hydrotatic nuclear burning, since a synthesis of any heavier elements would not release but rather consume energy (an endothermic process).

Core collapse

The iron core, which is mostly stabilised by the quantum electron degeneracy pressure, continues to contract (to release further gravitational binding energy) and grow (because of the silicon shell burning) until it reaches approximately the Chandrasekhar mass of $\approx 1.44\ M_\odot$. At this stage, the core, which has a typical diameter of 3000 km, a central temperature around 10^{10}K and a density of several 10^9 g cm^{-3}, becomes unstable. High energy photons start to disintegrate iron nuclei to α particles and free nucleons. Hence, part of the thermal energy is lost in this endothermic process. Moreover, the reaction rates of electron capture on heavy nuclei and on free protons increase. In this process of deleptonisation, a neutron (bound or free) and a neutrino are created. The latter can freely escape from the core carrying away some of its energy. Consequently, the electron fraction, Y_e, (the number of electrons to the number of all nucleons) drops from $Y_e \approx 0.5$

does not occur (yet, some off-centre neon burning is possible). The exact thresholds for carbon and neon burning are not exactly known (for a detailed discussion, see, e.g. Woosley et al. (2002)).

[2]The progenitors with masses of 8–10 $M_\odot$ develop ONeMg (oxygen, neon, magnesium) cores, instead. However, in order not to complicate the discussion, we will not consider this case. For the details, see, e.g. Janka et al. (2007).

to $Y_e \approx 0.3$, the electron degeneracy pressure considerably decreases and it is no longer able to balance the gravitational force.

The core starts to collapse - its matter almost freely falls onto the centre (upper left panel of Fig. 1.2). After ≈ 100 ms, the central density reaches 10^{12} g cm^{-3} and, despite their tiny cross sections, neutrinos created in the process of deleptonisation are trapped by the matter, i.e. their diffusion timescale exceeds the free-fall time, and they can no longer escape draining the energy from the centre. In spite of the neutrino trapping, the collapse cannot be halted until the matter reaches nuclear saturation densities ($\rho \approx 2.7 \times 10^{14}$ g cm^{-3}) within a fraction of a second (after ≈ 110 ms from the collapse onset). The *proto-neutron star* (PNS) is formed.

At this point, in the innermost regions, because of the repulsive contribution to the nucleon interaction potential, the matter becomes almost incompressible. The subsonically collapsing matter of the inner core decelerates and rebounds, at roughly 10 km, to the surrounding supersonically infalling layers and a strong shock wave forms (upper right panel of Fig. 1.2). In the early days of supernova research, it was speculated that the shock could be strong enough to stop the collapse and to trigger the explosion (a so called "prompt explosion mechanism"). However, the shock's energy is insufficient and most of it is used to dissociate heavy nuclei into nucleons in the outer regions of the core. After ≈ 200 ms (from the beginning of the core collapse), the shock stalls approximately 200 km from the centre (middle left panel of Fig. 1.2). For a successful explosion, some other mechanism, which would transfer a part of the binding energy released during the core collapse to the stalled shock, is necessary. Colgate & White (1966) suggested that neutrinos could be this missing agent.

After core bounce, the proto-neutron star rapidly accretes the infalling matter until the explosion sets in. Depending on the initial mass of the progenitor, the PNS may transform into a neutron star (NS) or a black hole (BH). It was thought that the former case would occur for stars with an initial mass smaller than roughly 25 $M_\odot$, and the latter case would happen for more massive progenitors (see, e.g. Janka et al. (2007)). However, recent studies show that the formations of a BH from stars whose mass is below 20 $M_\odot$ (in a failed explosion), and of a NS from progenitors with the mass in the range 20–40 $M_\odot$ are also possible (Ugliano et al. 2012). In the nascent PNS, the matter is so dense that neutrinos are trapped (their mean free path is significantly shorter than the neutron star radius). It takes them seconds to diffuse out.

In the "delayed neutrino-heating explosion mechanism", the stalled shock can be revived by the outgoing neutrinos, which carry most of the gravitational energy binding released in the collapse. On their way out, the neutrinos can provide additional pressure and deposit some of their energy in the layers between the PNS and the stalled shock (middle right panel of Fig. 1.2). The shock will start to expand and after a few 100 ms the explosion should set in. It is interesting to note that only a small fraction of the energy carried by the neutrinos (of order 10^{53} erg) is sufficient to trigger the explosion (whose energy is of order 10^{51} erg). However, in numerical simulations, the delayed neutrino-heating not always produces a successful explosion and if it does, explosion energies still are on the low side.

Consequently, some other processes, which would facilitate the explosion, like convection or the *standing accretion shock instability* (SASI; Blondin et al. (2003)), are considered. The latter introduces non-radial deformations of the accretion shock. In another so-called "*magnetohydrodynamical* (MHD) mechanism" (Meier et al. (1976)), for certain progenitors, the magnetic fields could trigger by themselves or support neutrinos in triggering an explosion.

If the neutrinos, supported by convection, the SASI or magnetic fields, successfully initiate the explosion, the shock starts to expand rapidly (bottom left panel of Fig. 1.2). During the expan-

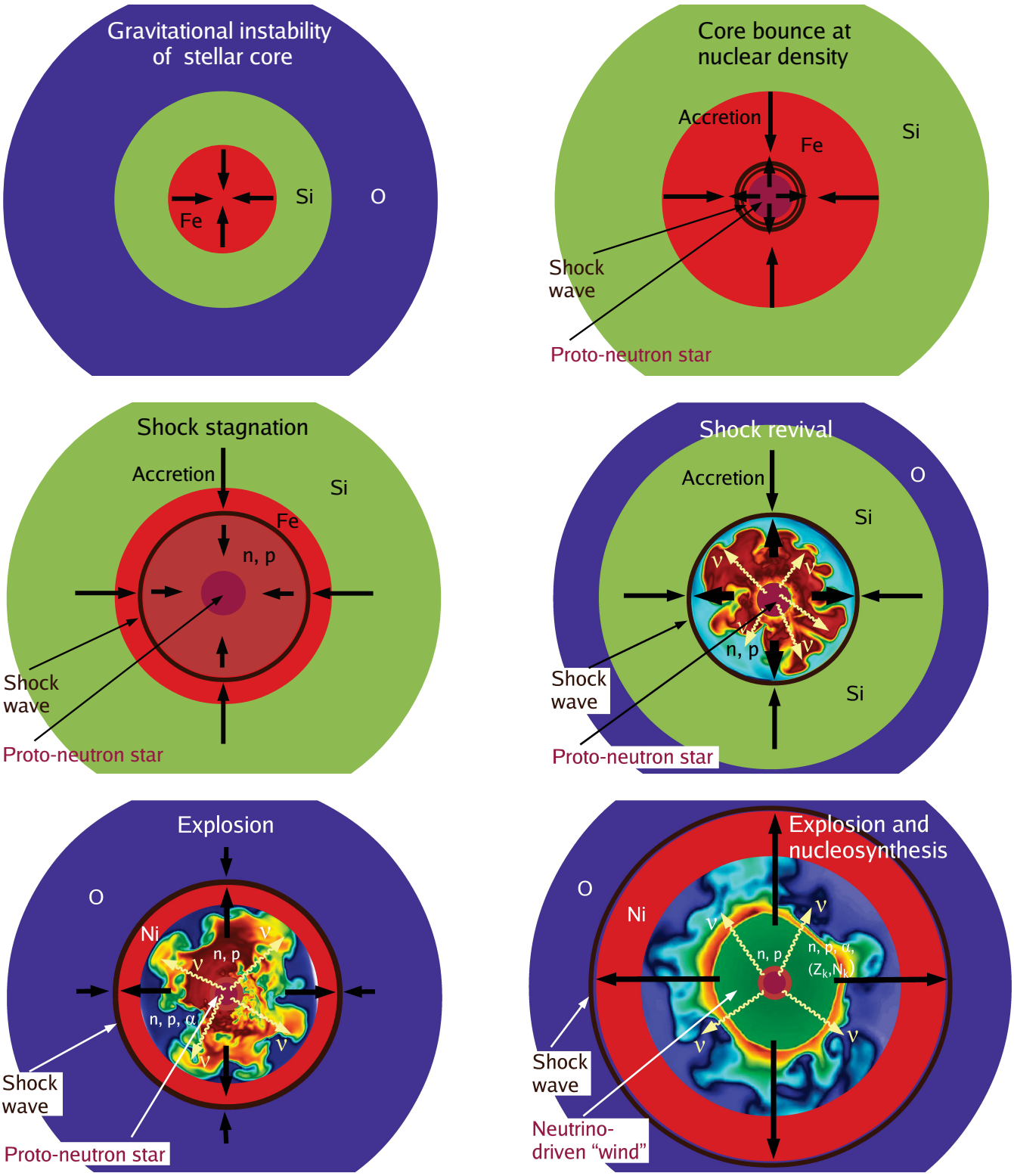

Figure 1.2: A schematic representation of core-collapse supernova evolution stages. *Top left:* the iron core collapses. *Top right:* the matter in the core reaches nuclear densities and the proto-neutron star (PNS) is formed. The core bounces and the shock wave is created. *Middle left:* the shock stagnates and quasi-stationary accretion sets in. *Middle right:* the shock is revived by the neutrinos streaming out from the PNS. *Bottom left:* the beginning of the re-expansion of the shock wave, the explosion sets in. *Bottom right:* further nuclear processes take place in the expanding shock wave. The figure is reproduced with permission from Janka et al. (2012).

sion, among other nuclear reactions, the so-called r-process (rapid neutron capture) occurs, during which elements heavier than iron are created (bottom right panel of Fig. 1.2). The matter in the outer layers is expelled to the interstellar medium, and the compact remnant, the proto-neutron star, either forms a neutron star or collapses to a black hole.

The study of core-collapse supernovae are extremely challenging, because the physics involved in the explosion mechanisms is very complex and many "ingredients" have to be taken into account: nuclear equation of state, nuclear reactions, radiative transport of neutrinos, magneto-hydrodynamics and general relativity, to name a few. A 3D simulation, in which all these aspects were included, would be beyond the capabilities of any supercomputer in the predictable future.[3] Therefore, some approximations are necessary in the studies, e.g. in 2D simulations axial symmetry is assumed. In a simulation with a detailed equation of state (or neutrino transport), general relativistic effects are often neglected, whereas in a simulation concentrating on these effects, a simplified equation of state and neutrino transport are used.

In our studies, we investigate the magnetic field amplification in the nascent proto-neutron star in the post-bounce phase. We use Newtonian MHD[4] equations with a simplified equation of state. The influence of neutrinos (and nuclear reactions) is neglected (which should be a fairly good approximation, since at the considered time, the majority of the neutrinos are still trapped in the PNS). The time for magnetic field amplification at this stage is constrained to a few 100 ms by the interplay between neutrinos and the infalling matter. In the case of a successful supernova explosion, after a few 100 ms, the outgoing neutrinos will revive the shock and the infalling matter and a part of the progenitor's magnetic field will be expelled from the surrounding of the PNS. Further magnetic field amplification around the PNS can continue, but it will be irrelevant for the explosion dynamics.
In the case of an unmagnetised progenitor for which a failed supernova occurs, the neutrinos will not be able to revive the shock and after a few 100 ms, the matter outside the shock radius will accrete onto the proto-neutron star. However, for the very same but magnetised progenitor, if its magnetic field is strong enough at this moment, it might be able prevent the collapse and trigger an explosion.

1.2 Magnetorotational instability in core-collapse supernovae

The amplification of the magnetic fields and their influence on the explosion mechanism is one of the least explored aspects of core-collapse supernovae. There are two good reasons to investigate this topic in more detail.

Firstly, it is known that only very strong magnetic fields, which are in equipartition with the kinetic energy density, i.e. of the order of 10^{15} G, can play a dynamically important role (see, e.g. Meier et al. (1976), Obergaulinger & Janka (2011)). However, according to state-of-the-art stellar evolution theory, the strongest magnetic fields of typical supernova progenitors are unlikely to exceed 10^9 G (Heger et al. 2005). Therefore, it is important to investigate whether and how they could be amplified by six orders of magnitude during a supernova explosion. Ideally, we would like to know for which initial conditions (i.e. types of progenitors) the magnetic fields can achieve such high amplitudes. On the one hand, since MHD simulations are computationally more expensive than purely hydrodynamical ones, it would be beneficial, from a purely practical point

[3] The closest to this goal so far is a recent 3D simulation of Hanke et al. (2013) with a detailed neutrino transport and general relativistic corrections to a Newtonian gravitational potential.

[4] The MHD approximation is discussed in Chapter 2.

of view, to know in advance whether magnetic fields can be neglected for a given progenitor. On the other hand, in certain types of core-collapse supernovae, they could play a crucial role and not taking them into account would be a mistake. For example, a fraction of the observed *gamma ray bursts* (long GRBs) is thought to be the result of the collapse of a rapidly rotating core to a black hole surrounded by a highly magnetised disc (Woosley et al. 1993).

There are several ways, in which the magnetic field could influence the dynamics of the system. Firstly, magnetic stresses can provide additional pressure, which counteracts the gravitational attraction and facilitates a supernova explosion. Secondly, magnetic field can extract differential rotational energy, converting it to magnetic energy, and transport angular momentum outwards. At some point, this energy could be transferred to kinetic and thermal energy in a violent process called magnetic field reconnection (see, e.g. Biskamp (1997); Biskamp (2005); Goedbloed et al. (2010)). One can speculate that this extra energy injection could play a crucial role in the explosion dynamics. However, this phenomenon has not yet (properly) been studied in core-collapse supernova simulations.[5] Even though the resistivity of the plasma is very small in this environment (i.e. the magnetic diffusion timescale exceeds the explosion timescale by many orders of magnitude), we cannot simply infer from this fact that the reconnection rates would be too small for this process to play an important role in the explosion. It is well known that the reconnection rates of the classical Sweet-Parker and Petschek models (i.e. in which the reconnection is driven only by resistivity) are insufficient to explain phenomena observed in the Solar corona (see, e.g. Biskamp (2005)). Similarly, the magnetic field diffusion rate in the Solar dynamo must be much higher than the value expected from the classical (Spitzer & Härm 1953) resistivity (see, e.g. Goedbloed & Poedts (2004)). Therefore, some turbulent reconnection models were proposed, in which the reconnection rate does not depend on resistivity (see, e.g. Lazarian & Vishniac (1999)). Magnetic field reconnection is a very complicated topic on its own, which is not yet fully understood. It is hard to predict when it will be possible to investigate the relevance of this process for core-collapse supernova explosions. Further advances from both the theoretical side and the computational side (more powerful supercomputers, which would allow using higher resolutions) are necessary.

Secondly, magnetised neutron stars, pulsars and magnetars, which are created during core-collapse supernova explosions, are known to have very strong magnetic fields of order 10^{12}–10^{13} G and 10^{14}–10^{15} G (Kouveliotou et al. 1998), respectively. Whereas in current supernova simulations, realistic initial magnetic fields can be amplified to the values observed in pulsars (i.e. 10^{12}–10^{13} G; Obergaulinger & Janka (2011)), the origin of the magnetic fields encountered in magnetars (10^{14}–10^{15} G) remains a puzzle. Meier et al. (1976) estimated an upper-limit for magnetic field amplification during a core-collapse supernova explosion of a differentially rotating progenitor. In their most optimistic scenario, amplitudes as high as a few times 10^{15} G could be reached. A recent estimate of Spruit (2008), which is based on data from modern stellar evolution- and supernova explosion-models, gives a similar result. However, since magnetic field amplification is a highly non-linear process, its details can be only studied numerically. It is also unclear whether and how such strong fields could be successfully trapped in a nascent proto-neutron star after the explosion (we will not investigate this issue in this thesis).

For non-rotating progenitors, the magnetic field can be amplified first by compression. The

[5] We can safely claim that results of any simulation in which reconnection was driven by numerical resistivity must merely be misleading for the following reason. In (non-turbulent) reconnection models, the reconnection rate is proportional to the (scalar) physical resistivity. Even in our local simulations from Chapter 2, which belong to the currently best resolved CC-SN MHD simulations, the numerical resistivity is higher than the expected physical resistivity by many orders of magnitude. This means that the rate of numerically driven reconnection (which is proportional to the numerical resistivity), will be higher than any plausible non-turbulent reconnection rate by many orders of magnitude.

degenerate stellar matter is highly conductive and the magnetic flux is frozen into it. During the collapse to a proto-neutron star, the magnetic field following the infalling gas is compressed and amplified by roughly two orders of magnitude. After the collapse, further amplification can be provided by hydrodynamic instabilities such as convection or the SASI. However, it can be estimated that these processes are insufficient to amplify the magnetic field by six orders of magnitude on the supernova timescale (see, e.g. Spruit (2008)). Recent 2D MHD core-collapse supernova simulations of Obergaulinger & Janka (2011) confirm this. These authors considered non-rotating progenitors with initial magnetic fields in the range from 10^9 to 10^{12} G and found that, independent of the initial amplitude, the magnetic field was amplified by the above mentioned processes by approximately three orders of magnitude. This means that unless unrealistically high initial amplitudes are used (of order 10^{12}G, which is three orders of magnitude higher than theoretically expected; Heger et al. (2005)), the magnetic field cannot reach 10^{15} G in the post-bounce phase. Obergaulinger & Janka (2011) reported that only such strong magnetic fields could significantly affect the dynamics of the system.

For differentially rotating progenitors, apart from compression (and later also convection and the SASI) there are two more known mechanism amplifying magnetic fields. One of them is *linear winding*, which creates (winds up) a toroidal component (i.e. B_ϕ in spherical or cylindrical coordinates) from the poloidal (i.e. the other) field components. This process increases the magnetic field strength at the expense of the rotational energy and operates linearly with time. Compression and linear winding were observed in several numerical simulations (see, e.g. Bisnovatyi-Kogan et al. 1976; Meier et al. 1976; Müller & Hillebrandt 1979; Symbalisty 1984; Yamada & Sawai 2004; Kotake et al. 2004; Ardeljan et al. 2005; Obergaulinger et al. 2006b,a; Cerdá-Durán et al. 2007; Burrows et al. 2007). However, in none of these, the magnetic field was amplified to 10^{15} G from theoretically expected initial values (of order 10^9 G). This negative result is in accordance with the estimate of Spruit (2008).

Another amplification mechanism was proposed by Akiyama et al. (2003). These authors pointed out that the matter of a differentially rotating nascent proto-neutron star can be unstable against the *magnetorotational instability* (MRI) (Balbus & Hawley (1991); Hawley & Balbus (1991)). The MRI amplifies the magnetic field exponentially with time, therefore even a weak seed field could possibly increase to a dynamically relevant strength in the post-bounce phase.

Since the pioneering work of Balbus & Hawley (1991), the MRI has been intensively studied in accretion discs (see, e.g. Balbus & Hawley (1998)), where it excites turbulence and enables the outwards transport of angular momentum, which is necessary for gas to be able to accrete onto the central object (star, neutron star or black hole). Numerical studies of this instability are challenging, since the scales on which it operates are much smaller than a typical accretion disc size. Therefore, it is impossible for current generation supercomputers to resolve the MRI evolution in global accretion disc simulations and a hybrid approach has to be used in these investigations. On the one hand, in local simulations (see, e.g. Hawley & Balbus 1991, 1992; Hawley et al. 1995; Brandenburg et al. 1995; Hawley et al. 1996; Stone et al. 1996; Sano et al. 2004; Fromang & Papaloizou 2007; Fromang et al. 2007) of a small part of an accretion disc, high enough spatial resolution can be used to follow the MRI evolution: the onset of the instability, the phase of exponential growth, its termination and the subsequent transition into the turbulent state. The main drawback of such simulations is that they cannot answer the question how the MRI can affect the global disc structure. Moreover, since they cover only a small fraction of an accretion disc, many simulations have to be done to explore different physical regimes encountered within the disc. Additionally, some simplified initial and boundary conditions have to be used. On the other hand, global simulations (see, e.g. Hawley 2000; Stone & Pringle 2001; Arlt & Rüdiger 2001; Hawley

et al. 2001; Hawley & Balbus 2002) allow testing of the influence of the MRI on the whole disc, however they fail to resolve the MRI structures for realistic initial magnetic fields. Therefore, one has to use artificially enhanced initial magnetic field amplitudes (the stronger the initial field, the larger the MRI structures) or the information obtained from local simulations. This combination of local and global simulations has been successful and gave a valuable insight into the accretion disc physics. Nevertheless, the saturation level of the MRI is still not fully understood.

The MRI results obtained in accretion disc studies cannot be easily extrapolated to core collapse supernovae, because the physical conditions in both systems are very different. The accretion discs have a Keplerian rotational profile and their matter can be well described with an ideal gas equation of state. In contrast, the hydrostatic equilibrium in the rotating supernova core is provided not only by the centrifugal force but also (mostly) by pressure gradients. Moreover, the proto-neutron star matter reaches nuclear densities and an equation of state that includes nuclear interactions has to be used to describe its properties. It is not clear either how convective instabilities and neutrino transport influence the growth and termination of the MRI. Therefore, there is a need to study the MRI in core-collapse supernova simulations.

Obergaulinger et al. (2006b) and Obergaulinger et al. (2006a) identified the MRI in global MHD core-collapse supernova simulations (for a more recent work, see also Sawai et al. (2013)). However, as it was pointed out by these authors, the fastest growing MRI modes have wavelengths of order of (at most) a meter and because of the insufficient resolution it was impossible to resolve them in these simulations. Consequently, Obergaulinger et al. (2009) performed local simulations to study the development of the instability in more detail (see also Masada et al. (2012)). Their results confirmed that the MRI growth-rates are high enough for the instability to present a viable amplification mechanism in a proto-neutron star. However, because of limited computational resources,these authors used artificially enhanced initial magnetic fields (so that the MRI structures were larger) of order 10^{13} G, which were then amplified by the MRI to $\approx 10^{15}$ G within a few tens of milliseconds. Therefore, it is still unclear whether much weaker, but realistic magnetic fields can be amplified to the same (dynamically relevant) amplitudes. This uncertainty results from two facts. Firstly, we lack an understanding of the MRI growth termination physics and of the subsequent non-linear turbulent phase. Secondly, it is unclear to what degree the results of Obergaulinger et al. (2009) are affected by numerical errors (numerical viscosity and resistivity[6]). Being aware of this problem, these authors tried to estimate the influence of the numerical dissipation of their code, but they did not give a reliable prescription how to extrapolate their results to the parameter space regime that is relevant for core-collapse supernovae.

The early phase of the MRI is characterised by coherent laminar flows (channel modes) that are unstable against secondary (or parasitic) instabilities (Goodman & Xu 1994) driven by the flow (Kelvin-Helmholtz) or the current (tearing modes). When these parasites disrupt the channel modes, the growth of the MRI terminates. Based on theoretical analysis, Pessah (2010) suggested that the saturation level of MRI-driven turbulence and therefore the final magnetic field strength can be estimated by a study of the parasitic instabilities.

The main goal of this thesis is to test this hypothesis in local three-dimensional resistive-viscous magnetohydrodynamical (MHD) simulations of the MRI in core-collapse supernovae. Thereby, we extend the studies of Obergaulinger et al. (2009), which were done in the ideal-MHD limit. We also investigate the influence of the numerical dissipation on the simulation results. Moreover, we plan to find a prescription, which will allow us to extrapolate them to the parameter space regime that is relevant for the core-collapse supernovae. As a result, we want to give an upper limit for

[6]These notions are defined in Chapter 2.

MRI-driven magnetic field amplification. We also note that the MRI can only play and important role in core-collapse supernova explosions of progenitors, which are both strongly magnetised and rapidly rotating. These conditions are met in less than 1% of all cases.

1.3 Plan of the thesis

Chapter 2 is a brief introduction to *magnetohydrodynamics* (MHD). We begin with a derivation of *non-ideal* (i.e. containing resistive and viscous terms) *MHD equations*. Then, we discuss the *ideal MHD* limit, which is an excellent approximation for many astrophysical phenomena. Next, we describe numerical methods used to integrate MHD equations. We explain why any numerical solution inevitably differs from the real solution, and we name standard ways of measuring numerical errors. They are very useful when assessing or designing a numerical scheme, yet their application is very limited when interpreting results of time-dependent simulations whose purpose is to investigate (new) physical phenomena (and not merely to test numerical methods). We argue that in the case of computational MHD, numerical errors can be often interpreted as numerical resistivity and viscosity. Verifying this claim is the main goal of Chapter 3. First, we propose a simple prescription, which, after calibrating it with some simulations, can be used to estimate the numerical dissipation (i.e. resistivity and viscosity) of any grid-based MHD code for any initial conditions. Then, we test this prescription with the help of wave damping- and tearing mode-simulations. Chapter 4 deals with the main goal of this thesis: the magnetorotational instability in core-collapse supernovae in the framework of non-ideal MHD. We investigate, whether the MRI is able to amplify a progenitor's initial magnetic field to dynamically relevant strengths (amplitudes of order 10^{15} G), i.e. at which the magnetic field energy amounts to a considerable fraction of the kinetic energy. Finally, in Chapter 5, we summarise our results and discuss their implications for core-collapse supernovae. No matter how exhaustive one's work is, there is always room for improvements. Therefore, we conclude with an outlook on further research.

Chapter 2

Magnetohydrodynamics

2.1 Magnetohydrodynamics equations

Magnetohydrodynamics (MHD) equations describe the motion of a *plasma*[1](later also called *fluid* in this thesis) interacting with a magnetic field. They emerge from combining *Maxwell's equations*, which describe interactions of electromagnetic fields, with equations of fluid dynamics. In this thesis, vectors and tensors are written in bold. We omit the tensor dot product symbol, $\otimes$. According to this notation, in the equation $\mathbf{D} = \mathbf{AC} \equiv \mathbf{A} \otimes \mathbf{C}$, $\mathbf{D}$ is a second rank tensor if $\mathbf{A}$ and $\mathbf{C}$ are vectors. We use CGS units with a redefined magnetic field $\mathbf{b} \equiv \mathbf{B}/\sqrt{4\pi}$,[2] in which Maxwell's equations read

$$\nabla \times \mathbf{E} = -\frac{\sqrt{4\pi}}{c}\partial_t \mathbf{b}, \tag{2.1}$$

$$\nabla \times \mathbf{b} = \frac{1}{\sqrt{4\pi}c}\partial_t \mathbf{E} + \frac{\sqrt{4\pi}}{c}\mathbf{j}, \tag{2.2}$$

$$\nabla \cdot \mathbf{E} = 4\pi\rho_c, \tag{2.3}$$

$$\nabla \cdot \mathbf{b} = 0, \tag{2.4}$$

where $\mathbf{E}$ is the electric field, ρ_c and $\mathbf{j}$ denote the density of electric-charge and -current, respectively, and $c \approx 3 \times 10^{10}$ cm s^{-1} is the speed of light.

The fluid dynamics equation consist of: (i) the conservation of mass

$$\partial_t \rho + \nabla \cdot (\rho \mathbf{v}) = 0,, \tag{2.5}$$

where ρ and $\mathbf{v}$ are fluid density and velocity, respectively, (ii) the conservation of energy, which we discuss later, and (iii) the *Navier-Stokes equations* describing the motion of a fluid element

$$\rho\left(\partial_t \mathbf{v} + \mathbf{v} \cdot \nabla \mathbf{v}\right) = -\nabla p + \nabla \cdot \mathbf{T} + \mathbf{f}, \tag{2.6}$$

[1] Plasma is an ionised gas.

[2] There is no other area of physics but electrodynamics, where six different systems of units exist (see, e.g. Jackson (1998)) and four of them (Gaussian, Heaviside-Lorentz, Planck and SI) are commonly used. Therefore, the reader may question the reasonableness of introducing yet another system modification. The main advantage of the units used by us is the elimination of many somewhat awkward 4π factors, which is beneficial for numerical calculations. The MHD equations in this system look like SI equations with the magnetic permeability equal to one, i.e. $\mu_0 = 1$, e.g. the Alfvén speed reads $c_\mathrm{A} = b/\sqrt{\rho}$, instead of $c_\mathrm{A} = B/\sqrt{4\pi\rho}$.

where $\mathbf{T}$ and $\mathbf{f}$ are the viscous stress tensor and the density of external forces, respectively. We consider a scalar model for viscosity, which is valid for isotropic fluids. In this approximation, the stress tensor reads

$$\mathbf{T} = \rho\nu\left((\nabla\mathbf{v}) + (\nabla\mathbf{v})^T\right) + \rho(-\tfrac{2}{3}\nu + \xi)(\nabla\cdot\mathbf{v})\mathbf{I}, \tag{2.7}$$

where ν and ξ are the (kinematic) shear and bulk viscosity,[3] respectively, and $\mathbf{I}$ denotes the identity matrix. In the presence of an electromagnetic field, the Lorentz force will act on the fluid element. Additionally, in the external gravitational potential φ, the fluid will be attracted with the gravity force density equal to $-\rho\nabla\varphi$. Hence,

$$\mathbf{f} = \rho_c\mathbf{E} + \frac{\sqrt{4\pi}}{c}\mathbf{j}\times\mathbf{b} - \rho\nabla\varphi. \tag{2.8}$$

For non-relativistic motions, i.e. for $v \ll c$, the above equations can be simplified. The displacement current ($\partial_t\mathbf{E}/\sqrt{4\pi}c$) in Ampère's law with Maxwell's correction (2.2) is of order $O(v^2/c^2)$ and can be neglected. The electric current can be determined from the original Ampère's law instead:

$$\mathbf{j} = \frac{c}{\sqrt{4\pi}}\nabla\times\mathbf{b}. \tag{2.9}$$

Moreover, one can easily show that in the Newtonian limit, the electrostatic contribution to the Lorentz force is negligible, i.e. $\rho_c|\mathbf{E}| \ll |(\sqrt{4\pi}/c)\mathbf{j}\times\mathbf{b}|$. Therefore, we no longer need Poisson's law (2.3) to determine the spatial distribution of the charge. The electric field becomes a secondary quantity, which can be eliminated from Maxwell's equation. By combining Ohm's law:

$$\mathbf{E} = -\frac{\sqrt{4\pi}}{c}\mathbf{v}\times\mathbf{b} + \frac{4\pi\eta}{c^2}\mathbf{j}, \tag{2.10}$$

where η denotes resistivity,[4] with Faraday's law (2.1), we obtain the induction equation

$$\partial_t\mathbf{b} = \nabla\times(\mathbf{v}\times\mathbf{b}) - \nabla\times(\eta\nabla\times\mathbf{b}). \tag{2.11}$$

The gas's specific internal energy, e, can be increased by Ohmic dissipation ($4\pi\eta j^2/c^2$) and viscous heating ($\nabla\mathbf{v}:\mathbf{T}$):

$$\begin{aligned}\rho(\partial_t e + \mathbf{v}\cdot\nabla e) + (\Gamma-1)\rho e\nabla\cdot\mathbf{v} = \eta(\nabla\times\mathbf{b})^2 + \rho\nu(\nabla\mathbf{v}) : \left((\nabla\mathbf{v}) + (\nabla\mathbf{v})^T\right) + \\ \rho(-\tfrac{2}{3}\nu + \xi)(\nabla\cdot\mathbf{v})^2\mathbf{I},\end{aligned} \tag{2.12}$$

where the colon denotes the double-dot product, i.e.

$$\nabla\mathbf{v} : \mathbf{T} \equiv \sum_i\sum_j \frac{\partial v_j}{\partial x^i}T^{ij}. \tag{2.13}$$

From Eq. (2.12), a gas pressure, p, can be determined. For an ideal gas equation of state (EOS), we have

$$p = (\Gamma-1)e\rho, \tag{2.14}$$

where Γ is the adiabatic index.

[3] In this thesis by *viscosity* we always mean the *kinematic viscosity*, which is related to the *dynamic viscosity*, μ, by the relation $\mu = \nu\rho$.

[4] In MHD also called *magnetic diffusivity*.

Eqs. (2.4), (2.5), (2.6), (2.11) and (2.12) constitute the final set of Newtonian *resistive-viscous MHD equations* in an external gravitational field:

$$\partial_t \rho + \nabla \cdot (\rho \mathbf{v}) = 0, \tag{2.15}$$

$$\rho\left(\partial_t \mathbf{v} + \mathbf{v}\cdot\nabla\mathbf{v}\right) = -\nabla p + \rho\left(\xi + \tfrac{\nu}{3}\right)\nabla(\nabla\cdot\mathbf{v}) + \nu(\nabla\rho)\cdot\left((\nabla\mathbf{v}) + (\nabla\mathbf{v})^T\right) + \left(\xi - \tfrac{2}{3}\nu\right)(\nabla\cdot\mathbf{v})\nabla\rho + \rho\nu\nabla^2\mathbf{v} + (\nabla\times\mathbf{b})\times\mathbf{b} - \rho\nabla\varphi, \tag{2.16}$$

$$\rho(\partial_t e + \mathbf{v}\cdot\nabla e) + (\Gamma-1)e\rho\nabla\cdot\mathbf{v} = \eta(\nabla\times\mathbf{b})^2 + \rho\nu(\nabla\mathbf{v}) : \left((\nabla\mathbf{v}) + (\nabla\mathbf{v})^T\right) + \rho(-\tfrac{2}{3}\nu + \xi)(\nabla\cdot\mathbf{v})^2\mathbf{I}, \tag{2.17}$$

$$\partial_t \mathbf{b} = \nabla\times(\mathbf{v}\times\mathbf{b}) - \nabla\times(\eta(\nabla\times\mathbf{b})), \tag{2.18}$$

$$\nabla\cdot\mathbf{b} = 0. \tag{2.19}$$

Not in every physical system, the influence of resistivity or viscosity is equally important. The measure for that are two very important dimensionless numbers. The hydrodynamic Reynolds number, or just the *Reynolds number*, is a ratio of internal to viscous forces:

$$R_\mathrm{e} \equiv \frac{LV}{\nu}, \tag{2.20}$$

where L and V respectively are the characteristic length and velocity of the system. The Reynolds number determines the character of a flow. For $R_\mathrm{e} \lesssim 2000$, the flow is *laminar* (smooth and orderly), for $R_\mathrm{e} \gtrsim 4000$, the flow becomes *turbulent* (randomly fluctuating and disorderly). The exact values of these numbers depend on the geometry of the system. In the limit of infinitely large Reynolds number, the flow is inviscid. The *magnetic Reynolds number* is a ratio of magnetic field advection to diffusion:

$$R_\mathrm{m} \equiv \frac{LV}{\eta}. \tag{2.21}$$

For $R_\mathrm{m} \ll 1$, the fluid motion can be neglected in the induction equation (2.18), which becomes the magnetic diffusion equation

$$\partial_t \mathbf{b} = \eta\nabla^2\mathbf{b}. \tag{2.22}$$

For $R_\mathrm{m} \to \infty$, resistive effects become negligible and the induction equation can be approximated as

$$\partial_t \mathbf{b} = \nabla\times(\mathbf{v}\times\mathbf{b}), \tag{2.23}$$

which has two direct consequences: *flux freezing* and *conservation of flux*. The former one means that magnetic field lines always co-move with the fluid (as if they were "frozen in" the plasma). The latter one states that if there is no magnetic dissipation in the system, the magnetic flux is conserved. Another dimensionless quantity, which can be constructed from the Reynolds numbers, is the *magnetic Prandtl number*:

$$P_\mathrm{m} \equiv \frac{R_\mathrm{m}}{R_\mathrm{e}} = \frac{\nu}{\eta}. \tag{2.24}$$

It is the ratio of kinetic to magnetic dissipation.

Many astrophysical flows are characterised by very large hydrodynamic and magnetic Reynolds numbers of order $R_\mathrm{e}, R_\mathrm{m} \sim 10^6$–$10^{16}$. For such systems, the resistive and viscous effects can be neglected and the flow evolution can be very well approximated by *ideal MHD equations*. They are obtained from Eqs. (2.15)–(2.19) by putting $\nu = \xi = \eta = 0$. This simplification not only removes some terms from the non-ideal MHD equations, but also changes their mathematical properties. We will discuss this issue later in the text.

Ideal MHD is described by a set of non-linear hyperbolic[5] partial differential equations, which can be written in a *conservation form*, i.e.

$$\partial_t \mathbf{U} + \nabla \cdot \mathcal{F}(\mathbf{U}) = 0, \tag{2.25}$$

where $\mathbf{U}$ is a set of conserved quantities and $\mathcal{F}$ is a set of associated fluxes. We neglect the gravity effects and after some algebra, we can cast the ideal MHD equations in their conservation form (the details can be found in, e.g. Goedbloed & Poedts (2004)):

$$\partial_t \rho + \nabla \cdot (\rho \mathbf{v}) = 0, \tag{2.26}$$

$$\partial_t (\rho \mathbf{v}) + \nabla \cdot \left[\rho \mathbf{v}\mathbf{v} + \left(p + \tfrac{1}{2}b^2\right)\mathbf{I} - \mathbf{b}\mathbf{b}\right] = 0, \tag{2.27}$$

$$\partial_t \left(\tfrac{1}{2}\rho v^2 + \rho e + \tfrac{1}{2}b^2\right) + \nabla \cdot \left[\left(\tfrac{1}{2}\rho v^2 + \rho e + p + b^2\right)\mathbf{v} - \mathbf{v}\cdot\mathbf{b}\mathbf{b}\right] = 0, \tag{2.28}$$

$$\partial_t \mathbf{b} + \nabla \cdot (\mathbf{v}\mathbf{b} - \mathbf{b}\mathbf{v}) = 0, \tag{2.29}$$

$$\nabla \cdot \mathbf{b} = 0. \tag{2.30}$$

The conserved quantities in ideal MHD are (in the brackets we write their densities): mass (ρ), momentum ($\pi = \rho\mathbf{v}$) , total energy ($e_{\rm tot} = \frac{1}{2}\rho v^2 + \rho e + \frac{1}{2}b^2$) and magnetic flux ($\mathbf{b}$). Their associated fluxes can be expressed as a combination of $\rho, \pi, e_{\rm tot}$ and $\mathbf{b}$. From the mathematical and physical point of view, both formulations of the ideal MHD equations, i.e. Eqs. (2.15)-(2.19) expressed in the primitive (not conserved) variables $\mathbf{v}, \mathbf{b}, \rho, e$, (or a combination of any two thermodynamical variables) and Eqs. (2.26)-(2.30) expressed in the conserved variables $\pi, \mathbf{b}, \rho, e_{\rm tot}$, are equivalent. However, as we will see in the next section, the latter formulation is much more suitable for numerical integration.

The non-ideal MHD equations can also be cast into conservative form (2.25). After some calculations, from Eqs. (2.15)-(2.19), we obtain

$$\partial_t \rho + \nabla \cdot (\rho \mathbf{v}) = 0, \tag{2.31}$$

$$\begin{aligned}\partial_t (\rho \mathbf{v}) + \nabla \cdot \Big[\rho \mathbf{v}\mathbf{v} + \left(p + \tfrac{1}{2}b^2\right)\mathbf{I} - \mathbf{b}\mathbf{b} - \\ \rho\nu\left((\nabla\mathbf{v}) + (\nabla\mathbf{v})^T\right) + \rho\left(\tfrac{2}{3}\nu - \xi\right)(\nabla\cdot\mathbf{v})\mathbf{I}\Big] = 0,\end{aligned} \tag{2.32}$$

$$\begin{aligned}\partial_t \left(\tfrac{1}{2}\rho v^2 + \rho e + \tfrac{1}{2}b^2\right) + \nabla \cdot \Big[\left(\tfrac{1}{2}\rho v^2 + \rho e + p + b^2\right)\mathbf{v} - \mathbf{v}\cdot\mathbf{b}\mathbf{b} + \\ \eta(\mathbf{b}\cdot\nabla\mathbf{b} - \tfrac{1}{2}\nabla b^2) - \rho\nu(\tfrac{1}{2}\nabla v^2 + \mathbf{v}\cdot\nabla\mathbf{v}) - \rho(-\tfrac{2}{3}\nu + \xi)\mathbf{v}(\nabla\cdot\mathbf{v})\Big] = 0,\end{aligned} \tag{2.33}$$

$$\partial_t \mathbf{b} - \nabla \times [\mathbf{v}\times\mathbf{b} + \eta(\nabla\times\mathbf{b})] = 0, \tag{2.34}$$

$$\nabla \cdot \mathbf{b} = 0. \tag{2.35}$$

We see a few differences with respect to the ideal MHD Eqs. (2.26)-(2.30). First of all, shear and bulk viscosity enter the fluxes of momentum- and energy-density, giving rise to additional ways of transporting these quantities. Shear and bulk viscosities are also sometimes called diffusion or transport coefficients. Similarly, magnetic flux can be transported not only by the flow but also by resistivity, which will try to remove (smooth out) magnetic field gradients. Because of this feature, resistivity is also sometimes called magnetic diffusivity. A term proportional to resistivity is also present in the flux of the energy density, because magnetic field energy can be converted to internal or kinetic energy. Another difference can be noted in the induction Eq. (2.34), which we wrote in a somewhat different conservation form, i.e.

$$\partial_t \mathbf{U} + \nabla \times \mathcal{F}(\mathbf{U}) = 0, \tag{2.36}$$

[5] We explain this term in the next section.

which is, in general, valid only for vector quantities (and in MHD only for a magnetic field).

MHD equations can be extended to take into account additional physical phenomena. One of the most important of them for astrophysical applications is gravity. Including terms proportional to the gravitational force density, $-\rho\nabla\varphi$, where φ is an external gravitational potential, in the MHD Eqs. (2.31)-(2.35), leads to

$$\partial_t \rho + \nabla\cdot(\rho\mathbf{v}) = 0, \tag{2.37}$$

$$\partial_t(\rho\mathbf{v}) + \nabla\cdot\left[\rho\mathbf{v}\mathbf{v} + \left(p+\tfrac{1}{2}b^2\right)\mathbf{I} - \mathbf{b}\mathbf{b} - \right.$$

$$\left.\rho\nu\left((\nabla\mathbf{v}) + (\nabla\mathbf{v})^T\right) + \rho\left(\tfrac{2}{3}\nu - \xi\right)(\nabla\cdot\mathbf{v})\mathbf{I}\right] = -\rho\nabla\varphi, \tag{2.38}$$

$$\partial_t\left(\tfrac{1}{2}\rho v^2 + \rho e + \tfrac{1}{2}b^2\right) + \nabla\cdot\left[\left(\tfrac{1}{2}\rho v^2 + \rho e + p + b^2\right)\mathbf{v} - \mathbf{v}\cdot\mathbf{b}\mathbf{b} + \right.$$

$$\left.\eta(\mathbf{b}\cdot\nabla\mathbf{b} - \tfrac{1}{2}\nabla b^2) - \rho\nu(\tfrac{1}{2}\nabla v^2 + \mathbf{v}\cdot\nabla\mathbf{v}) - \rho(-\tfrac{2}{3}\nu + \xi)\mathbf{v}(\nabla\cdot\mathbf{v})\right] = -\rho\mathbf{v}\cdot\nabla\varphi, \tag{2.39}$$

$$\partial_t\mathbf{b} - \nabla\times[\mathbf{v}\times\mathbf{b} + \eta(\nabla\times\mathbf{b})] = 0, \tag{2.40}$$

$$\nabla\cdot\mathbf{b} = 0. \tag{2.41}$$

In the presence of an external gravitational potential, total momentum and energy are no longer conserved.[6] Note also that it is no longer possible to write Eqs. (2.37)-(2.41) in a homogeneous conservative form (Eqs. (2.25) and (2.36)). The reason for this is that the terms proportional to the gravitational force density cannot be written as a divergence but give rise to source terms. Eqs. (2.37)-(2.41) are written in an inhomogeneous conservation form , i.e.

$$\partial_t\mathbf{U} + \nabla\cdot\mathcal{F}(\mathbf{U}) = \mathbf{S}, \tag{2.42}$$

$$\partial_t\mathbf{U} + \nabla\times\mathcal{F}(\mathbf{U}) = \mathbf{S}, \tag{2.43}$$

$$\tag{2.44}$$

where $\mathbf{S}$ are source terms. Another example of a physical process leading to additional source terms are nuclear reactions. They can cause energy release or consumption, giving rise to source and sink terms, respectively, in the energy equation.

MHD is described by non-linear partial differential equations which for many physical systems are too complicated to be solved analytically. Therefore, computer simulations become an indispensable tool for studying MHD phenomena. In this dissertation, we use an Eulerian finite-volume MHD code, AENUS, developed by Obergaulinger (2008). In the next section, we briefly discuss how to solve MHD equations numerically. Since it is a very broad topic (see the book by Goedbloed et al. (2010)), we will mainly concentrate on the methods used in AENUS.

2.2 Numerical methods

In this section, we introduce methods of computational MHD. We begin with discussing general problems of numerical analysis, in particularly, the origin of numerical errors. Then, we describe the ideal MHD equations' mathematical properties. They are exploited in constructing appropriate numerical schemes for MHD. In general, we can say that they heavily rely on methods developed for computational hydrodynamics (see, e.g. Toro (1997), Laney (1998), LeVeque (2002)). Next, we show how inclusion of non-ideal effects, i.e. viscosity and resistivity, changes mathematical features of the MHD equations. At the end of this section, we once again discuss numerical errors of computational MHD, this time from a different perspective. We introduce the concept of numerical viscosity and resistivity.

[6] By "total" momentum and energy, we mean the momentum and the energy of the considered plasma, which should be treated as a subsystem of some global system, whose energy and momentum must be always conserved.

2.2.1 Numerical errors

Real functions cannot be exactly represented in computers for several reasons. Firstly, already storing a single real number consisting of infinitely many digits would require an infinite computer memory. Secondly, a function $f(x)$ defined on an interval $[a,b]$ should be represented for infinitely many points. Not to mention the fact, that the set of real number is uncountable. Therefore, in any computational approach, the function $f(x)$ needs to be represented discretely, e.g. for a finite number of points $\{x_1,\ldots,x_N\} \in [a,b]$. Such a discretised approximation of $f(x)$ will be denoted with $\hat{f}^N(x)$. We have just described a numerical representation of functions by points, which is used in so-called *finite difference* methods. However, some other representations are possible. In *finite volume* methods, functions are approximated (represented) by their cell averages. In *finite element* methods, functions are approximated by *basic functions*, i.e. a finite set of local piecewise polynomials. In this section, we will present equations for calculating numerical errors which are only valid for finite difference methods. However, writing analogous equations for the other representations is rather straightforward (yet the final form of these equations is somewhat longer). We will discuss finite volume methods in Sec. 2.2.2.

Many computational problems consist in solving differential equations. For each of them, we should choose a suitable numerical method, with which an approximate solution $\hat{f}^N(x)$ will be found. We should be able to estimate how much this approximation differs from the exact solution $f(x)$. This can be done with the help of a norm function. Although one can define infinitely many of them, only several norm functions are commonly used, e.g. the popular in functional analysis L^2-norm for quadratically integrable functions is given by

$$||f-g||_2 \equiv \left(\int_a^b [f(x)-g(x)]^2 \mathrm{d}x/(b-a) \right)^{1/2}. \tag{2.45}$$

One can also define its counterpart in discrete analysis. In general, the L^p-norm for discrete functions is defined as

$$||f-\hat{f}^N||_p \equiv \left(\frac{1}{N} \sum_{i=1}^{N} |f(x_i)-\hat{f}^N(x_i)|^p \right)^{1/p}. \tag{2.46}$$

The most popular ones are the L^1- and the L^2-norms. With one of these norms, say the L^2, we can measure the *global truncation error*, i.e. the difference between the approximate solution $\{\hat{f}^N(x)\} \equiv \{\hat{f}^N(x_1),\ldots,\hat{f}^N(x_N)\}$ and the exact solution $f(x)$. One of the basic requirements for any sound numerical scheme is that for $N \to \infty$, the global truncation error vanishes, i.e

$$\lim_{N\to\infty} ||f-\hat{f}^N||_2 = 0. \tag{2.47}$$

We say then that the approximate solution converges to the exact solution in the norm L^2.

Eq. (2.46) gives the difference between the functions in the whole domain. It is sometimes useful to consider the *local truncation error* E_i:

$$E_i \equiv f(x_i) - \hat{f}^N(x_i). \tag{2.48}$$

It measures the difference between the exact and approximate solution at a given point, x_i.

As we have already written before, real numbers have infinitely many decimals, whereas in computer calculations, we can only use numbers with a finite number of significant digits (typically ≈ 10). This leads to the so-called *round-off error* R_i:

$$R_i \equiv \hat{f}^N(x_i) - \hat{f}^N_{\mathrm{num}}(x_i), \tag{2.49}$$

where $\hat{f}^N(x_i)$ is the theoretical value for the given numerical scheme, when operating on real numbers and $\hat{f}^N_{\rm num}(x_i)$ is the actually calculated value by the computer. Note that the convergence in the sense of Eq. (2.47) is only possible if working with real numbers.

Finally, we define the *total error* as $|f(x_i) - \hat{f}^N_{\rm num}(x_i)|$. It is elementary to show, that

$$|f(x_i) - \hat{f}^N_{\rm num}(x_i)| \leq |E_i| + |R_i|. \tag{2.50}$$

The total error is limited by the sum of the absolute values of the truncation and round-off error. Usually, the latter is much smaller than the former. Typically, in computational astrophysics we deal with time dependent problems. Therefore, it is of crucial importance to use only methods for which the truncation errors do not grow unboundedly with time.

2.2.2 Hyperbolic conservation laws

As we have already written in Sec. 2.1, MHD equations consist of a set of nonlinear conservation laws. In nonlinear dynamics, shocks, contact and tangential discontinuities can spontaneously arise from continuous initial data. Across these discontinuities, the so-called Rankine-Hugoniot (or jump) conditions must hold (see, e.g. Goedbloed & Poedts (2004)), i.e. fluxes of conserved quantities must be continuous. It is very important that these conditions are also fulfilled in a discretised version of MHD equations. Hou & Le Floch (1994) showed through a rigorous mathematical analysis that using any *finite difference* scheme in a non-conservative form to solve numerically a scalar conservation law will lead to significant errors growing with time. This is why the MHD Eqs. (2.15)–(2.19) are not suitable for a numerical integration and we transformed them to an inhomogeneous conservation form (Eqs. (2.37)–(2.41)), which in general can be written as

$$\partial_t \mathbf{U} + \nabla \cdot \mathcal{F}(\mathbf{U}) = \mathbf{S}, \tag{2.51}$$

$$\partial_t \mathbf{U} + \nabla \times \mathcal{F}(\mathbf{U}) = \mathbf{S}, \tag{2.52}$$

where $\mathbf{U}$ is a set of conserved variables (which can be vectors or scalars for Eq. 2.52 and only vectors for Eq. (2.52)), $\mathcal{F}(\mathbf{U})$ and $\mathbf{S}$ are fluxes and sources associated with them, respectively. With the help of Gauss's and Stokes' theorems, we can cast the differential conservation laws (2.51) and (2.52) into their integral form, i.e.

$$\int_{\mathcal{V}} \partial_t \mathbf{U} \mathrm{d}\mathcal{V} + \int_{\partial\mathcal{V}} \mathcal{F} \cdot \mathbf{n} \mathrm{d}\Sigma = \int_{\mathcal{V}} \mathbf{S} \mathrm{d}\mathcal{V}, \tag{2.53}$$

$$\int_{\Sigma} \partial_t \mathbf{U} \mathrm{d}\Sigma + \int_{\partial\Sigma} \mathcal{F} \cdot \mathbf{l} \mathrm{d}\mathcal{L} = \int_{\Sigma} \mathbf{S} \mathrm{d}\Sigma, \tag{2.54}$$

where $\mathcal{V}$, Σ and $\mathcal{L}$ are volume, surface and surface's contour (boundary), respectively, $\mathbf{n}$ is a vector normal to the surface and $\mathbf{l}$ is a vector tangent to the surface's contour. Eq. (2.53) states that the amount of conserved quantities $\mathbf{U}$ in a given volume can only change due to fluxes $\mathcal{F}$ passing through its boundaries and due to sources $\mathbf{S}$ creating or destroying $\mathbf{U}$ within the volume. Eq. (2.54) has an analogous interpretation for quantities conserved on a surface. In the absence of external forces and sinks, MHD equations can be written in a homogeneous conservation form (see Eqs. (2.26)-(2.30) or Eqs. (2.31)-(2.35)), i.e.

$$\partial_t \mathbf{U} + \nabla \cdot \mathcal{F}(\mathbf{U}) = 0, \tag{2.55}$$

$$\partial_t \mathbf{U} + \nabla \times \mathcal{F}(\mathbf{U}) = 0. \tag{2.56}$$

For the sake of simplicity, we begin with a discussion of the conservation law (2.55) in one spatial dimension, i.e.

$$\partial_t \mathbf{U} + \nabla_x \cdot \mathcal{F}(\mathbf{U}) = 0. \tag{2.57}$$

This equation can be brought to a quasi-linear form,

$$\partial_t \mathbf{U} + \mathfrak{F} \partial_x \mathbf{U} = 0, \tag{2.58}$$

where

$$\mathfrak{F}_{ij} \equiv \frac{\partial \mathcal{F}_i}{\partial U^j} \tag{2.59}$$

is the Jacobian matrix of the transformation. System (2.57) is called *hyperbolic* if $\mathfrak{F}$ is diagonalisable and all its eigenvalues, $\lambda_i, i = 1, \ldots, n$, are real. Moreover, if all of them are additionally distinct, the system is called *strictly hyperbolic*. If none of the eigenvalues is real, the system is called *elliptic*. Note that from the dimensional analysis of Eq. (2.58), we see that the eigenvalues of $\mathfrak{F}$ must have a dimension of velocity. For ideal MHD equations, which are hyperbolic, $\mathfrak{F}$ is diagonalisable and can be decomposed into

$$\mathfrak{F} = \mathbf{R} \mathbf{\Lambda} \mathbf{R}^{-1}, \tag{2.60}$$

where $\mathbf{\Lambda} = \mathrm{diag}(\lambda_1, \ldots, \lambda_n)$ is a diagonal matrix of eigenvalues and $\mathbf{R} = (\mathbf{r}_1 | \ldots | \mathbf{r}_n)$ is a matrix of right eigenvectors, i.e.

$$\mathfrak{F} \mathbf{r}_i = \lambda_i \mathbf{r}_i \qquad \text{for} \quad i = 1, \ldots, n. \tag{2.61}$$

After changing to characteristic variables

$$\mathbf{Q} \equiv \mathbf{R}^{-1} \mathbf{U}, \tag{2.62}$$

with the help of decomposition (2.60), we can cast Eq. (2.58) into its characteristic form, i.e.

$$\partial_t \mathbf{Q} + \mathbf{\Lambda} \partial_x \mathbf{Q} = 0. \tag{2.63}$$

Note that since $\mathbf{\Lambda}$ is diagonal, the original system of partial differential equations (PDEs; Eq. (2.58)) decouples into n independent scalar equations. From the above equation, we see that characteristic variables Q_i remain constant on curves $\mathrm{d}x = \lambda_i \mathrm{d}t$ (called characteristics of PDEs), in the (x,t) plane. Due to this fact, characteristic variables are also called Riemann invariants. They propagate at the speed given by a corresponding eigenvalue λ_i. Therefore, λ_i are called characteristic velocities of the system. Note that if all eigenvalues λ_i are constant, Eq. (2.63) basically consists of n independent linear advection equations, where the advection velocity of the i-th characteristic variable Q_i is given by λ_i. In general, eigenvalues are only approximately constant in the vicinity of a given point in the (x,t) plane. The method of characteristics can be used to solve an initial value problem of PDEs (2.58). If we decompose conserved quantities into Riemann invariants (with the help of transformations (2.62), we can locally compute the temporal evolution by advecting the latter ones with their corresponding characteristic velocities λ_i. In a system with $n = 2$ conserved quantities, it is always possible to find both Riemann invariants. For $n > 2$, we may not always be able to find a full set of Riemann invariants obeying Eq. (2.63).

Unusual, but useful notation

Since the super- and sub-scripts will be quite "overloaded" in our discussion, it is very important at this point to set and use a consistent notation. In Sec. 2.2.2, we defined $\mathbf{U}$ as a set of

conserved variables, which could be scalars or vectors (or in principle even tensors of a higher rank). Hence, $\mathbf{U}$ can be imagined as a somehow ordered combination of these quantities, e.g. $\mathbf{U} = (U^j) = (a^1, a^2, a^3, b, c^1, c^2, c^3)$, where $\mathbf{a}$ is conserved vector quantity and a^1, a^2, a^3 are its components, b is a conserved scalar and c^1, c^2, c^3 are components of another conserved quantity. From now on, we will not perform calculations for any particularly chosen component of $\mathbf{U}$, therefore we will use neither super- nor sub-scripts to specify components of $\mathbf{U}$, i.e. $\mathbf{U}^j \neq (U^j)$ and $\mathbf{U}_j \neq (U_j)$. We just want to "free" these indices for other purposes. To reduce possible confusion and simplify notation, we will use variable u in some equations, which should be understood as representing any component of $\mathbf{U}$. Hence, if we write an equation, which holds for u, it should be understood that we have in mind a set of equations holding for every (U^j). Analogically, we introduce the variable s to represent the components of sources (S^j) in a similar way. The set of fluxes can be written as a two-dimensional matrix $\mathcal{F}$ (a representation of a second rank tensor). Therefore, we need two indices to specify a component of $\mathcal{F}$, i.e. $\mathcal{F} = (F^{ij})$, where the first index, $i \in \{1,2,3\}$, refers to the spatial direction in which the flux of the conserved variable U^j moves. However, in a one dimensional system, we can "forget" about the tensorial nature of $\mathcal{F}$, as $i \equiv 1$, i.e. the flux can only move in one direction. Therefore, when limiting our considerations to one spatial dimension, we will use the variable f to represent the components (F^{1j}).

To illustrate these newly introduced conventions, let us consider Eq. (2.51), i.e.

$$\partial_t \mathbf{U} + \nabla \cdot \mathcal{F}(\mathbf{U}) = \mathbf{S}.$$

In the standard index notation (which we will not use, apart from this example), it can be written as

$$\partial_t U^j + \partial_{x^i} F^{ij} = S^j, \quad \forall j \tag{2.64}$$

where $i = \{1,2,3\}$, and the Einstein summation convention was used. In a one dimensional system, the above equation simplifies to

$$\partial_t \mathbf{U} + \nabla_x \cdot \mathcal{F}(\mathbf{U}) = \mathbf{S}, \tag{2.65}$$

or equivalently in the index notation

$$\partial_t U^j + \partial_x F^{1j} = S^j, \quad \forall j \tag{2.66}$$

According to our convention, this equation can be simply written as

$$\partial_t u + \partial_x f = s. \tag{2.67}$$

Eq. (2.67) looks like a scalar conservation law, but in our notation, it is equivalent to Eq. (2.65). We hope that these newly adapted convention will not lead to any confusion.

Spatial discretisation

To integrate hyperbolic equations numerically, we have to decompose their continuous domain (both in space in time) into discrete elements. In *high-resolution shock-capturing* (HRSC) schemes,[7] the physical domain is divided into a finite number of fixed in space zones $\mathcal{Z}_i$ of volumes

[7] In *shock capturing* methods, as opposed to *shock-fitting* or (also sometimes called) *shock-tracing*-methods, Rankine-Hugoniot are not explicitly enforced. Shock capturing methods must be conservative, since conservative numerical methods automatically locate shocks correctly (see, e.g. Laney (1998)).

$\mathcal{V}_i$. In *finite difference* schemes,[8] conserved variables $\mathbf{U}(\mathbf{x})$ are approximated by their values at the zone centres, i.e.

$$\mathbf{U}_i = \mathbf{U}(\mathbf{x}_i), \tag{2.68}$$

where $\mathbf{x}_i$ is the centre of $\mathcal{Z}_i$. Note that in $\mathbf{U}_i$, the subscript i does not refer to the i-th component of $\mathbf{U}$, but to the approximation of (the whole vector) $\mathbf{U}$ in the i-th zone (which is also a vector). In the standard index notation, the above equation would read

$$(U^j)_i = (U^j)(\mathbf{x}_i), \quad \forall j \tag{2.69}$$

which according to our convention, can be simply written as[9]

$$u_i = u(\mathbf{x}_i). \tag{2.70}$$

In *finite volume* schemes, $u(\mathbf{x})$ is approximated by its volume averages, i.e.

$$u_i = \frac{1}{\mathcal{V}_i}\int_{\mathcal{Z}_i} u(\mathbf{x})\mathrm{d}\mathcal{V}, \tag{2.71}$$

where

$$\mathcal{V}_i = \int_{\mathcal{Z}_i} \mathrm{d}\mathcal{V}. \tag{2.72}$$

Eq. (2.71) is equivalent to

$$\mathbf{U}_i = \frac{1}{\mathcal{V}_i}\int_{\mathcal{Z}_i} \mathbf{U}(\mathbf{x})\mathrm{d}\mathcal{V}. \tag{2.73}$$

In the rest of this chapter, we will mainly focus on the finite volume methods.

The temporal evolution of u is determined from a discretised version of the integral conservation law (2.53), i.e.

$$\partial_t \mathbf{U}_i + \frac{1}{\mathcal{V}_i}\int_{\partial\mathcal{Z}_i} \mathcal{F}\cdot\mathbf{n}\mathrm{d}\Sigma = \frac{1}{\mathcal{V}_i}\int_{\mathcal{Z}_i} \mathbf{S}_i\mathrm{d}\mathcal{V} \tag{2.74}$$

(we remind the reader that the subscript i enumerates zones and not vector components). After neglecting source terms, we obtain the *flux-conservative* form of the above equation

$$\partial_t \mathbf{U}_i + \frac{1}{\mathcal{V}_i}\int_{\partial\mathcal{Z}_i} \mathcal{F}\cdot\mathbf{n}\mathrm{d}\Sigma = 0. \tag{2.75}$$

For the sake of simplicity, we will consider the above equations in one spatial dimension. A generalisation to multi-dimensional systems will be discussed later. Each zone $\mathcal{Z}_i$ extends from its left interface $\mathcal{I}_{i-\frac{1}{2}}$ (at $x_{i-\frac{1}{2}}$) to its right interface $\mathcal{I}_{i+\frac{1}{2}}$ (at $x_{i+\frac{1}{2}}$). The zone centre is located at x_i. The areas of zone surfaces at the left- and the right-interfaces are denoted as $\mathcal{A}_{i-\frac{1}{2}}$ and $\mathcal{A}_{i+\frac{1}{2}}$, respectively. With the help of these definitions, for a one dimensional system, Eq. (2.75) can be written as

$$\partial_t u_i + \frac{1}{\mathcal{V}_i}\left(\mathcal{A}_{i+\frac{1}{2}}\bar{f}_{i+\frac{1}{2}} - \mathcal{A}_{i-\frac{1}{2}}\bar{f}_{i-\frac{1}{2}}\right) = 0, \tag{2.76}$$

[8] Finite-difference schemes derived from a conservation form (e.g. MHD Eqs. (2.26)-(2.30)) tend to be conservative, whereas finite-difference schemes derived from other differential forms (e.g. MHD Eqs. (2.15)-(2.19)) are usually not conservative.

[9] Personally, out of Eqs. (2.68)–(2.70), we find the last one the most transparent, after one gets used to our convention.

where $\bar{f}_{i\pm\frac{1}{2}}$ are surface-averaged fluxes passing through the surfaces $\mathcal{A}_{i\pm\frac{1}{2}}$. To integrate the above equation numerically, we need to find discrete approximations of $\bar{f}_{i\pm\frac{1}{2}}$, which we will simply denote as $f_{i\pm\frac{1}{2}}$. Using this definition, we rewrite Eq. (2.77) as

$$\partial_t u_i(t) + \frac{1}{\mathcal{V}_i}\left(\mathcal{A}_{i+\frac{1}{2}} f_{i+\frac{1}{2}}(t) - \mathcal{A}_{i-\frac{1}{2}} f_{i-\frac{1}{2}}(t)\right) = 0, \tag{2.77}$$

where we explicitly marked the time dependence of the conserved variables and their fluxes. We obtained the above ordinary differential equation (ODE) by discretising original Eq. (2.53) only in space, but not in time. Therefore, the form of Eq. (2.77) is called *semi-discrete*. Once the averaged fluxes $f_{i-\frac{1}{2}}(t)$ and $f_{i+\frac{1}{2}}(t)$ are determined, the above ODE can be integrated numerically in time with, e.g. the Euler method or one of the Runge-Kutta (RK) schemes. Now, we will discuss the time integration procedure in more detail. Later, we will show how to compute the surface-averaged fluxes $f_{i\pm\frac{1}{2}}(t)$ from the volume averaged conserved variables $\{\ldots, u_{i-1}, u_i, u_{i+1}, \ldots\}$.

Time integration

Our goal it to integrate Eq. (2.77) numerically from some initial time t_0 to some final time t_f. Obviously, $u_i(t)$ cannot be determined for every $t \in [t_0, t_\mathrm{f}]$, because the equation's continuous time domain consists of infinitely many points. Therefore, the domain has to be discretised, i.e. represented by a finite number of points $\{t^0, t^1, \ldots, t^n, \ldots, t^N\} \in [t_0, t_\mathrm{f}]$, where $t^0 = t_0$, $t^n < t^{n+1}$, and $t^N = t_\mathrm{f}$. Given that at the initial time $t^0 = t_0$, the zone averages of the conserved variables, $u_i(t^0)$ (shortly denoted as u_i^0), and surfaces averages of their fluxes at the zone interfaces, $f_{i\pm\frac{1}{2}}(t^0)$ (shortly denoted as $f^0_{i\pm\frac{1}{2}}$), are known, we can compute the values of u_i at the time $t^1 = t^0 + \Delta t$ with the help of Eq. (2.77).

The value of the timestep Δt cannot be arbitrarily large for stability reasons. To prevent numerical instabilities, no information is allowed to propagate through more than one zone in one timestep (see, e.g. Laney (1998)). As already discussed before, the information propagation speed is determined by the eigenvalues λ_j of the flux matrix's Jacobian (see Eq. (2.59)). We denote the modulus of the maximum (in absolute value) eigenvalue in the zone $\mathcal{Z}_i$ as $\lambda^i_{\max}$ and the zone width as Δx_i (i.e. $\Delta x_i = x_{i+\frac{1}{2}} - x_{i-\frac{1}{2}}$). Using these definitions, we can express the Courant-Friedrichs-Lewy condition (CFL condition) for the allowed timestep, as

$$\Delta t \leq (\Delta t)^{\max} = \min\left\{\frac{(\Delta x_i)}{\lambda^i_{\max}}\right\}, \tag{2.78}$$

where the index i enumerates all zones in the physical domain. Additionally, we define the CFL factor, which we use to set the maximum timestep in a given simulation, as

$$\Delta t = C_{\mathrm{CFL}} (\Delta t)^{\max}. \tag{2.79}$$

Obviously, from condition (2.78), this factor must not exceed one, i.e.

$$C_{\mathrm{CFL}} \leq 1. \tag{2.80}$$

We rewrite Eq. (2.77) in a somewhat simpler *semi-discrete* form

$$\frac{\mathrm{d}u_i}{\mathrm{d}t} = R_i(u_i, t), \tag{2.81}$$

where $R_i(u_i,t) = -\left(\mathcal{A}_{i+\frac{1}{2}} f_{i+\frac{1}{2}}(t) - \mathcal{A}_{i-\frac{1}{2}} f_{i-\frac{1}{2}}(t)\right)/\mathcal{V}_i$ (the fluxes $f_{i\pm\frac{1}{2}}$ are functions of u_i). For the sake of simplicity, in this paragraph, we drop the subscript i denoting that the variable u was averaged in the zone $\mathcal{Z}_i$. Eq. (2.81) reads then

$$\frac{\mathrm{d}u}{\mathrm{d}t} = R(u,t). \tag{2.82}$$

The value of u after n timesteps will be shortly denoted as

$$u^n \equiv u(t^n). \tag{2.83}$$

Hence, given u^n and Eq. (2.82), our task is to compute u^{n+1} numerically.

The simplest and least accurate way of doing it, is by directly using the definition of the first derivative, i.e.

$$\frac{\mathrm{d}u^n}{\mathrm{d}t} \approx \frac{u^{n+1}-u^n}{\Delta t}, \tag{2.84}$$

hence,

$$u^{n+1} \approx u^n + \Delta t \frac{\mathrm{d}u^n}{\mathrm{d}t} = u^n + \Delta t R(u^n,t^n). \tag{2.85}$$

This is the so-called forward Euler integration scheme, which is only first order accurate. This means that the error, i.e. the difference between the real value of u^{n+1} and its approximation given by the above equation, is proportional to $(\Delta t)^2$. To show this, we use the Taylor expansion to compute u^{n+1} exactly,

$$u^{n+1} = u^n + \sum_{i=1}^{\infty} \frac{\mathrm{d}^i u^n}{\mathrm{d}t^i} \frac{(\Delta t)^i}{i!}. \tag{2.86}$$

We see that the terms of Eq. (2.85) are equal to the expansion up to the terms containing Δt. The Euler scheme has not only a low accuracy order, but is also often unstable.

Runge-Kutta methods One can do a much better job by integrating Eq. (2.82) using a more sophisticated numerical scheme. The commonly used Runge-Kutta methods employ additional trial steps in the interval $[t^n,t^{n+1}]$, in which the values of R(u,t) are computed. With the help of this information, the integration accuracy can be significantly improved. The Runge-Kutta method of the first order is equivalent to the Euler method. The classical fourth order Runge-Kutta method (RK4) uses four steps, i.e.

$$u^{n+1} = u^n + \Delta t \tfrac{1}{6}(k_1 + 2k_2 + 2k_3 + k_4) + O(\Delta t^5), \tag{2.87}$$

where

$$k_1 = R(t^n, u^n), \tag{2.88}$$

$$k_2 = R(t^n + \frac{1}{2}\Delta t, u^n + \frac{1}{2}\Delta t k_1), \tag{2.89}$$

$$k_3 = R(t^n + \frac{1}{2}\Delta t, u^n + \frac{1}{2}\Delta t k_2), \tag{2.90}$$

$$k_4 = R(t^n + \Delta t, u^n + \Delta t k_3). \tag{2.91}$$

A Runge-Kutta method of the q-th order (RK-q) employs q steps

$$u^{n+1} = u^n + \Delta t F(k_1,\ldots,k_q) + O(\Delta t^{q+1}), \tag{2.92}$$

where $F(k_1,\dots,k_q)$ is a linear combination of $k_1,\dots,k_q$. This scheme is equal to Taylor expansion (2.86) up to the terms containing $(\Delta t)^q$, i.e.

$$\Delta t F(k_1,\dots,k_q) = \Delta t \sum_{i=1}^{q} \frac{\mathrm{d}^i u^n}{\mathrm{d}t^i} \frac{(\Delta t)^{i-1}}{i!} + \Delta t \sum_{i=q+1}^{\infty} a_i \frac{\mathrm{d}^i u^n}{\mathrm{d}t^i} \frac{(\Delta t)^{i-1}}{i!}, \tag{2.93}$$

where the coefficients a_i depend on the used scheme and, in principle, can be computed, e.g. for the Euler scheme $q = 1$ and $\forall i, a_i = 0$. In general, we say that an ODE integration scheme is of the q-th order if it differs from the Taylor expansion by terms containing $(\Delta t)^{q+1}$.

Interface fluxes

In the previous paragraphs, we showed how to integrate Eq. (2.77) in time numerically, once the fluxes $f_{i\pm\frac{1}{2}}(t)$ are known. Now, we must discuss how to determine the surface-averaged fluxes $f_{i\pm\frac{1}{2}}(t)$ at the zone interfaces $\mathcal{I}_{i\pm\frac{1}{2}}$, from the zone averages u_i. In the finite volume schemes, we first reconstruct the values of the conserved variables at the zone interfaces, i.e. $u(x_{i\pm\frac{1}{2}})$, from the zone averaged values $\{\dots,u_{i-1},u_i,u_{i+1},\dots\}$. Next, we compute the interface fluxes from the interface values of u. Finally, we apply a *flux function* to determine the fluxes.

Reconstruction Our task is to determine the value of the variable u at a given point x, i.e. $u(x)$, from the zone averages $\{u_{i-m_1},\dots,u_{i-1},u_i,u_{i+1},\dots u_{i+m_2}\}$ (they are called the reconstruction *stencil*, and the *stencil width* equals m_1+m_2+1, where in general not necessarily $m_1 = m_2$). To proceed with computing fluxes, we need to reconstruct the values of the conserved variables at the zone interfaces $\mathcal{I}_{i\pm\frac{1}{2}}$, i.e. $u(x_{i\pm\frac{1}{2}})$. For each zone $\mathcal{Z}_i$, we will construct a function $\hat{u}^i(x)$,[10] which will locally approximate u in the vicinity of $\mathcal{Z}_i$. Note that with this procedure, we obtain two distinct values for $u(x_{i-\frac{1}{2}})$, i.e. $\hat{u}^{i-1}(x_{i-\frac{1}{2}})$ and $\hat{u}^i(x_{i-\frac{1}{2}})$ at the interface $\mathcal{I}_{i-\frac{1}{2}}$, which we will call the left and the right state, respectively, and denote as u^{L} and u^{R}. Hence, at each interface, a discontinuity in the conserved variables arises and we have to solve a Riemann problem to compute the resulting fluxes. We will come back to this problem later, after discussing how to construct functions $\hat{u}^i$ approximating u.

There are three basic requirements, which the interpolating functions $\hat{u}^i$ have to fulfil. Firstly, they have to be *consistent*, i.e. for each zone in the stencil, $\mathcal{Z}_j$ (where $j \in i-m_1,\dots,i+m_2$), the zone average of $\hat{u}^i(x)$ has to be equal to the original zone average u_j, i.e.

$$\int_{\mathcal{Z}_j} \hat{u}^i(x)\mathrm{d}\mathcal{V} = u_j. \tag{2.94}$$

Secondly, $\hat{u}^i$ have to approximate the true function $u(x)$ *accurately*, i.e. the relative error $|\hat{u}^i(x) - u(x)|/|u(x)|$ has to be small within the zone. Thirdly, the reconstruction has to be *stable*.

The simplest reconstruction scheme is a so called *piecewise-constant* (PM) method, which is the least accurate, yet most stable. Its stencil consists of only one zone and the interpolating functions are given by

$$\hat{u}^i(x) = u_i, \quad \text{for } x \in [x_{i-\frac{1}{2}}, x_{i+\frac{1}{2}}]. \tag{2.95}$$

[10] The superscript i for functions $\hat{u}^i$ does not refer to the time dependence of these functions (as it was in the paragraphs on the time integration), but simply enumerates them. We simply came across another quite common situation in mathematics and physics, where in spite of using two different alphabets (i.e. latin and greek), super- and sub-scripts, we could not introduce an unambiguous notation ...

This method is only first-order accurate, i.e. the truncation errors are proportional to the grid width, Δx. We will now demonstrate this rather elementary fact in detail, as this discussion will be an introduction to yet another topic considered later in this chapter. From definition (2.71) of u_i, we have

$$u_i \equiv \frac{1}{\Delta x_i} \int_{x_{i-\frac{1}{2}}}^{x_{i+\frac{1}{2}}} u(x)\mathrm{d}x, \tag{2.96}$$

where $\Delta x_i \equiv x_{i+\frac{1}{2}} - x_{i-\frac{1}{2}}$. With the help of the *first integral mean value theorem*, we can further calculate

$$\frac{1}{\Delta x_i} \int_{x_{i-\frac{1}{2}}}^{x_{i+\frac{1}{2}}} u(x)\mathrm{d}x = \frac{1}{\Delta x_i} u(x_s) \int_{x_{i-\frac{1}{2}}}^{x_{i+\frac{1}{2}}} \mathrm{d}x = u(x_s), \tag{2.97}$$

where $x_{i-\frac{1}{2}} \leq x_s \leq x_{i+\frac{1}{2}}$. Hence, we see that at least at one point, i.e. $x = x_s$, the interpolation function $\hat{u}^i$ defined in Eq. (2.95), gives an exact prediction for the conserved variable u, namely

$$\hat{u}^i(x_s) = u(x_s). \tag{2.98}$$

With the help of the Taylor expansion, we can easily estimate the "reconstruction error" (i.e. $|\hat{u}^i - u|$) at any other point $x \in [x_{i-\frac{1}{2}}, x_{i+\frac{1}{2}}]$, namely

$$|\hat{u}^i(x) - u(x)| = |u(x_s) - u(x)| = |(x - x_s)\partial_x u(x) + O((x - x_s)^2)| \leq |(\Delta x)\partial_x u(x) + O((\Delta x)^2)|, \tag{2.99}$$

where we used the fact that for $x \in [x_{i-\frac{1}{2}}, x_{i+\frac{1}{2}}]$, $|x - x_s| \leq \Delta x$. As we can see, the (maximum) reconstruction error linearly scales with Δx,

$$|\hat{u}^i(x) - u(x)| \propto \Delta x. \tag{2.100}$$

In general, we say that a reconstruction scheme is of the r-th order, when its errors are proportional to $(\Delta x)^r$. Note the difference with respect to the definition of ODE numerical integrators' order. We wrote that a given scheme was of the q-th order, when its errors scaled like $(\Delta t)^{q+1}$ (see the paragraphs on the time integration).

The PM reconstruction scheme belongs to the family of so-called *piecewise-polynomial methods* (the piecewise constant interpolants $\hat{u}^i$ can be treated as 0-th order polynomials). Schemes which have a higher accuracy order are based on wider stencils and employ higher order polynomials to reconstruct the function u. We will demonstrate this for the *piecewise-linear* (PL) reconstruction, which is second-order accurate (i.e. its errors are proportional to $(\Delta x)^2$). We begin the reconstruction process by first constructing two auxiliary first order polynomials

$$\hat{u}^i_+(x) = \frac{u_{i+1} - u_i}{x_{i+1} - x_i}(x - x_i) + u_i, \tag{2.101}$$

$$\hat{u}^i_-(x) = \frac{u_i - u_{i-1}}{x_i - x_{i-1}}(x - x_i) + u_i \tag{2.102}$$

Both of them have the same value at the zone centre, i.e. $\hat{u}^i_+(x_i) = \hat{u}^i_-(x_i) = u_i$. Away from extrema or discontinuities, we could use either of the functions $\hat{u}^i_+(x)$, $\hat{u}^i_-(x)$ as an approximation (final reconstruction) of $u(x)$. However, a problem arises near a discontinuity. An approximation of $u(x)$ based on one-sided gradients can lead to a significant overshooting, creating additional extrema. In a dynamic situation, this can trigger spurious oscillations around discontinuities, which can eventually destabilise the whole system. Therefore, for stability reasons, we require that the *total variation*, i.e.

$$TV[u] \equiv \sum_i |u_{i+1} - u_i| \tag{2.103}$$

does not increase with time. This *total variation diminishing* (TVD) constraint forbids the development of new extrema. From the mathematical point of view, the TVD constraint is exactly fulfilled for linear advection equations, however it may be violated for more general hyperbolic systems. Still, it provides a valuable stability criterion for theses systems and therefore, we are going to use it.

Note that to approximate $u(x)$, we can not only use either $\hat{u}^i_+(x)$ or $\hat{u}^i_-(x)$, but also any normalised linear combination of them. We denote the slopes of the interpolants $\hat{u}^i_\pm$ (i.e. the constant coefficients multiplying x) with the symbols $m^i_\pm$, i.e.

$$m^i_+ = \frac{u_{i+1} - u_i}{x_{i+1} - x_i}, \tag{2.104}$$

$$m^i_- = \frac{u_i - u_{i-1}}{x_i - x_{i-1}}. \tag{2.105}$$

Using these two slopes, we can construct a new slope m^i for the interpolant $\hat{u}^i(x)$ with the help of a so-called slope limiter SL,

$$m^i = \mathrm{SL}(m^i_+, m^i_-). \tag{2.106}$$

Hence, the final form of the interpolant $\hat{u}^i(x)$ will read

$$\hat{u}^i(x) = u_i + m^i(x - x_i). \tag{2.107}$$

For the PL method to fulfil the TVD constraint, we have to construct an appropriate slope limiter. There are many different ways in which it can be done, as an example we will only present the so-called *minmod* slope limiter (see, e.g. Laney (1998)),

$$\mathrm{SL}(m^i_+, m^i_-) = \begin{cases} \frac{m^i_+ + m^i_-}{2}, & \text{for} \quad \mathrm{sign}(m^i_+) = \mathrm{sign}(m^i_-), \\ 0, & \text{for} \quad \mathrm{sign}(m^i_+) \neq \mathrm{sign}(m^i_-). \end{cases} \tag{2.108}$$

The slopes can have different signs in the vicinity of a discontinuity or a maximum. Hence, to prevent spurious oscillations in the former case, the limiter returns 0, basically reverting from the PL reconstruction to the more stable PC reconstruction. Unfortunately, based only on the first derivatives, the TVD limiters cannot distinguish between a discontinuity and a maximum, which leads to an undesired accuracy reduction in the latter case.

To improve this situation, more sophisticated reconstruction methods can be used. The highest order reconstruction schemes implemented in AENUS, are the so-called *monotonicity preserving* (MP) schemes of the 5-th, 7-th and 9-th order (later denoted as the MP5, the MP7 and the MP9 scheme, respectively), which are based on polynomials of the corresponding orders (Suresh & Huynh 1997). In short, all monotonicity preserving methods do not allow for the development of spurious oscillations from monotone initial conditions, which is a stabilising property (however, see the discussion in Laney (1998) on drawback of low order MP schemes). The MP5, the MP7 and the MP9 schemes allow for a good reproduction of smooth extrema and at the same time efficiently suppress spurious oscillations near discontinuities.

Once we construct appropriate interpolants $\hat{u}^i(x)$, we can finally use them to determine interface values of the conserved quantities. In the finite volume approach, we have to compute their averages ($u_{i-\frac{1}{2}}$) in zones $\mathcal{Z}_{i-\frac{1}{2}}$ (ranging from x_{i-1} to x_i), which are staggered with respect to $\mathcal{Z}_i$. Note that to do this, we can use either the interpolants $\hat{u}^i(x)$ or the interpolants $\hat{u}^{i-1}(x)$, which were

obtained from the reconstruction centred at the zone $\mathcal{Z}_i$, or $\mathcal{Z}_{i-1}$, respectively. Both methods will (usually) lead to two distinct interface values,

$$u^{\mathrm{R}}_{i-\frac{1}{2}} = \frac{1}{\mathcal{V}_{i-\frac{1}{2}}} \int_{\mathcal{Z}_{i-\frac{1}{2}}} \hat{u}^{i}(x)\mathrm{d}\mathcal{V}, \tag{2.109}$$

$$u^{\mathrm{L}}_{i-\frac{1}{2}} = \frac{1}{\mathcal{V}_{i-\frac{1}{2}}} \int_{\mathcal{Z}_{i-\frac{1}{2}}} \hat{u}^{i-1}(x)\mathrm{d}\mathcal{V}, \tag{2.110}$$

which we denoted as $u^{\mathrm{R}}_{i-\frac{1}{2}}$ and $u^{\mathrm{L}}_{i-\frac{1}{2}}$, were R and L stand for the *right* and *left* state, respectively.

Flux functions After the reconstruction, we know the interface values of the conserved variables from which we can compute the interface fluxes. At each interface $\mathcal{I}_{i-\frac{1}{2}}$, we have a discontinuity between the left (u^{L}) and the right (u^{R}) states, resulting from using the reconstruction centred at zones $\mathcal{Z}_{i-1}$ and $\mathcal{Z}_i$, respectively. To compute the resulting fluxes, we have to solve a Riemann problem at each interface. Using the upwind properties of hyperbolic systems, we can derive methods to determine a final interface flux by following all waves within the so-called "Riemann fan" explicitly.

In the case of linear advection equations, we can identify a well-defined upwind direction with the help of the sign of the advection velocity v. The final flux should be equal to the upwind one, i.e.

$$f_{i-\frac{1}{2}} = \begin{cases} f^{\mathrm{R}}_{i-\frac{1}{2}}, & \text{for} \quad v \geq 0, \\ f^{\mathrm{L}}_{i-\frac{1}{2}}, & \text{for} \quad v < 0, \end{cases} \tag{2.111}$$

For more complicated non-linear systems, we should first locally transform the system to its characteristic variables. As a result, we would obtain a system of decoupled linear advection equations (see Eq. (2.63)). For each of them, we could use then prescription (2.111) to advect each Riemann invariant with the corresponding eigenspeed (independently of the other eigenstates). We just describe how to construct a so-called *exact Riemann solver* (RS). This procedure introduces a small amount of numerical diffusion to the solution, which is required for a stable evolution.

The main drawback of the exact RSs, however, is that to construct them, we need to find all characteristic variables, i.e. the eigenvectors of the flux Jacobian (defined in Eq. (2.59)). For many systems, it may be complicated or even impossible to do it. Therefore, instead of an exact RS, we may use an *approximate Riemann solver*, which is based on only a limited subset of the characteristic velocities. Approximate RSs do not "open" the full Riemann fan, i.e. they do not follow all waves (which propagate at different speeds) explicitly, but rather describe them by a few representatives. The minimum required information for the simplest approximate RS is the fastest (in absolute value) eigenspeed, $\lambda_{\max}$. The *Lax-Friedrichs* (LF) solver (see, e.g. Laney (1998)) uses this information to compute the (LF) flux,

$$f_{i-\frac{1}{2}} = \frac{1}{2}\left(f^{\mathrm{R}}_{i-\frac{1}{2}} + f^{\mathrm{L}}_{i-\frac{1}{2}}\right) + \frac{\lambda_{\max}}{2\Delta x}\left(u^{\mathrm{R}}_{i-\frac{1}{2}} - u^{\mathrm{L}}_{i-\frac{1}{2}}\right), \tag{2.112}$$

where $f^{\mathrm{L,R}}_{i-\frac{1}{2}} = f(u^{\mathrm{L,R}}_{i-\frac{1}{2}})$ are the right and the left states of the fluxes. The term proportional to $\lambda_{\max}$ in the above expression acts like "numerical diffusion" damping possibly arising numerical instabilities. It makes the LF solver rather diffusive but stable. The main advantage of this solver is that it is very simple and therefore fast.

The LF solver always computes the flux symmetrically, from the left and the right contributions. This feature makes the solver quite inaccurate in a situation, when all characteristic velocities have the same sign, i.e. all waves are moving to the left or to the right (which is the case for *supersonic* flows in hydrodynamics and *supermagnetosonic*[11] flows in magnetohydrodynamics). To improve the accuracy when calculating the flux, we can use two eigenvalues, i.e. the maximum and the minimum ones ($\lambda_{\max}$ and $\lambda_{\min}$, respectively), rather than only the former. This is done in the *Harten-Lax-van Leer* (HLL) Riemann solver (see, e.g. Laney (1998)), whose flux reads

$$f_{i-\frac{1}{2}} = \frac{\lambda^{+}_{i-\frac{1}{2}} f^{\mathrm{L}}_{i-\frac{1}{2}} - \lambda^{-}_{i-\frac{1}{2}} f^{\mathrm{R}}_{i-\frac{1}{2}} + \lambda^{+}_{i-\frac{1}{2}} \lambda^{-}_{i-\frac{1}{2}} (u^{\mathrm{R}}_{i-\frac{1}{2}} - u^{\mathrm{L}}_{i-\frac{1}{2}})}{\lambda^{+}_{i-\frac{1}{2}} - \lambda^{-}_{i-\frac{1}{2}}}, \tag{2.113a}$$

where $\lambda^{+,-}_{i-\frac{1}{2}}$ are given by:

$$\lambda^{+}_{i-\frac{1}{2}} = \max(0, \lambda^{\mathrm{L}}_{i-\frac{1}{2}\,\max}, \lambda^{\mathrm{R}}_{i-\frac{1}{2}\,\max}), \tag{2.113b}$$

$$\lambda^{-}_{i-\frac{1}{2}} = \min(0, \lambda^{\mathrm{L}}_{i-\frac{1}{2}\,\min}, \lambda^{\mathrm{R}}_{i-\frac{1}{2}\,\min}). \tag{2.113c}$$

This solver opens the Riemann fan more accurately (i.e. represents it by more waves). The HLL solver will be especially superior to the LF solver in the above described situation, namely the HLL flux will be one-sided (coming only from one direction).

The most sophisticated approximate Riemann solver implemented in AENUS, is the so-called HLLD solver (Miyoshi & Kusano 2005). It represents the Riemann fan with one more eigenvalue[12] than the HLL solver.

Multidimensional problems

In multidimensional problems, AENUS uses the *dimensional splitting* technique. It successively applies one-dimensional algorithms for every dimension using the *method of lines* (see, e.g. Shu (1997)). For each one dimensional *sweep*, it uses the same initial data, i.e. values of conserved variables, which were determined at the beginning of a timestep.

Constraint transport

One of additional challenges of the numerical MHD, in comparison with hydrodynamics, is the constraint $\nabla \cdot \mathbf{b} = 0$. Due to non-linearities of shock-capturing methods, $\nabla \cdot \mathbf{b} \neq 0$ can be generated from divergence free initial conditions. The transformation of the MHD Eqs. (2.15)-(2.19) to conservation form (2.31)-(2.35) is done with the help of well known vector identities (we omitted the details earlier in the text). They give rise to terms proportional to $\nabla \cdot \mathbf{b}$, which identically are equal to zero and do not enter the final equations. Therefore, $\nabla \cdot \mathbf{b} \neq 0$ would not only lead to creation of artificial magnetic monopoles (sources), but also "modify" (spoil) the Lorenz force. It can be correctly computed from Eq. (2.27) or (2.38),

$$\nabla \cdot (\tfrac{1}{2} b^2 \mathbf{I} - \mathbf{b}\mathbf{b}) = -(\nabla \times \mathbf{b}) \times \mathbf{b} - \mathbf{b}(\nabla \cdot \mathbf{b}), \tag{2.114}$$

[11] Magnetosonic waves will be introduced in Chapter 3.

[12] Hence, in total the HLLD solver employs 5 out of 7 MHD waves, namely two fast magnetosonic- , two Alfvén-waves and a central entropy wave (thus neglecting two slow magnetosonic waves). We will discuss the MHD waves in more detail in Chapter 3.

only if $\nabla \cdot \mathbf{b} = 0$. The non-vanishing magnetic divergence is not only physically undesirable, but can also lead to numerical instabilities. For these reasons, it is crucial for any MHD code to be able to keep the magnetic field divergence-free. There are several different techniques with which it can be achieved (see, e.g. Goedbloed et al. (2010)). We only describe a method, which is implemented in AENUS, i.e. the so-called *constraint transport* (CT). Originally, it was proposed by Evans & Hawley (1988) for finite difference schemes. Its key idea is to insist on maintaining $\nabla \cdot \mathbf{b} = \text{const.}$ (up to round-off errors) in every timestep in a particular discretisation. One needs to make sure then that the initial conditions fulfil the divergence free constraint, $\nabla \cdot \mathbf{b} = 0$, in the chosen discretisation. In CT schemes, the magnetic field is updated with the help of the induction equation (2.1), which has the form of a conservation law (2.54). Hence, we need to formulate the induction equation (2.1) in a semi-discrete form,

$$\partial_t b^x_{i-\frac{1}{2},j,k} = -\frac{c}{\sqrt{4\pi}\mathcal{A}^x_{i-\frac{1}{2},j,k}}\Big[\Big(\mathcal{L}^z_{i-\frac{1}{2},j+\frac{1}{2},k}E^z_{i-\frac{1}{2},j+\frac{1}{2},k} - \mathcal{L}^z_{i-\frac{1}{2},j-\frac{1}{2},k}E^z_{i-\frac{1}{2},j-\frac{1}{2},k}\Big) - \Big(\mathcal{L}^y_{i-\frac{1}{2},j,k+\frac{1}{2}}E^y_{i-\frac{1}{2},j,k+\frac{1}{2}} - \mathcal{L}^y_{i-\frac{1}{2},j,k-\frac{1}{2}}E^y_{i-\frac{1}{2},j,k-\frac{1}{2}}\Big)\Big], \tag{2.115}$$

$$\partial_t b^y_{i,j-\frac{1}{2},k} = -\frac{c}{\sqrt{4\pi}\mathcal{A}^y_{i,j-\frac{1}{2},k}}\Big[\Big(\mathcal{L}^x_{i+\frac{1}{2},j-\frac{1}{2},k}E^x_{i+\frac{1}{2},j-\frac{1}{2},k} - \mathcal{L}^x_{i-\frac{1}{2},j-\frac{1}{2},k}E^x_{i-\frac{1}{2},j-\frac{1}{2},k}\Big) - \Big(\mathcal{L}^z_{i,j-\frac{1}{2},k+\frac{1}{2}}E^z_{i,j-\frac{1}{2},k+\frac{1}{2}} - \mathcal{L}^z_{i,j-\frac{1}{2},k-\frac{1}{2}}E^z_{i,j-\frac{1}{2},k-\frac{1}{2}}\Big)\Big], \tag{2.116}$$

$$\partial_t b^z_{i,j,k-\frac{1}{2}} = -\frac{c}{\sqrt{4\pi}\mathcal{A}^z_{i,j,k-\frac{1}{2}}}\Big[\Big(\mathcal{L}^y_{i+\frac{1}{2},j,k-\frac{1}{2}}E^y_{i+\frac{1}{2},j,k-\frac{1}{2}} - \mathcal{L}^y_{i-\frac{1}{2},j,k-\frac{1}{2}}E^y_{i-\frac{1}{2},j,k-\frac{1}{2}}\Big) - \Big(\mathcal{L}^x_{i,j+\frac{1}{2},k-\frac{1}{2}}E^x_{i,j+\frac{1}{2},k-\frac{1}{2}} - \mathcal{L}^x_{i,j-\frac{1}{2},k-\frac{1}{2}}E^x_{i,j-\frac{1}{2},k-\frac{1}{2}}\Big)\Big], \tag{2.117}$$

where $\mathcal{L}^x_{i,j-\frac{1}{2},k-\frac{1}{2}}$ denotes the length of zone $\mathcal{Z}_{i,j,k}$'s edge at $y = y_{j-\frac{1}{2}}$ and $z = z_{k-\frac{1}{2}}$, etc. After introducing discretised magnetic fields, whose components are defined as a mean over the cell surface orthogonal to the given component, e.g.

$$b^x_{i-\frac{1}{2},j,k} = \frac{1}{\mathcal{A}^x_{i-\frac{1}{2},j,k}}\int_{\mathcal{A}^x_{i-\frac{1}{2},j,k}} b^x(\mathbf{x})\mathrm{d}\Sigma, \tag{2.118}$$

we can write a discretised version of the divergence constraint as

$$(\nabla\cdot\mathbf{b})_{i,j,k} = \frac{1}{\mathcal{V}_{i,j,k}}\Big[\Big(\mathcal{A}^x_{i+\frac{1}{2},j,k}b^x_{i+\frac{1}{2},j,k} - \mathcal{A}^x_{i-\frac{1}{2},j,k}b^x_{i-\frac{1}{2},j,k}\Big) + \Big(\mathcal{A}^y_{i,j+\frac{1}{2},k}b^y_{i,j+\frac{1}{2},k} - \mathcal{A}^y_{i,j-\frac{1}{2},k}b^y_{i,j-\frac{1}{2},k}\Big) + \Big(\mathcal{A}^z_{i,j,k+\frac{1}{2}}b^z_{i,j,k+\frac{1}{2}} - \mathcal{A}^z_{i,j,k-\frac{1}{2}}b^z_{i,j,k-\frac{1}{2}}\Big)\Big]. \tag{2.119}$$

The divergence of the magnetic field is conserved if consistent electric field components are used in Eqs. (2.115)–(2.117). Note that Eqs. (2.115)–(2.117) and (2.119) require a staggered grid, which is typical (but not necessary) for CT schemes, i.e. thermodynamical variables are defined as (volume) averages over cells, surface averages of magnetic field are localised at cell surfaces and electric field components are localised at cell edges (see Fig. (2.1)). In CT schemes, there is no unique way to compute line averages of electric field components and the Lorentz force components. In Obergaulinger (2008), the interested reader will find an extended discussion on this topic and a detailed description of the implementation of two different CT schemes to AENUS.

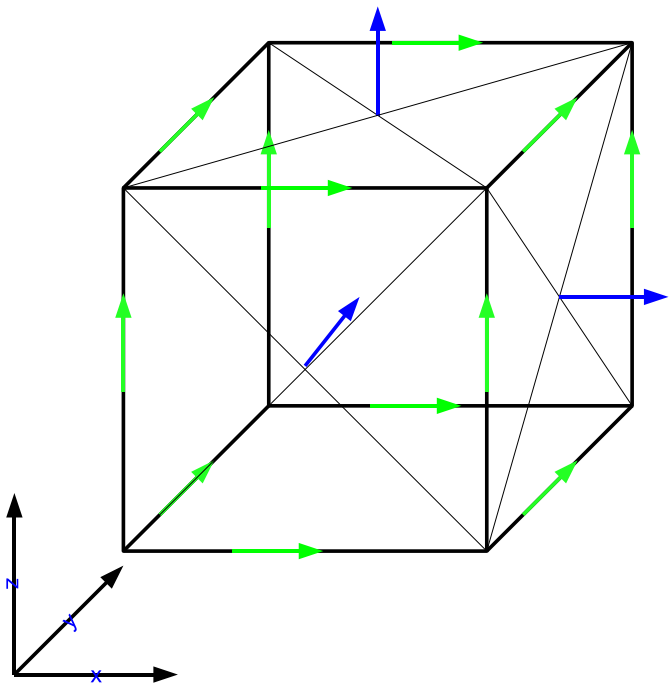

Figure 2.1: A sketch of an MHD grid cell. Magnetic field components (i.e. zone surfaces) are denoted with blue vectors. Electric field components are presented by green vectors. The figure is reproduced with permission from Obergaulinger (2008).

Source and non-ideal MHD terms

Ideal MHD equations constitute a set of not strictly hyperbolic PDEs, i.e. some of their eigenvalues may be degenerate, which makes the design of an exact Riemann solver more complicated than in hydrodynamics. However, this problem does not concern us, since we only use approximate RS that do not require the knowledge of all seven eigenvalues.

The presence of additional resistive and viscous terms in non-ideal MHD equations change their mathematical character from hyperbolic to mixed hyperbolic-parabolic PDEs (in Newtonian physics). However, as long as the (magnetic) diffusion timescale is much larger than the MHD timescale, no special code modifications are required. Instead of ideal MHD fluxes (Eqs. (2.26)-(2.30)), "non-ideal fluxes" (Eqs. (2.31)-(2.35)) should be used.

To the homogeneous MHD Eqs. (2.26)-(2.30) or (2.31)-(2.35), source terms, such as gravitational force (or in coordinates other than Cartesian - geometric source terms) , can be added. We discretise the source terms by integrating them over grid cells.

2.2.3 Numerical viscosity and resistivity

The numerical errors discussed in Sec. 2.2.1 have a limited applicability. They can be useful for testing newly developed numerical schemes, or for debugging a new implementation of a well known method. Their main disadvantage is, however, that we need to know the analytical solution of a given problem in order to use them. This is almost never the case in computational astrophysics.

Numerical errors are one of the main problems and challenges of computational physics. They are omnipresent in simulations, can manifest themselves in various ways, yet they are difficult to measure. It often requires a profound understanding of both the simulated system's physics and the used numerical methods, to tell apart physical effects from numerical artefacts. One of the standard techniques of investigating the influence of the numerical errors are so-called convergence tests. They consist in running simulations with the same physical and numerical setup but higher and higher resolutions. The first simulation is performed with a default resolution, which should be high enough to capture the interesting physics, and another one with a higher (usually twice in every spatial direction) resolution. If the results differ, numerical errors played an important role at least in the first simulation. Hence, we need to run a third simulation with an even higher resolution (usually four times higher than the default one) and compare its results with those of the second simulation. And so on. This procedure should be repeated until two subsequent simulations give (almost) the same results. We say that we obtained convergence. However, one should be careful drawing conclusions from such convergence tests. First of all, it may turn out that both simulations resolve equally well some part of the important physical phenomena, whereas other crucial effects remain still underresolved. As an example, let us consider the following simple problem. Assume that for a given system, there are two waves of very different wavelengths λ_1 and λ_2, say $\lambda_2 = 10^{-2}\lambda_1$. If the "default resolution", amounts to 30 zones per λ_1, we will be able to resolve the first wave very well, whereas the second one will be underresolved. In another simulation with a twice higher resolution, there will be 60 zones per λ_1, which should not lead to noticeable improvements in resolving the first wave, but the second wave is still underresolved (i.e. less than one zone per λ_2). If we had no analytical solution of the considered problem (i.e. we did not know about the existence of λ_2, which could, say, play an important role in the system), we could draw the conclusion at this point that we reached numerical convergence, hence we resolve "all relevant phenomena" of the system. Second of all, numerical convergence does not necessarily imply mathematical convergence. To illustrate this, consider a problem whose solution is influenced by a ratio of two distinct numerical errors. Lowering the resolution could decrease the errors by the same factor, but their ratio would remain constant. In such a situation, we would see that the simulation results converge, yet they would differ from the mathematical solution. Let these complications aside, the major drawback of convergence tests is often their high computational cost. The goal of scientific super-computations is often to resolve physical phenomena better than it was ever done before. This can be achieved by means of more sophisticated methods, which usually are more time consuming, and higher resolutions. In practice, it means that we usually run simulations with resolutions as high as possible to obtain results within a reasonable time. Doubling the resolution in 2D and 3D simulations increases the computational cost at least 8 and 16 times,[13] respectively. This means that the convergence tests are often out of the question. In this subsection we introduce an alternative view of numerical errors in computational MHD. We show that in some situations, they can be interpreted as numerical viscosity and resistivity.

Error analysis of an equation, method or approximation usually leads to more complicated (and longer) expressions than the "original problem". As a simple example of this statement, let us consider a function h which depends on the variable a in the following way

$$h(a) = c^{a^2}\sqrt{1+a^2}, \tag{2.120}$$

where c is a constant. Let us further assume that a was determined (or measured) with an error

[13] Doubling the resolution in each spatial direction, increases the computational cost by a factor of two. Moreover, becasue the maximum allowed timestep reduces by half, twice more timesteps are required.

δa. Then the error of h is given by

$$\delta h = \left(2a \ln(c) c^{a^2} \sqrt{1+a^2} + \frac{a c^{a^2}}{\sqrt{1+a^2}} \right) \delta a. \tag{2.121}$$

The above equation is still not very complex, yet it is more complicated than the original expression (2.120) for the function h, whose error we wanted to estimate. Coming back to the main discussion, we would like to perform some error analysis of the numerical schemes, which were discussed in Sec. 2.2.2. Since these methods usually involve (or lead to) quite complicated expressions, a rigorous analysis of errors introduced by these schemes would be quite hopeless. Therefore, we will consider only a few simplified problems, upon which we can gain some intuitive understanding of numerical errors in computational MHD.

The Navier-Stokes equation (2.38) for a one dimensional system, with a constant shear viscosity ν and without magnetic fields, bulk viscosity and any external forces reads

$$\partial_t(\rho v) + \partial_x(\rho v^2 + p) = \partial_x(\tfrac{4}{3}\nu\rho\partial_x v), \tag{2.122}$$

where v is the velocity in the x direction. Additionally, assuming a constant density, the above equation can be written as

$$\partial_t(\rho v) + \partial_x(\rho v^2 + p) = \tfrac{4}{3}\nu\partial_x^2(\rho v), \tag{2.123}$$

which after neglecting viscosity simply reads

$$\partial_t(\rho v) + \partial_x(\rho v^2 + p) = 0. \tag{2.124}$$

This is a one dimensional scalar conservation law (in this section, we abandon our "unusual, but useful notation" introduced in Sec. 2.2.2), i.e.

$$\partial_t u + \partial_x f(u) = 0, \tag{2.125}$$

where $u = \rho v$ is the conserved variable and $f = \rho v^2 + p$ is the conserved flux. Our task now is to investigate how spatial discretisation and numerical integration errors change the above equation. Usually, in textbooks (see, e.g. Laney (1998)), it is written, that e.g. for Euler equation (2.124), some spatial discretisation errors of velocity v will be proportional to $\partial_x^2 v$ and hence they will introduce additional terms proportional to $\partial_x^2 v$ into the original Eq. (2.124). From a comparison of this equation to Eq. (2.123), we see that these extra terms could be identified with terms proportional to viscosity in the latter equation. Therefore, it is sometimes said that numerical errors introduce *numerical* (or *artificial*) *viscosity*. As we will try to show briefly in this section, from a mathematical point of view, this statement is wrong and cannot be well justified. However, in hydrodynamical simulations it is often observed that numerical errors manifest themselves in a similar way to physical viscosity, e.g. they can smooth out sharp velocity profiles and discontinuities or damp propagating (e.g. sound) waves. Similarly, in ideal MHD simulations, numerical errors can lead to magnetic field reconnection or diffusion, and these processes are only allowed if physical resistivity is present in the system. These are commonly known facts in the numerical (M)HD community. Moreover, we demonstrate and extensively investigate the above described phenomena in Chapter 3. All in all, from the a purely pragmatical point of view, the notions of *numerical viscosity* and *numerical resistivity* are useful, when interpreting simulation results.

Let us demonstrate now, in a naive way, with the help of Eqs. (2.123)–(2.125), how numerical errors can give rise to numerical viscosity. We begin by rewriting Eq. (2.125) as

$$\partial_t u + \frac{\partial f}{\partial u}\partial_x u = 0 \tag{2.126}$$

and "numerically integrating it". In our "toy model discussion", we assume that the terms $\partial_t u$ and $\partial_u f$ can be computed "perfectly" (or that the errors related to them are negligible) and that a given numerical scheme only introduces errors related to the last term $\partial_x u$. Moreover, we will "forget" about most "ingredients" and assumptions of HRSC schemes, i.e. zones, zone averages, interfaces, computing fluxes, reconstruction etc. We will just selectively refer to some of these "components", to make our point. Hence, we say that a 'numerical" version of Eq. (2.126) reads

$$(\partial_t u)_{\text{num}} + \left(\frac{\partial f}{\partial u}\right)_{\text{num}} (\partial_x u)_{\text{num}} = 0, \tag{2.127}$$

where the subscript *num* means that a given value was determined numerically. According to our assumption, only the last term was computed "inaccurately" and for the other terms: $(\partial_t u)_{\text{num}} = (\partial_t u)$ and $(\partial_u f)_{\text{num}} = (\partial_u f)$. Thus, Eq. (2.127) reads

$$\partial_t u + \partial_u f (\partial_x u)_{\text{num}} = 0. \tag{2.128}$$

Now, we assume that errors in determining $\partial_x u$ were caused by a reconstruction scheme. For the PM method, which is first order accurate, the difference between u_{num} and u, keeping the lowest order terms, could be estimated as (see Eq. (2.99))

$$u(x) = u(x)_{\text{num}} + (\Delta x)\partial_x u(x). \tag{2.129}$$

Already this equation is from a mathematical point of view not "well defined"(i.e. just incorrect), but we will come back to this issue later. After plugging Eq. (2.129) into Eq. (2.128), we obtain a "modified differential equation"

$$\partial_t u + (\partial_u f)\partial_x (u - (\Delta x)\partial_x u) = 0, \tag{2.130}$$

which can be rewritten as

$$\partial_t u + (\partial_u f)\partial_x u = (\Delta x)(\partial_u f)\partial_x^2 u. \tag{2.131}$$

Hence, now we could identify the term on the RHS of the above equation with the viscous term from Navier-Stokes equation (2.123), i.e.

$$(\Delta x)(\partial_u f)\partial_x^2 u \simeq \tfrac{4}{3}\nu\partial_x^2(\rho v), \tag{2.132}$$

where $u = \rho v$ and $f = (\rho v^2 + p)$. Thus numerical viscosity, ν_*, would be given by

$$\nu_* = \tfrac{3}{4}(\Delta x)\partial_u f. \tag{2.133}$$

Already from this mathematically inconsistent derivation, we can draw two (correct) conclusions. Firstly, the lower the resolution, the lower the numerical viscosity. Secondly, for a given resolution (i.e. given (Δx)), numerical viscosity is not a constant scalar value, since it depends on $\partial_u f$.

After these comments, we can start with criticising "our own derivation" (in fact, it is not "our derivation", but rather a typical argumentation (encountered in textbooks, lectures and talks) how terms proportional to viscosity and resistivity appear in the process of numerical solving (M)HD equations) and show where all mistakes were made. First of all, even if Eq. (2.129) were correct, we could not simply plug it into Eq. (2.128) and later say that we obtained modified differential equation (2.131). Note in Eq. (2.128), we substituted u_{num} by $u - (\Delta x)\partial_x u$ with the help of Eq. (2.129) and in the end obtained Eq. (2.131). However, u from Eq. (2.129) is a solution of the original equation (2.126). On the other hand, if we treat Eq. (2.131) as a differential equation,

because it does look like a differential equation, then its solution will be a different function u. Hence the only common feature of functions u from Eqs. (2.126) and (2.131) is that we denote them with the same later "u". To stress it explicitly, we could rewrite the latter equation using a different symbol to denote the sought function, say $\tilde{u}$. Then Eq. (2.131) would read

$$\partial_t \tilde{u} + (\partial_{\tilde{u}} \tilde{f}) \partial_x \tilde{u} = (\Delta x)(\partial_{\tilde{u}} \tilde{f}) \partial_x^2 \tilde{u}. \tag{2.134}$$

Now, the temptation to interchange freely functions u from Eq. (2.126) and $\tilde{u}$ from the above differential equation should be weaker. At this point a natural question arises how Eq. (2.131), bearing in mind its derivation, should be then interpreted. It is s not a "modified" differential equation, but only "spoilt" by numerical errors differential equation (2.126). The problems starts with Eq. (2.130), which in fact, is not a valid equation. From Eq. (2.126), we have $\partial_t u + (\partial_u f)\partial_x u = 0$, and therefore according to Eq. (2.130),

$$-(\partial_u f)(\Delta x)\partial_x^2 u = 0 \tag{2.135}$$

should hold which is in general not true, i.e. it is just a nonsense expression, because neither $\partial_u f = 0$, nor $\partial_x^2 u = 0$ must hold. To make this statement even clearer, let us consider the following example. Let us assume that we know that for a given system, a law (or a relation)

$$y + z = 100, \tag{2.136}$$

where y and z are scalars or scalar functions. However, from a numerical simulation (or a physical experiment), we can only determine numerical (experimental) values of y_{num} and z_{num}. Let us further assume that real values of y and z equal 80 and 20, respectively and in the simulation (experiment), we obtained $y_{\text{num}} = 80$ and $z_{\text{num}} = 21$. Hence, we could perform the following fallacious reasoning: since Eq. (2.136) holds, therefore also

$$y_{\text{num}} + z_{\text{num}} = 100, \tag{2.137}$$

must be true and consequently

$$80 + 21 = 100, \tag{2.138}$$

and as a result

$$1 = 0. \tag{2.139}$$

In these idealised example, Eqs. (2.136), (2.138) and (2.139) correspond to Eqs. (2.126), (2.130) and (2.131), respectively, from the "original" scalar conservation law problem. There is no difference in saying that because of numerical viscosity, we obtained a "modified differential equation" (2.131), and claiming that Eq. (2.139) is true. Both statements are simply incorrect. A correct conclusion, which can be drawn from these examples is that in numerical simulations, not every equation (like Eq. (2.126)) or law (2.136) will be strictly fulfilled, because numerical errors can lead to their violation. And as long as this violation is not too big[14], we can trust the results of a given simulation. However, numerical errors should not be "over-interpreted" and we should not look for their deeper (mathematical) meaning.

Alternatively, if we wanted to treat Eq. (2.130) as a "well defined' differential equation, it would have to be written as

$$\partial_t \bar{u} + (\partial_{\bar{u}} \bar{f})(\partial_x u - (\Delta x)\partial_x u) = 0, \tag{2.140}$$

[14] We do not specify how to measure this violation, since these are irrelevant (and possibly complicated) details for the current discussion.

which is a "hybrid" equation without an easy interpretation. The function u should be given by original Eq. (2.130), and some different $\bar{u}$ and $\bar{f}$ must be found, so that Eq. (2.140) is fulfilled. Or the other way round, $\bar{u}$ and $\bar{f}$ should fulfil Eq. (2.130) and some new u would need to be determined. All in all, we can say that because of numerical errors, the functions u_{num} and f_{num} do fulfil some kind of a differential equation (which on the top of everything, can have a different form after every timestep), but for sure it does not have form (2.131). In each timestep, the code tries to solve Eq. (2.126), but fails to do it exactly.

Second of all, expressing reconstruction errors in neat mathematical form (2.129) is also incorrect. What we could show is that in the PM method, the "numerical function" $u_{\text{num}}(x)$ gave an exact prediction for $u(x)$ at least for one point in each zone (see Eq. (2.98)), which we denote with x_s, i.e.

$$u(x_s)_{\text{num}} = u(x_s). \tag{2.141}$$

The reconstruction error at any other point within this zone could be expressed with the help of Taylor expansion. Since (keeping the lowest order terms)

$$u(x) = u(x_s) + (x - x_s)\partial_x u(x)_{|x=x_s} \tag{2.142}$$

and

$$u(x)_{\text{num}} = u(x_s)_{\text{num}} = u(x_s), \tag{2.143}$$

therefore

$$u(x) = u(x)_{\text{num}} + (x - x_s)\partial_x u(x)_{|x=x_s}, \tag{2.144}$$

where $|x - x_s| \leq \Delta x$. However, we do not know the real $u(x)$ and its first derivative $\partial_x u(x)$. Moreover, the first integral mean value theorem guarantees us that there is a point x_s in each zone for which Eq. (2.141) holds, but we do not even know where this point is exactly. Hence Eq. (2.129) is wrong and we cannot use it for the following reasons. Firstly, we did the Taylor expansion in one point x and not for two distinct points (x and x_s). Secondly, we do not know the location of x_s. Thirdly, we do not have an "access" to $\partial_x u$. Fourthly, the displacement Δx in the Taylor expansion should be replaced by $\tilde{\Delta x} \equiv x - x_s$, which is by definition different at every point. Therefore, even though Eq. (2.129) looks as if it was ready to be used to obtain "modified differential equation" (2.131), it is simply wrong.

Having criticised what there was to be criticised, we proceed with error analysis for higher order reconstruction methods. Even though the derivation of Eq. (2.131) was mathematically inconsistent, we will now repeat the same steps to obtain a similar expression for higher order schemes. The reader may find this approach to error analysis quite dubious. However, our main goal is neither to study rigorously how numerical errors change mathematical properties of differential equations, nor to give exact prescriptions for estimating errors. We only want to obtain some expression, which could be helpful in numerical error studies, which will be performed Chapter 3. Hence, on the one hand, we want to derive theoretically expected dependence of numerical errors as a function of resolution. On the other hand, we want to stress that error assessing expressions obtained in this and in the next chapter do not have a solid mathematical justification. We will postulate and "derive" some prescriptions and later show that they work. Finally, we will argue that they are useful because they do work. It is a purely pragmatical, yet useful approach.

In Sec. 2.2.2, we wrote that a reconstruction scheme is of the r-th order, when its errors are proportional to $(\Delta x)^r$. With the help of the Taylor expansion, analogically to Eq. (2.129), this statement could be expressed as (keeping the lowest order terms)

$$u(x) = u(x)_{\text{num}} + n(\Delta x)^r \partial_x^r u(x), \tag{2.145}$$

where n is a constant factor. Similarly, to Eq. (2.129), the above equation is not fully correct (see the discussion on Eq. (2.129) above). After plugging Eq. (2.145) to Eq. (2.128), we obtain another "modified differential equation"

$$\partial_t u + (\partial_u f)\partial_x u = n(\Delta x)^r (\partial_u f)\partial_x^{r+1} u. \tag{2.146}$$

Comparing it with Eq. (2.123), we can identify the therm on the RHS of the above equation with numerical viscosity, i.e.

$$\nu_* = \frac{3}{4} n(\Delta x)^r \partial_u f \left(\frac{\partial^{r+1} u}{\partial x^{r+1}}\right)\left(\frac{\partial^2 u}{\partial_x^2}\right)^{-1}. \tag{2.147}$$

Hence, as we see, for $r > 1$, the argument that "numerical errors introduce terms proportional to $\partial_x^2 u$ and therefore they can be interpreted as numerical viscosity" is no longer valid. Terms proportional to $\partial_x^{r+1} u$, for $r > 1$, do not have their physical counterparts. Still, we will identify them with numerical viscosity.[15]

Now, we will repeat a similar analysis for time integration errors. In non-ideal MHD equations (2.31)-(2.35), there are no terms which are proportional to higher than the first time derivative of a conserved variable, i.e. $\partial_t u$. However, we will once again try to identify terms proportional to $\partial_t^q u$, where $q > 1$, with numerical viscosity or resistivity. We come back to Euler equation (2.124), which has a form of scalar conservation law (2.125), i.e.

$$\partial_t u + \partial_x f(u) = 0. \tag{2.148}$$

This time, we will assume that errors related to reconstruction (and interpolation) of $u(x)$ and calculation of its flux $f(u)$ are negligible and we will only consider time integration errors. Once $\partial_x f(u)$ is known at a given time, we want to advance the system by one timestep. We can rewrite Eq. (2.148) as

$$\partial_t u = -\partial_x f \tag{2.149}$$

and employ an RK-q (i.e. Runge-Kutta of the q-th order) scheme to perform numerical time integration, i.e.

$$u^{n+1} = u^n + \Delta t F(k_1, \ldots, k_q) + O(\Delta t^{q+1}), \tag{2.150}$$

where $F(k_1, \ldots, k_q)$ was defined in Eq. (2.92) and $O(\Delta t^{q+1})$ is simply the scheme's error in determining u^{n+1}. We remind the reader that $u^n \equiv u(t^n)$, etc. Eq. (2.149) can be written with the help of Taylor series as

$$u^{n+1} = u^n + \Delta t \left[-\partial_x f + \sum_{i=2}^{\infty} \frac{\partial^i u^n}{\partial t^i} \frac{(\Delta t)^{i-1}}{i!}\right]. \tag{2.151}$$

From the RK-q time integration, we obtain

$$u^{n+1} \approx u^n + \Delta t \left[-\partial_x f + \sum_{i=2}^{q} \frac{\partial^i u^n}{\partial t^i} \frac{(\Delta t)^{i-1}}{i!} + \sum_{i=q+1}^{\infty} a_i \frac{\partial^i u^n}{\partial t^i} \frac{(\Delta t)^{i-1}}{i!}\right], \tag{2.152}$$

where coefficients a_i were defined in Eq. (2.93), which can be rewritten as

$$u^{n+1} \approx u^n + \Delta t \left[-\partial_x f + \sum_{i=2}^{\infty} \frac{\partial^i u^n}{\partial t^i} \frac{(\Delta t)^{i-1}}{i!}\right] + \sum_{i=q+1}^{\infty} (a_i - 1) \frac{\partial^i u^n}{\partial t^i} \frac{(\Delta t)^i}{i!}. \tag{2.153}$$

[15] Terms proportional to $\partial_x^{r+1} u$, for even $r+1$ are sometimes called numerical dissipation, and for odd $r+1$ numerical dispersion. However, we will not make this distinction in this thesis.

Note that we cannot just say that because of the RK-q time integration, we obtain a different prescription for u^{n+1}:

$$u^{n+1} = u^n + \Delta t \left[-\partial_x f + \sum_{i=2}^{\infty} \frac{\partial^i u^n}{\partial t^i} \frac{(\Delta t)^{i-1}}{i!} \right] + \sum_{i=q+1}^{\infty} (a_i - 1) \frac{\partial^i u^n}{\partial t^i} \frac{(\Delta t)^i}{i!}, \tag{2.154}$$

which corresponds to a "modified differential equation"

$$\partial_t u + \partial_x f = \sum_{i=r+1}^{\infty} (a_i - 1) \frac{\partial^i u}{\partial t^i} \frac{(\Delta t)^{i-1}}{i!}. \tag{2.155}$$

Such an argumentation is fallacious for the following reason. The derivatives $\partial_x f$ and $\partial_t^i u^n$ in Eq. (2.154) are determined from original Eq. (2.125). They differ from derivatives $\partial_x f$ and $\partial_t^i u^n$ computed from Eq. (2.155), because functions u and f in Eqs. (2.125) and (2.155) are simply distinct. Therefore, recovering Eq. (2.155) from Eq. (2.154) is mathematically incorrect. What we can write, however, is that with the RK-q scheme, we can find $\tilde{u}^{n+1}$, which is an approximation of u^{n+1} given by Eq. (2.152). Instead of Eq. (2.153), we should write

$$\tilde{u}^{n+1} = u^n + \Delta t \left[-\partial_x f + \sum_{i=2}^{\infty} \frac{\partial^i u^n}{\partial t^i} \frac{(\Delta t)^{i-1}}{i!} \right] + \sum_{i=q+1}^{\infty} (a_i - 1) \frac{\partial^i u^n}{\partial t^i} \frac{(\Delta t)^i}{i!}, \tag{2.156}$$

or equivalently

$$\tilde{u}^{n+1} = u^{n+1} + \sum_{i=q+1}^{\infty} (a_i - 1) \frac{\partial^i u^n}{\partial t^i} \frac{(\Delta t)^i}{i!}. \tag{2.157}$$

The function $\tilde{u}$ depends on u. Ideally, we would like to find a modified Eq. (2.125) for $\tilde{u}$ (something like Eq. (2.155)), from which the dependence on u would be removed (of course terms proportional to u^0 must be taken as initial conditions). We must remember about one fact, however. The difference between $\tilde{u}^{n+1}$ and u^{n+1} in Eq. (2.157) resulted from numerical errors introduced only in the $n+1$-th timestep and not after $n+1$ timesteps. In fact, each of them would introduce terms like $\sum_{i=q+1}^{\infty}(a_i-1)\partial_t^i u(\Delta t)^i/(i!)$. From this brief discussion, we see that an attempt to write a consistent partial differential equation for $\tilde{u}$, from which we could make use, is hopeless. Obviously, we could write a formal equation containing many terms proportional to series like $\sum_{i=q+1}^{\infty}(a_i-1)\partial_t^i u^0(\Delta t)^i/(i!)$, but its practical application would be rather dubious.

At this point, to make further progress, we abandon this mathematically rigorous approach. Similarly, like in the case of Eqs. (2.131) and (2.146), we identify the term on the RHS of "modified differential equation" (2.155) with the terms proportional to viscosity in Navier Stokes equation (2.123). From this comparison, we can determine numerical viscosity ν_*,

$$\nu_* = \frac{3}{4} \left(\frac{\partial^2 u}{\partial x^2} \right)^{-1} \sum_{i=q+1}^{\infty} (a_i - 1) \frac{\partial^i u}{\partial t^i} \frac{(\Delta t)^{i-1}}{i!} \tag{2.158}$$

Keeping only the lowest order terms in Δt, we obtain

$$\nu_* = \frac{3}{4} (a_{r+1} - 1) \left(\frac{\partial^2 u}{\partial x^2} \right)^{-1} \frac{\partial^{q+1} u}{\partial t^{q+1}} \frac{(\Delta t)^q}{(q+1)!} + O(\Delta t^{q+1}). \tag{2.159}$$

Numerical viscosity should scale like $(\Delta t)^q$. However, if $|\partial_t^{q+1} u| \ll \Delta t |\partial_t^{q+2} u|$, then it will scale like Δt^{q+1}, because the first term on the RHS can be neglected.

Finally, we would like to point out an interesting relation between the orders of a reconstruction and a time integration scheme. We say that a reconstruction method has an order r when its errors scale like $(\Delta x)^r$, whereas a time integration scheme has an order q when its errors scale like $(\Delta t)^{q+1}$. This may look like a somewhat inconsistent (not introduced by us, but commonly used) definition of method orders. However, numerical viscosity introduced by these schemes is (coincidentally) proportional to their orders, i.e. $\nu_* \propto (\Delta x)^r$ and $\nu_* \propto (\Delta t)^q$, respectively (see Eqs. (2.147) and (2.159)).

So far, we have only shown, that numerical errors could be maybe treated like numerical shear viscosity. Similar analysis can be easily performed for numerical bulk viscosity and resistivity. The latter appears as a result of discretisation and numerical integration of the induction equation (2.18). The former, like shear viscosity, results from spatial and temporal errors of momenta.

The idea to treat any leading spatial and temporal discretisation errors as numerical dissipation (viscosity or resistivity) seems heuristic and should be empirically verified. Therefore, in the next chapter, we test this hypothesis with the help of various simulations.

Chapter 3

Numerical resistivity and viscosity

THE TRUTH IS RARELY PURE AND NEVER SIMPLE.

Oscar Wilde, *The Importance of Being Earnest*

3.1 Introduction

One could naively think, that a difference between an ideal and a non-ideal MHD simulation is rather trivial. The latter merely needs to be run with the very same setup but with non-zero resistivity or viscosity. However, the reality is far from being that simple. It is well known that every Eulerian MHD code has a non-zero *numerical resistivity* and *viscosity*, which are *a priori* unknown. Should one run a simulation with a physical resistivity, which is lower than the numerical one, one can at best learn nothing new, or even arrive at wrong conclusions, e.g. by claiming that resistivity has no influence on a particular system. Therefore, before we tackle the main goal of this dissertation, i.e. the non-ideal effects in the magneto-rotational instability, we need to learn more about the numerical resistivity and viscosity of numerical codes. It is a challenging task, since they depend on many factors, e.g. resolution, numerical scheme and physical setup. Both temporal and spatial discretisation errors contribute to the numerical dissipation and, ideally, one would like to know which of the two errors dominantes in a given simulation. This would allow one to decide, whether in order to reduce the numerical resistivity and viscosity, it suffices to reduce the time-step or to increase the grid resolution.[1] One can determine the numerical resistivity (or viscosity) of the code with the help of a physical system whose dependence on resistivity is known. Unfortunately, there are only a few problems that can be solved analytically in resistive-viscous MHD, yet under some approximations, which it are difficult or even impossible to fulfil in a numerical experiment. Even after overcoming all these difficulties and successfully measuring the numerical resistivity and viscosity for a given setup, one is faced with the problem of generalising the results. For this purpose, we propose a simple prescription to estimate the numerical dissipation of a code for any simulation. We do not claim that this prescription will always give an exact prediction, but it is a first step towards a better understanding and estimate of numerical errors in MHD simulations.

[1] Halving the time-step, increases the computational time twice, whereas doubling the resolution increases the computational time by factor 2^{n+1}, where n is the dimension of the simulation. This relation holds under perfect weak scaling assumption. Should the weak scaling of the code be worse, the computational time will increase even more.

3.2 Ansatz

In CGS units both resistivity and viscosity have dimension of $[\mathrm{cm}^2\mathrm{s}^{-1}]$. Therefore, any prescription for their numerical counterparts has to have the same dimension. It seems the most natural to use an ansatz for, say, the numerical shear viscosity of the form $\nu_* \propto \mathcal{V} \times \mathcal{L}$, where $\mathcal{V}$ and $\mathcal{L}$ are the (still unknown) characteristic velocity and length of a simulated system, respectively. Numerical errors come from the spatial (Δx) and temporal discretisation (Δt). Therefore terms proportional to $(\Delta x)^r$ and $(\Delta t)^q$, where r and q depend on the numerical schemes' order, should enter the sought equation. Since Δx has a dimension [cm], $(\Delta x)^r$ should be additionally multiplied by $\mathcal{L}^{-r}$. The resulting term $(\Delta x/\mathcal{L})^r$ has a simple interpretation: the more zones used to resolve the characteristic length the lower numerical viscosity. The same argumentation holds for the time integration errors, which should enter the prescription in the form $(\Delta t\mathcal{V}/\mathcal{L})^q$. Therefore, the final form of the ansatz for the numerical shear viscosity ν_* should read

$$\nu_* = \mathfrak{N}_\nu^{\Delta x} \times \mathcal{V} \times \mathcal{L} \times \left(\frac{\Delta x}{\mathcal{L}}\right)^r + \mathfrak{N}_\nu^{\Delta t} \times \mathcal{V} \times \mathcal{L} \times \left(\frac{\mathcal{V}\Delta t}{\mathcal{L}}\right)^q, \tag{3.1}$$

where $\mathfrak{N}_\nu^{\Delta x}$, $\mathfrak{N}_\nu^{\Delta t}$, r, and q are constant for a given numerical scheme, $\mathcal{L}$ and $\mathcal{V}$ are the characteristic length and speed of the system, respectively. Using the CFL factor definition (2.79), for an equidistant grid, the above equation can be rewritten as

$$\nu_* = \mathfrak{N}_\nu^{\Delta x} \times \mathcal{V} \times \mathcal{L} \times \left(\frac{\Delta x}{\mathcal{L}}\right)^r + \mathfrak{N}_\nu^{\Delta t} \times \mathcal{V} \times \mathcal{L} \times \left(\frac{C_{\mathrm{CFL}}\Delta x}{\mathcal{L}}\right)^q \times \left(\frac{\mathcal{V}}{v_{\max}}\right)^q, \tag{3.2}$$

where $v_{\max}$ is the maximum velocity of the system limiting the timestep. If for a given system $\mathcal{V} = v_{\max}$, the above equation simplifies to

$$\nu_* = \mathfrak{N}_\nu^{\Delta x} \times \mathcal{V} \times \mathcal{L} \times \left(\frac{\Delta x}{\mathcal{L}}\right)^r + \mathfrak{N}_\nu^{\Delta t} \times \mathcal{V} \times \mathcal{L} \times \left(\frac{C_{\mathrm{CFL}}\Delta x}{\mathcal{L}}\right)^q. \tag{3.3}$$

The same ansatz should hold for the numerical bulk viscosity ξ_* and the resistivity η_*, with the coefficients $\mathfrak{N}_\eta^{\Delta x}$, $\mathfrak{N}_\eta^{\Delta t}$, $\mathfrak{N}_\xi^{\Delta x}$ and $\mathfrak{N}_\xi^{\Delta t}$:

$$\xi_* = \mathfrak{N}_\xi^{\Delta x} \times \mathcal{V} \times \mathcal{L} \times \left(\frac{\Delta x}{\mathcal{L}}\right)^r + \mathfrak{N}_\xi^{\Delta t} \times \mathcal{V} \times \mathcal{L} \times \left(\frac{\mathcal{V}\Delta t}{\mathcal{L}}\right)^q, \tag{3.4}$$

$$\eta_* = \mathfrak{N}_\eta^{\Delta x} \times \mathcal{V} \times \mathcal{L} \times \left(\frac{\Delta x}{\mathcal{L}}\right)^r + \mathfrak{N}_\eta^{\Delta t} \times \mathcal{V} \times \mathcal{L} \times \left(\frac{\mathcal{V}\Delta t}{\mathcal{L}}\right)^q, \tag{3.5}$$

where we postuatle that r and q should have the same values in Eqs. (3.1)–(3.5). Once the unknown coefficients $\mathfrak{N}$, r and q are determined, the above prescription can be used to estimate the numerical resistivity and viscosity in any simulation performed with the same code. However, one also needs to correctly identify the characteristic velocity and length of the system, which may be not trivial and require a good understanding of the problem (see the tearing mode simulations in Section 3.4). Note, that once the numerical resistivity and viscosity are known, one can easily express simulation results in terms of numerical Reynolds numbers.

In order to test the robustness of the above ansatzes [2] and determine the unknown coefficients, we use four tests, which have analytically known solutions in resistive-viscous MHD: sound-,

[2] The author wishes to apologise the German native speakers reading this thesis for using the genitive of the noun *Ansatz* in the function of its plural. We decided to follow Wiktionary's recommendation, yet knowing that the "correct" plural form should be *Ansätze*.

Alfvén- and fast magnetosonic-wave damping, and the tearing mode instability. Since the slow magnetosonic waves will not be discussed in the remaining part of this chapter, we will often write *magnetosonic*-, having in mind *fast magnetosonic*-waves

We remind the reader that the equations are given in CGS units with a redefined magnetic field $b = B/\sqrt{4\pi}$, in which the Alfvén speed reads: $c_\mathrm{A} = b/\sqrt{\rho}$. It is a common practice in numerical simulations to work in dimensionless units. To achieve this one needs to set a certain scale for MHD equations, e.g. for the magnetic field such a transformation would read

$$\tilde{\mathbf{b}} = \frac{\mathbf{b}}{b_0}, \tag{3.6}$$

where $\tilde{\mathbf{b}}$ is now dimensionless and b_0 is an arbitrarily chosen scalar of dimension [G]. In all simulations discussed in this chapter, we will make such a transformation without explicitly mentioning it. We will also drop the tilde symbol above the dimensionless quantities. "We set $b_x = 1$" should be read as "we set $\tilde{b_x} = 1$ (hence $b_x = 1 \times b_0$)", etc. This simplifies the notation and should not lead to any confusion.

3.3 Wave damping

There are four different types of waves, which are solutions of linearised MHD equations: Alfvén, fast- and slow-magnetosonic, and entropy waves. In the absence of a magnetic field, the magnetosonic waves reduce to the sound waves. In ideal MHD, these waves propagate with constant speed and amplitude. Resistivity and viscosity will decrease their amplitude with time. Unfortunately, none of these waves is damped just by one of the viscosities or resistivity, which would allow us to measure them separately, but always by a linear combination of these. In the following tests, we simulated sound waves, which are affected by shear and bulk viscosity, Alfvén waves, influenced by shear viscosity and resistivity, and fast magnetosonic waves, which are susceptible to both viscosities and resistivity. These tests were done to determine the numerical dissipation of our code and validate ansatzes (3.1), (3.4) and (3.5).

All wave simulations were performed in 1D and if not otherwise stated, the box length and the wavevector were set to $L = 1$ and $k = 2\pi$, respectively. An ideal gas equation of state (EOS) with the adiabatic index $\Gamma = 5/3$ was used.

3.3.1 Sound waves

In the following simulations, we measure the numerical shear and bulk viscosity of the code. We set the background density and pressure to $\rho_0 = p_0 = 1$, and perturbed the system with a sound wave

$$v_{1x}(x, t = 0) = \varepsilon \sin(kx), \tag{3.7}$$

$$\rho_1(x, t = 0) = \frac{v_{1x}(x, 0)}{c_\mathrm{s}} \rho_0, \tag{3.8}$$

$$p_1(x, t = 0) = \frac{v_{1x}(x, 0)}{c_\mathrm{s}} \Gamma p_0, \tag{3.9}$$

where $c_s = \sqrt{\Gamma p_0/\rho_0}$ is the sound speed and the velocity amplitude[3] was set to $\varepsilon = 10^{-5}$.In ideal hydrodynamics, the wave will propagate with a constant amplitude with the sound speed. However, in the presence of viscosity, the wave will be damped with time. Inserting a plane wave solution $v_{x1}(x,t) = \hat{v}_{x1}\exp[i(kx-\omega t)]$ into the Navier-Stokes equations (Eqs. (2.15)–(2.17) without magnetic field and gravity) , one finds from the dispersion relation

$$\omega = \frac{-i(4\nu/3+\xi)k^2}{2} \pm kc_s\sqrt{1-\frac{k^2\rho_0(4\nu/3+\xi)^2}{4\Gamma p_0}}. \tag{3.10}$$

In the weak damping approximation, i.e. if

$$\frac{k^2\rho_0(4\nu/3+\xi)^2}{4\Gamma p_0} \ll 1, \tag{3.11}$$

the phase velocity remains constant and the solution can be written as

$$v_x(x,t) = \hat{v}_{1x}\exp[-(k^2/2)(4\nu/3+\xi)t]\exp[ik(x-c_s t)]. \tag{3.12}$$

If we define the sound damping coefficient as

$$\mathfrak{D}_s = \frac{k^2}{2}\left(\frac{4}{3}\nu+\xi\right), \tag{3.13}$$

Eq. (3.12) can be rewritten as

$$v_x(x,t) = \hat{v}_{1x}e^{-\mathfrak{D}_s t}e^{ik(x-c_s t)}. \tag{3.14}$$

The sound wave will propagate with a constant speed and its amplitude will decrease over time.

As a first step, we tested Eq. (3.14). We ran simulations with a very high resolution (128 zones for one wavelength in x - direction) and a small time step ($C_{\rm CFL} = 0.5$), so that the numerical dissipation was very low. The monotonicity preserving reconstruction scheme of the 9th order (MP9), the HLL Riemann solver and the Runge-Kutta time integrator of the 3rd order (RK3) were used. For different values of the wavevector, shear and bulk viscosity (from 10^{-6} to 10^{-3}), we measured the damping coefficient of the kinetic energy, which should be equal to $2\mathfrak{D}_s$, and found a perfect agreement between theory and numerical experiment (see Fig. 3.1).

Next, we determined the coefficients $\mathfrak{N}_\nu^{\Delta x}$ and $\mathfrak{N}_\xi^{\Delta x}$ (see Eqs. (3.1) and (3.4)) for four different reconstruction schemes: the piecewise-linear (PL), the MP5, the MP7 and the MP9. We ran several simulations with resolutions from 8 to 1024 zones[4]with the HLL Riemann solver and the RK3 integrator. To keep the contribution of the time integration errors as small as possible, we chose a very small time-step ($C_{\rm CFL} = 0.01$). For every simulation, we measured the kinetic energy damping, from which we computed the numerical viscosity of the code:

$$\frac{4}{3}\nu_* + \xi_* = \frac{2}{k^2}\mathfrak{D}_{s*}. \tag{3.15}$$

[3]Notice that the velocity amplitude should be much smaller than the sound speed, not only to fulfil the linearised equations, but also to prevent wave steepening, see e.g. Shore (2007). We noticed that this effect was important for a typical simulation time (of the order of 10 time units) for an initial velocity amplitude range $\varepsilon \gtrsim 10^{-4}$–$10^{-3}$.

[4]Resolutions with ≤ 8 zones were achieved by simulating two wavelengths in a twice longer box. This simple trick allowed us to overcome the stencil limitations (the number of zones used in the physical domain must be greater than the number of ghost zones).

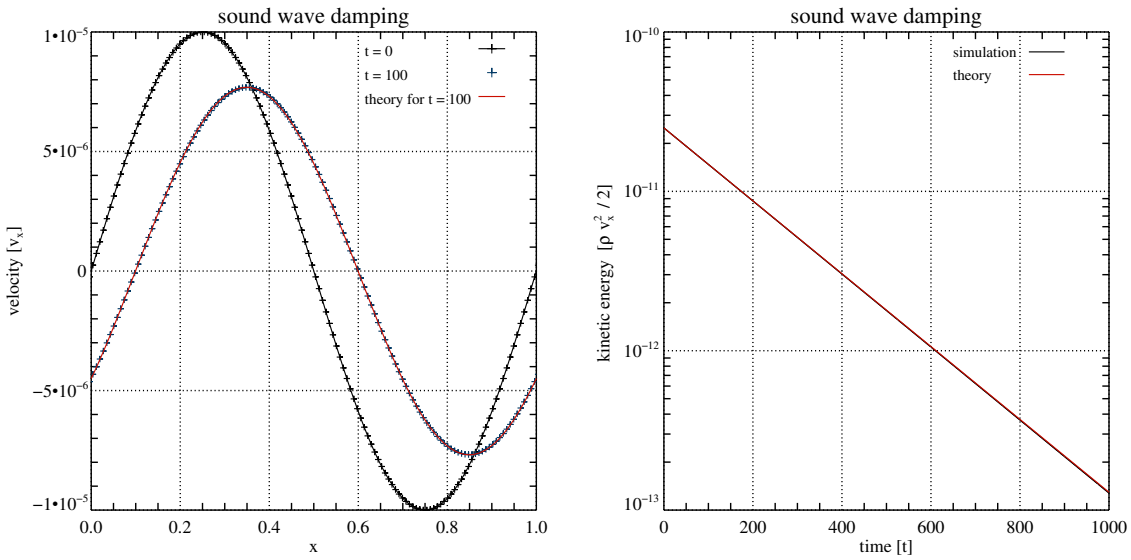

Figure 3.1: *Left:* Velocity profile in a sound wave simulation with the shear viscosity set to $\nu = 10^{-4}$. The MP9 reconstruction scheme, the HLL Riemann solver and the RK3 time integrator with $C_{\mathrm{CFL}} = 0.5$ are used. The grid resolution is 128 zones. The initial state is depicted with black plus signs connected by a line. The blue plus signs show the evolved wave after 100 time units. The analytical prediction for $t = 100$ is given by the red curve. The agreement between theory and simulation is excellent. *Right:* The evolution of the kinetic energy. The black curve depicts the simulation results. The analytical prediction is shown in red. Both curves are indistinguishable.

Note that in the case of sound waves one cannot determine ν_* and ξ_* separately, but only a linear combination of both quantities. For every reconstruction scheme, we fitted the function

$$\ln(\frac{4}{3}\nu_* + \xi_*) = r\ln(\Delta x) + d, \tag{3.16}$$

where r is the measured scheme's order of convergence and from the estimator of d one can compute $\frac{4}{3}\mathfrak{N}_\nu^{\Delta x} + \mathfrak{N}_\xi^{\Delta x}$. The results are presented in Table 3.1 and Fig. 3.2. From the table, we see that all schemes but the MP9 have at least their theoretical order. The piecewise-linear method, theoretically of second-order, has a third accuracy order.

To compare the influence of the LF, the HLL and the HLLD Riemann solvers on the code's dissipation, we ran several simulations with the MP5 reconstruction scheme and the RK3 time

reconstruction scheme	$\frac{4}{3}\mathfrak{N}_\nu^{\Delta x} + \mathfrak{N}_\xi^{\Delta x}$	r
PL	14.26 ± 0.71	3.049 ± 0.009
MP5	43.4 ± 2.5	4.961 ± 0.014
MP7	302 ± 20	6.897 ± 0.021
MP9	830 ± 340	8.42 ± 0.15

Table 3.1: Comparison of the reconstruction scheme's contribution to the numerical viscosity for the sound wave simulations. For all schemes the HLL Riemann solver and the RK3 time integrator are used. The CFL factor is set to 0.01, so that the time integration errors are negligible. For the definition of $\mathfrak{N}_\nu^{\Delta x}$ and $\mathfrak{N}_\xi^{\Delta x}$, see Eqs. (3.1) and (3.4).

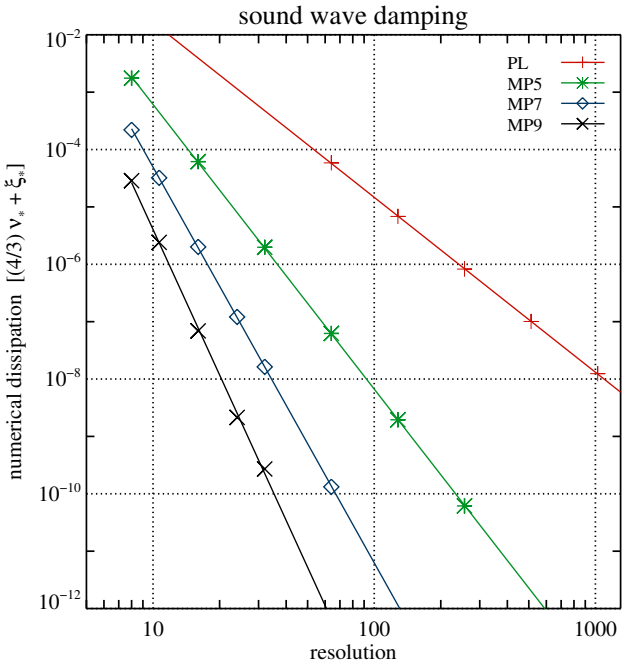

Figure 3.2: Numerical dissipation as a function of resolution for different reconstruction schemes: the piecewise linear (PL - red pluses), the monotonicity preserving of the 5th order (MP5 - green asterisks), the MP7 (blue diamonds) and the MP9 (black crosses). Straight lines of corresponding colours are linear fits of the simulation results (see main text for more details). Grid resolutions 8 to 1024 zones are used. In order to keep the time integration errors negligible the 4th order Runge-Kutta (RK4) method is used and the CFL factor is set to 0.01.

integrator with $C_{\rm CFL} = 0.01$. We chose resolutions ranging from 8 to 256 zones. The data analysis was performed like in the previous paragraph. The results are presented in Table 3.2.

In order to determine $\mathfrak{N}_\nu^{\Delta t}$ and $\mathfrak{N}_\xi^{\Delta t}$, we ran several simulations with either a fixed CFL factor ($C_{\rm CFL} = 0.5$) and different resolutions, or with a constant resolution and a varying $C_{\rm CFL}$ from 0.1 to 0.9. Because of Eq. (3.3), both approaches should be equivalent. To keep the contribution of the spatial discretisation errors as low as possible, we used the MP9 scheme. The RK3 time integrator and the HLL Riemann solver were used. The results are presented in Table 3.3 and Fig. 3.3. From the table, we see that in both cases the RK3 scheme has the third order of accuracy and the estimators of $\frac{4}{3}\mathfrak{N}_\nu^{\Delta t} + \mathfrak{N}_\xi^{\Delta t}$ are equal within the error limit. We also ran a few simulations with the RK4 time integrator, but for these simulations the sound damping coefficient was negative,

Riemann solver	$\frac{4}{3}\mathfrak{N}_\nu^{\Delta x} + \mathfrak{N}_\xi^{\Delta x}$	r
LF	42.9 ± 2.3	4.957 ± 0.013
HLL	43.4 ± 2.5	4.961 ± 0.014
HLLD	42.7 ± 2.2	4.956 ± 0.013

Table 3.2: Comparison of the Riemann solvers' contribution to the numerical shear and bulk viscosity for the sound wave simulations. For all simulations the MP5 scheme and the RK3 time integrator are used. The CFL factor is set to 0.01, so that the time integration errors are negligible. For the definition of $\mathfrak{N}_\nu^{\Delta x}$ and $\mathfrak{N}_\xi^{\Delta x}$ see Eqs. (3.1) and (3.4).

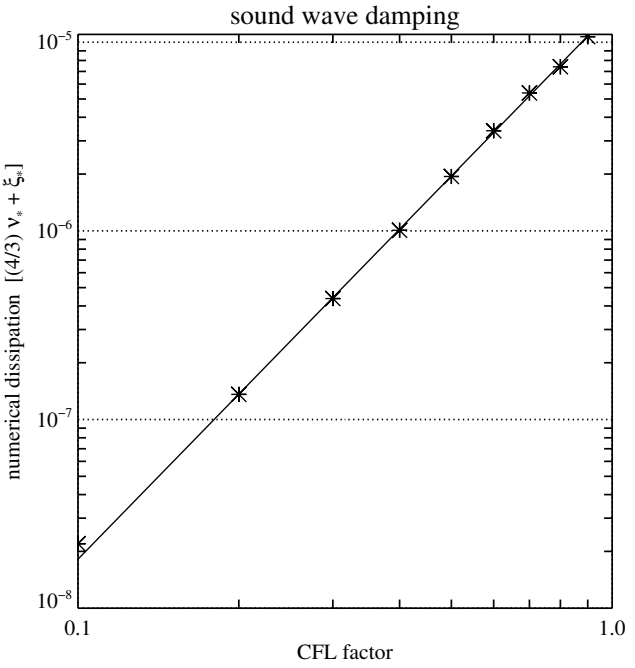

Figure 3.3: Numerical dissipation as a function of CFL factor (and hence effectively size of the timestep) for the RK3 time integrator. The resolution is set to 32 zones. To keep the contribution of the spatial discretisation errors at a negligible level, the MP9 reconstruction scheme is used. Simulation results are marked with asterisks and the straight line is a linear fit of them.

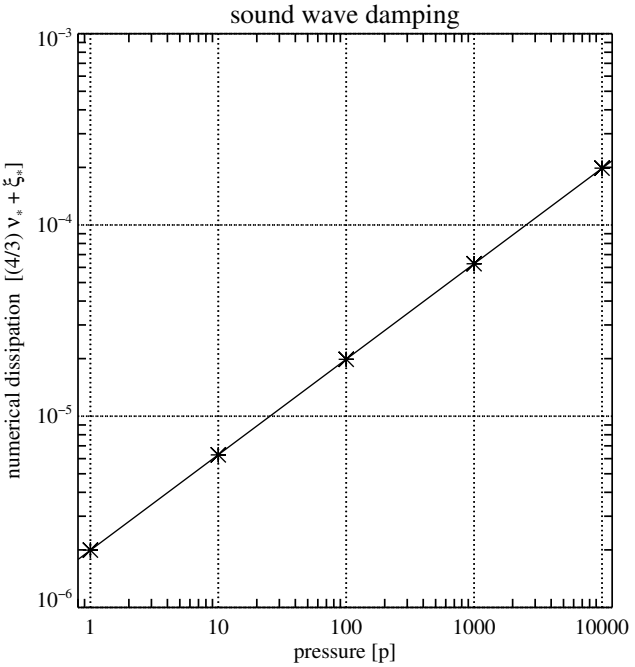

Figure 3.4: Dependence of the numerical dissipation on the characteristic speed, which is changed by varying the background pressure ($c_s \propto \sqrt{p}$). Simulation results are marked with asterisks and the straight line is a linear fit of them. The resolution is set to 32 zones. the MP5 scheme and RK3 time integrator are used and the CFL factor is set to 0.01.

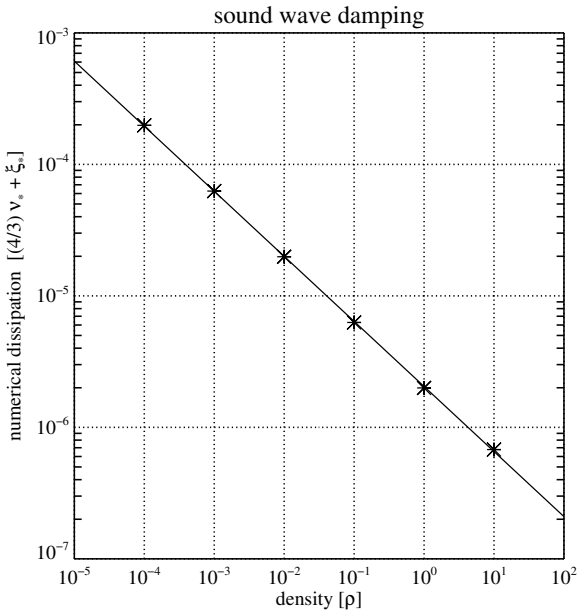

Figure 3.5: Same as Fig. 3.4 with the difference that the characteristic speed is changed by varying the background density ($c_s \propto \rho^{(-1/2)}$).

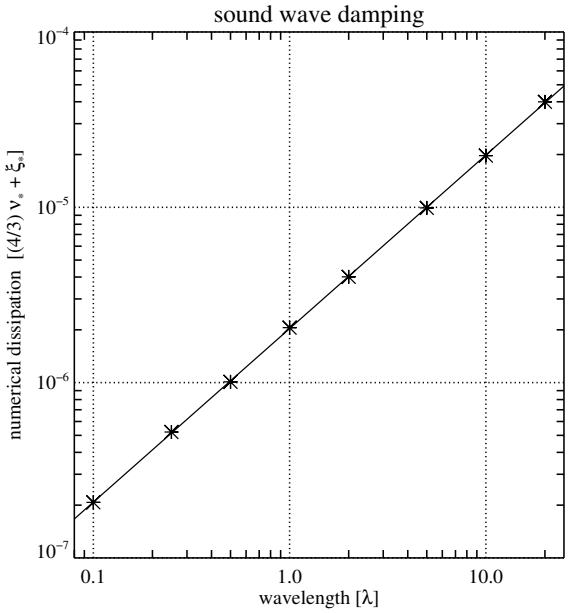

Figure 3.6: Dependence of the numerical dissipation on the characteristic length for the sound wave simulations. The results are marked with asterisks and the straight line is a linear fit of them (see main text for details). To simulate different wavelengths the box size has to be changed accordingly. The resolution is set to 32 zones. MP5 scheme and RK4 time integrator are used, the CFL factor is set to 0.01.

varied quantity	$\frac{4}{3}\mathfrak{N}_{\nu}^{\Delta t}+\mathfrak{N}_{\xi}^{\Delta t}$	q
CFL factor	2.0 ± 0.4	2.906 ± 0.042
grid resolution	2.45 ± 0.17	2.95 ± 0.013

Table 3.3: Contribution of the RK3 time integrator to the numerical viscosity for the sound wave simulations using the HLL Riemann solver and the MP9 reconstruction schemes. To determine the integrator's order either the CFL factor was changed for fixed resolution (first row in the table) or the factor is set to $C_{\rm CFL}=0.5$ and the resolution was changed (second row in the table). According to Eqs. (3.1) and (3.3) both approaches are equivalent. For all simulations, the dissipation of the reconstruction scheme is negligible. For the definition of $\mathfrak{N}_{\nu}^{\Delta t}$ and $\mathfrak{N}_{\xi}^{\Delta t}$, see Eqs. (3.1) and (3.4).

varied quantity	$\frac{4}{3}\mathfrak{N}_{\nu}^{\Delta x}+\mathfrak{N}_{\xi}^{\Delta x}$	a
pressure	45.3 ± 2.3	0.49935 ± 0.00023
density	43.4 ± 2.4	-0.4949 ± 0.0026
wavelength	46.2 ± 2.4	0.9899 ± 0.0024

Table 3.4: The results of simulations aiming to identify the characteristic velocity and length for the sound wave simulations (for more details see main text). For all simulations, the MP5 reconstruction scheme, the HLL Riemann solver and the RK3 time integrator are used. The CFL factor is set to 0.01, so that the time integration errors are negligible. For the definition of $\mathfrak{N}_{\nu}^{\Delta x}$ and $\mathfrak{N}_{\xi}^{\Delta x}$ see Eqs. (3.1) and (3.4).

which is unphysical. However, the modulus of that "positive damping" was much smaller than the modulus of the damping caused by the RK3 integrator.

To demonstrate that the numerical viscosity is proportional to the characteristic speed of the system ($\nu_*\propto\mathcal{V}$ and $\xi_*\propto\mathcal{V}$), we ran several simulations with 32 zones, the MP5 reconstruction scheme and the HLL Riemann solver. The natural choice for the characteristic velocity is the sound speed, i.e. one should expect $\nu_*\propto c_{\rm s}=\sqrt{\Gamma p_0/\rho_0}$. We changed the value of the background pressure from 1 to 10^4 keeping the density constant ($\rho_0=1$). For each simulation, we determined the numerical viscosity, and we fitted the results with the function

$$\ln(\frac{4}{3}\nu_*+\xi_*)=a\ln(p_0)+d. \tag{3.17}$$

If ansatz (3.1) is correct, one would expect $\nu_*\propto\sqrt{p_0}$, and hence a should be equal to $1/2$. In another set of simulations, we kept the pressure constant ($p_0=1$) varying the background density from 10^{-4} to 10. We fitted the measured numerical viscosities with another function:

$$\ln(\frac{4}{3}\nu_*+\xi_*)=a\ln(\rho_0)+d, \tag{3.18}$$

this time expecting $a=-1/2$. The results are presented in Table 3.4, and Figs. 3.4 and 3.5. They clearly indicate that we correctly identified the characteristic velocity of the system. At this point, we would like to note that the magnetosonic speed reduces to the sound speed in the absence of the magnetic field. Therefore equally well, we could say that the system's characteristic velocity is the magnetosonic speed.

Another set of simulations allowed us to determine the system's characteristic length, for which the most natural candidate in wave simulations it the wavelength. We ran several simulations with the MP5 reconstruction scheme, the HLL Riemann solver, the RK3 integrator and $C_{\rm CFL}=0.01$.

We chose wavelengths λ ranging from 0.1 to 20. The box size was changed accordingly ($L = \lambda$). The resolution was set to 32 zones. For every, simulation we determined the numerical damping. We fitted the results with the function

$$\ln(\frac{4}{3}\nu_* + \xi_*) = a\ln(\lambda) + d, \tag{3.19}$$

expecting $a = 1$. The results, presented in Table 3.4 and in Fig. 3.6, confirm our hypothesis.

3.3.2 Alfvén waves

Another type of waves allowed us to determine a linear combination of the numerical shear viscosity and resistivity of the code. We set the background magnetic field and density to $b_{0x} = \rho = 1$, and the pressure to $p = 2 \times 10^{-3}$. We perturbed the system with an Alfvén wave:

$$b_{1y}(x,0) = \varepsilon \sin(kx), \tag{3.20}$$

$$v_{1y}(x,0) = -\frac{b_{y1}}{\sqrt{\rho}}. \tag{3.21}$$

In ideal MHD, the wave would propagate with a constant amplitude at the Alfvén speed $c_\mathrm{A} = b_{0x}/\sqrt{\rho}$. In the presence of viscosity and resistivity, the wave amplitude will decrease with time. In the weak damping approximation, i.e. for $k^4(\nu+\eta)^2/(4c_\mathrm{A}^2) \ll 1$, the velocity evolution reads (for the derivation, see Campos (1999))

$$v_y(x,t) = v_0 e^{-(k^2/2)(\eta+\nu)t} e^{ik(x+(b_{0x}/\rho)t)}. \tag{3.22}$$

We define the Alfvén damping coefficient as

$$\mathfrak{D}_\mathrm{A} = \frac{k^2}{2}(\eta+\nu) \tag{3.23}$$

and rewrite Eq. (3.22) as

$$v_y(x,t) = v_0 e^{-\mathfrak{D}_\mathrm{A} t} e^{ik(x+c_\mathrm{A}t)}. \tag{3.24}$$

We first tested Eq. (3.23) by running simulations with different values of the physical shear viscosity and resistivity (from 10^{-4} to 10^{-3}). The MP9 reconstruction scheme, the RK3 time integrator and the HLL Riemann solvers were used. In order to keep the numerical dissipation low, the resolution was set to 512 grid zones and the CFL factor to 0.5. The measured the damping of the magnetic energy's y component should equal to $2\mathfrak{D}_\mathrm{A}$. We found a very good agreement between theory and numerical experiment. We also ran a few simulations with non-zero bulk viscosity, which, as expected, had no influence on the damping coefficient.

The remaining simulations were analogous to the sound wave tests. We compared the influence of the MP5, MP7 and MP9 reconstruction schemes on the numerical shear viscosity ν_* and resistivity η_*. We ran several Alfvén wave simulations in ideal MHD with resolutions from 8 to 256 zones. We used the HLL Riemann solver, the RK3 time integrator with $C_\mathrm{CFL} = 0.01$, so that the temporal errors were negligible. For every simulation, we measured the kinetic energy damping, from which we determined a linear combination of the numerical shear viscosity and resistivity

$$\nu_* + \eta_* = \frac{2}{k^2}\mathfrak{D}_\mathrm{A}. \tag{3.25}$$

reconstruction scheme	$\mathfrak{N}_\nu^{\Delta x} + \mathfrak{N}_\eta^{\Delta x}$	r
MP5	42.6 ± 2.1	4.965 ± 0.013
MP7	44 ± 53	6.194 ± 0.034
MP9	1190 ± 190	8.57 ± 0.06

Table 3.5: Comparison of reconstruction schemes' contribution to the numerical shear viscosity and resistivity for Alfvén wave simulations. For all schemes the HLL Riemann solver and the RK3 time integrator are used. The CFL factor is set to 0.01, so that the time integration errors are negligible. For the definition of $\mathfrak{N}_\nu^{\Delta x}$ and $\mathfrak{N}_\eta^{\Delta x}$ see Eqs. (3.1) and (3.5).

Riemann solver	$\mathfrak{N}_\nu^{\Delta x} + \mathfrak{N}_\eta^{\Delta x}$	r
LF	41.9 ± 2.9	4.95 ± 0.02
HLL	42.6 ± 2.1	4.96 ± 0.013
HLLD	42.1 ± 2.8	4.95 ± 0.02

Table 3.6: Comparison of the Riemann solvers' contribution to the numerical shear viscosity and resistivity for the Alfvén wave simulations. For all simulations the MP5 scheme and the RK3 time integrator are used. The CFL factor is set to 0.01, so that the time integration errors are negligible. For the definition of $\mathfrak{N}_\nu^{\Delta x}$ and $\mathfrak{N}_\eta^{\Delta x}$ see Eqs. (3.1) and (3.5).

time integrator	$\mathfrak{N}_\nu^{\Delta t} + \mathfrak{N}_\eta^{\Delta t}$	q
RK3	0.86 ± 0.08	2.949 ± 0.022
RK4	7.6 ± 2.5	5.181 ± 0.096

Table 3.7: The RK3 and RK4 time integrators' contribution to the numerical shear viscosity and resistivity for the Alfvén wave simulations. In all of them the HLL Riemann solver and the MP9 reconstruction schemes are used. For all simulations the reconstruction scheme's dissipation is negligible. For the definition of $\mathfrak{N}_\nu^{\Delta t}$ and $\mathfrak{N}_\eta^{\Delta t}$ see Eqs. (3.1) and (3.5).

varied quantity	$\mathfrak{N}_\nu^{\Delta x} + \mathfrak{N}_\eta^{\Delta x}$	a
magnetic field	44 ± 2	0.9998 ± 0.0001
pressure	38 ± 2	0.49792 ± 0.0008
density	44 ± 2	-0.50001 ± 0.00006
wavelength	44 ± 2	-1.0003 ± 0.0003

Table 3.8: The results of simulations aiming to identify the system's characteristic velocity and length (for details, see main text). For all simulations, the MP5 reconstruction scheme, the HLL Riemann solver and the RK3 time integrator are used. The CFL factor is set to 0.01, so that the time integration errors were negligible. For the definition of $\mathfrak{N}_\nu^{\Delta x}$ and $\mathfrak{N}_\xi^{\Delta x}$ see Eqs. (3.1) and (3.5).

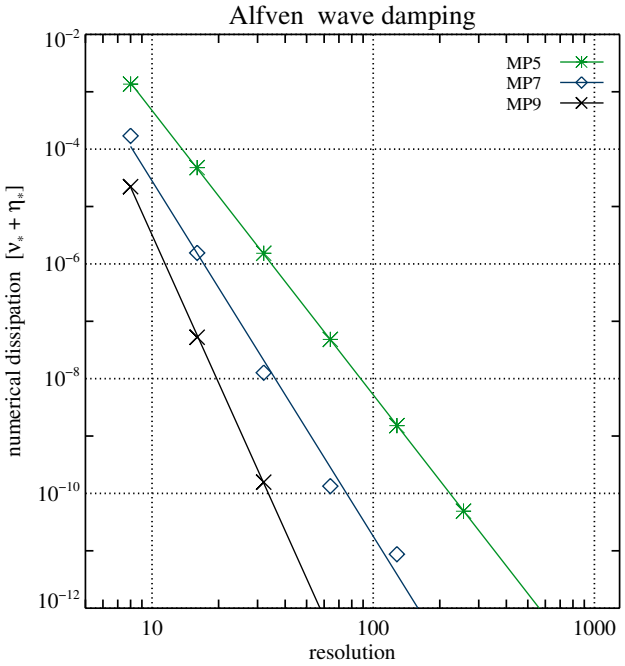

Figure 3.7: Numerical dissipation as a function of resolution for the MP5 (green asterisks), the MP7 (blue diamonds) and the MP9 (black crosses) reconstruction schemes in Alfvén wave simulations. Straight lines of corresponding colours are linear fits of the simulation results. To keep the time integration errors negligible, the RK4 method with the CFL factor set to 0.01 were used.

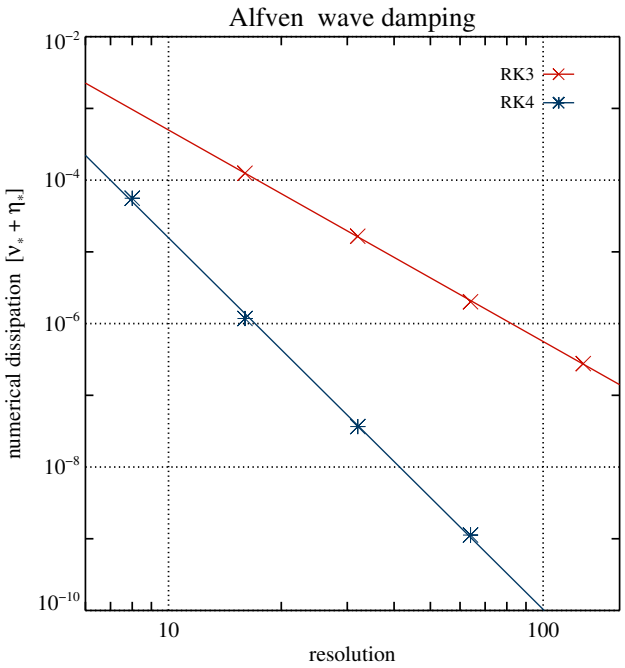

Figure 3.8: Numerical dissipation as a function of resolution (hence effectively timestep) for the RK3 (red crosses) and the RK4 (blue asterisks) time integrators in Alfvén wave simulations. The HLL Riemann solver and the MP9 reconstruction scheme are used. The spatial discretisation errors are negligible. The red and blue straights result from the linear fit to the data points.

The simulation results were fitted with the function

$$\ln(\nu_* + \eta_*) = r \ln(\Delta x) + d, \tag{3.26}$$

where r is the order of the reconstruction scheme. From the estimator of d, with the help of Eqs. (3.1), (3.5) and (3.25), we determined $\mathfrak{N}_\nu^{\Delta x} + \mathfrak{N}_\eta^{\Delta x}$.[5] The results are presented in Table 3.5 and Fig. 3.7. The MP5 and the MP9 schemes were approximately of 5th and 9th order of accuracy, respectively , whereas the order of the MP7 was lower than theoretically expected.

Next, we investigated the contribution of the LF, HLL and HLLD Riemann solvers to the numerical dissipation. We used the MP5 reconstruction scheme and the RK3 time integrator with $C_{\mathrm{CFL}} = 0.01$. We ran simulations with 8 to 256 zones. Since the further analysis was analogous to the previous simulation set, we omit the details here. The results are presented in Table 3.6. All three Riemann solvers were equally dissipative within the errors.

Another set of simulations allowed us to determine the dependence of the numerical dissipation on the RK3 and RK4 time integrators. The HLL Riemann solver and the MP9 reconstruction were used. We set $C_{\mathrm{CFL}} = 0.8$ and with both integrators, we ran several simulations with resolutions from 8 to 128 zones. The results are presented in Table 3.7 and Fig. 3.8. Note that equally well, we could keep the resolution fixed and change the CFL factor, as we did for the sound waves (see Table 3.7 and Fig. 3.3). To determine the system's characteristic length we ran several simulations with wavelengths from $\lambda = 0.01$ to 10 (changing the box size accordingly, $L = \lambda$). We set the resolution to 32 zones and used the HLL Riemann solver, the MP5 reconstruction and the RK3 time integrator with $C_{\mathrm{CFL}} = 0.01$. We fitted the simulation results with the function

$$\ln(\nu_* + \eta_*) = a \ln \lambda + d. \tag{3.27}$$

Should $a = 1$, the wavelength is the system's characteristic length. From the estimator of d we determined $\mathfrak{N}_\nu^{\Delta x}$ and $\mathfrak{N}_\eta^{\Delta x}$. The results, presented in Table 3.8 and in Fig. 3.9, confirm our hypothesis.

When it comes to the characteristic velocity, the situation becomes a bit more complicated than for the sound waves. The Alfvén speed seems to be a natural candidate for the system's characteristic velocity. In the end, we simulate Alfvén waves. However, we must not forget that the LF, HLL and HLLD solvers do not use the full solution of the Riemann problem. They employ the two[6] fastest (in absolute value) wave speeds to approximately represent the Riemann fan. The fastest MHD waves are the magnetosonic ones. Their speed for a wavevector parallel to the background magnetic field reads

$$c_{\mathrm{ms}} = \max\{c_{\mathrm{A}}, c_{\mathrm{s}}\}. \tag{3.28}$$

This means that there should be a simple test to determine whether the Alfvénor magnetosonic speed is the characteristic velocity $\mathcal{V}$. For $c_{\mathrm{A}} \geq c_{\mathrm{s}}$ both speeds are equal and we expect $\mathcal{V} \propto b_0$. However, for $c_{\mathrm{A}} < c_{\mathrm{s}}$ there are two possible scenarios: either this proportionality still holds or $\mathcal{V}$ becomes independent of b_0. In the first case, the system's characteristic velocity is the Alfvén speed, in the second case, it is the magnetosonic speed. We ran several simulations with $\rho = 1, p_0 = 0.1$ and a magnetic field b_0 in the range from 10^{-3} to 200 with a resolution of 32 zones. The HLL Riemann solver, the MP5 reconstruction and the RK3 integrator with $C_{\mathrm{CFL}} = 0.01$ were used. To the measured numerical dissipation from simulations with $b_0 \geq 0.5$, we fitted the function

$$\ln(\nu_* + \eta_*) = a \ln(b_0) + d. \tag{3.29}$$

[5] For the characteristic velocity we put $\mathcal{V} = 1$. See later in this subsection for an extended discussion.

[6] The more accurate HLLD solver uses one additional wave.

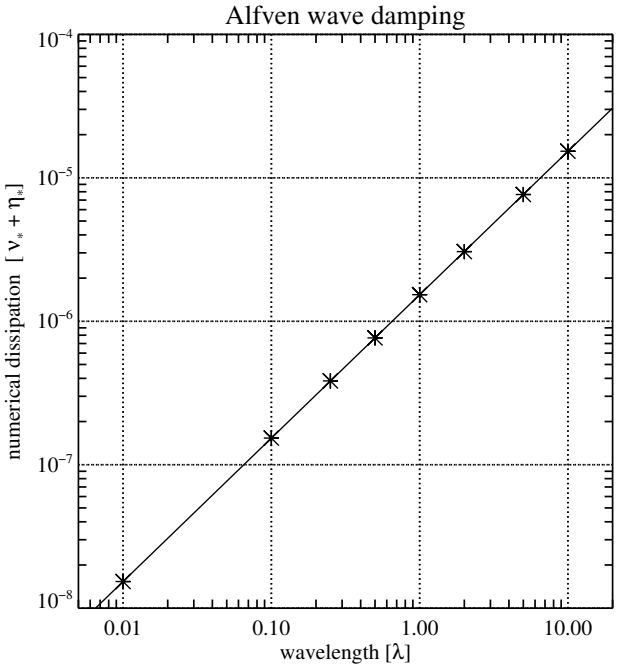

Figure 3.9: Dependence of the numerical dissipation on the characteristic length for the Alfvén wave simulations. The results are marked with asterisks and the straight line is a linear fit of the data. The resolution is set to 32 zones. The MP5 scheme and the RK4 time integrator are used, the CFL factor is set to 0.01

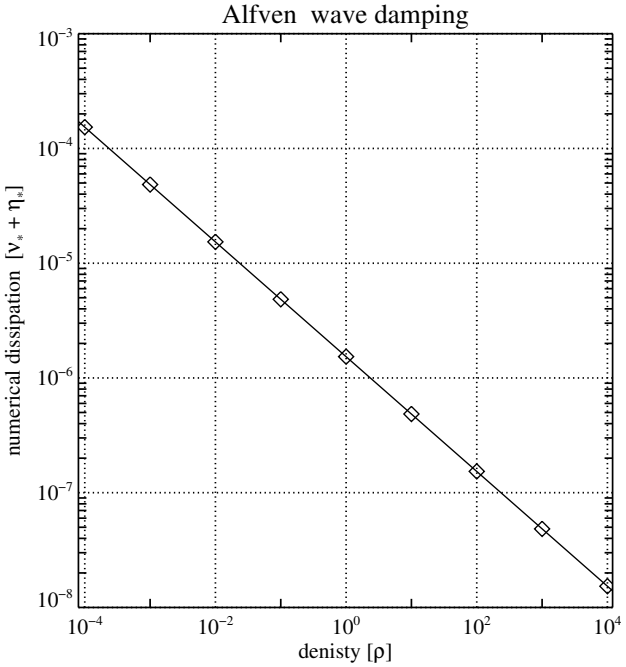

Figure 3.10: Dependence of the numerical dissipation on the system's characteristic, i.e. fast magnetosonic, velocity for the Alfvén wave simulation. The numerical setup is like in simulations presented in Fig. 3.9. The magnetosonic speed is inversely proportional to the square root of the density. The line is a fit to the simulation data.

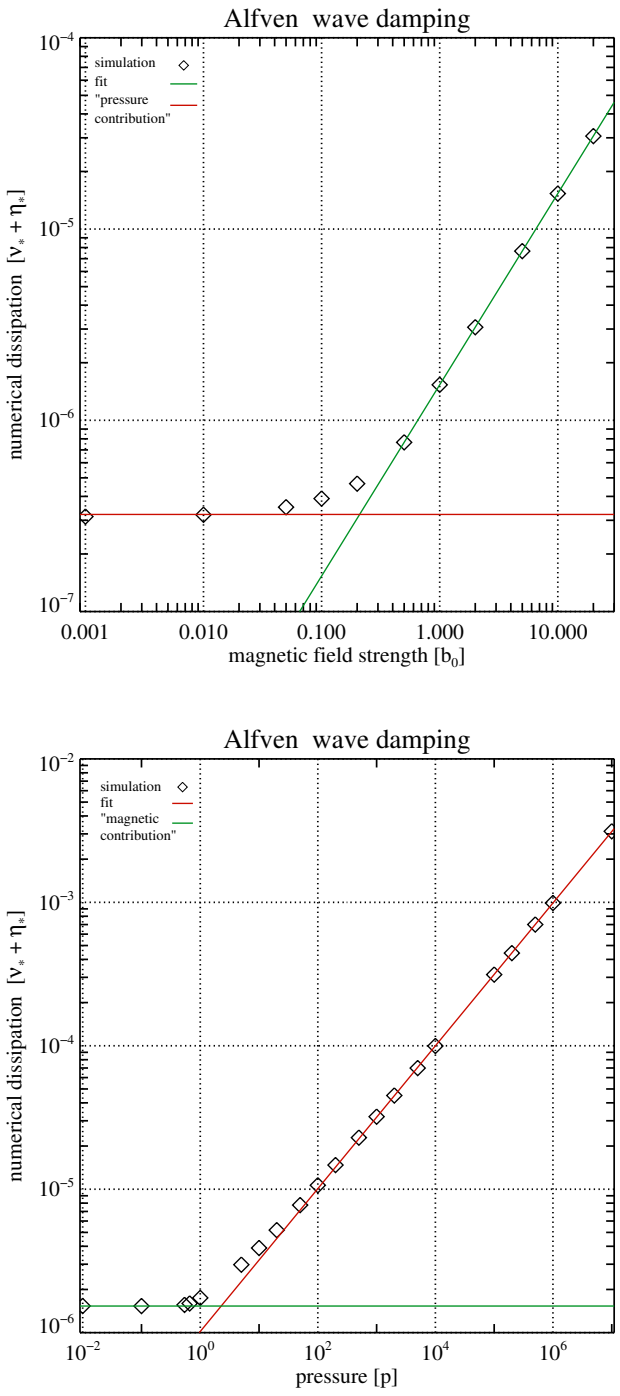

Figure 3.11: Dependence of the numerical dissipation dependence on the system's characteristic, i.e. fast magnetosonic, velocity for the Alfvén wave simulation. The numerical setup is like in simulations presented in Fig. 3.9. *Top:* The green straight line results from a fit to the points with $b_0 > 0.5$, where the magnetosonic speed linearly depends on the magnetic field. For $b_0 < 0.4$, the magnetosonic velocity equals the sound speed, which is constant in all simulations. The expected numerical dissipation for this regime is marked with the red line. *Bottom:* The red straight results from a fit to the points with $p > 10^3$, where the magnetosonic speed linearly depends on the square root of the pressure. For $p < 0.7$, the magnetosonic velocity equals the Alfvén speed, which is constant in all simulations. The expected numerical dissipation for this regime is marked with the green line.

As expected, a equals 1 within the errors. From the estimator of d, we computed $\mathfrak{N}_\nu^{\Delta x} + \mathfrak{N}_\eta^{\Delta x}$. The results are presented in Table 3.8 and in the upper panel of Fig. 3.11. For $b_0 < 0.4$, the sound speed ($c_\mathrm{s} \approx 0.4$) is higher than the Alfvén speed ($c_\mathrm{A} = b_0$) and the magnetosonic speed equals to the former. The values of numerical damping from simulations with such low magnetic fields no longer lie on the green fitting straight line. For $b_0 \leq 0.01$, the numerical dissipation becomes independent of the magnetic field. Hence, the system's characteristic velocity must be the magnetosonic speed. With the red horizontal line, described as "pressure contribution", we marked the expected numerical damping, assuming that the characteristic velocity is equal to the sound speed. The expected value was determined in the following test (see the bottom panel of Fig. 3.11). For simulations with $c_\mathrm{A} \approx c_\mathrm{s}$ ($b_0 \approx 0.4$), the numerical dissipation is somewhat higher than expected. We note that for this particular configuration and $c_\mathrm{A} = c_\mathrm{s}$ a so called *triple umbilic point* (see, e.g. Goedbloed & Poedts (2004)) is encountered, where four MHD characteristics, i.e. the Alfvén , sound, slow and fast magnetosonic wave speeds coincide. This means that probably all of these waves are more likely to appear as a result of errors caused by approximately solving the Riemann problem. Naturally, all these spurious waves will have negligible amplitudes, still they will drain energy from the Alfvén wave. This probably explains why both the magnetic field and the gas pressure contribute to the numerical damping additively and not only one of them exclusively, as expected from the equation for the magnetosonic speed of a wave propagating parallel to the background magnetic field. Since such a degeneracy of the MHD wave speeds is rather an exception than a rule, we can conclude that ansatzes (3.1) and (3.5) work well the Alfvén waves and we correctly identified the system's characteristic velocity.

Another set of simulations was run to investigate the influence of the pressure on the numerical damping. For the same numerical setup like in the previous test, we put $b_0 = \rho = 1$ and chose pressure values from 10^{-2} to 10^7. The measured values of the numerical damping are presented in the bottom panel of Fig. 3.11. As expected, for simulations with $p < 0.1$, the numerical dissipation is pressure independent. In this regime the magnetosonic speed is equal to the Alfvén speed. With the green curve we mark the expected numerical damping if the system's characteristic velocity were the Alfvén speed. To the data from simulations with $p \geq 10^3$, we the fitted the function

$$\ln(\nu_* + \eta_*) = a \ln(p) + d. \tag{3.30}$$

The fitting straight line is drawn in red in Fig. 3.11. The value of a, as expected, is equal to $1/2$ within the error. From the estimator of d, we computed $\mathfrak{N}_\nu^{\Delta x} + \mathfrak{N}_\eta^{\Delta x}$. The results are presented in Table 3.8. In the intermediate regime, where $c_\mathrm{s} \approx c_\mathrm{A}$, like in the previous tests, both the magnetic field and the gas pressure contribute to the numerical dissipation.

Rather as a formality, we also checked the dependence of the numerical damping on the background density ρ. We ran several simulations for $b_0 = 1$, $p = 2 \times 10^{-3}$ and densities from 10^{-4} to 10^4. To the simulation data, we fitted the function

$$\ln(\nu_* + \eta_*) = a \ln(\rho) + d. \tag{3.31}$$

The results are presented in Fig. 3.10 and in Table 3.8. As expected, the estimator of a equals $-1/2$ within the errors. This confirms our finding on the system's characteristic speed.

Additionally, we investigated whether spatial discretisation- and time integration-errors are additive. For this purpose we ran a set of simulations in the parameter space region, where both terms from Eq. (3.1) for the numerical shear viscosity, i.e. $\mathfrak{N}_\nu^{\Delta x} \times \mathcal{V} \times \mathcal{L} \times \left(\frac{\Delta x}{\mathcal{L}}\right)^r$ and $\mathfrak{N}_\nu^{\Delta t} \times \mathcal{V} \times \mathcal{L} \times \left(\frac{\gamma \Delta t}{\mathcal{L}}\right)^q$, should be comparable. Analogically, both terms from Eq. (3.5) should contribute to the numerical resistivity. The HLL Riemann solver, the RK3 time integrator with $C_\mathrm{CFL} = 0.5$ and

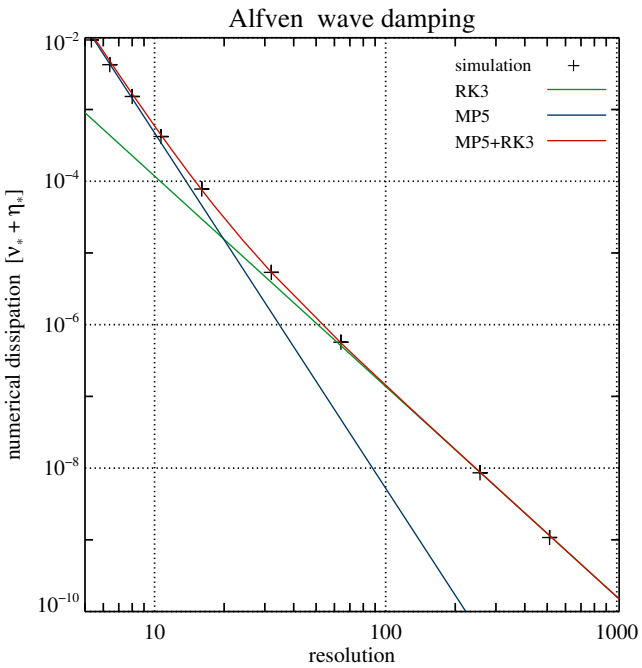

Figure 3.12: Numerical dissipation as a function of resolution for the MP5 reconstruction scheme and the RK3 time integrator. The CFL factor is set to 0.5. The simulation results are marked with black pluses. The green straight line depicts the predicted numerical dissipation of the RK3 time integrator for the given CFL factor. The blue straight shows the theoretical prediction for the MP5 scheme. The red curve is a sum of both types of numerical dissipation. For resolutions ≤ 16 zones, Alfvén waves are mainly damped by spatial discretisation errors, and for ≥ 128 zones by time integration errors. In the intermediate regime ($16 \sim 128$ zones), both types of errors add linearly (like proper scalars).

the MP5 reconstruction were used. We ran simulations with ≈ 5 to 1024 zones. [7] The simulation results are presented in Fig. 3.12. Additionally, we marked the expected numerical dissipation of the RK3 integrator (green), the MP5 reconstruction (blue) and the sum of both contributions (red). As we see from the figure, the errors add linearly.

3.3.3 Magnetosonic Waves

With the help of magnetosonic wave simulations, we determined the numerical resistivity and viscosity of the code. If not otherwise written, the background pressure, density and magnetic field were set to $p_0 = \rho_0 = 1$ and $\mathbf{b_0} = b_{0y}\hat{\mathbf{y}}$, respectively. We perturbed the system with a fast

[7] See the comment in Footnote 4 on page 42.

magnetosonic wave

$$v_{x1}(x,0) = \varepsilon sin(k_x x), \tag{3.32}$$

$$v_{y1}(x,0) = v_{x1}\frac{k_x^2 b_{0x} b_{0y}}{b_{0x}^2 k_x^2 - \rho_0 \omega^2}, \tag{3.33}$$

$$b_{y1}(x,0) = v_{x1}\frac{k_x b_{0y} \omega \rho_0}{\rho_0 \omega^2 - b_{0x}^2 k_x^2}, \tag{3.34}$$

$$\rho_1(x,0) = v_{x1}\frac{k_x \rho_0}{\omega}, \tag{3.35}$$

$$e_1(x,0) = v_{x1}\frac{k_x p_0 \Gamma}{\omega(\Gamma - 1)} \tag{3.36}$$

where

$$\omega = \frac{k}{\sqrt{2\rho_0}}\sqrt{\mathbf{b_0}^2 + \Gamma p_0 + \sqrt{\left(\mathbf{b_0}^2 + \Gamma p_0\right)^2 - 4\mathbf{b_0}^2 \Gamma p_0 \cos^2\theta}} \tag{3.37}$$

is the wave frequency, θ is the angle between the wavevector and the background magnetic field, e_1 is a perturbation of the total specific energy and the velocity amplitude was set to $\varepsilon = 10^{-5}$. For $\theta = \frac{\pi}{2}$ (the angle chosen in almost all simulations), the magnetosonic speed reads

$$c_{\rm ms} \equiv \frac{\omega}{k} = \sqrt{\frac{\mathbf{b_0}^2 + \Gamma p_0}{\rho_0}}. \tag{3.38}$$

In the presence of viscosity or resistivity, the wave will be damped over time, e.g. the evolution of the velocity's x component will read

$$v_x(x,t) = \varepsilon e^{-\mathfrak{D}_{\rm ms} t} e^{ik(x + c_{\rm ms} t)}, \tag{3.39}$$

where the damping coefficient for the fast magnetosonic wave propagating perpendicularly to the background magnetic field reads (for the derivation, see Campos (1999))

$$\mathfrak{D}_{\rm ms} = \frac{k^2}{2}\left(\frac{4}{3}\nu + \xi + \frac{\eta}{1 + c_{\rm s}^2/c_{\rm A}^2}\right). \tag{3.40}$$

It not only depends on viscosity and resistivity but also on the sound to Alfvén speed ratio. Therefore, for the fast magnetosonic waves, unlike for the Alfvén waves, one can control the contribution of the resistivity to the total damping. In the two most extreme cases, i.e. for $c_{\rm s} \ll c_{\rm A}$, $\mathfrak{D}_{MS} \approx (k^2/2)(\frac{4}{3}\nu + \xi + \eta)$ and for $c_{\rm s} \gg c_{\rm A}$, $\mathfrak{D}_{MS} \approx (k^2/2)(\frac{4}{3}\nu + \xi)$. [8] We will exploit this feature later in the tests.

Like for the previous wave simulations, we verified the analytical predictions for damping coefficient (3.40), performing several simulations with the HLL Riemann solver, the MP9 reconstruction and the RK3 time integrator with $C_{\rm CFL} = 0.1$. The resolution was set to 128 zones. Checking the dependence of $\mathfrak{D}_{\rm s}$ on ν and ξ was rather straightforward. The term containing resistivity is proportional to $1/(1 + c_{\rm s}^2/c_{\rm A}^2)$, which we will denote as α and call the *resistivity contribution*. We ran a few simulations changing α from $\approx 10^{-4}$ to ≈ 1. The lowest value was achieved for $b_0 = 0.1$ and $p = 100$, and the highest one for $b_0 = 10$ and $p = 0.01$. The resistivity was set to either 10^{-4} or 10^{-5}. The measured damping values are presented in Fig. 3.19, where red and blue straight lines mark the theoretical predictions for the higher and lower resistivity, respectively. The agreement between the theory and simulations is excellent.

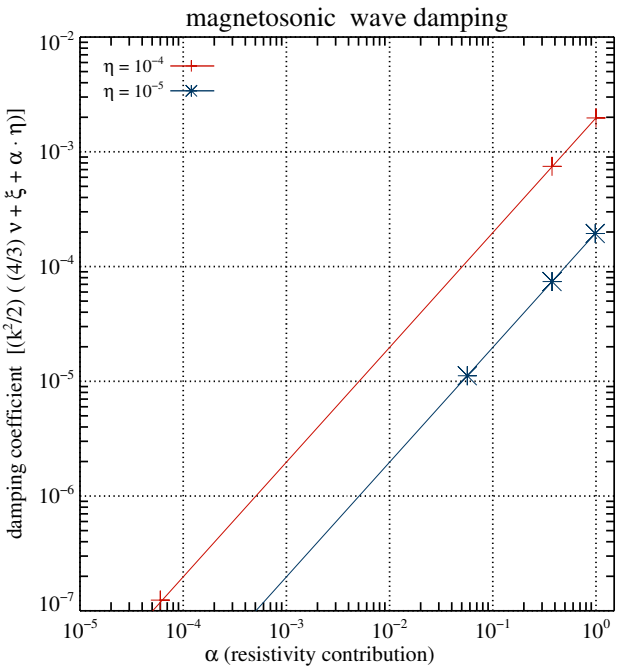

Figure 3.13: The resistivity contribution, $\alpha \equiv 1/(1+c_s^2/c_A^2)$, to the magnetosonic wave damping (see Eq. (3.40) and discussion below it). The simulations are run with the HLL Riemann solver, the MP9 reconstruction and the RK3 time integrator with $C_{\rm CFL} = 0.1$. The resolution is set to 128 zones. The resistivity is set to 10^{-4} (red pluses) or 10^{-5} (blue asterisks). The analytical predictions are marked with the straight lines of the corresponding colour.

reconstruction scheme	$\frac{4}{3}\mathfrak{N}_\nu^{\Delta x} + \mathfrak{N}_\xi^{\Delta x} + \frac{3}{8}\mathfrak{N}_\eta^{\Delta x}$	r
MP5	39.5 ± 2.7	4.95 ± 0.02
MP7	288 ± 20	6.903 ± 0.023
MP9	1970 ± 160	8.82 ± 0.03

Table 3.9: Comparison of reconstruction scheme's contribution to the numerical shear and bulk viscosity, and resistivity for the magnetosonic wave simulations. For all schemes, the HLL Riemann solver and the RK3 time integrator are used. The CFL factor is set to 0.01, so that the time integration errors are negligible. For the definition of $\mathfrak{N}_\nu^{\Delta x}$, $\mathfrak{N}_\xi^{\Delta x}$ and $\mathfrak{N}_\eta^{\Delta x}$, see Eqs. (3.1), (3.4) and (3.5).

time integrator	$\frac{4}{3}\mathfrak{N}_\nu^{\Delta t} + \mathfrak{N}_\eta^{\Delta t} + \frac{3}{8}\mathfrak{N}_\eta^{\Delta t}$	q
RK3	1.77 ± 0.06	2.9774 ± 0.0066
RK4	4.34 ± 0.75	4.834 ± 0.013

Table 3.10: The RK3 time integrator contribution to the numerical dissipation for the magnetosonic wave simulations. In all of them, the HLL Riemann solver and the MP9 reconstruction schemes are used. In all simulations, spatial discretisation errors are negligible. For the definition of $\mathfrak{N}_\nu^{\Delta t}$, $\mathfrak{N}_\xi^{\Delta t}$ and $\mathfrak{N}_\eta^{\Delta t}$, see Eqs. (3.1), (3.4), and (3.5).

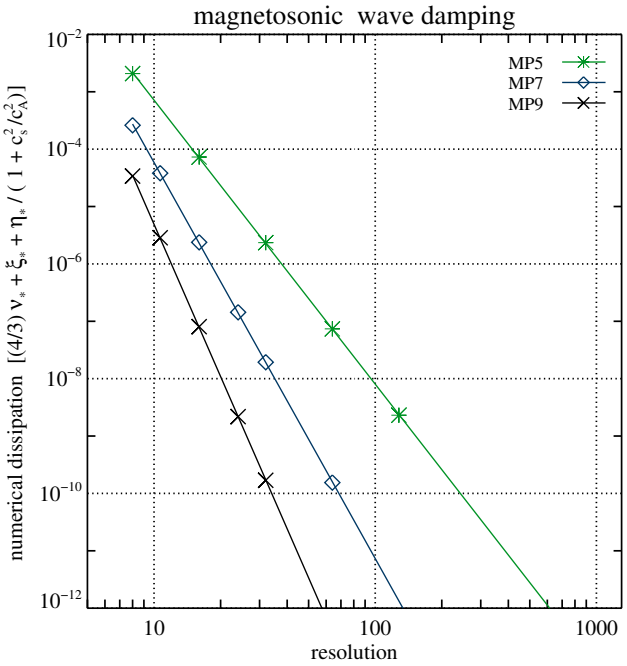

Figure 3.14: Numerical damping (see Eq. (3.40)) in magnetosonic wave simulations as a function of grid resolution for three reconstruction schemes: the MP5 (green asterisks), the MP7 (blue diamonds) and the MP9 (black crosses). In the simulations, the HLL Riemann solver, the RK3 time integrator are used. The CFL factor is set to 0.01, so that temporal errors are negligible.

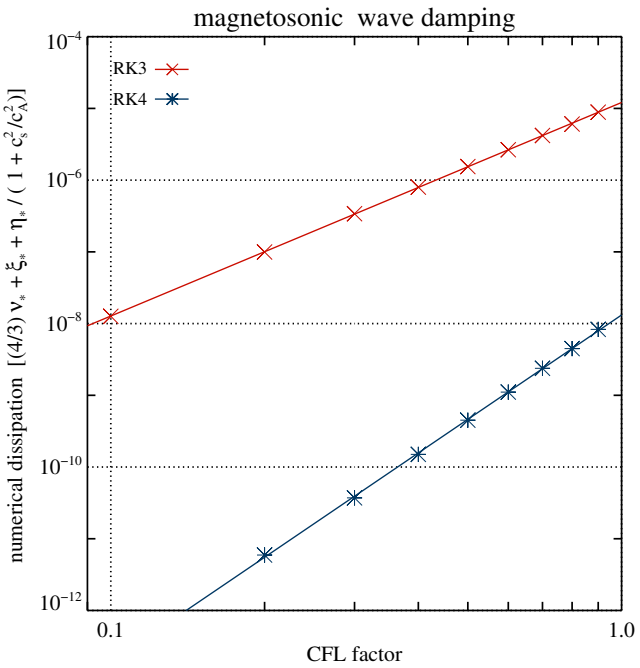

Figure 3.15: The influence of the RK3 (red crosses) and RK4 (blue asterisks) time integrators on the numerical dissipation in magnetosonic wave simulations with the HLL Riemann solver, the MP9 reconstruction scheme and a resolution of 64 zones. The spatial discretisation errors are negligible. The red and blue straight lines result from a linear fit to the data points.

Next, we investigated the influence of the MP5, MP7 and MP9 reconstruction schemes on the numerical dissipation. We chose $b_0 = p_0 = 1$, for which $\alpha = 3/8 = 0.375$. We ran several magnetosonic wave simulations in ideal MHD with resolutions from 8 to 256 zones. We used the HLL Riemann solver and the RK3 time integrator with $C_{\mathrm{CFL}} = 0.01$. For every simulation we measured the kinetic energy damping, from which we determined the linear combination of the numerical resistivity, and shear and bulk viscosity

$$\frac{4}{3}\nu_* + \xi_* + \frac{3}{8}\eta_* = \frac{2}{k^2}\mathfrak{D}_{\mathrm{ms}}. \tag{3.41}$$

To the simulation results, we fitted the function

$$\ln\left(\frac{4}{3}\nu_* + \xi_* + \frac{3}{8}\eta_*\right) = r\ln(\Delta x) + d, \tag{3.42}$$

where r is the reconstruction scheme order. From the estimator of d, with the help of Eqs. (3.1), (3.4), (3.5) and (3.41), we determined $\frac{4}{3}\mathfrak{N}_\nu^{\Delta x} + \mathfrak{N}_\xi^{\Delta x} + \frac{8}{3}\mathfrak{N}_\eta^{\Delta x}$. The results are presented in Table 3.9 and Fig. 3.14.

With another set of simulations, we determined the RK3 and RK4 time integrators' contribution to the numerical dissipation. The HLL Riemann solver and the MP9 reconstruction were used. We set the resolution to 64 zones and for both integrators we ran several simulations with the CFL factor from 0.1 to 0.9. The results are presented in Table 3.10 and Fig. 3.15. Note that the RK4 integrator's order was higher by one than theoretically expected.

There was no surprise in determining the system's characteristic velocity. It was the magnetosonic speed. To demonstrate that, we ran three groups of simulations with the HLL Riemann solver, the MP5 reconstruction and the RK3 time integrator with $C_{\mathrm{CFL}} = 0.01$. The resolution was set to 32 zones. In the first set of simulations, the background pressure and density were $p_0 = \rho_0 = 1$ and the magnetic field strength ranged from 10^{-4} to 10^3. To the measured numerical dissipation, we fitted the function

$$\ln\left(\frac{4}{3}\nu_* + \xi_* + \frac{3}{8}\eta_*\right) = a\ln\left(\sqrt{(\Gamma p_0 + b_0^2)/\rho_0}\right) + d. \tag{3.43}$$

From the estimator of d, we computed $\frac{4}{3}\mathfrak{N}_\nu^{\Delta x} + \mathfrak{N}_\xi^{\Delta x} + \frac{3}{8}\mathfrak{N}_\eta^{\Delta x}$. The results are presented in the upper panel of Fig. 3.16 and Table 3.11. As expected, $a = 1$ within the measurement errors. In the asymptotic regime $b_0 \ll p_0$, the numerical damping is independent of the magnetic field, while for $b_0 \gg p_0$ proportional to it . In the second set of simulations, the background magnetic field and density were $b_0 = \rho_0 = 1$ and the pressure ranged from 10^{-4} to 10^4. The further data analysis was analogous to the previous one, i.e. the fitting function was like in Eq. (3.43). The results, presented in the lower panel of Fig. 3.16 and Table 3.11, once again confirm the hypothesis on the system's characteristic velocity. In the third set of simulations, the background magnetic field and pressure were $b_0 = p_0 = 1$ and the density ranged from 10^{-3} to 10^4. To the simulation results, we fitted the function

$$\ln\left(\frac{4}{3}\nu_* + \xi_* + \frac{3}{8}\eta_*\right) = a\ln(\rho_0) + d. \tag{3.44}$$

The outcome is presented in Fig. 3.17 and Table 3.11. As expected, $s = -1/2$ within the measurement errors. With this, we conclude that the system's characteristic velocity is the magnetosonic speed. Since we already showed twice that for the wave simulations the characteristic length is the wavelength, we did not design any further tests to verify it for a third time.

[8] For $c_{\mathrm{A}} \to 0$, a magnetosonic wave becomes a sound wave and the damping coefficient does not depend on the resistivity and is equal to the sound wave damping coefficient (see Eq. (3.13)).

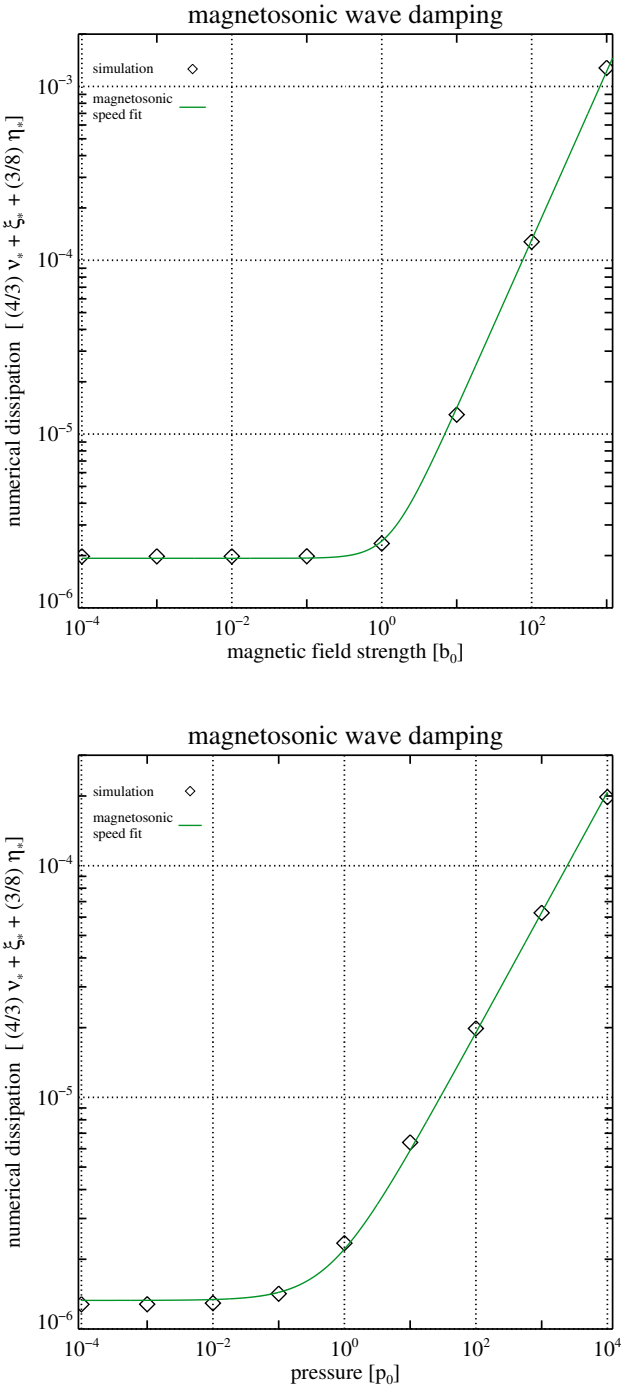

Figure 3.16: Dependence of the numerical dissipation on the system's characteristic velocity $\mathcal{V}$ for the magnetosonic wave simulations. The resolution is set to 32 zones, the HLL Riemann solver, the MP9 reconstruction and the RK3 time integrator with $C_{\rm CFL} = 0.01$ are used. In the *upper panel*, all simulations have $p_0 = 1$ and different values of the magnetic field amplitude, whereas in the *bottom panel*, the magnetic field is constant ($b_0 = 1$) and background pressure varies. The green curves in both panels are assuming $\mathcal{V} = c_{\rm ms} = \sqrt{(\Gamma p_0 + b_0^2)/\rho_0}$.

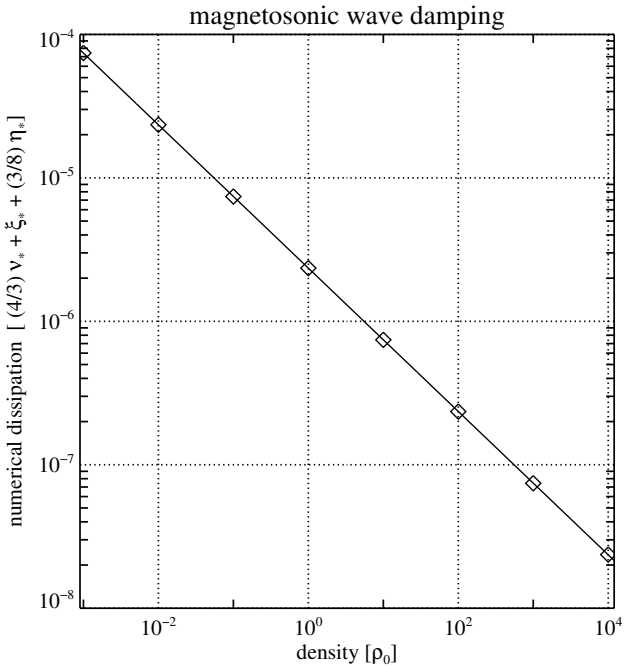

Figure 3.17: Dependence of the numerical dissipation on the background density for the magnetosonic wave simulations. The resolution is set to 32 zones, the HLL Riemann solver, the MP9 reconstruction and the RK3 time integrator with $C_{\mathrm{CFL}} = 0.01$ are used. The straight line is a fit to the simulation points (diamonds).

varied quantity	$\frac{4}{3}\mathfrak{N}_\nu^{\Delta t} + \mathfrak{N}_\eta^{\Delta t} + \frac{3}{8}\mathfrak{N}_\eta^{\Delta t}$	a
magnetic field	42.6 ± 3.8	0.970 ± 0.008
pressure	36.6 ± 3.4	1.04 ± 0.01
density	40.7 ± 2.8	-0.49969 ± 0.00015

Table 3.11: The results of tests aiming to identify the system's characteristic speed in magnetosonic wave damping simulations (for more details, see main text). For all simulations, the MP5 reconstruction scheme, the HLL Riemann solver and the RK3 time integrator are used. The CFL factor is set to 0.01, so that the time integration errors are negligible. For the definition of $\mathfrak{N}_\nu^{\Delta x}$, $\mathfrak{N}_\xi^{\Delta x}$ and $\mathfrak{N}_\eta^{\Delta x}$, see Eqs. (3.1), (3.4) and (3.5).

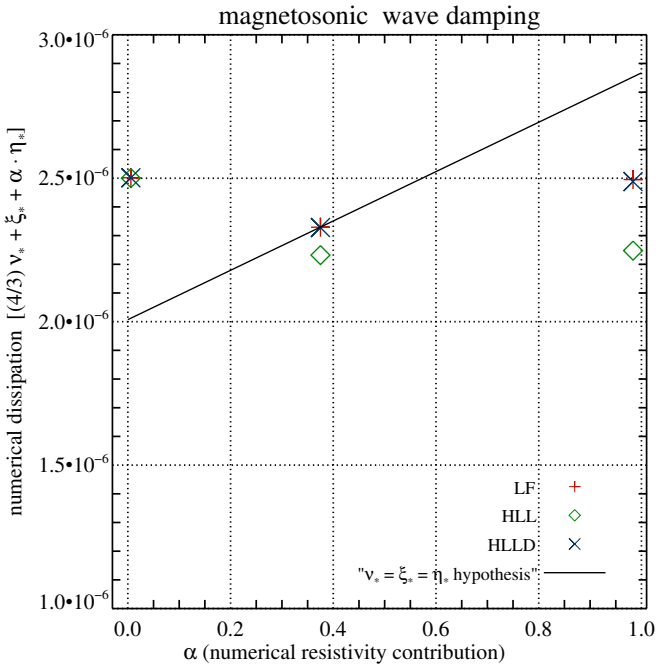

Figure 3.18: Dependence of the total numerical damping on the numerical resistivity contribution α (see Eq. (3.40) and discussion below it). The resolution is set to 32 zones, the MP5 reconstruction scheme and the RK3 time integrator with $C_{\mathrm{CFL}} = 0.01$ are used. The results for the LF, HLL and HLLD Riemann solvers are marked with the red pluses, green diamonds and blue x symbols, respectively. The black straight line is a theoretical prediction assuming that $\eta_* = \nu_* = \xi_*$. This hypothesis must be wrong and $\eta_* \ll \nu_* + \xi_*$.

As already mentioned before, the resistivity contribution α to the magnetosonic wave damping depends on the Alfvén to sound speed ratio (see Eq. (3.40)), or equivalently on the *plasma* β parameter ($\beta \equiv p_0/(2b_0^2)$). Exploiting this feature, we can measure the numerical resistivity. For each Riemann solver we ran three simulations with constant pressure, $p_0 = 1$, and magnetic fields $b_0 = 10, 1$ and 0.1 which correspond to $\alpha \approx 0.984, 0.375$ and 0.006, respectively. The density was chosen such that the characteristic velocity remained constant. The resolution was set to 32 zones, and the MP5 reconstruction scheme and the RK3 time integrator with $C_{\mathrm{CFL}} = 0.01$ were used. The measured values of the numerical damping are presented in Fig. 3.18. Additionally, with the black straight line, we mark the expected damping, assuming that the numerical resistivity, and shear and bulk viscosity are equal, i.e. $\eta_* = \nu_* = \xi_*$. We calibrated the straight line to give the correct values, by definition, for the simulations with the LF and HLLD Riemann solvers and $\alpha = 0.375$. As we can see, the hypothesis that $\eta_* = \nu_* = \xi_*$ must be wrong. The only conclusion that we can draw from the figure is that the numerical resistivity must be much lower than the sum of the numerical bulk and shear viscosity.

One could argue that the influence of the numerical resistivity is negligible because the wave propagates along the x axis, which is a numerically favoured direction (the same like y and z axes in multidimensional simulations). One could test this hypothesis with 2D simulations where the wavevectors are neither aligned to the x- nor to the y-axis. This would require non-standard and somewhat complicated boundary conditions that keep the periodicity in the wave propagation direction. Even if we implemented them to the, we would still not be able to tell how much they

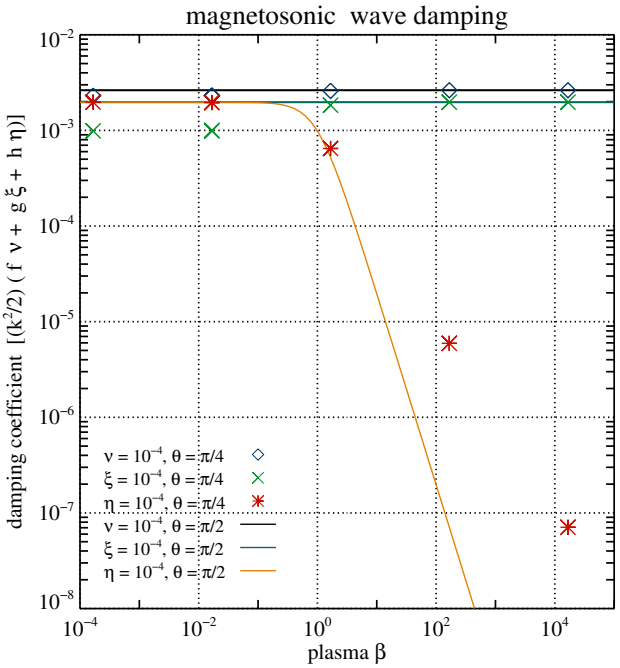

Figure 3.19: Dependence of the magnetosonic wave damping on the resistivity, shear and bulk viscosity for different values of plasma β. The solid curves depict the analytical predictions from Eq. (3.40) for $\theta = \frac{\pi}{2}$ (the angle between the wavevector and the background magnetic field) for shear viscosity (black), bulk viscosity (blue) and resistivity (orange). The values for $\theta = \frac{\pi}{4}$ are obtained from simulations (for details see main text) with physical shear viscosity (blue diamonds), bulk viscosity (green crosses) or resistivity (red asterisks).

contribute to the total numerical damping. Therefore, we did not test this hypothesis. Another possible reason for the negligible numerical resistivity is the particular angle chosen between the background magnetic field and the wave vector ($\theta = \frac{\pi}{2}$). We decided to investigate this matter more closely. Even though the analytical form of the damping coefficient $\mathfrak{D}_{MS}$ is unknown for $\theta \neq \frac{\pi}{2}$, one can guess some of its features from dimensional analysis. The damping coefficient must have a dimension of $[\mathrm{s}^{-1}]$. Therefore, it seems natural to postulate that in general

$$\mathfrak{D}_{MS}(\theta) = \frac{k^2}{2}\left(\nu f(\theta, \frac{c_\mathrm{s}}{c_\mathrm{A}}) + \xi g(\theta, \frac{c_\mathrm{s}}{c_\mathrm{A}}) + \eta h(\theta, \frac{c_\mathrm{s}}{c_\mathrm{A}})\right), \tag{3.45}$$

where f, g and h are dimensionless functions. Note that for $\theta = \pi/2$, we have $f = \frac{4}{3}, g = 1$ and $h = 1/(1 + c_\mathrm{s}^2/c_\mathrm{A}^2)$. To learn more about the functions f, g and h, we ran several simulations for $\theta = \frac{\pi}{4}$, with 128 zones, the HLL Riemann solver, the MP9 reconstruction, the RK3 integrator with $C_\mathrm{CFL} = 0.5$, and different values of the plasma β. The magnetic field and pressure were in the range $b_0 = 0.1$–10 and $p_0 = 0.01$–100, respectively. For every simulation, we set either the resistivity or one of the viscosities to 10^{-4} and measured the wave damping. The simulation results are presented in Fig. 3.19. Additionally, for comparison, with the solid curves we marked the analytical predictions for $\theta = \frac{\pi}{2}$. In general, we see similar damping behaviour for both angles. In the high β regime, the resistivity contribution becomes negligible, being higher for $\theta = \frac{\pi}{4}$. This again allowed us to try to measure the numerical resistivity for $\theta = \frac{\pi}{4}$. Like in the simulations with $\theta = \frac{\pi}{2}$, we ran several ideal MHD simulations with 32 zones for different plasma β parameters. The MP5 reconstruction scheme and the RK3 time integrator with $C_\mathrm{CFL} = 0.01$ were used. For

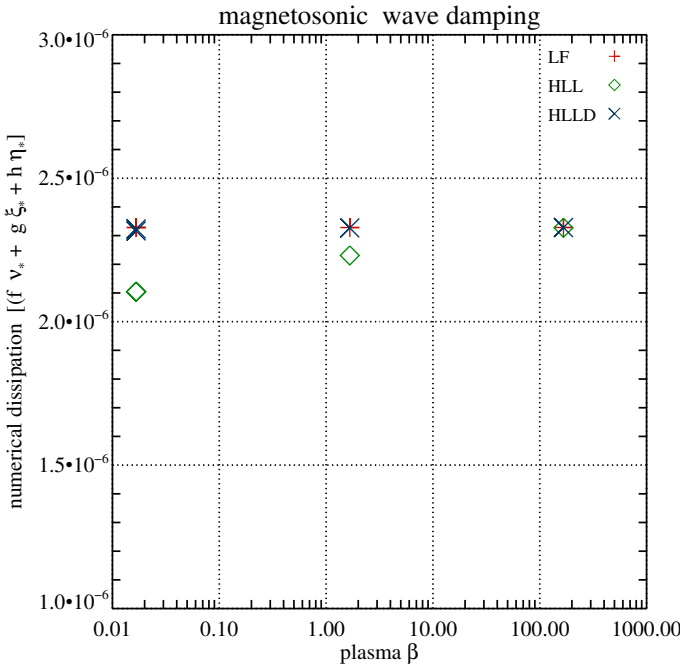

Figure 3.20: Dependence of the total numerical damping on the plasma β for $\theta = \frac{\pi}{4}$. The resolution is set to 32 zones, the MP5 reconstruction scheme and the RK3 time integrator with $C_{\mathrm{CFL}} = 0.01$ are used. The results for the LF, the HLL and the HLLD Riemann solvers are marked with red plus signs, green diamonds and blue crosses, respectively. The independence of the numerical damping on β implies that $\eta_* \ll \nu_* + \xi_*$.

three Riemann solvers we measured the numerical damping. The results are presented in Fig. 3.20. Once again we do not see any significant dependence of the numerical damping on the plasma β. This means that the numerical resistivity must be much smaller than the sum of the numerical viscosities.

3.3.4 Summary of the wave tests

The wave damping simulations were computationally inexpensive, yet provided useful results. They confirmed the correctness of ansatzes (3.1), (3.4) and (3.5) for the numerical shear and bulk viscosity, and the resistivity, respectively. In almost all simulations, the reconstruction schemes and the RK time integrators had the theoretically expected order. There were two somewhat unexpected results, however. For the magnetosonic wave simulations, the numerical resistivity was much lower than the numerical viscosity. The characteristic velocity for the Alfvén wave simulations turned out to be another surprise. However, this could be a consequence of solving the Riemann problem only approximately. Anyway, we can formulate a general statement that for all MHD waves their characteristic velocity and length are the fast magnetosonic speed and the wavelength, respectively.

So far we, measured the numerical damping for three wave types separately. For each type of a wave, the damping coefficient depends on a linear combination of the resistivity, shear- and bulk-viscosity (see Eqs. (3.13), (3.23) and (3.40)). This gives three linearly independent equations with three unknowns. From the mathematical point of view, such a system should have a unique

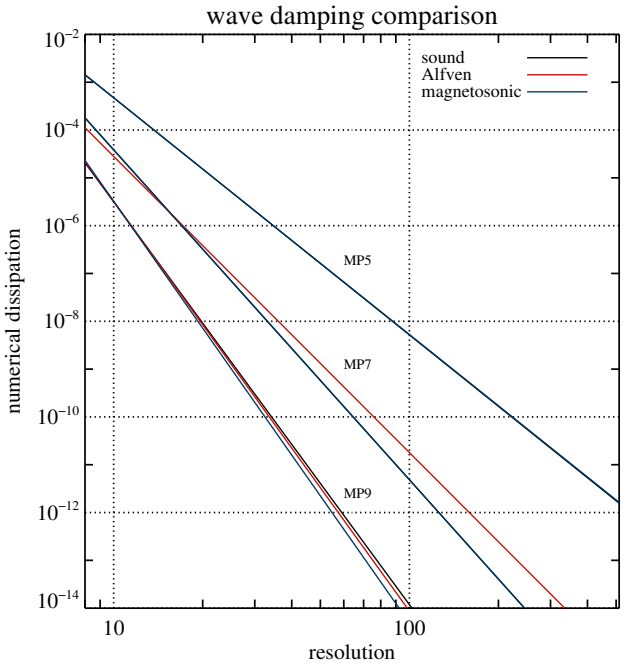

Figure 3.21: Numerical dissipation in the wave simulations. The numerical damping is proportional to $\frac{4}{3}\nu_* + \xi_*$ for sound waves (black), $\nu_* + \eta_*$ for Alfvén waves (red), and $\frac{4}{3}\nu_* + \xi_* + \frac{3}{8}\eta_*$ for magnetosonic waves (blue). The straight lines are a graphical presentation of the data from Tables 3.1, 3.5 and 3.9, respectively. The numerical dissipation for the MP5 scheme is almost identical for all wave types. The same holds for the MP7 scheme for the sound and magnetosonic waves.

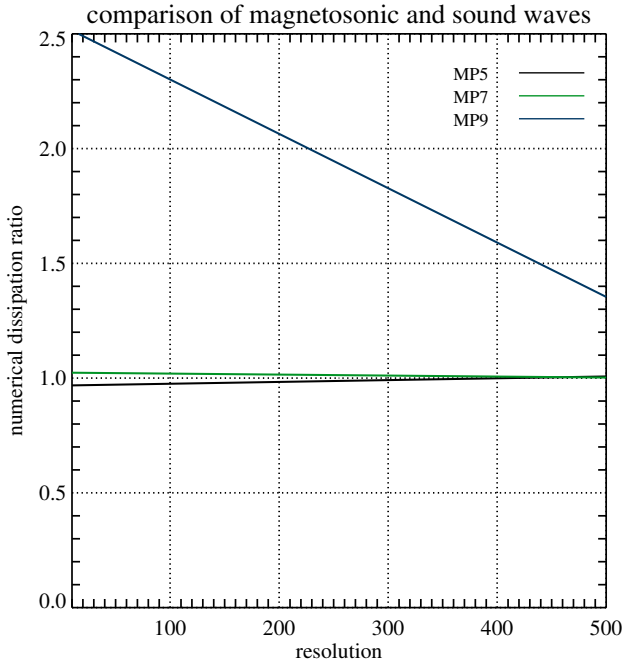

Figure 3.22: The ratio of numerical dissipation in magnetosonic wave simulations to numerical dissipation in sound wave simulations for the MP5, MP7 and MP9 reconstruction schemes (for details, see main text).

solution. Hence, if a given reconstruction scheme has the same order of accuracy for all three types of waves, we can determine the coefficients $\mathfrak{N}_\nu^{\Delta x}, \mathfrak{N}_\xi^{\Delta x}$ and $\mathfrak{N}_\eta^{\Delta x}$ separately (see Eqs. (3.1), (3.4) and (3.5)) , provided that the coefficients only depend on the numerical methods and not on the simulated physical problem.

In Fig. 3.21, we show the numerical dissipation for sound waves ($\nu_* + \eta_*$), Alfvén waves ($4\nu_*/3 + \xi_*$) and magnetosonic waves ($4\nu_*/3 + \xi_* + 3\eta_*/8$),[9] the straight lines being a graphical representations of the results from Tables 3.1, 3.5 and 3.9. There are nine lines in total, but only six are visible, because the numerical dissipation for the MP5 scheme is almost identical for all wave types. The same holds for the MP7 scheme for sound and magnetosonic waves. The numerical dissipation is very similar for all wave simulations, which is good news.

Unfortunately, based on these data, it was impossible to determine $\mathfrak{N}_\nu^{\Delta x}, \mathfrak{N}_\xi^{\Delta x}$ and $\mathfrak{N}_\eta^{\Delta x}$ separately. To demonstrate the reason for this, we present in Fig. 3.22 the ratio of the numerical dissipation in magnetosonic wave simulations to the numerical dissipation in sound wave simulations, i.e.

$$\mathfrak{r} \equiv \frac{[(4/3)\nu_* + \xi_* + (3/8)\eta_*]_{\text{magnetosonic}}}{[(4/3)\nu_* + \xi_*]_{\text{sound}}}. \tag{3.46}$$

If $\mathfrak{N}_\nu^{\Delta x}, \mathfrak{N}_\xi^{\Delta x}$ and $\mathfrak{N}_\eta^{\Delta x}$ were independent of the simulated physical problem, the above ratio would be constant, and $\mathfrak{r} \geq 1$ (for a negligible numerical resistivity $\mathfrak{r} = 1$). As we can see from the figure, in the shown resolution regime, $\mathfrak{r} < 1$ for the MP5 scheme, and $\mathfrak{r} > 1$ for the MP7 scheme. Hence, the coefficients $\mathfrak{N}_\nu^{\Delta x}, \mathfrak{N}_\xi^{\Delta x}$ and $\mathfrak{N}_\eta^{\Delta x}$ must (at least weakly) depend on the simulated physical problem. The MP9 reconstruction scheme has a different order of accuracy for sound and magnetosonic wave simulations (see Tables 3.1 and 3.9, respectively), which makes it impossible even to define the ratio $\mathfrak{r}$ properly.

3.4 Tearing modes

The tearing modes (TM) are a resistive MHD instability, which can develop in *current sheets*,[10] and break and rejoin magnetic field lines (see Fig. 3.23). Its linear theory, in the context of plasma fusion physics, was extensively studied in a seminal paper by Furth, Killeen & Rosenbluth (Furth et al. (1963); later referred to as FKR). The instability is a much more complex process than a mere wave damping. During the tearing mode evolution, resistivity manifests itself not only by dissipating magnetic energy into thermal energy, but also by converting one magnetic field component into another one. This makes the instability an excellent candidate for determining an MHD code's numerical resistivity. Tearing modes are of also relevance in astrophysics. They can play an important role in the magneto-rotational instability.

However, before one can start using tearing modes as a tool for measuring the numerical resistivity, it is necessary to understand their physics better. We recommend Schnack (2009) for a concise introduction to the topic. A very pedagogical and yet mathematically rigorous description, the reader will find in Goedbloed et al. (2010). In the next subsection, we describe the linear tearing mode theory. Then, we discuss our numerical setup and the obtained results.

[9] We would like to remind the reader that the third damping coefficient does depend on the resistivity contribution α (see Eq. (3.40) and the discussion below), which for $p_0 = b_0 = 1$ and $\Gamma = 5/3$ is $\alpha = 3/8$.

[10] Current sheets are formed by magnetic shear. As a direct consequence of Ampère's law, with every spatial change of the magnetic field direction there is associated a current.

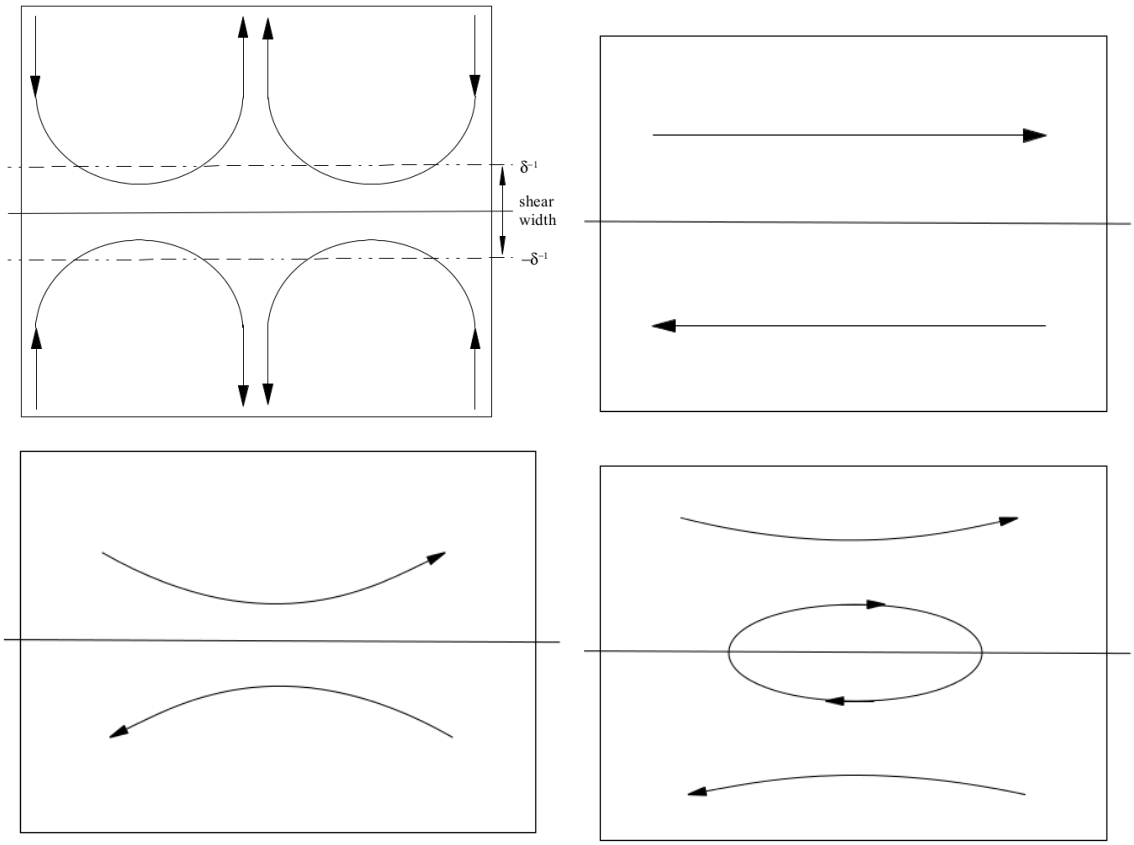

Figure 3.23: Schematic presentation of the tearing mode instability and our numerical setup. The figures are not to scale. *Upper left:* The velocity stream lines for a tearing motion. The magnetic shear extends from $-\delta^{-1}$ to δ^{-1}. *Top right:* Magnetic field lines at the initial time. *Bottom left:* Later evolutionary stage: magnetic fields are stretched by the fluid motion. *Bottom right:* Eventually, magnetic field lines of different polarities will meet in the centre. If resistivity is present in the system, they can break and rejoin, i.e. *reconnect*.

3.4.1 Theoretical introduction

FKR, in their original paper on the tearing mode instability (Furth et al. 1963), account for many physical factors, like position dependent: background density, temperature and resistivity. We will restrict ourselves to a much simpler system, yet demonstrating the key features of the instability.

First, we present a detailed derivation of the tearing mode equations in resistive MHD, based on Goedbloed et al. (2010).[11] We decided not to introduce dimensionless variables but at the very late derivation stage, however. Even though working with dimensionless variables has obvious theoretical advantages, it can sometimes obscure an intuitive interpretation of equations. The reader is forced to remember all preceding transformations to dimensionless variables to be able to decipher physical meaning of dimensionless equations. We hope that our presentation is relatively easy to follow without auxiliary tools like pen and paper already at first reading .

Next, we briefly discuss how to generalise the results in the presence of viscosity, which was

[11] However, these authors used a different background magnetic field, i.e. $b_{0x} = b_0 \sin(\delta y)$, where the symbols in this equation are explained after Eq. (3.47).

already done by FKR. We derive a more accurate tearing mode growth rate equation for the used background magnetic field configuration.

Consider a two dimensional system of constant density $\rho_0 = 1$, threaded by a background magnetic field [12]

$$b_{0x} = b_0 \tanh(\delta y), \tag{3.47}$$

where b_0 is the magnetic field amplitude and δ defines the shear length.[13] Such a magnetic field configuration forms a current sheet at $|\delta y| \approx 0$. To balance the resulting non-zero magnetic pressure gradient, one can either introduce a gas pressure gradient, so that $\nabla_y(p + b_{x0}^2/2) = 0$ (a so called *pressure equilibrium* configuration) or an additional magnetic field component, so that $\nabla_y(b_{x0}^2/2 + b_{z0}^2/2) = 0$ (a so called *force-free* configuration). Such a system is stable in ideal MHD. However, in resistive MHD, the system may become tearing mode unstable.

To derive the instability criterion and the growth rate, we use linearised resistive-viscous MHD equations in the incompressible limit. Linearisation is justified, when the perturbations (denoted with the subscript "1") are much smaller than the initial background quantities (denoted with the subscript "0"),[14] e.g. the magnetic field can be decomposed to $\mathbf{b} = \mathbf{b_0} + \mathbf{b_1}$, where $|\mathbf{b_1}| \ll |\mathbf{b_0}|$. The incompressible approximation, i.e. $\nabla \cdot \mathbf{v} = 0$, holds for the fluid velocities much smaller than the sound speed, i.e. $|\mathbf{v}| \ll c_\mathrm{s}$.

After introducing perturbations in velocity $\mathbf{v_1}$ and magnetic field $\mathbf{b_1}$ to the system, the linearised incompressible resistive-viscous MHD equations read

$$\partial_t \mathbf{b} = \nabla \times (\mathbf{v_1} \times \mathbf{b_0}) + \eta \nabla^2 \mathbf{b}, \tag{3.48}$$

$$\rho_0 \partial_t \mathbf{v_1} = -\nabla p + (\nabla \times \mathbf{b_1}) \times \mathbf{b_0} + (\nabla \times \mathbf{b_0}) \times \mathbf{b_1} + \rho_0 \nu \nabla^2 \mathbf{v_1}, \tag{3.49}$$

$$\nabla \cdot \mathbf{v} = 0, \tag{3.50}$$

$$\nabla \cdot \mathbf{b} = 0. \tag{3.51}$$

To simplify the notation, we will further omit the subscript "1" for the velocity perturbations. To solve the above equations we use a WKB ansatz

$$v_y(x,y,t) = v(y) e^{ikx+\gamma t}, \tag{3.52}$$

$$b_{1y}(x,y,t) = b_1(y) e^{ikx+\gamma t}, \tag{3.53}$$

where k is the wavevector in the x direction and γ is the growth rate of the tearing mode instability. We will consider perturbations whose wavelength in x direction is comparable to the shear width, i.e.

$$k \sim \delta. \tag{3.54}$$

Note that one only needs to solve Eqs. (3.48) and (3.49) for v_y and b_{1y} and the other components can be easily determined from the conditions $\nabla \cdot \mathbf{b} = \nabla \cdot \mathbf{v} = 0$. For this ansatz to be justified, two further conditions must be met. Firstly, the diffusion time scale must be much larger than the instability time scale, i.e. $1/(\delta^2 \eta) \gg \gamma^{-1}$, so that the background magnetic field can be treated as constant. Secondly, the Alfvén crossing time must be sufficiently short, i.e. $L_y/c_\mathrm{A} \ll \gamma^{-1}$,

[12] We use a rather "non-standard" magnetic field configuration. In the majority of the literature $B_{0y} = B_{0y}(x)$ is considered (see, e.g. Furth et al. (1963), Goedbloed et al. (2010)). Our choice is due to the numerical setup that we used, which was initially based on Landi et al. (2008).

[13] We remind the reader, that we use CGS units with a redefined magnetic field $\mathbf{b} = \mathbf{B}/\sqrt{\rho}$.

[14] With the exception of the velocity perturbations, which must be much smaller than the sound speed.

where L_y is the system length in y direction.[15] One can treat then the Alfvén speed as infinite, i.e. $c_\mathrm{A} \to \infty$, and not allow for wave solutions in the WKB ansatz. Physically it means, that any information spreads instantaneously through the whole system. The two above conditions can be combined to

$$\frac{1}{\delta^2 \eta} \gg \gamma^{-1} \gg \frac{L_y}{c_\mathrm{A}}. \tag{3.55}$$

We insert the WKB ansatz to Eqs. (3.48) and (3.48) and take curl of the latter, to eliminate the pressure from the equation. The y component of the induction equation and the derivative ∂_x of the z component of the equation of motion, respectively, read

$$\gamma b_{1y} = [\nabla \times (\mathbf{v} \times \mathbf{b_0})]_y + \eta(-k^2 + \partial_y^2) b_{1y}, \tag{3.56}$$

$$\gamma \rho_0 (-k^2 + \partial_y^2) v_y = \partial_x \{\nabla \times [(\nabla \times \mathbf{b_1}) \times \mathbf{b_0} + (\nabla \times \mathbf{b_0}) \times \mathbf{b_1} + \rho_0 \nu \nabla^2 \mathbf{v}]\}_z. \tag{3.57}$$

After some algebra we arrive at

$$\gamma b_{1y} = ikv_y b_{0x} + \eta(-k^2 + \partial_y^2) b_{1y}, \tag{3.58}$$

$$\gamma \rho_0 (-k^2 + \partial_y^2) v_y = \rho_0 \nu (k^4 - 2k^2 \partial_x^2 + \partial_x^4) v_y + ik[-b_{1y} \partial_y^2 b_{0x} + b_{0x}(-k^2 + \partial_y^2) b_{1y}]. \tag{3.59}$$

Unfortunately, it is impossible to integrate the above equations analytically. Therefore, we will solve this problem with a so-called *boundary layer analysis* method. We divide the equations' domain into three regions: two outer ones ($-L_y \le y < -y_\varepsilon$ and $y_\varepsilon < y \le L_y$, where y_ε is a small positive constant such that $\delta y_\varepsilon \ll 1$) in which dissipative effects can be neglected, and one inner layer ($-y_\varepsilon < y < y_\varepsilon$) in which resistivity (and viscosity) play an important role. Once the solutions of the Eqs. (3.58) and (3.59) are obtained in the separate regions, they have to be matched at the regions' boundaries.

Outer layer To solve Eqs. (3.58) and (3.59) in the outer regions, i.e. for $|y| > y_\varepsilon$, we make the following approximations. We note that from condition (3.55), we have $\gamma \gg \delta^2 \eta \sim k^2 \eta$ (in the last step, we used assumption 3.54), hence the term containing resistivity in the induction equation (3.58) can be neglected, i.e.

$$ikv_y = \frac{\gamma b_{1y}}{b_{0x}}. \tag{3.60}$$

Physically, it means that the magnetic field does not experience any strong spatial variations in the outer layers, consequently resistive effects are unimportant. Furthermore, from the second part of condition (3.55), we have $\gamma \ll c_\mathrm{A}/L_y \sim c_\mathrm{A} k$. This inequality and Eq. (3.60) allow us to estimate that terms proportional to velocity (gradients) in Eq. (3.59) are negligible, i.e. $|\gamma \rho_0 k^2 v_y| \ll |ik^3 b_{0x} b_{1y}|$. This means that the tearing mode evolution is so slow that the plasma interia (terms containing $\rho_0 v_y$ in Eq. (3.59)) can be neglected on the ideal MHD time scale. Finally, Eqs. (3.58) and (3.59) in the outer layers simplify to

$$ikv_y = \frac{\gamma b_{1y}}{b_{0x}}, \tag{3.61}$$

$$ik[-b_{1y} \partial_y^2 b_{0x} + b_{0x}(-k^2 + \partial_y^2) b_{1y}] = 0. \tag{3.62}$$

[15] The definition of L_y is somewhat arbitrary and should be more precisely specified at this point. L_y should be understood as a distance from the centre (magnetic field shear) at which the background magnetic field is already almost homogeneous (for a profile $b_{0x} \propto \tanh(\delta y)$). Obviously, L_y cannot be arbitrarily large (i.e. $L_y \to \infty$), because then the inequality $L_y/c_\mathrm{A} \ll \gamma^{-1}$ could be only fulfilled for $c_\mathrm{A} \to \infty$. As a rule of thumb, L_y should be of the order of (at least) δ^{-1}.

So far, we have not made any assumptions about background magnetic field. For $b_{0x}(y) = b_0 \tanh(\delta y)$, the solution of Eq. (3.62) reads[16]

$$b_{1y}(y) = b_1 \frac{[1-\tanh(\delta y)]^{\frac{2\delta-k}{2\delta}}[1+\tanh(\delta y)]^{\frac{k}{2\delta}}[-k+\delta\tanh(\delta y)]}{\delta\Gamma(\frac{2\delta-k}{\delta})[1-\tanh(\delta y)]}, \tag{3.63}$$

where b_1 is a constant (initial perturbation amplitude) and Γ is the *Euler gamma function*. The velocity perturbations can be easily determined combining Eqs. (3.61) and (3.63):

$$v_{1y}(y) = \frac{\gamma b_1}{ikb_0} \frac{[1-\tanh(\delta y)]^{\frac{2\delta-k}{2\delta}}[1+\tanh(\delta y)]^{\frac{k}{2\delta}}[-k+\delta\tanh(\delta y)]}{\delta\Gamma(\frac{2\delta-k}{\delta})[1-\tanh(\delta y)]\tanh(\delta y)}. \tag{3.64}$$

Eqs. (3.61) and (3.64) are valid in the outer layers, i.e. for $|y| > y_\varepsilon$. However, for $|\delta y| \to 0$, Eq. (3.61) has a singularity, i.e. as $|b_{0x}| \to 0$, $|v_y| \to \infty$ (since $b_{1y}(0) \neq 0$). As we can see, ideal MHD equations break down in this region. Resistivity, which was neglected in the outer layers, will play a crucial role in the inner layer by smoothing out ("renormalising") the singularity. This will give rise to a new phenomenon, i.e. tearing mode solutions, which are forbidden in the ideal MHD limit.

Inner layer Resistive (and viscous) terms can no longer be neglected and we have to solve Eqs. (3.58) and (3.59) simultaneously. Since in the inner region, $|\delta y| \ll 1$, we can approximate the background magnetic field as

$$b_{0x}(y) = b_0 \tanh(\delta y) \approx b_0 \left(\partial_y \tanh(\delta y)_{|y=0}\right) y = b_0 \delta y. \tag{3.65}$$

Moreover, in this region, perturbations in both velocity and magnetic field experience much stronger variations in the y than in the x direction, i.e. $|k^2 v_y| \ll |\partial_y^2 v_y|$ and $|k^2 b_{1y}| \ll |\partial_y^2 b_{1y}|$.[17] Therefore, we can neglect the terms proportional to k^2 in Eqs. (3.58) and (3.59), obtaining

$$\gamma b_{1y} = ikv_y b_0 \delta y + \eta \partial_y^2 b_{1y}, \tag{3.66}$$

$$\gamma\rho_0 \partial_y^2 v_y = \rho_0 \nu(-2k^2\partial_y^2 + \partial_y^4)v_y + ikb_0\delta y \partial_y^2 b_{1y}, \tag{3.67}$$

where we additionally used approximation (3.65). Finally, we can eliminate terms containing b_{1y} between the equations, arriving at a complicated sixth order ordinary differential equation (ODE) for v_y, i.e.

$$\begin{aligned} v_y^{(6)}[\nu\eta\rho_0 y^2] + v_y^{(5)}[-2\nu\eta\rho_0 y] + v_y^{(4)}[-(\gamma(\eta+\nu)+2\nu\eta k^2)\rho_0 y^2 + 2\nu\eta\rho_0] + \\ v_y^{(3)}[2\eta\rho_0(\gamma+2\nu k^2)y] + v_y^{(2)}[k^2\delta^2 b_0^2 y^4 + \gamma(\gamma+2\nu k^2)\rho_0 y^2 - 2\eta\rho_0(\gamma+2\nu k^2)] + \\ v_y^{(1)}[2k^2\delta^2 b_0^2 y^3] = 0, \end{aligned} \tag{3.68}$$

[16] Goedbloed et al. (2010) used a different background magnetic field, i.e. $b_{0x}(y) = b_0 \sin(\delta y)$ (written in our notation), for which the outer solution has a less complicated form. However, it does not mean that we obtained an original result. Both magnetic field configurations were already considered by Furth et al. (1963), who wrote that Eq. (3.62), given $b_{0x}(y) = b_0 \tanh(\delta y)$, can be solved in terms of associated Legendre functions. We only found their explicit form in *Mathematica 8*.

[17] As an example, we will consider velocity perturbations. From Eq. (3.61), assuming for the time being that $b_{1y} =$ const., we have $|\partial_y^2 v_y| \sim |v_y/y^2|$ (where we also used approximation (3.65)). Since in the inner layer $|y| \ll \delta^{-1}$, and from Eq. (3.54), we have $\delta \sim k$, hence finally $|v_y/y^2| \gg |v_y k^2|$. Eq. (3.61) holds only in the outer layers, yet it should be still (roughly) valid at the border with the inner region. The assumption $b_{1y} =$ const. was only made to simplify the calculations, relaxing it does not change the estimates made here.

where $v_y^{(n)} \equiv \partial_y^n v_y$. The above equation is too complex to be integrated analytically and some further approximations are necessary. Before we proceed with mathematical details, a few comments are appropriate. Apart from the innermost region of the inner layer, velocity perturbations will have a solution of type $v_y \propto y^{-1}$ for $|\delta y| \ll 1$. Therefore, terms with highest order derivatives of v_y are dominant in ODE (3.68) (i.e. $|\partial_y v_y| \ll |\partial_y^2 v_y| \ll |\partial_y^3 v_y|$ and so on). Consequently, further approximations made to solve the above equation will basically consist in neglecting lower order derivatives. Note that two terms with the highest order derivatives (i.e. $\partial_y^6 v_y$ and $\partial_y^5 v_y$) contain viscosity. We will consider ODE (3.68) in two different cases: with and without viscosity. However, from the solution in resistive-viscous MHD, we will not be able to obtain the resistive-non-viscous solution in the limit $\nu \to 0$, because in both cases, we will keep different dominant terms in ODE (3.68). In the following subsection, we integrate Eqs. (3.66) and (3.67) without viscosity. Next, we show how to generalise these results in the presence of viscosity.

Non-viscous case

Note that in the non-viscous case, i.e. for $\nu = 0$, Eq. (3.68) reduces to a fourth order differential equation, which is still too complicated to be solved analytically. Therefore, following FKR, we will make a so-called *constant ψ approximation*. These authors noted that it is the function v_y that has a singularity in ideal MHD (i.e. $v_y \propto y^{-1}$ for $y \to 0$; see Eq. (3.61)) and therefore it should exhibit large variations in the limit of small resistivity. The function b_{1y} should vary less for $|\delta y| \approx 0$ and can be approximated by a constant $b_{1y}(y) \approx b_{1y}(0)$ for $|\delta y| \approx 0$.[18] Under this approximation, Eqs. (3.66) and (3.67) reduce to

$$\gamma\eta\rho_0\partial_y^2 v_y - k^2\delta^2 b_0^2 v_y y^2 = ik\gamma b_0 \delta y b_{1y}(0), \tag{3.69}$$

$$\partial_y^2 b_{1y} = \frac{\gamma\rho_0}{ikb_0\delta y}\partial_y^2 v_y. \tag{3.70}$$

Note the huge difference, Eq. (3.68) for v_y reduced from a sixth order ODE to a second order ODE (3.69). We can solve the above system of equations by first integrating Eq. (3.69). Once the function v_y is known, we can plug it into Eq. (3.70) to find a solution for b_{1y}.

To express the above equations in a dimensionless form, we introduce new dimensionless variables:[19]

$$s = y\left(\frac{k^2\delta^2 b_0^2}{\gamma\eta\rho_0}\right)^{\frac{1}{4}} \equiv \frac{y}{\varepsilon_R}, \tag{3.71}$$

$$\Phi = iv_y\left(\frac{b_0^2\rho_0\eta k^2\delta^2}{b_{1y}^4(0)\gamma^3}\right)^{\frac{1}{4}}, \tag{3.72}$$

$$\psi = \frac{b_{1y}}{b_{1y}(0)}, \tag{3.73}$$

$$\lambda = \gamma\left(\frac{\rho_0}{k^2\delta^2\eta b_0^2}\right)^{\frac{1}{3}} \tag{3.74}$$

[18] FKR worked with dimensionless variables in which $\psi \propto b_{1y}$ in our notation. Hence, the name of the approximation, which is commonly used in the literature, see e.g. Goedbloed et al. (2010) and Schnack (2009).

[19] We hope that the reader now understands why we refrained from introducing dimensionless variable until it was really necessary.

where we have additionally defined

$$\varepsilon_{\rm R} \equiv \left(\frac{\gamma \eta \rho_0}{k^2 \delta^2 b_0^2} \right)^{\frac{1}{4}}. \tag{3.75}$$

In these new variables, Eqs. (3.69) and (3.70) read

$$\frac{{\rm d}^2\Phi}{{\rm d}s^2} - s^2\Phi = -s, \tag{3.76}$$

$$\frac{{\rm d}^2\psi}{{\rm d}s^2} = -\lambda^{3/2}\frac{1}{s}\frac{{\rm d}^2\Phi}{{\rm d}s^2}. \tag{3.77}$$

At first, $\varepsilon_{\rm R}$ may look like a parameter introduced just to write the ODEs in a dimensionless from. However, as we will see later, it has a well defined physical meaning (and will play a key role in our numerical studies).

The solution of Eq. (3.76) can be written as an integral over an auxiliary variable u (Goedbloed et al. 2010): [20]

$$\Phi = \frac{s}{2}\int_0^1 (1-u^2)^{-1/4} e^{-s^2 u/2} {\rm d}u. \tag{3.78}$$

The function Φ (depicted with black in Fig. 3.24) is always positive for $s > 0$ and has a global maximum at $s \approx 1.48$. Furthermore,

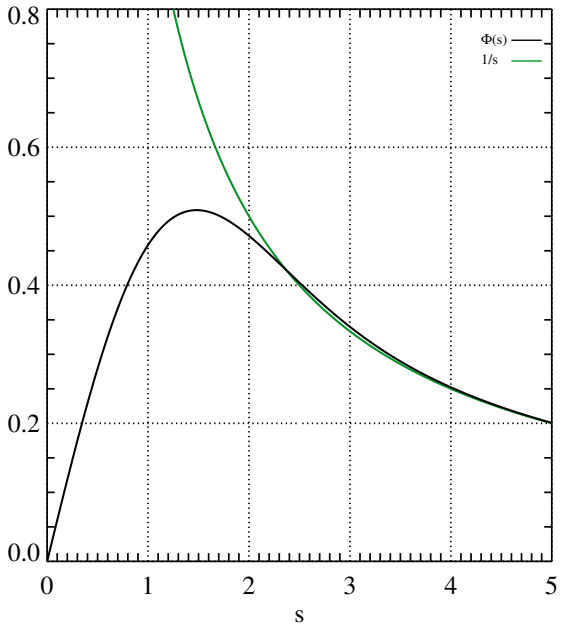

Figure 3.24: Graphical illustration of functions $\Phi(s)$ (black), defined in Eq. (3.78), and $1/s$ (green). Velocity perturbations, v_y, are exactly proportional to the former in the inner region and approximately proportional to the latter in the outer region for $|\delta y| \ll 1$. For $s \gtrsim 2.5$ both functions are very similar.

[20] We also integrated Eq. (3.76) in *Mathematica 8* and obtained that Φ is a linear combination of modified Bessel and Struve functions.

$$\Phi(s) \approx \frac{2.12}{2\sqrt{\pi}} s \qquad \text{for} \quad s \ll 1 \qquad \text{and} \quad \Phi(s) \approx \frac{1}{s} \qquad \text{for} \quad s \gg 1. \tag{3.79}$$

In ideal MHD, the velocity has a singularity ($v_y \propto y^{-1}$) for $y \to 0$ (see Eq. (3.61)). Resistivity regularises this misbehaving solution.

Matching To find the final form of the velocity perturbations, v_y, in the inner layer (given by Eqs. (3.72) and (3.78)), we need to determine the tearing mode growth rate, γ. It can be calculated from matching the inner and outer solutions of v_y (the former given by Eq. (3.64)) in a certain point y_m, where the subscript m stands for "matching". This should be done in an intermediate region, where both solutions are valid and overlap (i.e. give the same predictions for velocity and magnetic field perturbations). The value of y_m must be "large enough", so that $\Phi(s)$ can be approximated as $\Phi(s) \approx s^{-1}$, i.e. $s \gg 1$, yet "small enough" that the outer ideal MHD solution behaves like $v_y \propto y^{-1}$ (for $y \to 0$). Moreover, we must also remember that the inner resistive solution was found for such small values of y, that $b_{0x}(y)$ could be approximated as $b_{0x}(y) \approx b'_{0x}(0) y = b_0 \delta y$. Therefore, $y_m \ll \delta^{-1}$ must hold. When we recall that $s = 1$ for $y = \varepsilon_\mathrm{R}$, we can combine the above conditions as

$$\varepsilon_\mathrm{R} \ll y_\mathrm{m} \ll \delta^{-1}. \tag{3.80}$$

The rest of the matching procedure is conceptually rather straightforward. From comparing Eqs. (3.78) and (3.64) in the vicinity of y_m, we can determine the tearing mode growth rate, γ. We omit the details of these calculations[21] and just give the final form of the tearing mode growth rate in resistive (-non-viscous) MHD:

$$\gamma = \left(\frac{2}{2.12}\right)^{4/5} \eta^{3/5} \left(\frac{b_0 k}{\sqrt{\rho}}\right)^{2/5} \delta^{6/5} \left(\frac{\delta}{k} - \frac{k}{\delta}\right)^{4/5}. \tag{3.81}$$

For $k > \delta$, this expression would have a complex value (because of the term $((\delta/k - k/\delta)^{4/5})$. This means that the system is tearing mode unstable only for perturbations with wavevectors

$$k < \delta \quad (\text{instability}). \tag{3.82}$$

On the other hand, for $k \to 0$, the instability growth rate seems to diverge, i.e. $\gamma \propto k^{-2/5} \to \infty$ (?). However, this is not the case, because for $k \to 0$, ε_R, which can be now computed from Eq. (3.75):

$$\varepsilon_\mathrm{R} = \left(\frac{2}{2.136}\right)^{1/5} \eta^{2/5} \left(\frac{\sqrt{\rho_0}}{b_0 k}\right)^{2/5} \left(\frac{1}{\delta}\left(\frac{\delta}{k} - \frac{k}{\delta}\right)\right)^{1/5}, \tag{3.83}$$

would also diverge, i.e. $\varepsilon_\mathrm{R} \propto k^{-3/5} \to \infty$ (?). Hence, condition (3.80) would be violated. It does not mean, however, that tearing modes cannot grow for $k \to 0$, but rather that growth rate expression (3.81) and also Eq. (3.83) are no longer valid in that limit. Tearing modes must develop at considerably lower rates in this regime. Based on these considerations, we see that it is not easy to find the fastest growing tearing mode, because for its wavevector k, condition (3.80) must be violated and the analytical predictions break down.

At this point, we would like to make some more comments on the parameter, ε_R. When looking at its definition (3.75), we could think that it merely is another parameter introduced to transform

[21] To put it in a nutshell, we must impose that $v_y(y)$ (3.64) in the outer layer and its counterpart in the inner layer ($v_y(y) = v_y(\Phi(s))$ (3.78) and their first derivatives are equal in the vicinity of y_m. Furth et al. (1963) and Goedbloed et al. (2010) did this function sewing for magnetic field perturbations. However, in our numerical studies we will be more interested in velocity perturbations, therefore we paid more attention to them in the theoretical introduction.

differential equations to a dimensionless form. As we have already written, the matching of the outer ideal MHD solution with the inner resistive MHD solution can be done for such "large" value of s that $\Phi(s) \approx s^{-1}$. From Fig. 3.24, we can see that this condition is roughly met at $s = 2.5$. Hence, maybe already for $s > 2.5$, instead of resistive MHD equations, we could use the ideal ones. Physically speaking, resistive effects are important only for $s \leq 2.5$. Recalling that $s = y/\varepsilon_{\mathrm{R}}$ (Eq. 3.71), we see that ε_{R} defines the width of a thin layer (which we will call *resistive layer*) where resistive effects are important, i.e. ε_{R} is not just another parameter, but it has sound physical interpretation. We should note however, that the exact definition of the resistive layer is somewhat arbitrary, e.g. Goedbloed et al. (2010) define this layer to extend up to $s \approx 1$. On the other hand, the inner resistive MHD equations should be still valid for, say, $s = 10$. From Fig. 3.24, we can see that the "resistive smoothing" of the velocity is strongest for $s \lesssim 2$. We decided to use a pragmatic definition, i.e. we say that the *resistive layer* width equals $s = 1.48$ (hence $1.48\varepsilon_{\mathrm{R}}$ in dimensional units)[22], where the function $\Phi(s)$ has a well defined maximum, which can be easily measured in simulations.

There is one misconception that could possibly appear in the readers mind at this moment. Even though we wrote that the whole "resistive action" takes place in the resistive layer and that the tearing modes are a resistive instability, it would be wrong to say that only the inner region determines the dynamics of the whole system and the outer (ideal MHD) solution was just "glued" to fulfil the boundary conditions. Note that the instability growth rate was determined from matching of Eq. (3.78) with Eq. (3.64), and the latter does depend on the background magnetic field in the outer region. To illustrate this, we consider, the background magnetic field

$$b_{0x} = b_0 \sin(\delta y), \tag{3.84}$$

whose Taylor expansion is the same as for the magnetic field given by Eq. (3.47) in the inner region, i.e. $b_{0x}(y) \approx b_0 \delta y$ (for $|\delta y| \ll 1$), yet the instability growth rate is different (see, e.g. Goedbloed et al. (2010)), i.e

$$\gamma = \left(\frac{2}{2.12}\right)^{4/5} \eta^{3/5} \left(\frac{b_0 k}{\sqrt{\rho}}\right)^{2/5} \delta^{6/5} \left(\sqrt{1-(k/\delta)^2}\cot\left(\frac{1}{2}\sqrt{1-(k/\delta)^2}\right)\right)^{4/5}. \tag{3.85}$$

Eqs. (3.64), (3.78) and (3.63) (supplemented by Eq. (3.81) and transformations (3.71) and (3.72)), for the velocity, v_y, and the magnetic field, b_{1y}, perturbations practically constitute a complete solution of the tearing mode problem in resistive MHD. The magnetic field perturbations, b_{1y}, in the inner layer can be approximated by a constant, i.e. $b_{1y}(y \leq y_{\mathrm{m}}) \approx b_{1y}(y_{\mathrm{m}})$, and the other perturbation components, i.e. v_x and b_{1x}, can be determined from the condition $\nabla \cdot \mathbf{b} = \nabla \cdot \mathbf{v} = 0$.

We remind the reader that our main goal is to use tearing modes as a tool to determine the numerical resistivity of our code. To put it in a nutshell, our strategy would be to run a simulation in ideal MHD and observe whether tearing modes driven by numerical resistivity, η_*, develop in the system. If they do, we could measure their growth rate, γ, and from Eq. (3.81), calculate the numerical resistivity in a given setup. However, in practice, Eq. (3.81) cannot be used for that purpose, since it does not include the effect of (numerical) viscosity, which is always present in simulations. Therefore, our next step is to generalise the obtained results to resistive-viscous MHD.

[22] Counting from the origin of the Y axis, hence the actual (total) width is twice larger, i.e. from $y = -1.48\varepsilon_{\mathrm{R}}$ to $y = 1.48\varepsilon_{\mathrm{R}}$.

Viscous case

The derivation of the tearing mode solution in resistive-viscous MHD is in many steps similar to the non-viscous case. Therefore, we will only briefly sketch the further procedure (the interested reader will find the details in Furth et al. (1963)). Once again, Eqs. (3.58) and (3.59) are integrated separately in the outer and inner region. In the former, we can again neglect dissipative terms and momenta (i.e. use ideal MHD equations), hence magnetic field, b_{1y}, and velocity, v_y, perturbations are still given by Eqs. (3.63) and (3.63), respectively. The differences become apparent in the inner region. This time, we have to integrate the full sixth order ODE (3.68) (and not the 4th order equation, which we obtain after putting $\nu = 0$). After once again using the constant ψ approximation, this ODE for v_y reduces to a fourth order equation (which includes viscous terms). To further simplify that equation, FKR neglected terms with lower order derivatives, which should be a good approximation for magnetic Prandtl numbers $P_\mathrm{m} \equiv \nu/\eta \geq 0.1$ (this step limits the validity of their final results to $P_\mathrm{m} \geq 0.1$). Next, these authors made another transformation to dimensionless variables, where the interesting for us details of it read

$$\tilde{s} = \frac{y}{\varepsilon_\mathrm{RV}} \tag{3.86}$$

$$\tilde{\Phi} \propto v_{1y}, \tag{3.87}$$

with

$$\varepsilon_\mathrm{RV} = (\eta\nu)^{1/6} \left(\frac{\sqrt{\rho_0}}{b_0 \delta k} \right)^{1/3}. \tag{3.88}$$

This time the width of a layer where dissipative effects are important is proportional to a different parameter, ε_RV. As we can see, both resistivity and viscosity affect the size of this region, which we will call *resistive-viscous layer*. The function $\tilde{\Phi}(\tilde{s})$, which is proportional to velocity perturbations in the inner region, has a similar shape to $\Phi(s)$ (defined in Eq. (3.78)), but its maximum is located at $\tilde{s} \approx 1.76$. In the resistive-viscous case, matching condition (3.80) hast to be replaced by

$$\varepsilon_\mathrm{RV} \ll y_\mathrm{m} \ll \delta^{-1}. \tag{3.89}$$

From the matching of $\tilde{\Phi}(\tilde{s})$ with Eq. (3.64) in this intermediate regime, we obtain the tearing mode growth rate in resistive-viscous MHD:

$$\gamma \approx \frac{2}{3} 2^{1/3} \eta^{5/6} \nu^{-1/6} \left(\frac{b_0 k}{\sqrt{\rho_0}} \right)^{1/3} \delta^{4/3} \left(\frac{\delta}{k} - \frac{k}{\delta} \right). \tag{3.90}$$

The above expression differs from the result of Furth et al. (1963) (see Eq. (H.8) in their paper), because these authors derived their equation in the $k/\delta \ll 1$ limit (in our units). For the background magnetic field $b_{0x} = b_0 \tanh(\delta y)$, we calculated the growth rate more accurately. Note that we used the symbol "$\approx$", instead of "$=$", in the above equation, because FKR only approximately solved ODE (3.68) (after already using the constant ψ approximation). Therefore, the above equation could be off by a small constant numerical factor.

3.4.2 Numerical simulations

Verification of the theory

Our initial setup was based on Landi et al. (2008) (later referred to as LLVB), who were mainly interested in the non-linear phase of tearing modes, i.e. the formation of magnetic islands and the

onset of turbulence. Since we wanted to study the exponential growth phase of a single tearing mode in more detail, we modified the setup for our purposes. We used a box of the size $(-L_x, L_x) \times (-L_y, L_y)$, where $L_x = L_y = \pi/3$, with periodic and open boundary conditions in x and y direction, respectively. We set the density and pressure to $\rho_0 = p_0 = 1$ and used the ideal EOS with $\Gamma = 5/3$. The default background magnetic field was set to

$$b_{0x} = b_0 \tanh(\delta y), \tag{3.91}$$

with $b_0 = 1$ and $\delta = 10$. As already mentioned in Sec. 3.4.1, in order to keep the system in equilibrium, one needs to balance the non-zero magnetic pressure gradient. We tested both the pressure equilibrium and force-free configurations and found that only the latter was suitable for our numerical experiments.[23] To obtain the force-free configuration we set

$$b_{0z} = \frac{b_0}{\cosh(\delta y)}. \tag{3.92}$$

Initially, we only perturbed the velocity v_{1y} of the system according to the prescription of Landi et al. (2008). However, those perturbations could trigger the tearing mode instability only for very high resistivities ($\eta \geq 10^{-5}$), while for lower values ($\eta \leq 10^{-6}$) the onset of the instability was too strongly postponed, which made the whole investigation computationally very expensive. [24] Therefore, we decided to use other perturbations both for the velocity and the magnetic field. We introduced

$$v_y(x, y, t = 0) = v(y) \sin(kx), \tag{3.93}$$

$$b_{1y}(x, y, t = 0) = b_1(y) \cos(kx), \tag{3.94}$$

where $k = 3$ and the function $v(y)$ is given by Eqs. (3.64) and (3.78) in the outer and inner regions, respectively, and for the function $b_1(y)$ we use Eq. (3.63) in the outer regions and the constant ψ approximation in the inner region, i.e. $b_1(y \leq y_\mathrm{m}) = b_1(y_\mathrm{m})$ (for the details, see the previous section). The functions $v_{1x}(x, y, t = 0)$ and $b_{1x}(x, y, t = 0)$ are determined from the divergence free conditions, i.e. $\nabla \cdot \mathbf{b} = \nabla \cdot \mathbf{v} = 0$. In order to reduce the computational cost, we chose such a value of k that exactly one tearing mode would fit into the box.

We can use Eq. (3.81) or (3.90) for predicting the TM growth rate in resistive or resistive-viscous MHD, respectively, only in the parameter range, where both the spatial (Eq. (3.80)) and the temporal (Eq. (3.55)) conditions are met. For the reader's convenience we write again the time-scale conditions (3.55)

$$\frac{1}{\delta^2 \eta} \gg \gamma^{-1} \gg \frac{L_y}{c_\mathrm{A}}. \tag{3.95}$$

For a typical resistivity $\eta \sim 10^{-5}$ and the above chosen parameters we obtain $1/(\delta^2 \eta) \approx 10^3$, $\gamma^{-1} \sim 10^2$ and $L_y/c_\mathrm{A} = 1$. As we can see, the first part of this condition is not (or just marginally)

[23] In the pressure equilibrium configuration, the initial gas pressure profile tended to "diffuse with time" in simulations of too low resolutions, i.e. the pressure maximum would spread after several time units. This would lead to a small total pressure imbalance, in the vicinity of the magnetic field shear, around which two (from both sides of the y axis) "pressure humps" would from. These positive pressure gradients would partially slow down incoming fluid perturbations and consequently reduce the tearing mode growth rate. This phenomenon was very subtle and needed several time units to be operational, yet it was noticeable in our studies, where a growth rate reduction by a factor of $\sim 10\%$ is considered relevant.

[24] LLVB did not experience this problem, because they always used very high resistivities. However, in that case, the analytical expressions (3.81) and (3.90) for the tearing mode growth rate cannot be used. In our studies a typical numerical resistivity was of the order $\eta_* \sim 10^{-6}$.

fulfilled, since it is arguable to claim that $10^3 \gg 10^2$. For $\eta = 10^{-4}$, the situation becomes even worse (the inequality $1/(\delta^2\eta) \gg \gamma^{-1}$ is clearly violated, since it is not true that $10^2 \gg 10^2$). An obvious remedy to this problem would be using much lower values of resistivity. However, this is impractical in our case for several reasons. Firstly, lowering resistivity would considerably increase the computational cost, because it would decrease the TM growth rate and the lower growth rate, the longer time needed to observe a growth of the instability. Moreover, higher resolutions would be required. Secondly, our goal is to investigate how the code behaves in rather underresolved systems and to measure its numerical resistivity and viscosity. Therefore, we needed to validate Eq. (3.81) also for rather high values of resistivity ($\eta \sim 10^{-5}$–10^{-4}). We circumvented the violation of the condition (3.95) with the help of a numerical trick. Instead of solving the proper induction equation

$$\partial_t \mathbf{b} = \nabla \times (\mathbf{v} \times \mathbf{b}) + \eta \nabla^2 \mathbf{b}, \tag{3.96}$$

we used a modified (physically incorrect!) version

$$\partial_t \mathbf{b} = \nabla \times (\mathbf{v} \times \mathbf{b}) + \eta \nabla^2 (\mathbf{b} - \mathbf{b_0}), \tag{3.97}$$

so that resistivity does not act on the background magnetic field $\mathbf{b_0}$. In this way, we eliminated a rather trivial, yet problematic, effect of the background magnetic field diffusion. We would like to point out that there is no difference between using Eq. (3.97), instead of Eq. (3.96), in a simulation, and assuming that the background field is constant in the analytical derivation.

The second important 'spatial condition' (3.80) is

$$\varepsilon_\mathrm{R} \ll y_\mathrm{m} \ll \delta^{-1}. \tag{3.98}$$

Once again, we are faced with the question what "$a \ll b$" numerically means. Probably, there is no good answer to this question and in general it will be problem dependent. Assuming that

$$\varepsilon_\mathrm{R} \lesssim \frac{y_\mathrm{m}}{100} \quad \text{and} \quad y_\mathrm{m} \lesssim \frac{\delta^{-1}}{100} \tag{3.99}$$

properly satisfy condition (3.98), we are faced with a serious computational problem. In order to resolve the resistive-viscous layer one needs a few, say 5, zones. Then for the whole box of size $2L_y = 2\pi/3 \approx 20\delta^{-1}$ we would need 10^6zones,[25] which is numerically unfeasible, even in 2D. Were we interested in studying the physical aspects of the TM growth, it would be beneficial to use a non-equidistant grid, e.g. with a logarithmic spacing. This could probably reduce the amount of necessary zones to as few as 100. However, since our main goal is to study the numerical resistivity and viscosity of the code, we chose on purpose a "non-optimal" Cartesian grid. Condition (3.80) arises from the matching problem of the inner and outer solution. The inner function $\Phi(s)$ should be matched when $\Phi(s) \approx 1/s$, which is the case for $s \gg 1$. We found before that this asymptotic behaviour is already seen for $s > 2.5$ (see Fig. 3.24), i.e. the relative difference between the functions $\Phi(s)$ and $1/s$ is of order 10^{-2}. So the first necessary condition is $y_\mathrm{m} > 2.5\varepsilon_\mathrm{R}$. The upper limit for y_m comes from the fact, that in our derivation, we used the approximation $\tanh(\delta y) \approx \delta y$. For $\delta y = 0.25$ the relative error of this approximation is $\approx 2 \times 10^{-2}$, which we consider as still acceptable. To summarise, a necessary but not yet sufficient condition for inequality (3.80) to hold can be written as

$$2.5\varepsilon_\mathrm{R} < y_\mathrm{m} < 0.25\delta^{-1}. \tag{3.100}$$

[25] From Eq. (3.99), we estimate $\delta^{-1} \approx 10^4 \varepsilon_\mathrm{R}$, and hence $2L_y \approx 2 \times 10^5 \varepsilon_\mathrm{R}$. Thus, 5 zones per ε_R give 10^6 zones per $2L_y$.

Recalling that y_m has no real physical meaning, this inequality can be interpreted as a relation between the resistive layer and the magnetic shear length (proportional to δ^{-1}), i.e.

$$\varepsilon_R < \frac{\chi}{10\delta}, \tag{3.101}$$

where χ is a small number (i.e $\chi \leq 1$, ideally $\chi \ll 1$) that needs to be determined from numerical experiments. We need to stress one fact here, however. Inequality (3.98) (or (3.101)) is a criterion not for the onset of the instability, but for the validity of the analytical expression (3.81) for the tearing mode growth rate. Therefore, one can determine χ in a rather straightforward manner. For given b_0, δ, k and ρ_0, one should run simulations with different values of η, so that the size of the resistive layer changes, and measure γ. If the theoretical growth rate disagrees with the numerical one, the width of the resistive is too large and a smaller value of η should be chosen.

We did not find a full agreement between theory and experiment for any value of resistivity for the non-viscous case. The analytical predictions overestimate the growth rate by a factor of ≈ 1.5–1.8. The source of that discrepancy is the non-zero numerical viscosity, which is present in every simulation. Equations for the TM growth rate were derived either for no viscosity $\nu = 0$, (Eq. (3.81)), or for $\nu > 0.1\eta$ (Eq. (3.90)). Unfortunately, we do not have a suitable analytical expression at our disposal that is valid in the limit of small Prandtl number, i.e for $\nu \ll \eta$. Note that in ODE (3.68) for v_y (valid in the resistive-viscous layer), viscosity couples with the highest order derivatives of v_y, which are dominant in that equation. Therefore even a very small (numerical) viscosity can have a non-negligible effect on the system.

As a next step, we studied tearing modes in the presence of viscosity. In order to have initial perturbations as close as possible to the real viscous tearing mode solution, function $\Phi(s)$ (which is proportional to velocity) should be replaced with $\tilde{\Phi}(\tilde{s})$ (see Subsection 3.4.1) in the inner layer. However, the qualitative difference between both functions is not very big, i.e. they have a similar shape, and the former has a maximum at $s \approx 1.48$, whereas the latter at $\tilde{s} \approx 1.76$. In practice, we used non-viscous initial perturbations (Eqs. (3.93) and (3.93)), which were able to trigger tearing modes quickly enough for our purposes.[26]One important physical aspect changes, however. Inequality (3.101) should be replaced for the viscous case with

$$\varepsilon_{RV} < \frac{\chi}{10\delta}, \tag{3.102}$$

where $\chi \leq 1$, ideally $\chi \ll 1$, and the subscript "TM" in ε_{RV} stands for *resistive-viscous*.

As a first step, we tried to verify the theoretical predictions for the TM growth rate in the presence of viscosity (Eq. (3.90)). We ran several simulations with the HLL Riemann solver, the MP9 reconstruction scheme, a very high resolution (2048×2048 zones), constant viscosity $\nu = 10^{-4}$ and resistivity ranging from $\eta = 10^{-7}$ to 10^{-5}. We explain the procedure of growth rate measuring on an exemplary simulation with resistivity set to $\eta = 10^{-5}$. The y components of initial magnetic field and velocity perturbations are shown in left right panels of Fig. 3.25 (top and bottom panel, respectively), and the ones after 100 time units in the right panels. Apart from higher amplitudes, the evolved perturbations do not differ much from the initial ones. Thus, the initial perturbations based on the tearing mode solution in resistive-non-viscous MHD (in the constant ψ approximation) are very similar to the eigenfunctions of resistive-viscous tearing modes. The upper right panel of Fig. 3.26 depicts a one dimensional projection of the initial and the evolved magnetic field perturbations from Fig. 3.25 at $x = -0.5$. The amplitude of the latter ones is

[26] We also observed that it was sufficient to use initial perturbations only in either velocity or magnetic field. However, in such simulations the instability onset was delayed.

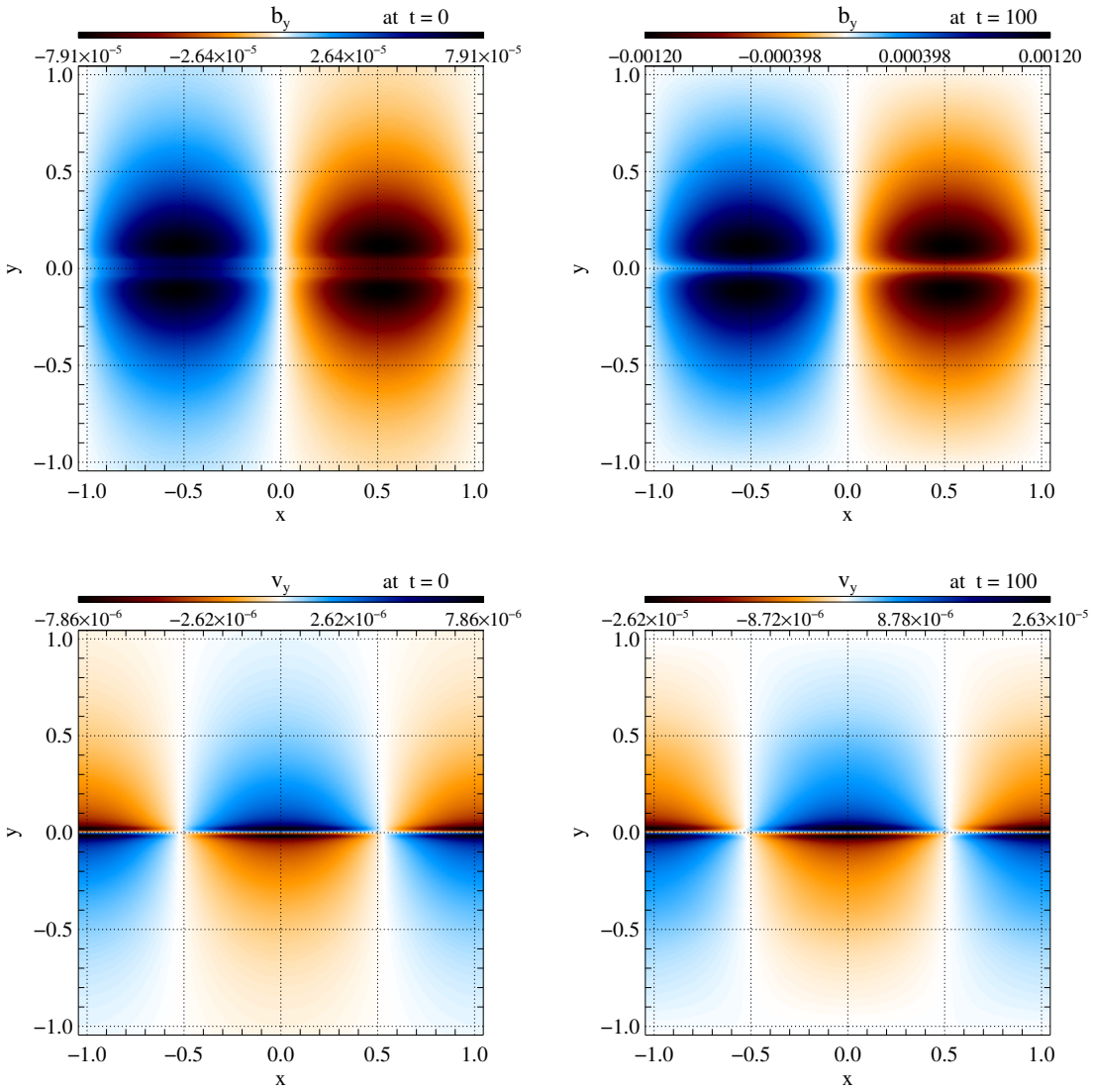

Figure 3.25: Perturbations of the magnetic field and the velocity in a tearing mode simulation with resistivity and viscosity set to $\eta = 10^{-5}$ and $\nu = 10^{-4}$, respectively. The HLL Riemann solver and the MP9 reconstruction schemes were used. The simulation domain was resolved with 2048×2048 zones. *Top left:* Initial magnetic field perturbations, b_y. *Top right:* Magnetic field perturbations, b_y, after 100 time units. Apart from the innermost region (i.e. for $y \approx 0$) (and obviously the amplitude) their shape has not changed much over time, which means that the initial perturbations were very similar to the tearing mode eigenfunction. *Bottom left:* Initial velocity perturbations, v_y. *Bottom right:* Velocity perturbations, v_y, after 100 time units. Their shape is very similar to the initial perturbations. Only the amplitude has increased by roughly one order of magnitude.

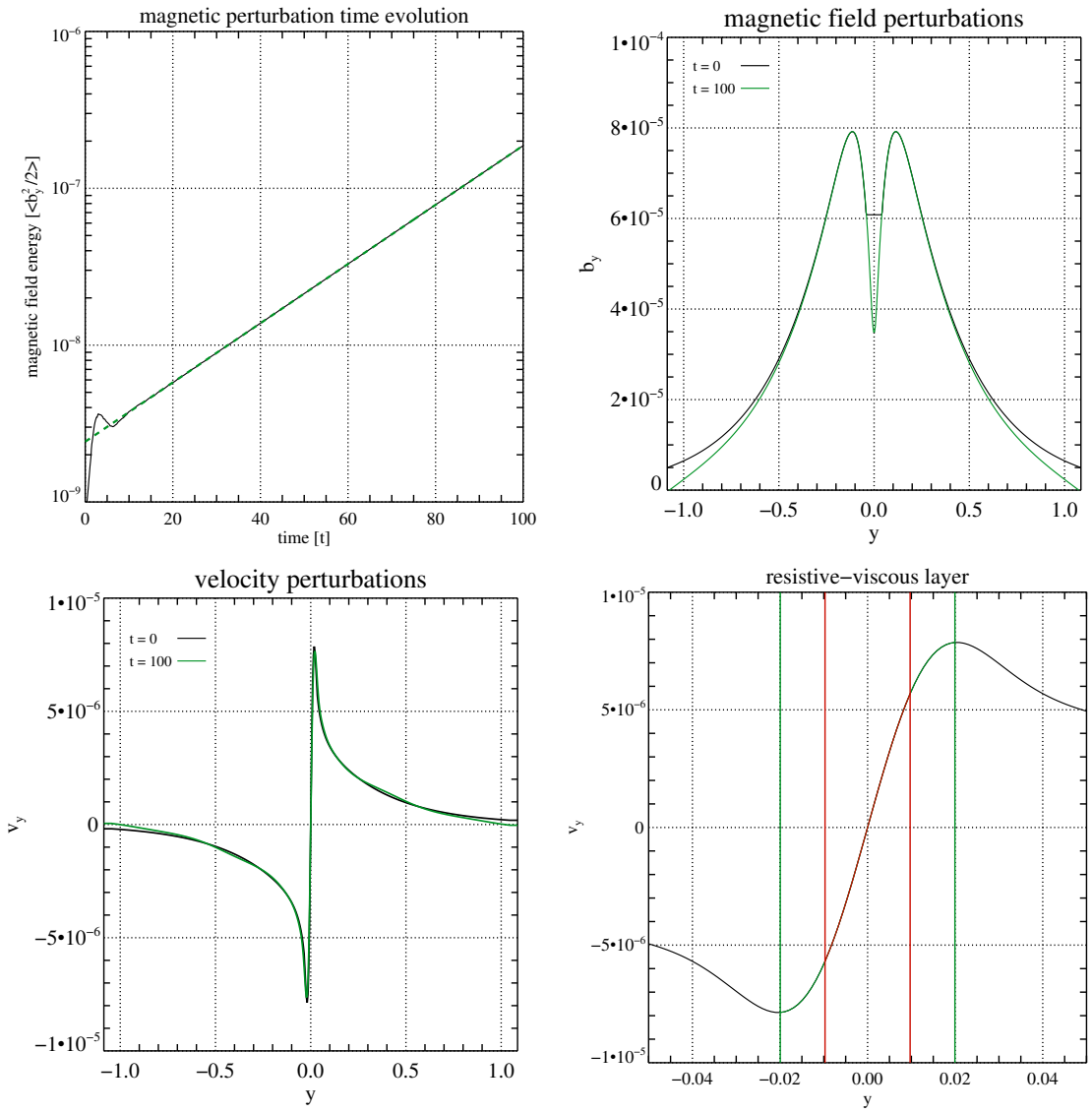

Figure 3.26: Results of a tearing mode simulation with resistivity and viscosity set to $\eta = 10^{-5}$ and $\nu = 10^{-4}$, respectively. The HLL Riemann solver and the MP9 reconstruction scheme were used in the simulation and its domain was resolved with 2048×2048 zones. *Top left:* Time evolution of $\bar{E}_{\mathrm{mag}^y}$ (see Eq. (3.103); black solid curve). After ≈ 15 time units, the instability is fully operational. The green dashed line results from a linear fit to the logarithm of $\bar{E}_{\mathrm{mag}^y}$ for $t \geq 20$, from which the instability growth rate can be measured.*Top right:* Initial (black) and evolved (after 100 time units; green) magnetic field perturbations, b_{1y}. The amplitude of the latter ones was normalised to the initial amplitude. Both curves are almost identical, but in the innermost region, where the constant ψ approximation was used for the initial perturbations. *Bottom left:* Analogous, to the upper right panel, plot of the velocity perturbations, v_y. At $y \approx -0.02$ and $y \approx 0.02$ two velocity peaks, which (according to our definition) determine the width of the resistive-viscous layer, are clearly visible. *Bottom right:* The innermost part of the evolved velocity perturbations, v_y from the bottom left panel. The region where the modulus of the dimensionless parameter $\tilde{s}$ (Eq. (3.88)) is smaller than one, is marked in red. Two points where $y = \pm\varepsilon_{\mathrm{RV}}$, are marked with red vertical lines. According to our definition, the green vertical lines delimit the resistive-viscous layer, where velocity perturbations, v_y, have the characteristic maxima.

normalised to the initial amplitude. In the bottom left panel of Fig. 3.26, we present an analogous comparison of the velocity perturbations at $x = 0$. In the bottom right panel of Fig. 3.26, which is a zoom of the evolved velocity perturbations (from the bottom left panel) around the magnetic shear layer (i.e. for $\delta y \ll 1$), two velocity peaks, which are characteristic for tearing modes, are clearly visible. With green vertical lines, we mark the width of the resistive-viscous layer (according to our definition). For each simulation, we measured the tearing mode growth rate in the following way. For every time output, we computed

$$\bar{E}_{\mathrm{mag}^y} \equiv \int_{-L_x}^{L_x} \int_{-0.1}^{0.1} \frac{b_y^2}{2} \, \mathrm{d}x\mathrm{d}y, \tag{3.103}$$

which is a contribution of the component b_y to the magnetic field energy in the inner region of the box (i.e. $-0.1 < y < 0.1$). The integration was performed only in this inner region, to reduce a potential influence of boundary conditions on the real solution. Typically after approximately 20 time units, $\bar{E}_{\mathrm{mag}^y}$ grows at a constant rate, i.e. by that time the tearing mode is fully operational and all discrepancies between the initial perturbations and the real solution are carried away from the system. Since $b_y \propto \exp(\gamma t)$, by taking the logarithm of Eq. (3.103), we arrive at

$$\frac{1}{2} \ln\left(\bar{E}_{\mathrm{mag}_y}\right) = \gamma t + \mathrm{const.}, \tag{3.104}$$

where the constant depends on the initial perturbation amplitude and the box size. From the above equation, by means of a simple linear regression, we computed the instability growth rate. In the upper left panel of Fig. 3.26, the black solid line depicts time evolution of $\bar{E}_{\mathrm{mag}_y}$ from the above describe simulation (with i.e. $\eta = 10^{-5}$), and the green dashed line results from a linear fit according to Eq. (3.104).

For every simulation (with constant viscosity $\nu = 10^{-4}$ and resistivity in the range $\eta = 10^{-7}$–10^{-5}), we measured the instability growth rate, whose logarithm should theoretically read (see Eq. (3.90))

$$\ln(\gamma) = \frac{5}{6}\ln(\eta) + \ln\left(\frac{2}{3} 2^{1/3} \nu^{-1/6} \left(\frac{b_0 k}{\sqrt{\rho_0}}\right)^{1/3}\right) \delta^{5/3} \left(\frac{\delta}{k} - \frac{k}{\delta}\right), \tag{3.105}$$

which for our numerical setup ($\delta = 10, k = 3, b_0 = \rho_0 = 1$) gives

$$\ln(\gamma) = 0.8\bar{3}\eta + 5.907 \tag{3.106}$$

(where $0.8\bar{3} \equiv 0.8333\ldots$). Fitting the function

$$\ln(\gamma) = a \ln(\eta) + c. \tag{3.107}$$

to the simulation results (Fig. 3.27), a linear regression gives

$$a = 0.7994 \pm 0.0012, \tag{3.108}$$

$$c = 5.377 \quad \pm 0.015. \tag{3.109}$$

The difference between the theoretical value of c and the estimator of c equals ≈ 0.53, which cannot be explained by the statistical error. Were $a = 0.8\bar{3}$, this would lead to a growth rate overestimation by a factor of ≈ 3. This discrepancy could still be eliminated by multiplying the right hand side of Eq. (3.90) by that numerical constant. In the end, in that equation the symbol "$\approx$" was used instead of the sign "$=$", to indicate that it is just an approximate result (even within linearised MHD). Unfortunately, the exponent estimator a does not agree either. One could conclude at this point that, since no use of Eq. (3.90) and Eq. (3.81) can be made, the whole theoretical effort to understand the tearing modes better was in vain. However, we decided to adopt a different approach and we proposed a semi-analytical equation for the tearing-mode growth rate.

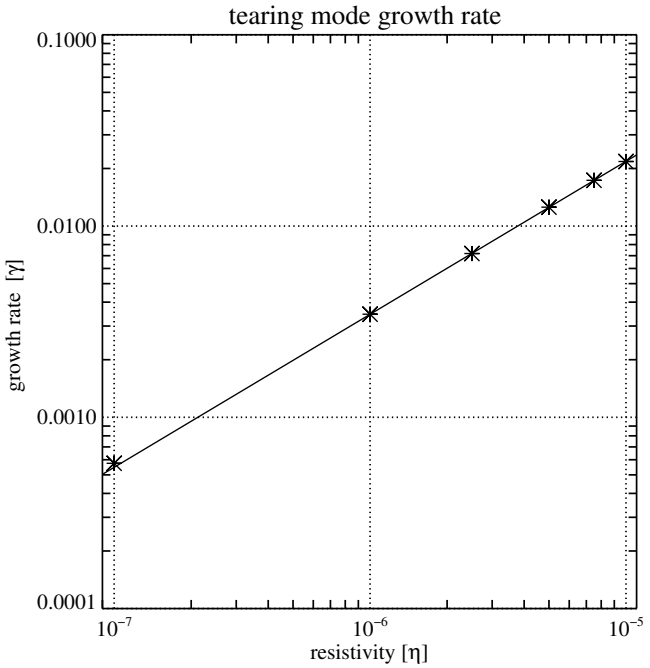

Figure 3.27: Tearing mode growth rate as a function of resistivity. Asterisks denote results of simulations run with $\nu = 10^{-4}$, the HLL Riemann solver, the MP reconstruction scheme and a resolution of 2048×2048 zones. The solid line is a result of a linear fit to the logarithm of the measured growth rates.

Semi-analytical theory

The general form of equation for the tearing-mode growth rate can be postulated based on the theoretical insight gained after all the analytical derivations, whereas the details and exact numbers will need to be found with the help of numerical simulations. In the analytical expressions (3.81) and (3.90), the growth rate of the tearing mode is proportional to a product of resistivity, (viscosity,) Alfvén speed, δ, k and $(\delta/k - k/\delta)$, all of them to a certain different power. Based on this observation, we postulate an ansatz:

$$\gamma \stackrel{?}{=} n_0 \eta^{n_1} \nu^{n_2} \left(\frac{b_0}{\sqrt{\rho_0}} \right)^{n_3} k^{n_4} \delta^{n_5} \left(\frac{\delta}{k} - \frac{k}{\delta} \right)^{n_6}, \tag{3.110}$$

where n_0 is a constant and $n_1, \ldots, n_6$ are fractionals, which need to be determined by numerical simulations.

Similarly, since the analytical expression (3.90) for the growth rate of the tearing mode in resistive-viscous MHD does not agree with our simulation results, there is no reason either to trust Eq. (3.88) for $\varepsilon_{\mathrm{RV}}$, which is proportional to the width of the resistive-viscous layer. Instead, we can formulate a similar (to Eq. (3.110)) ansatz for $\varepsilon_{\mathrm{RV}}$, i.e.

$$\varepsilon_{\mathrm{RV}} \stackrel{?}{=} \eta^{m_1} \nu^{m_2} \left(\frac{b_0}{\sqrt{\rho_0}} \right)^{m_3} k^{m_4} \delta^{m_5}, \tag{3.111}$$

where $m_1, \ldots, m_6$ are fractional numbers This time, we did not introduce a constant m_0, since $\varepsilon_{\mathrm{RV}}$ cannot be measured directly from simulations. It should just be thought as a prescription to

transform y in ODE (3.68) to a dimensionless variable $\tilde{s} \equiv y/\varepsilon_{\mathrm{RV}}$. What we can expect however, is that the characteristic velocity peak, v_y, (which according to our convention defines the width of the resistive-viscous layer) should be present for the same value of $\tilde{s}$ (i.e. the function $\tilde{\Phi}(\tilde{s})$ has a maximum for a certain constant $\tilde{s}$). In other words, the distance of the velocity peak from the centre, which we will denote with the symbol $L_{\varepsilon_{\mathrm{RV}}}$, should be proportional to $\varepsilon_{\mathrm{RV}}$. Therefore, the width of the resistive-viscous layer should be equal to

$$L_{\varepsilon_{\mathrm{RV}}} \stackrel{?}{=} m_0 \varepsilon_{\mathrm{RV}} \stackrel{?}{=} m_0 \eta^{m_1} \nu^{m_2} \left(\frac{b_0}{\sqrt{\rho_0}} \right)^{m_3} k^{m_4} \delta^{m_5}, \tag{3.112}$$

where m_0 is a constant to be determined by simulations.

The verification of ansatzes (3.110) and (3.112), and the determination of the unknown constants $n_0, \ldots, n_6$ and $m_0, \ldots, m_5$ is a tedious task. Therefore, we decided to describe it in detain in Appendix A. In short, from dimensional analysis, we obtain some constraints on the constants $n_1, \ldots, n_6$ and $m_1, \ldots, m_5$. Next, we perform various simulations to determine these constants and to test different aspects of ansatzes (3.110) and (3.112). In principle, we could find all the unknown constants $n_0, \ldots, n_6$ and $m_0, \ldots, m_5$ with the method described in Appendix A. However, to save computational time, we only determined these which were necessary for our main purpose, i.e. measuring the numerical resistivity of our code.

We found that the equations for the growth rate of the tearing modes and for the width of the resistive-layer read (see Eqs. (A.51) and (A.52) from Appendix A)

$$\gamma = n_0 \eta^{4/5} \nu^{-1/5} \left(\frac{b_0}{\sqrt{\rho_0}} \right)^{2/5} k^{n_4} \delta^{n_5} \left(\frac{\delta}{k} - \frac{k}{\delta} \right)^{n_6} \quad \text{and} \tag{3.113}$$

$$L_{\varepsilon_{\mathrm{RV}}} = m_0 (\eta \nu)^{1/6} \left(\frac{b_0}{\sqrt{\rho_0}} \right)^{-1/3} k^{m_4} \delta^{m_5}, \tag{3.114}$$

respectively, where n_1 and m_0 are constants, n_4, n_5, n_6 and m_4, m_5 are fractionals, $n_4 + n_5 = 8/5$ and $m_4 + m_5 = -2/3$.

Additionally, we calibrated these equations for $k = 3$ and $delta = 10$ (which are default parameters in our simulations) with the help of very high resolution simulations (of 2048×2048 zones): (see Eqs. (A.53) and (A.54) in Appendix A)

$$\gamma(k = 3, \delta = 10) = 34.56 \eta^{4/5} \nu^{-1/5} \left(\frac{b_0}{\sqrt{\rho_0}} \right)^{2/5} \quad \text{and} \tag{3.115}$$

$$L_{\varepsilon_{\mathrm{RV}}}(k = 3, \delta = 10) = 0.634 (\eta \nu)^{1/6} \left(\frac{b_0}{\sqrt{\rho_0}} \right)^{-1/3}. \tag{3.116}$$

We now refer the interested reader to Appendix A, where we explain how Eqs. (3.113)–(3.116) were obtained. Moreover, we discuss there possible explanations of the discrepancy between the theoretical predictions for the tearing-mode growth rate (Eq. (3.90)) and the simulation results.

Numerical tearing modes

After the tedious derivation of the semi-analytical Eqs. (3.115) and (3.116), we are ready to measure the code's numerical resistivity. Unlike the wave damping tests, tearing mode simulations are quite complicated system and full of pitfalls when interpreting their results. We hope that by

the end of this subsection, we will have convinced the reader that it was worth spending so much effort on a better understanding their theory.

Let us have a look at the whole problem with the eye of a physicist, who is familiar with our ansatzes (3.1), (3.4) and (3.5) for numerical dissipation, but has only a superficial knowledge of tearing mode theory. The physicist would know that in order to make use of the ansatzes, it is necessary to determine the system's characteristic velocity and length. A natural candidate for the former seems to be the Alfvén speed, since it explicitly enters the growth rate equations (3.81), (3.90) and (3.113). Taking the box length, $2L_y$, as the characteristic length would be a clear misunderstanding. Yet, many authors use in their numerical simulations the whole box size to define Reynolds numbers, forgetting that the actual physical phenomenon can take place only in a much smaller region. In our case, the magnetic shear width, proportional to δ^{-1}, seems to be a good candidate for the characteristic length of the system.[27] In the end, the whole interesting physics takes place there. Unfortunately, both educational guesses are wrong. Neither the system's characteristic velocity is the Alfvén speed, nor is its characteristic length the shear width. we go back to the main discussion.

The idea behind using tearing modes to determine the code's numerical resistivity, η_*, is quite simple. If a simulation is run without any physical resistivity and the instability is still observed, it means that it must have been driven by numerical one. From the growth rate Eq. (3.115),

$$\gamma(k=3,\delta=10) = 34.56\eta_*^{4/5}\nu^{-1/5}\left(\frac{b_0}{\sqrt{\rho_0}}\right)^{2/5}, \tag{3.117}$$

the numerical resistivity can be easily computed

$$\eta_* = \left(\frac{\gamma(k=3,\delta=10)}{34.56}\right)^{5/4}\nu^{1/4}\left(\frac{\sqrt{\rho_0}}{b_0}\right)^{1/2}. \tag{3.118}$$

Alternatively, one could measure the resistive-viscous layer width (Eq. (3.116)), from which

$$\eta_* = \left(\frac{L_{\varepsilon_{\mathrm{RV}}}(k=3,\delta=10)}{0.634}\right)^{6}\nu^{-1}\left(\frac{b_0}{\sqrt{\rho_0}}\right)^{2}. \tag{3.119}$$

This method is much less accurate, however. Firstly, $L_{\varepsilon_{\mathrm{RV}}}$ measurements have rather high relative errors (order of 0.1). Secondly, because $\eta_* \propto L_{\varepsilon_{\mathrm{RV}}}^6$, they would lead to even higher relative errors of η_*.

At first, we compared the numerical resistivity of three Riemann solvers: the LF, the HLL and the HLLD. We used the MP5 reconstruction scheme, the RK3 time integrator with a CFL factor equal to 0.7. For the standard parameters, i.e. $\delta = 10, k = 3, b_0 = \rho_0 = 1, \nu = 10^{-4}$, and no resistivity, we ran simulations with resolutions from 128×128 to 1024×1024 zones. For the LF solver, tearing modes appeared and, as expected, the higher the resolution, the lower the instability growth rate (see Fig. 3.28). For resolutions less than 320×320 zones, the resistive-viscous layer was so wide, that condition (A.56) was violated, making Eq. (3.115) invalid. Therefore, these results had to be discarded for further data analysis. In the simulations with the HLL and HLLD Riemann solvers, the instability was not observed at all, even for the lowest resolution. We conclude that their numerical resistivities, although undetermined, must be much lower than that of the LF solver. In the wave damping simulations, all three solvers exhibited a very similar behaviour, yet the tearing modes showed a clear difference among them. We can think of two possible

[27] For sure, we would use this quantity to compute the Reynolds numbers.

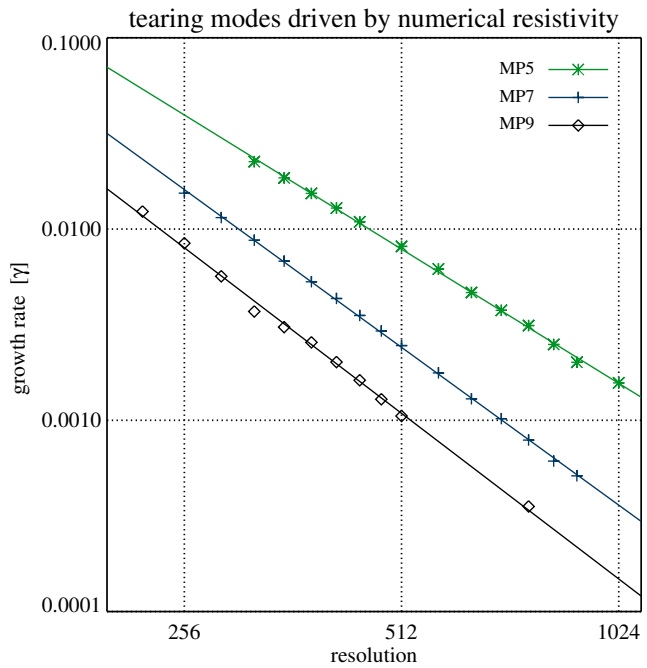

Figure 3.28: Tearing mode growth rate as a function of resolution in simulations in which the instability is driven only by numerical resistivity. In all simulations, viscosity was set to $\nu = 10^{-4}$ and the LF Riemann solver was used. The results of simulations with the MP5, the MP7 and the MP9 reconstruction scheme are marked with green asterisks, blue plus signs and black diamonds, respectively. The straight lines of corresponding colours result from linear fits to the logarithms of tearing-mode growth rates.

explanations for this fact. The first one is that ansatzes (3.1), (3.4) and (3.5) for numerical dissipation do not work universally for all physical problems. One of the assumptions made was that the coefficients $\mathfrak{N}_\nu^{\Delta x}, \mathfrak{N}_\xi^{\Delta x}$ and $\mathfrak{N}_\eta^{\Delta x}$ depend only on the numerical schemes used in a simulation. The LF solver's coefficient would be almost equal to the HLL- and HLLD solver's coefficients for the wave damping, but larger for more complicated physical problems. Another explanation is that in the wave damping simulations, the numerical resistivity of all Riemann solvers was negligible. This hypothesis is supported by the magnetosonic wave tests, but we could not conclude anything on that from the Alfvén wave simulations. The LF solver's coefficient $\mathfrak{N}_\eta^{\Delta x}$ could be much smaller than its $\mathfrak{N}_\nu^{\Delta x}$ and $\mathfrak{N}_\xi^{\Delta x}$, but sufficiently large to trigger the tearing mode instability numerically. The values of $\mathfrak{N}_\eta^{\Delta x}$ for the HLL and HLLD solvers could simply (always) be much smaller than those for the LF solver. It is also possible that a "mixture" of these two explanations holds.

In another two sets of simulations, we chose the same parameters but changed the reconstruction scheme to either the MP7 or the MP9. Like in all remaining tests, the LF Riemann solver was used. The results of an exemplary simulation with the MP7 reconstruction scheme and the resolution of 256×256 zones are presented in Fig. 3.29. The dependence of the instability growth rate on resolution is presented in Fig. 3.28. To the simulation results, w e fitted the functions

$$\begin{aligned} \ln(\gamma) &= a_5 \ln(\Delta x) + c_5, \\ \ln(\gamma) &= a_7 \ln(\Delta x) + c_7, \\ \ln(\gamma) &= a_9 \ln(\Delta x) + c_9, \end{aligned} \tag{3.120}$$

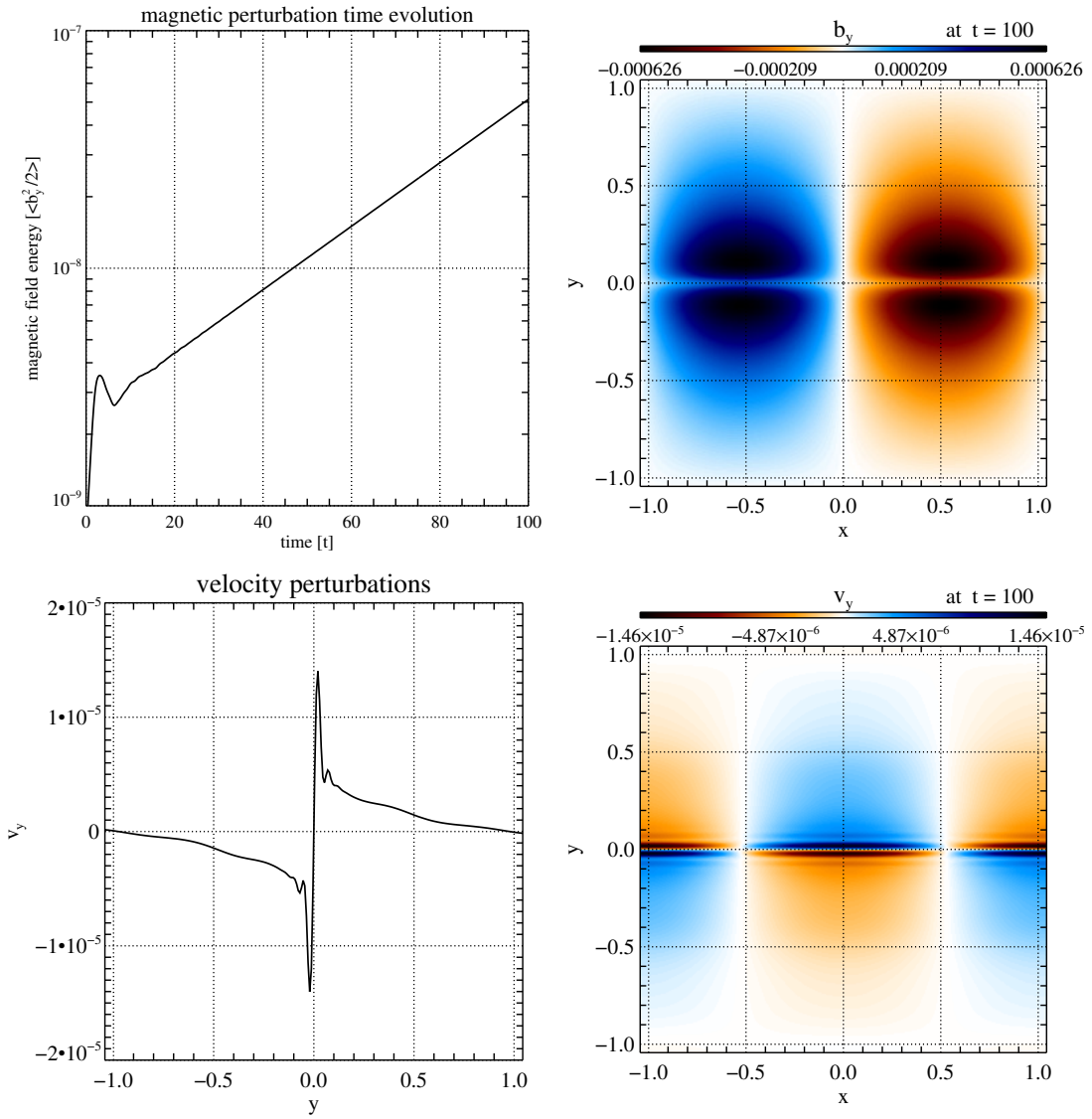

Figure 3.29: Results of a (tearing mode) simulation with viscosity set to $\nu = 10^{-4}$ and no physical resistivity (i.e. $\eta = 0$). The simulation domain was resolved with 256×256 zones. The LF Riemann solver and the MP7 reconstruction scheme were used. Theoretically, in non-resistive MHD, tearing modes should not develop and initial perturbations (very similar to those presented in the left panels of Fig. 3.25) should not grow with time. However, the tearing mode instability driven by numerical resistivity is observed in the simulation. *Top left:* For $t > 15$ time units, the energy of magnetic field perturbations grows exponentially with time, like in a simulation with non-zero physical resistivity (compare with the upper left panel of Fig. 3.26). *Top right:* Magnetic field perturbations after 100 time units look like those observed in a tearing mode simulation with physical resistivity (compare with the upper right panel of Fig. 3.25). *Bottom right:* Analogous plot for velocity perturbations (compare with the bottom right panel of Fig. 3.25). *Bottom left:* 1D projections at $x = 0$ of the velocity perturbations from the bottom right panel. Characteristic velocity peaks defining the resistive-viscous layer are clearly visible (compare with the upper left panel of Fig. 3.26).

where a_i and c_i are the coefficients of the reconstruction scheme of the $i-$th order. We obtained the following estimators

$$\begin{aligned} a_5 &= 2.355 \pm 0.021, & c_5 &= 9.85 \pm 0.13, \\ a_7 &= 2.740 \pm 0.015, & c_7 &= 11.06 \pm 0.09, \\ a_9 &= 2.876 \pm 0.051, & c_9 &= 11.1 \pm 0.3. \end{aligned} \tag{3.121}$$

At first, these results may look a bit puzzling. All three reconstruction schemes seem to have almost the same, quite low, third order of accuracy.[28] The first explanation that comes to mind is that the main contribution to the numerical resistivity is from the RK3 time integration errors. The order would agree more or less. To test this hypothesis, we ran additional simulations with different timesteps. For a given resolution and a CFL factor in the range 0.1–0.7, the instability growth rate was the same. This clearly indicates that numerical resistivity was caused mainly by spatial discretisation errors. The simulations with a CFL factor ≥ 0.8 exhibited a peculiar behaviour. The whole system became unstable against not the tearing modes but some other unphysical instability. Hence, the time integration errors either do not contribute to the numerical resistivity or give completely unphysical results.[29] This is another key difference between the tearing mode- and wave damping-simulations.

Having tested that the numerical dissipation arises from the spatial discretisation, we need to explain the apparently big reduction of the accuracy order. A physicist who is unfamiliar with the tearing mode theory and our ansatz (3.5) for the numerical resistivity, could prematurely conclude that high order reconstruction schemes are overrated (theoretically up to the 9th order, practically not even the 4th order) and not worth using. However, for lower order schemes (PL and MP3), it was impossible to simulate the tearing modes at all in the used resolution range, because the flow was spoilt by some unphysical instabilities.

Coming back to the main discussion, one has to be careful when using ansatz (3.5) for numerical the resistivity:

$$\eta_* = \mathfrak{N}_\eta^{\Delta x} \times \mathcal{V} \times \mathcal{L} \times \left(\frac{\Delta x}{\mathcal{L}}\right)^r, \tag{3.122}$$

where $\mathcal{V}$ and $\mathcal{L}$ are the system's characteristic speed and length, respectively, and r is the reconstruction order. If we assumed that $\mathcal{L} \propto \delta^{-1}$ (which is constant), once again we would obtain that $r_i = (5/4)a_i$. The conceptual mistake is that δ^{-1} is the correct choice for the characteristic length of the background magnetic field diffusion problem, but not for tearing modes, whose scale is much smaller than the shear width. It turns out that the system's characteristic length is proportional to the width of the resistive-viscous layer, i.e. $\mathcal{L} \propto \varepsilon_{\mathrm{RV}}$. This seems logical, because from the beginning, we assumed that Ohmic dissipation takes place only in the very narrow layer, where the non-ideal MHD equations are solved. It is somewhat arbitrary to specify the exact value of $\mathcal{L}$, because there should be a transition region, where both ideal and non-ideal MHD equations are valid. Therefore, saying that $\mathcal{L} = \varepsilon_{\mathrm{RV}}$ or $\mathcal{L} = 2\varepsilon_{\mathrm{RV}}$ does not really make sense. For our applications, we found a useful definition, however. For the wave simulations we assumed that $\mathcal{L} = \lambda$, which is a natural choice. If we want to compare both types of simulations, we should have the same convention for $\mathcal{L}$. We notice that in wave simulations, the distance between the points where velocity pertubations are equal to zero and reach the maximum is $\lambda/4$. Similarly, in a tearing mode

[28] In such a straightforward interpretation the reconstruction order of the MP9 scheme would be equal to $(5/4)a_9 \approx 3.6$.

[29] Numerical dissipation is, in the end, also unphysical, but at least we have a way to describe and estimate it.

simulation, velocity pertubations are equal to zero at $y = 0$ and reach the characteristic maximum at $y = L_{\varepsilon_{\rm RV}}$ (see bottom right panel of Fig. 3.26). This allows us identify "$L_{\varepsilon_{\rm RV}} \approx \lambda/4$", and hence

$$\mathcal{L} = 4L_{\varepsilon_{\rm RV}}. \tag{3.123}$$

This definition is somewhat arbitrary but it is unimportant how close the velocity profile resembles a sine function (in our case, both functions are indeed quite similar). The distinct velocity peak was the key aspect. For any physical problem viscosity and resistivity are important only in places where velocity or magnetic field experience strong variations. One should just consistently use one way of measuring these regions, e.g. with the help of some characteristic maxima,if they appear - like in our case, or non-zero velocity or magnetic fields gradients. Equally well, we could assume that for the wave simulations $\mathcal{L} = \lambda/4$ or $\mathcal{L} = 1/k$, which would only lead to a rescaling of $\mathfrak{N}_\eta^{\Delta x}$.

Before we can prove our statement about the characteristic length of the tearing mode, we must understand the consequences that it has for the numerical resistivity. Combining Eqs. (3.123) and (3.122), we obtain

$$\eta_* = \mathfrak{N}_\eta^{\Delta x} \times \mathcal{V} \times 4L_{\varepsilon_{\rm RV}} \times \left(\frac{\Delta x}{4L_{\varepsilon_{\rm RV}}}\right)^r. \tag{3.124}$$

On the other hand, from Eq. (3.116), we have

$$L_{\varepsilon_{\rm RV}}(k = 3, \delta = 10) = 0.634\eta_*^{1/6}\nu^{1/6}\left(\frac{b_0}{\sqrt{\rho_0}}\right)^{-1/3}. \tag{3.125}$$

Hence, the numerical resistivity depends on the width of the resistive-viscous layer, which in turn depends on the numerical resistivity. As we see, the situation becomes quite complicated. Increasing the resolution decreases Δx in the numerator of Eq. (3.124), which lowers the numerical resistivity. This reduces the width of the resistive-viscous layer, which depends on η_*. A smaller value of $L_{\varepsilon_{\rm RV}}$ in the denominator of Eq. (3.124) increases the numerical resistivity. And so on. Of course for a given $\mathfrak{N}_\eta^{\Delta x}$ and r, there is a unique solution of this problem. From this brief discussion we see why the MP5, the MP7 and the MP9 reconstruction schemes had apparently low orders of accuracy. Equation $r_i = (5/4)a_i$ is simply wrong as it does not take into account the influence of the characteristic length.

Once we know the characteristic length of the system, we can Eq. (3.124) into Eq. (3.117), obtaining

$$\gamma(k = 3, \delta = 10) = 34.56(\mathfrak{N}_\eta^{\Delta x})^{4/5}\mathcal{V}^{4/5}(4L_{\varepsilon_{\rm RV}})^{4(1-r)/5}(\Delta x)^{4r/5}\nu^{-1/5}\left(\frac{b_0}{\sqrt{\rho_0}}\right)^{2/5}. \tag{3.126}$$

This equation should be sufficient to determine the order of a reconstruction scheme, by taking the logarithm of both sides and fitting the function

$$\ln(\gamma) = \frac{4r}{5}\ln(\Delta x) + \frac{4(1-r)}{5}\ln(4L_{\varepsilon_{\rm RV}}) + c, \tag{3.127}$$

since γ and $L_{\varepsilon_{\rm RV}}$ can be measured in every simulation. The yet unknown characteristic velocity, $\mathcal{V}$, only contributes to the constant c. This approach has two drawbacks, however. First of all, we need to fit a function of two variables, which can lead to bigger uncertainties. What is even more important, unlike the growth rate, γ, and the zone length, Δx, the resistive-viscous layer width, $L_{\varepsilon_{\rm RV}}$, can be measured only relative error of up to 0.2.

What can be measured with negligible errors is the growth rate, from which the numerical resistivity can be easily determined. This suffices to compute the theoretical value of the resistive-viscous layer width without any error. In further calculations, we can proceed assuming that the code "knows" this value "for determining its own numerical resistivity", even though it cannot be exactly represented because of the finite grid resolution. In other words, we will treat $L_{\varepsilon_{\mathrm{RV}}}$ as a continuous function, blissfully ignoring its discrete nature. From combining Eq. (3.124) with Eq. (3.125), we find

$$\eta_* = (2.536)^{(6-6r)/(5+r)} (\mathfrak{N}_\eta^{\Delta x})^{6/(5+r)} \times \mathcal{V}^{6/(5+r)} \boldsymbol{\nu}^{(1-r)/(5+r)} \left(\frac{b_0}{\sqrt{\rho_0}} \right)^{(2r-2)/(5+r)} (\Delta x)^{6r/(5+r)}. \tag{3.128}$$

By plugging this expression into the growth rate equation (3.117), we obtain

$$\gamma(k=3, \delta=10) = 34.56 (\mathfrak{N}_\eta^{\Delta x})^{24/(25+5r)} \mathcal{V}^{24/(25+5r)} \times (2.536)^{(24-24)/(25+5r)} \boldsymbol{\nu}^{-(1+5r)/(25+5r)} \left(\frac{b_0}{\sqrt{\rho_0}} \right)^{(2+10r)/(25+5r)} (\Delta x)^{24r/(25+5r)}. \tag{3.129}$$

Even though $L_{\varepsilon_{\mathrm{RV}}}$ does not appear in this equation explicitly, we should bear in mind that its derivation heavily relies on the resistive-viscous layer concept. Especially, both equations (3.125) and (3.117), let alone ansatz (3.5), must hold for numerical resistivity, which is not obvious. In the end, numerical dissipation is just a sum of errors, which we try to describe as if they behaved like proper physical resistivity or viscosity. It cannot certainly be the case in every situation. Therefore, Eq. (3.129) can be used only for simulations in which from numerical resistivity, calculated from this growth rate equation, it is possible to determine the resistive-viscous layer width. It tests if both Eqs. (3.125) and (3.117) are fulfilled. If it is not the case, such a simulation should be discarded from the further statistical analysis.

In Fig. 3.30, black crosses depict the measured widths of the resistive-viscous layer in the simulations run with the MP7 reconstruction scheme, while the red curve presents a theoretically expected layer width (Eq. (3.125)) for the numerical resistivity determined from the measured growth rate Eq. (3.118).[30] The agreement between the theoretical and measured values is excellent. This result shows that our assumptions are correct, which is far from being obvious. In the end, we firstly postulated that (i) numerical errors can be called "numerical resistivity", (ii) this numerical resistivity can be treated as normal physical resistivity, and (iii) the same equations can be used to either determine it or predict its influence on the system. Moreover, we also had to make use of ansatz (3.5) for numerical resistivity.

With the help of Eq. (3.129), we can determine the order of the reconstruction schemes, i.e.

$$r = \frac{25a}{24 - 5a}, \tag{3.130}$$

where the coefficient a is obtained from the fitting results (3.121) of the corresponding scheme. To compute the coefficient $\mathfrak{N}_\eta^{\Delta x}$, the characteristic velocity $\mathcal{V}$ needs to be identified. As we will show later, it is the fast magnetosonic speed, which reads

$$\mathcal{V} = c_{ms} = \sqrt{c_{\mathrm{s}}^2 + c_{\mathrm{A}}^2} \approx 1.63. \tag{3.131}$$

[30] More precisely, instead of using measured growth rates for every resolution, we used expected values from linear fit (3.120) to the simulation data. However, the differences between the expected and measured growth rates are almost negligible (Fig. 3.28).

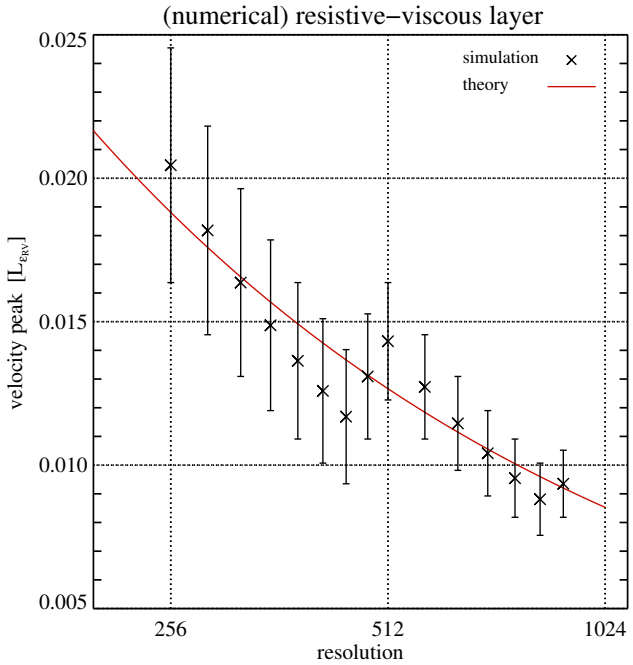

Figure 3.30: Width of the resistive-viscous layer as a function of resolution (i.e. numerical resistivity) in simulations of tearing modes driven by numerical resistivity . Black crosses depict measured values in the simulations run with the MP7 reconstruction scheme. The red curve presents the expected layer width (Eq. 3.125), given the numerical resistivity determined from the measured growth rate and Eq. (3.118). The agreement between the predicted and the measured layer widths is excellent.

Note that we assumed that the wavevector is perpendicular to the background magnetic field. We will discus this choice later.

Finally, we are ready to interpret the fitting results (3.121) correctly and to determine $\mathfrak{N}_\eta^{\Delta x}$ and r. Their uncertainties arise from the statistical errors of the estimators a_i and c_i. Since the error analysis equations are somewhat long and not very instructive, we do not write down their explicit form. The results are presented in Table 3.12. The MP5 scheme is almost 5th order accurate , whereas the MP7 and the MP9 schemes performed a bit below the theoretical expectations. The higher the reconstruction scheme, the higher the reduction of the accuracy order.[31]

[31] The graphical representation of the results is presented in Fig. 3.33 from Sec. 3.5. Note that quantities in this figure do not correspond to the parameters used in the tearing mode simulations. We put $\mathcal{L} = \mathcal{V} = 1$ for all points (i.e. such that the characteristic length is constant like in the wave damping simulations, and not a function of numerical resistivity as it is in the tearing mode simulations). The number of zones per characteristic length, 8 to 24 (abscissa in Fig. 3.33) ,

Reconstruction scheme	$\mathfrak{N}_\eta^{\Delta x}$	r
MP5	16 ± 5	4.814 ± 0.085
MP7	142 ± 33	6.65 ± 0.08
MP9	170 ± 220	7.56 ± 0.55

Table 3.12: Estimators of $\mathfrak{N}_\eta^{\Delta x}$ and the reconstruction scheme order, r, (for the definition, see Eq. (3.5)) determined in tearing mode simulations with the LF Riemann solver.

Another important task is to determine the system's characteristic velocity. There are three natural candidates, the Alfvén, the fast magnetosonic and the fluid perturbation speed. The third one can be discarded for the following reason. Velocity perturbations exponentially grow with time. If numerical resistivity depended on them, it should also increase with time. However, the numerically driven tearing mode growth rate remained constant. Additionally, we ran three simulations with the same parameters, but different initial perturbation amplitudes. We changed those by up to three orders of magnitudes, but this did not affect the growth rate at all. As a next step to identify the characteristic velocity, we ran several simulations with the background pressure in the range 0.01–900. We used the standard physical parameters ($\delta = 10, k = 3, b_0 = \rho_0 = 1, \nu = 10^{-4}$), no resistivity and the MP5 reconstruction scheme. The simulation box was resolved with 512×512 zones. Neither the Alfvén speed ($c_\mathrm{A} = b_0/\sqrt{\rho}$), nor the TM growth rate (see, e.g. Eq. (3.115)) depend on pressure, whereas the magnetosonic speed (Eq. 3.131)) changes from ≈ 1 to ≈ 39 in this pressure range. As we can see from the simulation results (upper panel of Fig. 3.31), the growth rate increases with pressure, which means that the numerical resistivity must have increased as well. This excludes the Alfvén speed to be the characteristic velocity. The only candidate left is the magnetosonic speed, which reads

$$c_\mathrm{ms} = \sqrt{\frac{1}{2}\left(c_\mathrm{A}^2 + c_\mathrm{s}^2 + \sqrt{(c_\mathrm{A}^2 + c_\mathrm{s}^2)^2 - 4c_\mathrm{A}^2 c_\mathrm{s}^2 \cos^2\theta}\right)}, \tag{3.132}$$

where θ is the angle between the perturbation wavevector and the background magnetic field. For the tearing modes, the perturbed fluid makes a "U-turn" in the vicinity of the magnetic shear (i.e. for $|\delta y| \ll 1$). Therefore, it does not make sense to specify for which value of θ the magnetosonic speed should be computed. Probably one could take a somehow averaged value along the fluid path. However, solving this problem accurately seems to be impossible and even counterproductive. All in all, we introduced ansatzes (3.1), (3.4) and (3.5) to have a simple way of estimating the code's numerical dissipation. Consequently, for further analysis, we take the maximum possible magnetosonic speed ($\cos\theta = 0$),

$$c_\mathrm{ms} = \sqrt{c_\mathrm{A}^2 + c_\mathrm{s}^2}. \tag{3.133}$$

This leads at most to a slight underestimation of $\mathfrak{N}_\eta^{\Delta x}$ in ansatz (3.5) for the numerical resistivity. However, if $\mathfrak{N}_\eta^{\Delta x}$ is given (from some other tests), it is better to overestimate rather than underestimate the numerical dissipation. Therefore, we recommend to always use the maximum possible value for the characteristic velocity. Already from looking at the upper panel of Fig. (3.31), we can suspect that it is the magnetosonic speed that affects the numerical resistivity for the following reasons. Firstly, regardless of the chosen θ in Eq. (3.132), for $c_\mathrm{s} \ll c_\mathrm{A}$, we have $c_\mathrm{ms} \approx c_\mathrm{A} = 1$ (i.e. c_ms very weakly depends on p) , and for simulations with $p \leq 0.1$, indeed the TM growth rate almost does not depend on pressure. Secondly, for $c_\mathrm{s} \gg c_\mathrm{A}$, $c_\mathrm{ms} \approx c_\mathrm{s} \propto \sqrt{p}$, and in this regime, the growth rate is proportional to pressure. To the growth rates from the simulations with $p \geq 20$, we performed the *asymptotic fit*

$$\ln(\gamma) = s\ln(p) + d \tag{3.134}$$

and obtained the following estimators

$$\begin{aligned} s &= 0.207 \pm 0.001, \\ d &= -4.8465 \pm 0.0044. \end{aligned} \tag{3.135}$$

The fitting straight line is marked with red in the figure.

corresponds to resolutions 224×224 to 1024×1024 zones for the whole box (abscissa in Fig. 3.28).

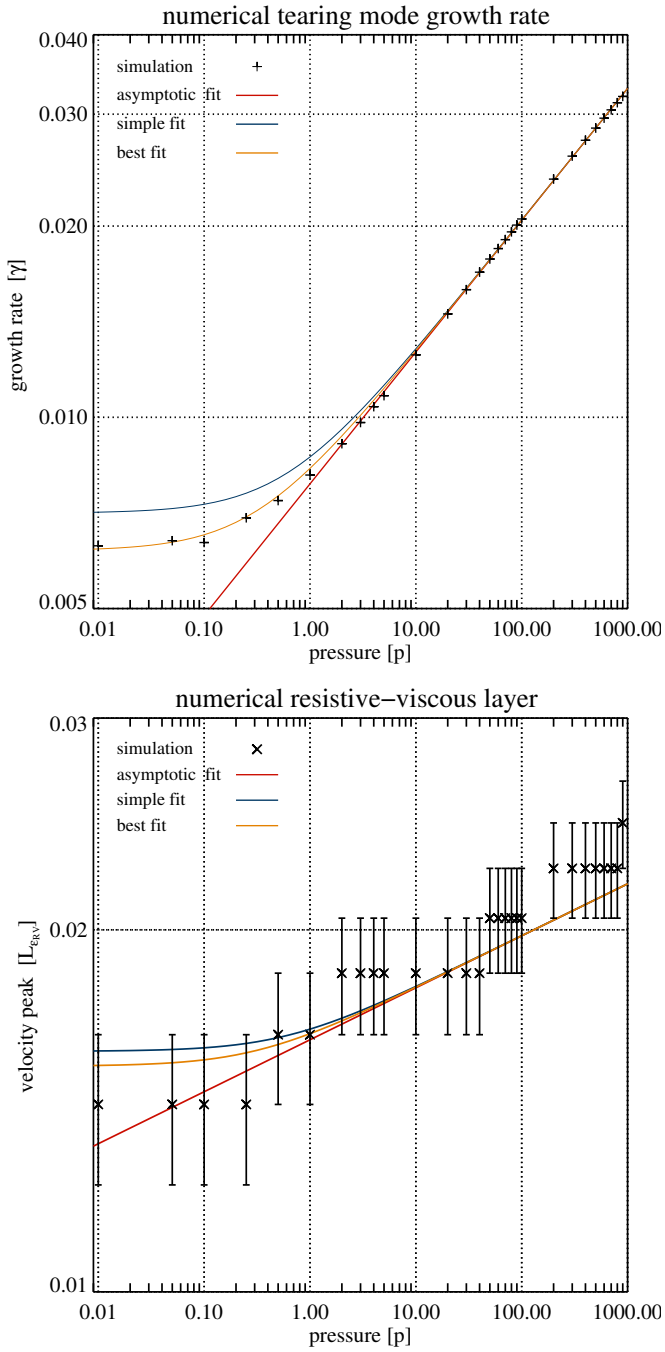

Figure 3.31: *Top panel:* Growth rate of tearing modes driven by numerical resistivity as a function of pressure. Results of simulations run with a resolution of 512×512 zones and the MP5 reconstruction scheme are marked with black plus signs. The growth rate (proportional to numerical resistivity) increases with pressure. Hence, the system's characteristic velocity must be pressure dependent. The red, blue and orange curves result from the *asymptotic*, *simple* and *best fit*, respectively (for details, see main text). *Bottom panel:* Resistive-viscous layer width (black crosses) as a function of pressure in the simulations presented in the upper panel. The red, blue and orange curves mark expected layer widths given the numerical resistivity resulting from the the *asymptotic*, *simple* and *best fit*, respectively, which were performed to the growth rates presented in the upper panel.

We must not forget that for the tearing modes, the characteristic velocity $\mathcal{V}$ changes the numerical resistivity not only directly, i.e. via Eq. (3.5), but also through the implicit dependence of η_* on the resistive viscous layer (Eq. (3.125)). Taking these two facts into account we arrive at

$$\gamma \propto \mathcal{V}^{24/(25+5r)} b_0^{(10r+2)/(25+5r)}. \tag{3.136}$$

By combining Eqs. (3.134) and (3.136), and putting $c_{\mathrm{ms}} \propto \sqrt{p}$ we obtain

$$s = \frac{12}{25+5r}. \tag{3.137}$$

From this equation, we estimated the order of the MP5 reconstruction scheme to be $r = 6.59 \pm 0.05$, which is a higher value than both theoretically expected and determined in the resolution studies ($r = 4.814 \pm 0.085$, see Table 3.12).[32] For lower pressure values ($p < 20$), the approximation $c_{\mathrm{ms}} \approx c_{\mathrm{s}}$ is no longer valid and the magnetic contributions become important in Eq. (3.133). We took it into account in the *simple fit* (blue curve in Fig. 3.31). We took the values of s and d from Eq. (3.135) and additionally put $\mathcal{V} = c_{\mathrm{ms}} = \sqrt{c_{\mathrm{A}}^2 + c_{\mathrm{s}}^2}$ for the characteristic velocity. As expected, for high pressure values, we obtain the same predictions as from the simple fit. For $p < 10$, the curve overestimated the growth rate values. This fact can be easily explained. Firstly, we used $b_0 = 1$ to compute the magnetosonic speed. However, around the shear, where numerical resistivity is most important, $b_0 \to 0$. It is impossible to tell *a priori* which value of b_0 should be taken. Secondly, we used Eq. (3.133), instead of a somehow averaged version of Eq. (3.132), to compute the characteristic velocity. To fit the simulation data even better, we varied the value of b_0 in Eq. (3.133). For $b_0 \approx 0.72$, we obtained the *best fit* (orange curve in Fig. 3.31). As we can see, all simulation results lie close to this curve. The value $b_0 \approx 0.72$ also seems quite reasonable. We conclude that the characteristic velocity for the tearing modes is the fast magnetosonic speed. In the bottom panel of Fig. 3.31, we plot the measured width of the resistive-viscous layer and also the theoretical predictions based on the asymptotic, simple and best fit. As we can see, all three of them agree with the simulation results within the measurement errors. This demonstrates that on the one hand our model is self-consistent. On the other hand the predictions based only on the resistive-viscous layer measurements are quite inaccurate, as they cannot distinguish between the fits.

Another set of simulations was run to reconfirm that the Alfvén speed is not the characteristic velocity. We used the standard parameters ($\delta = 10, k = 3, p_0 = \rho_0 = 1, \nu = 10^{-4}$), no resistivity and the MP9 reconstruction scheme. The simulation domain was resolved with 256×256 zones. The background magnetic field b_0 was in the range 1–10. To the measured growth rates, we fitted the function

$$\ln(\gamma) = s \ln(b_0) + d \tag{3.138}$$

[32] There are a few possible reasons of this discrepancy. First of all, in the derivation of Eq. (3.137), we assumed that numerical resistivity can be treated like a physical one and therefore Eqs. (3.117), (3.124) and (3.125) are exactly fulfilled. However, this may not always be the case, yet we did not write (and we do not know) how many uncertainties these equations could introduce. The error ± 0.05 results only from the final statistical fit to the simulation results and does not take the above mentioned problem into account. Second of all, the concept of the characteristic velocity may not always work in 100% correctly, either. In simulations with $c_{\mathrm{s}} \gg c_{\mathrm{A}}$, the characteristic velocity, i.e. c_{ms}, is mainly determined by the sound speed ($c_{\mathrm{ms}} \approx c_{\mathrm{s}}$), whereas tearing modes themselves are an MHD instability, in which the Alfvén speed plays a crucial role. Therefore, we could intuitively think that "pressure related errors" should be somewhat less important than "magnetic field related errors" in this problem. Consequently, the magnetosonic speed could influence numerical resistivity less than expected from the characteristic velocity concept. Moreover, it is also hard to imagine a more complicated and possibly more unreliable method to determine a reconstruction scheme order than the one based on Eq. (3.137). All in all, we do not think that this discrepancy of 1.5 accuracy orders (i.e. $r = 6.59 \pm 0.05$ instead of $r \approx 5$) is a failure of our ansatz (3.5).

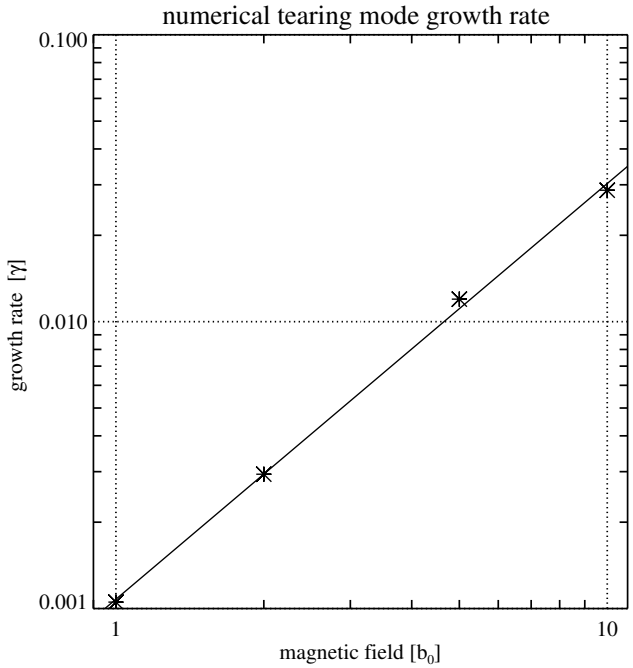

Figure 3.32: Growth rate of tearing modes driven by numerical resistivity as a function of background magnetic field. The results of simulations run with a resolution of 256×256 zones and the MP9 reconstruction scheme are marked with black plus signs. The straight line results from a linear fit to the logarithm of the growth rate.

and obtained the following estimators

$$\begin{aligned} s &= 1.45 \pm 0.04, \\ d &= -6.83 \pm 0.56. \end{aligned} \tag{3.139}$$

We interpret these results (see Fig. 3.32) testing the two hypothesis that the characteristic velocity is either equal to the Alfvén speed or independent of the background magnetic field.[33] According to the first hypothesis, from Eq. (3.136), we obtain

$$\gamma \propto \mathcal{V}^{24/(25+5r)} b_0^{(10r+2)/(25+5r)} \propto b_0^{(10r+26)/(25+5r)}. \tag{3.140}$$

Combining Eqs. (3.139) and (3.140), we determine the order of the MP9 scheme

$$s \stackrel{?}{=} \frac{26+10r}{25+5r}. \tag{3.141}$$

Hence, $r = 3.73 \pm 0.62$. The discrepancy between this value and the order of the MP9 reconstruction scheme determined in the resolution studies ($r = 7.55 \pm 0.55$; see Table 3.12), is too big and we can discard the first hypothesis. Given the second hypothesis, we have

$$\gamma \propto \mathcal{V}^{24/(25+5r)} b_0^{(10r+2)/(25+5r)} \propto b_0^{(10r+2)/(25+5r)} \tag{3.142}$$

and

$$s \stackrel{?}{=} \frac{10r+2}{25+5r}. \tag{3.143}$$

[33] Since these simulations are in the range, where $c_A \approx c_s$, it is impossible to draw any conclusion about the magnetosonic speed. Assuming that $\mathcal{V} = c_{ms}$, equation $\gamma \propto b_0^{\alpha}$, where α is a certain power, is simply invalid.

From this equation, we compute that $r = 12.4 \pm 1.2$, which once again contradicts our previous result. Therefore, we conclude that in the simulated regime, the characteristic velocity must depend on the magnetic field but not linearly as it is for the Alfvén speed, which once again indirectly hints that the magnetosonic speed is the characteristic one.

3.5 Summary and conclusions

We demonstrated that our ansatzes (3.1), (3.4) and (3.5) for the code's numerical dissipation work both for wave damping and tearing mode simulations. Everything worked for the former ones as expected. The system's characteristic length and velocity were the wavelength and the wavespeed, respectively. The orders of the reconstruction and time integration schemes were close to their theoretical values. Both temporal and spatial discretisation errors contribute to the numerical dissipation. The only surprise was that the numerical resistivity was much lower than the numerical viscosity. In other words, the numerical magnetic Prandtl number, $P_{\mathrm{m}*} \equiv \nu_*/\eta_*$, was not close to 1, as it is commonly suspected in the numerical community.[34] Unfortunately, it was impossible to measure precisely the numerical resistivity in magnetosonic wave simulations.

In the tearing mode simulations, the situation was not so obvious. It is hard to imagine a simpler, yet interesting MHD system. Still, its analysis was full of pitfalls. In order to use ansatz (3.5) for the numerical resistivity, the system's characteristic velocity and length needed to be identified. The "natural candidates", namely the Alfvén speed and the magnetic shear width turned out not to be the system's characteristic quantities. Their proper identification required a good understanding of tearing mode theory, especially of the concept of the resistive-viscous layer. However, not for every physical problem, such a theory will be at our disposal. Hence, a correct determination of a system's characteristic length may not always be straightforward. When it comes to the characteristic velocity, the situation seems to be simpler. Note that the fast magnetosonic speed in the absence of a magnetic field reduces to the sound speed. Thus, in all simulations discussed in this chapter, the characteristic velocity is equal to the magnetosonic speed.

Another issue concerns the discrepancy among the orders of the reconstruction schemes determined in the wave damping and tearing mode simulations (compare Tables 3.1, 3.5 and 3.9 with Table 3.12). In the former ones, the reconstruction schemes had their theoretical order, whereas in the latter ones, the schemes experienced an accuracy reduction. We think we can give a plausible explanation of this phenomenon. All schemes reconstruct a function from its zone averaged values using a Taylor expansion. For a scheme of r-th order, a reconstructed function, $\hat{f}(x_{i+1/2})$, is equal to its exact value, i.e. $f(x_{i+1/2})$, up to terms of r-th order, i.e.

$$|\hat{f}(x_{i+1/2}) - f(x_{i+1/2})| \sim |(\partial_x^r f(x_{i+1/2}))(\Delta x)^r + O((\Delta x)^{r+1})|, \tag{3.144}$$

where Δx is the zone width. Usually, because $(\Delta x)^r$ is small, the difference between the exact and reconstructed value is small, i.e.

$$\left| \frac{\hat{f}(x_{i+1/2}) - f(x_{i+1/2})}{f(x_{i+1/2})} \right| \ll 1. \tag{3.145}$$

This holds for functions, which do not have any singularities, like, e.g. any wave solution. However, this is not the case for tearing modes, where the y component of the velocity perturbations

[34] Private communication with Pablo Cerdá-Durán, Ewald Müller, Martin Obergauliner and Maxime Viallet.

experiences strong variations in the vicinity of the magnetic field shear, i.e. for $|\delta y| \ll 1$ (see, e.g. bottom left panel of Fig. 3.26). Especially in the ideal MHD limit, this function would behave like $v_y \propto 1/y$ for $|\delta y| \ll 1$ and would have a singularity at $y = 0$ (see Eq. (3.61); because of that, tearing modes were not allowed in ideal MHD and only resistivity could smooth (and remove) this singularity). Therefore, the difference between the exact value of $v_y(y)$ and its reconstructed value $\hat{v}_y(y)$ could behave like

$$|\hat{v}_y(y) - v_y(y)| \sim \left| \left(\frac{\partial^r}{\partial y^r} \frac{1}{y} \right) (\Delta y)^r \right| \sim \left| \frac{1}{y^{r+1}} (\Delta y)^{r+1} \right|, \tag{3.146}$$

which diverges for $y \to 0$. Consequently, the standard argument that "higher order terms in the Taylor expansion can be neglected" does not apply in this case. From the the above equation, we see why errors introduced by reconstruction schemes would not necessarily scale like $(\Delta y)^r$. Moreover, it may even seem surprising that these errors did not diverge for $y \approx 0$ leading either to a code crash or completely unphysical solutions. For lower order reconstruction schemes, i.e. the MP3 and the piecewise-linear, we did observe such pathological behaviour. One could say at this point that our tearing mode simulations disproved that ansatzes (3.1), (3.4) and (3.5) can be universally used to estimate the numerical dissipation in any MHD simulation. Ideally, we would like to have an expression, say for numerical resistivity (Eq. (3.5)), which after determining the coefficients $\mathfrak{N}_\eta^{\Delta x}$ and $\mathfrak{N}_\eta^{\Delta x}$, and the scheme orders r and q in one type of simulations, can be universally applied in any other MHD simulation. However, the orders of the MP7 and the MP9 reconstruction schemes, r, were lower in tearing mode simulations than in wave damping tests, which suggests that ansatzes (3.1), (3.4) and (3.5) are always problem dependent. To some extent, it is true. In the limit $\Delta x \to 0$, estimates of, say, the numerical dissipation introduced by the MP9 reconstruction scheme will differ by many orders of magnitude, depending whether the calibration was done with the help of (e.g. magnetosonic) wave damping tests or tearing mode simulations (because of different estimators of the scheme's order, $r = 8.82\pm$ and $r = 7.56 \pm 0.55$, respectively; see Tables 3.9 and 3.12). Nonetheless, we should also compare how much the predictions of these ansatzes, depending on the chosen calibration simulations, differ in an interesting, from the numerical point of view, parameter regime. We should consider how many zones we use in a typical MHD simulation to resolve a characteristic length. Five zones is probably the minimum "reasonable" number and it is unlikely that we will be able to use more 100 zones in multidimensional simulations (assuming that the characteristic length is considerably smaller than the box length).

In Fig. 3.33, we present a comparison of the expected numerical dissipation in magnetosonic (MS) wave damping simulations and tearing mode (TM) simulations, based on ansatzes (3.1), (3.4) and (3.5), and the estimators from Tables 3.9 and 3.12, respectively, given that the characteristic velocities and lengths are equal to one, i.e. $\mathcal{V} = \mathcal{L} = 1$. The box length is set to 1, hence "resolution" in the abscissa of this figure refers to the number of zones per characteristic length. 100 zones per resistive viscous-layer would roughly correspond to $\sim 10^4$ zones in y direction in a typical tearing mode simulation from Sec. 3.4.2. As we can see, the expected numerical dissipation based on calibration with the help of both types of simulations (MS waves and TM) is surprisingly similar. At this point, we would like make three comments. Firstly, whereas the characteristic length in a wave damping simulation is obviously the wavelength, the choice for tearing mode simulations is not as straightforward. Secondly, we should bear in mind that in Fig. 3.33, we basically compare numerical viscosity in wave damping simulations with numerical resistivity in tearing mode simulations. Therefore, we find a "good agreement" between two physically different quantities. Moreover, numerical resistivity seems to be much lower than numerical viscosity in wave damping simulations. As for tearing mode simulations, because of the restriction

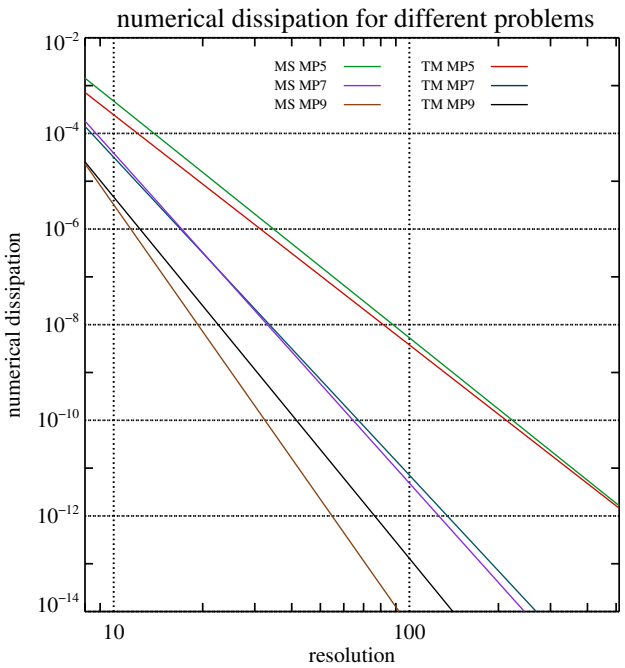

Figure 3.33: Comparison of the code's dissipation for two different physical problems: magnetosonic waves (MS) and tearing modes (TM). Numerical dissipation equals $(4/3)\nu_* + \xi_* + \eta_*/(1 + c_s^2/c_A^2)$ for the former ones and η_* for the latter ones. For the wave simulations, we determined that $\eta_*/(1+c_s^2/c_A^2) \ll (4/3)\nu_* + \xi_*$ (see Sec. 3.3.3). The MP5, the MP7 and the MP9 reconstruction schemes were used in both the MS wave damping (green, violet and brown curve, respectively) and in the TM simulations (red, blue and black curves, respectively). In the former and in the latter simulations, the HLL and the LF Riemann solvers were used, respectively. For the wave problems, both solvers introduce very similar dissipation, whereas for the TM simulations $\eta_*(\mathrm{HLL}) \ll \eta_*(\mathrm{LF})$. The CFL factor was chosen so that the errors of the time integration, performed with RK3, were negligible. The results are renormalised to the characteristic velocity and length equal one, i.e. $\mathcal{V} = \mathcal{L} = 1$.

on the Prandtl number (for the semi-analytical equations to be valid), i.e. $0.1\eta < \nu$, and the very weak dependence of the tearing mode growth rate on viscosity, i.e. $\gamma \propto \eta^{-1/5}$ (see Eq. (3.113)), we did not manage to determine the numerical viscosity in a reliable way.[35] Thirdly, the values of the numerical resistivity in the tearing mode simulations were obtained only for the LF Riemann solver. The other Riemann solvers (i.e. HLL and HLLD) had a much lower numerical resistivity. In wave damping simulations, all solvers had comparable numerical viscosity.

Readers interested in using our ansatzes (3.1), (3.4) and (3.5) to estimate the numerical dissipation of their MHD code, may feel confused at this moment. They may not know which tests should they use to calibrate these equations. As a rule of a thumb, we would recommend performing some wave damping tests, and for higher order schemes ($r > 5$), just subtract "by hand' one or two orders of magnitudes from the final estimator of r. We do believe that it is better to overestimate rather than underestimate numerical dissipation. We do not recommend using tearing

[35] Although, we did see its influence on the tearing mode growth rate. However, technical difficulties in designing suitable (and reliable) simulations and the measurement uncertainties were rather discouraging and we decided not to present these results. From these studies, it seems that numerical resistivity and viscosity are of the same order, however we do not have a sound statistical proof of this statement.

mode simulations for a “quick” calibration, because of their higher computational costs and more complicated implementation.

Chapter 4

Magnetorotational instability

4.1 Introduction

The magnetorotational instability (MRI) was first studied by Velikhov (1959) and Chandrasekhar (1960). However, it was only Balbus & Hawley (1991), who pointed out its importance for accretion disc physics. Already Shakura & Syunyaev (1973) suspected MHD turbulence to be the agent transporting angular momentum outwards, which is necessary for an efficient gas accretion onto a central (compact) object. However, the physical mechanism exciting the turbulence remained unknown. Balbus and Hawley identified the MRI as the most promising candidate. Ever since their pioneering work, the MRI has been an active field of research. Even though the instability has been studied for over twenty years, there are still many unanswered question regarding its nature (e.g. the saturation level of the instability, MRI driven turbulence and transport in accretion discs, influence of resistivity and viscosity, connection to disc dynamos, interplay with radiative transfer, convergence of numerical simulations).

The MRI can also possibly play an important role in certain core-collapse supernovae. Akiyama et al. (2003) pointed out that the magnetic field of an initially rotating progenitor, could be amplified by the MRI in the post-bounce phase of the supernova explosion.[1] Obergaulinger et al. (2009) confirmed this hypothesis by means of local numerical simulations. Their studies suggest that progenitor's magnetic field could be amplified to dynamically relevant values, i.e. of order 10^{15}G. However, because of limited computational resources, these authors used initial magnetic fields, which were a few orders of magnitude stronger than expected from stellar evolution models (Heger et al. 2005).[2] Moreover, even though the simulations of Obergaulinger et al. (2009) were done in the ideal MHD approximation, they must have been affected by numerical resistivity and viscosity, the consequences of the enhanced initial magnetic field and of the numerical dissipation on the results remaining unknown.

In this chapter, we investigate this problem with the help of an MRI termination model proposed and developed by Goodman, Xu and Pessah (later denoted as GXP) (Goodman & Xu (1994), Pessah & Goodman (2009), Pessah (2010)). GXP suggested that the initial exponential growth phase, in which MRI channels form, can be terminated by parasitic instabilities, i.e. the Kelvin-

[1] The supernova physics was discussed in more detail in Chapter 1.

[2] To put it in a nutshell, the greater the initial magnetic field strength, the larger the MRI structures form. Hence, in simulations with artificially enhanced initial magnetic fields, lower resolutions could be used. For an extended discussion, see also Sec. 4.5.1.

Helmholtz or tearing mode instability. We verify this hypothesis by means of 2D and 3D resistive-viscous MHD simulations.

In the next section, we explain the basic concepts of the MRI and give a criterion for its onset. In Section 4.3, we describe the Kelvin-Helmholtz instability and the tearing modes. In Section 4.4, we discuss Goodman, Xu and Pessah's MRI termination model, describing its assumption and pointing out some inconsistencies. We also propose an alternative description of the termination process, which is free from the GXP model's flaws. In Section 4.5, we present our 2D and 3D MRI simulation results and verify a modified GXP model. Finally, in Section 4.6, we discuss the implications of our findings for core-collapse supernovae.

4.2 The MRI exponential growth phase

Consider a differentially rotating fluid with velocity $\mathbf{v} = \Omega r\hat{\phi}$, whose angular velocity is given by

$$\Omega = \Omega_0 \left(\frac{r}{r_0}\right)^{\alpha}, \tag{4.1}$$

where Ω_0 is the angular velocity given at the radius, r_0, and α is a dimensionless parameter. The resulting centrifugal force has to be balanced by some additional forces, like gravity or pressure gradients, to provide an equilibrium. The corresponding local rotational shear, defined as

$$q = -\frac{\mathrm{d}\ln(\Omega)}{\mathrm{d}\ln(r)}, \tag{4.2}$$

reads

$$q = -\alpha. \tag{4.3}$$

The rotational profile (4.1) is quite generic in astrophysical system, e.g. for $\alpha = -3/2$, we recover a Keplerian profile (which is encountered in accretion discs) and for differentially rotating stars, $-3/2 < \alpha < 0$ (although in the case of the stars, this rotational profile is not a law of nature, but rather a convenient approximation).

In the absence of magnetic fields, a system with the rotational profile (4.1), is unstable against the *Rayleigh instability*, if the specific angular momentum of the flow, $j = \Omega r^2$, decreases with radius, i.e. for

$$\partial_r j < 0 \qquad \text{(instability)} \tag{4.4}$$

(hence for $\alpha < -2$). To understand this criterion, we consider the following Gedankenexperiment. Imagine that we perturb a fluid element of specific angular momentum j_0 from its initial orbit at r_0 to a new position $r_1 > r_0$ (where surrounding elements have less specific angular momentum). In the absence of forces which are able to redistribute the angular momentum (like, e.g. viscous or magnetic forces), the perturbed fluid element will retain its specific angular momentum. This means that at its new position, the fluid element will experience an excess centrifugal force and it will be pushed even further outwards. Consequently, the fluid element will run away from its initial orbit to infinity. Similarly, a fluid element perturbed slightly inwards to $r_1 < r_0$ will eventually fall onto the centre (to $r = 0$).

Since in differentially rotating stars and accretion discs, the specific angular momentum increases with radius, i.e.

$$\partial_r j > 0, \tag{4.5}$$

these systems are stable against the Rayleigh instability. A fluid element perturbed outwards (to $r_1 > r_0$) will not rotate fast enough at its new position and the excess gravitational force will start pulling it back inwards. When the fluid element returns to its initial orbit at r_0, it will have a non-zero (negative) radial velocity and hence it will continue to fall inwards until an excess centrifugal force will stop it at some radius $r_2 < r_0$ and then push it back outwards. As a results, the fluid element will oscillate around its initial orbit with an *epicyclic frequency*,

$$\kappa^2 = \frac{1}{r^3}\partial_r(r^2\Omega)^2, \tag{4.6}$$

which for the angular velocity profile (4.1) reads

$$\kappa = \sqrt{2(2+\alpha)}\Omega. \tag{4.7}$$

Accretion discs are stable against this purely hydrodynamical instability. However, the situation dramatically changes in the presence of even a very weak magnetic field. Balbus & Hawley (1991) found in their pioneering paper that such a system can be unstable against the magnetorotational instability (MRI). These authors considered an axisymmetric accretion disc of a finite vertical extent threaded by a vertical magnetic field, $\mathbf{b} = (0,0,b_{0z})$, whose dynamical equation read[3]

$$\frac{1}{\rho}(\partial_t + \mathbf{v}\cdot\nabla)\rho + \nabla\cdot\mathbf{v} = 0, \tag{4.8}$$

$$(\partial_t + \mathbf{v}\cdot\nabla)\mathbf{v} + \frac{1}{\rho}\nabla\left(p + \frac{b^2}{2}\right) - \frac{1}{\rho}(\mathbf{b}\cdot\nabla)\mathbf{b} + \nabla\varphi = 0, \tag{4.9}$$

$$\partial_t\mathbf{b} - \nabla\times(\mathbf{v}\times\mathbf{b}) = 0. \tag{4.10}$$

To investigate the stability of the system, Balbus & Hawley used a standard WKB ansatz for axisymmetric perturbations, whose dependence was of the form $e^{i(k_r r + k_z z - \omega t)}$ (we used the same technique to calculate the tearing mode growth rate in Chapter 3; see Eqs. (3.52) and (3.53)), in the Boussinesq approximation ($\nabla\cdot\mathbf{v} = 0$). These authors found that, independent of the initial magnetic field strength, the system is unstable against the MRI if its angular velocity decreases with radius, i.e. for

$$\partial_r\Omega^2 < 0 \qquad \text{(instability)}, \tag{4.11}$$

which is the case both for accretion discs and differentially rotating (proto-neutron) stars. Rather than deriving this instability criterion (the details can be found in Balbus & Hawley (1991)), we will just give an intuitive explanation of the MRI mechanism. To understand why even a weak magnetic field can change the dynamics of the system, we must first recall two facts from ideal MHD. Firstly, one of the consequences of the induction equation (2.23) is that a magnetic field flux is "frozen in" a fluid element, i.e. they are always co-moving. Secondly, magnetic field "does not like to be curved" - if it is bent, there will act on it a restoring (Lorenz) force (also called *magnetic field tension* in such a situation), trying to make the magnetic field line (again) "as straight as possible". Armed with this knowledge, we are ready to analyse what will happen with a fluid element perturbed from its initial position r_0 to $r_1 > r_0$ in a magnetised accretion disc. Since the magnetic field (line) is frozen in the fluid element, it will be stretched (hence, a non-zero b_r component will be created), and consequently it will try restore the fluid element to its initial

[3]The set of equations is completed with the entropy equation for adiabatic perturbations in the Boussinesq approximation.

position (to resist stretching) and at the same time it will try to enforce rigid rotation (to resist shearing). The former is clearly stabilising. The latter is at the heart of the MRI. Had it not for the magnetic field, the angular velocity of the fluid element would decrease at the new position, $r_1 > r_0$ (because of angular momentum conservation). However, this would create a shear, i.e. stretch the field line in the azimuthal direction (and produce a component b_ϕ). The magnetic field tries to counteract it by transferring some angular momentum (from other fluid elements connected by this line), to the displaced fluid element, so that the whole field line has a constant angular velocity Ω_0. However, now the fluid element will rotate faster (than other fluid elements at the position r_1) and experience an excess centrifugal force, which will push it further outwards. The magnetic field will once again try to enforce rigid rotation, and the fluid element will be driven by the excess centrifugal force even more outwards. The same considerations hold for a fluid element perturbed inwards to $r_2 < r_0$. This time, the magnetic field will drain angular momentum from the fluid element, which will consequently start falling towards the centre (to orbits with even smaller radii). When we consider these two fluids elements (one escaping from the accretion disc, and the other one falling to the centre) simultaneously, we see that the magnetic field (in the MRI) is an agent transferring angular momentum between them (outwards).

As we already wrote, systems in which condition (4.11) is met are MRI unstable, independent of the initial vertical magnetic field strength, however not for any perturbation wavelength. If the restoring force (the one resisting stretching), which is proportional the amplitude of and the curvature of the magnetic field, is strong enough, the fluid element will be pulled back to its initial position and the MRI will be suppressed. This means that there should exist a critical perturbation wavelength below which the system is stable against the MRI. This heuristic argumentation is confirmed by the calculations done by Balbus & Hawley (1991), who showed that only modes with wavevectors larger than a critical value

$$(k_z)^2_{\mathrm{crit}} = \frac{1}{2c^2_{\mathrm{A}z}} \left\{ \left[\left(N^2 + \frac{\mathrm{d}\Omega^2}{\mathrm{d}\ln R} \right)^2 - 4N_z^2 \frac{\mathrm{d}\Omega^2}{\mathrm{d}\ln R} \right]^{1/2} - \left[N^2 + \frac{\mathrm{d}\Omega^2}{\mathrm{d}\ln R} \right] \right\}, \tag{4.12}$$

are MRI unstable, where

$$c_{\mathrm{A}z} = \frac{b_{0z}}{\sqrt{\rho}} \tag{4.13}$$

is the Alfvén speed in the z direction and

$$N^2 = -\frac{1}{\Gamma\rho}(\nabla p)\cdot(\nabla \ln P\rho^{-\Gamma}) = N_r^2 + N_z^2, \quad \text{with} \tag{4.14}$$

$$N_i^2 = -\frac{1}{\Gamma\rho}(\nabla_i p)\cdot(\nabla_i \ln P\rho^{-\Gamma}), \quad i \in \{r,z\} \tag{4.15}$$

is the *Brunt-Väisälä* or *buoyancy frequency*,[4] and Γ is the adiabatic index. Even though, formally all wavevectors $|k| > |k_{\mathrm{crit}}|$ are unstable, the MRI growth rate goes to zero for very long modes, i.e. $\gamma_{\mathrm{mri}} \to 0$, for $|k| \to \infty$. Given rotational profile (4.1), the MRI has a maximum growth rate[5] (see, e.g. Pessah & Chan (2008))

$$\gamma_{\mathrm{MRI}} = -\frac{\alpha}{2}\Omega, \tag{4.16}$$

[4] In a convectively stable system, a perturbed fluid element will oscillate with a frequency $N^2 > 0$. In a convectively unstable system $N^2 < 0$.

[5] $\gamma_{\mathrm{MRI}} = -i\omega$, for the WBK ansatz used by Balbus & Hawley, i.e. $e^{i(k_r r + k_z z - \omega t)}$.

for the wavevector

$$k_{\mathrm{MRI}} = \sqrt{1 - \frac{(2+\alpha)^2}{4}}\Omega\frac{\sqrt{\rho}}{b_{0z}} = \sqrt{1 - \frac{(2+\alpha)^2}{4}}\frac{\Omega}{c_{\mathrm{A}z}}. \tag{4.17}$$

Note that we use capital letters in the subscripts to distinguish the fastest growing mode (with a growth rate and wavevector γ_{MRI} and k_{MRI}, respectively) from the other modes developing at a lower rate, i.e. $\gamma_{\mathrm{mri}}(k_{\mathrm{mri}}) < \gamma_{\mathrm{MRI}}$.

Imposing perturbations with a wavevector k_{mri}, Balbus & Hawley (1991) showed that for linearised MHD equations coherent *MRI channels* will emerge:

$$\mathbf{v}_{\mathrm{c}} = v_{\mathrm{c}}(t)(\hat{\mathbf{r}}\cos\phi_v + \hat{\boldsymbol{\phi}}\sin\phi_v)\sin(k_{\mathrm{mri}}z) = \tilde{v}_{\mathrm{c}}(\hat{\mathbf{r}}\cos\phi_v + \hat{\boldsymbol{\phi}}\sin\phi_v)\sin(k_{\mathrm{mri}}z)e^{\gamma_{\mathrm{mri}}t}, \tag{4.18}$$

$$\mathbf{b}_{\mathrm{c}} = b_{\mathrm{c}}(t)(\hat{\mathbf{r}}\cos\phi_b + \hat{\boldsymbol{\phi}}\sin\phi_b)\cos(k_{\mathrm{mri}}z) = \tilde{b}_{\mathrm{c}}(\hat{\mathbf{r}}\cos\phi_b + \hat{\boldsymbol{\phi}}\sin\phi_b)\cos(k_{\mathrm{mri}}z)e^{\gamma_{\mathrm{mri}}t}, \tag{4.19}$$

where the subscript c stands for *channel*, $\tilde{v}_{\mathrm{c}}$ and $\tilde{b}_{\mathrm{c}}$ are the initial amplitudes, ϕ_v and ϕ_b are the angles between the r axis and, respectively, the velocity and magnetic field channels (in ideal MHD, $\phi_v = \pi/4$ and $\phi_b = 3\pi/4$; see, e.g. Pessah & Chan (2008)). In ideal MHD, the magnetic field and velocity amplitudes are related by

$$v_{\mathrm{c}} = \sqrt{\frac{-\alpha}{4+\alpha}}\frac{b_{\mathrm{c}}}{\sqrt{\rho}} = \sqrt{\frac{-\alpha}{4+\alpha}}c_{\mathrm{Ac}}. \tag{4.20}$$

Goodman & Xu (1994) showed that the MRI channels not only fulfil linearised MHD equations, but also are an exact solution of non-linear ideal MHD equations in the incompressible limit in the *shearing sheet* (local) approximation. This approximation consists in transforming to a frame co-rotating with a fiducial fluid element and linearising the rotational profile around a radius r_0, i.e. $\Omega(r) \approx (r-r_0)\partial_r\Omega(r)_{|r_0}$. In this frame, gravitational and centrifugal force cancel out, but the Coriolis force hast to be taken into account. Hence, in the first stage of the MRI, i.e. the *exponential growth phase*, the equations for velocity and magnetic field, in the shearing sheet approximation, read

$$\mathbf{v} = -q\Omega_0(r-r_0)\hat{\boldsymbol{\phi}} + \mathbf{v}_{\mathrm{c}}, \tag{4.21}$$

$$\mathbf{b} = b_{0z}\hat{\mathbf{z}} + \mathbf{b}_{\mathrm{c}}, \tag{4.22}$$

where $\mathbf{v}_{\mathrm{c}}$ and $\mathbf{b}_{\mathrm{c}}$ are given by Eqs. (4.18) and (4.19), respectively, and q was defined in Eq. (4.2).

Obviously, the MRI channels cannot grow indefinitely, because the energy stored in them would constantly increase. Since the total energy of the system is finite, there must be a physical mechanism terminating MRI growth. GXP put forward a hypothesis that MRI channels can be disrupted by *parasitic* (or *secondary*) *instabilities* growing on top of them, i.e. by Kelvin-Helmholtz instability the tearing modes.

We briefly describe these secondary instabilities in Sec. 4.3 and discuss the GXP termination model in Sec. 4.4.

Magnetorotational instability in core-collapse supernovae

Since Akiyama et al. (2003) pointed out that the matter of rotating proto-neutron stars can be unstable against the MRI, this instability has attracted the attention of the supernova community. The MRI in core-collapse supernovae can be influenced by additional effects like thermal stratification

or viscosity (caused by neutrinos). Moreover, the instability analysis can no longer be restricted to the equatorial plane. Balbus (1995) added a thermal stratification to the MRI analysis and Menou et al. (2004) additionally included viscosity and resistivity, obtaining a complicated dispersion relation. Obergaulinger et al. (2009) discussed the instability criterion in core-collapse supernovae for any orientation of the perturbation wavevector. We restrict our analysis to the equatorial plane and vertical perturbation wavevectors (for which the MRI is known to develop fastest; see, e.g. Balbus & Hawley (1998)). Under these assumptions, the instability criterion reads (ignoring the dissipative effects):

$$N^2 + \frac{1}{r^3}\partial_r\Omega^2 < 0 \quad \text{(instability)}, \quad \text{or}$$
$$(-\partial_z p)\left[\partial_r\Omega^2\partial_z \ln(p\rho^{-\Gamma}) - \partial_z\Omega^2\partial_r \ln(P\rho^{-\Gamma})\right] < 0 \quad \text{(instability)}. \tag{4.23}$$

There are a few limiting cases, which are worth mentioning. In a system of constant entropy, this criterion reduces to the Balbus-Hawley criterion (Balbus & Hawley (1991)), which we discussed above. Positive entropy gradients in a system can stabilise it against the MRI. In a convectively unstable system (i.e. with negative entropy gradients) *magneto-buoyant* or *magneto-convective* instabilities can develop. The former resembles the MRI, however the instability is not driven by the angular velocity shear but an unstable stratification. The latter is a convective instability in a magnetised flow, where modes of short wavelengths can be stabilised by magnetic field tension. Obergaulinger et al. (2009) identified these regimes (and additional mixed regimes, in which two types of the above mentioned instabilities can be present simultaneously) in their numerical simulations.

The last issue, which needs to be discussed is the influence of viscosity and resistivity on the MRI. In this thesis, we are going to analyse only initial models with a constant entropy. In this case, the dispersion relation of Menou et al. (2004) reduces to the one analysed by Pessah & Chan (2008), which was obtained in the shearing sheet approximation in resistive-viscous MHD. The corresponding dispersion relation of Pessah & Chan (2008) is still quite complicated (for the details, see their paper). For the Reynolds numbers, defined as

$$R_\mathrm{e} = \frac{c_{\mathrm{A}z}^2}{\nu\Omega} \tag{4.24}$$
$$R_\mathrm{m} = \frac{c_{\mathrm{A}z}^2}{\mu\Omega}, \tag{4.25}$$

which we use in the simulations (i.e. $R_\mathrm{e}, R_\mathrm{m} > 10$), the corrections to the MRI unstable modes (their growth rates and the wavelength of the fastest growing mode) are small ($\approx 10\%$). Therefore, we do not discuss the results of Pessah & Chan (2008) here, but rather summarise them in Appendix B. To put it in a nutshell, resistivity and viscosity decrease the MRI growth rate (the smaller the perturbation wavelength, the larger the effect), its maximum being shifted towards longer modes (the larger the dissipation the larger the shift). Moreover, the angles ϕ_v and ϕ_b (defined in Eqs. (4.18) and (4.19)), which, the velocity and magnetic field channels, respectively, form with the r axis depend on resistivity and viscosity. In general, resistivity has a stronger influence on the MRI modes. For Reynolds numbers, which are encountered in core-collapse supernovae (i.e. $R_\mathrm{e}, R_\mathrm{m} \gg 10$), non-ideal MHD corrections to the MRI become completely negligible ($\ll 1\%$). Therefore, in the further analysis, we will often refer to these expressions (e.g. for the MRI growth rate) that are obtained in ideal MHD.

Figure 4.1: The Kelvin-Helmholtz instability developing in terrestrial clouds over Mount Duval in Australia. The picture is reproduced from Wikipedia (author: GRAHAMUK).

4.3 Parasitic instabilities

The Kelvin-Helmholtz and tearing mode instabilities are quite complex and each of them deserves to be a study subject of themselves. We are not going to describe them in too much detail, but rather highlight their key aspects that are relevant for the MRI.

4.3.1 Kelvin-Helmholtz instability

The Kelvin-Helmholtz instability can develop in systems with velocity shears. It mixes two fluid layers moving at different speeds and increases the vorticity of the system. The instability is commonly encountered in nature on many different scales, from the terrestrial clouds (see Fig. 4.1) to *intra-cluster medium*[6] (Roediger et al. 2011).

Consider an initial configuration with a constant density and pressure, and a velocity profile given by

$$v_{0x} = \begin{cases} v_0 & \text{for } y > 0 \\ -v_0 & \text{for } y < 0, \end{cases} \tag{4.26}$$

where v_0 is a constant. Such a system will be unstable against the KH instability. In ideal hydrodynamics, velocity perturbations around the shear will exponentially grow with time, i.e.

$$v_{1y}(x,y,t) = \tilde{v}_1(y)\sin(k_{\rm kh}x)e^{\gamma_{\rm kh}t}, \tag{4.27}$$

where $\tilde{v}_1(y)$ is an odd function peaked around $y = 0$ and vanishing for $y \to \infty$, $k_{\rm kh}$ is the wavevector of the initial perturbation in the x direction and $\gamma_{\rm kh}$ is the instability growth rate. For the velocity profile given by Eq. (4.26), the growth rate in the incompressible limit is given by (Chandrasekhar 1961)

$$\gamma_{\rm kh} = k_{\rm kh}v_0. \tag{4.28}$$

[6]Intracluster medium is superheated (to $\approx 10^7$–10^8 K) plasma in the centre of a galaxy cluster (the biggest gravitationally bound structure in the Universe).

In this idealised setup, the larger the wave-vector, the larger the growth rate. This peculiarity is caused by the singular jump in the velocity profile. For a shear layer of a finite width, $\gamma_{\rm kh}$ will be considerably reduced, e.g. for the velocity profile given by

$$v_{0x} = v_0 \tanh(\delta x), \tag{4.29}$$

where δ^{-1} is the shear width, the maximum growth rate,[7] $\gamma_{\rm KH} \approx 0.2\delta v_0$, is at $k_{\rm KH} \approx 0.45\delta$; for $k_{\rm kh} \gg \delta$, $\gamma_{\rm kh} \to 0$.

The initial perturbations of the KH instability cannot unboundedly grow with time, as it is suggested by Eq. (4.27), which is only valid during the early evolution of the instability. The perturbations grow at the expense of the kinetic energy stored in the shear flow. Once their kinetic energy, $E_{\rm kin}^{\rm pert}$, reaches around 0.01 of the total kinetic energy $E_{\rm kin}^{\rm tot}$, non-linear effects start to play an important role and the instability growth rate decreases (see, e.g. Keppens et al. (1999)). Eventually, when $E_{\rm kin}^{\rm pert} \approx 0.05 E_{\rm kin}^{\rm tot}$, the instability reaches saturation and further growth is halted.

The KH instability can be significantly affected by a magnetic field, whose influence depends on the Alfvénic Mach number (the ratio of the fluid to the Alfvénspeed) and the orientation of the field with respect to the direction of the fluid motion. Miura & Pritchett (1982), found that a constant magnetic field parallel to a velocity shear (in our case, the b_x component) has a stabilising effect on the instability. This result can be intuitively understood. During the instability evolution, the velocity component (v_{1y}) perpendicular to the shear flow is created. Fluid motions in this direction will stretch the magnetic field lines (create a b_y component). This will lead to a magnetic field tension ($b_x b_y$), which will try to restore the field lines to their initial configuration and prevent further fluid movements. The stronger the initial magnetic field, the stronger the stabilising effect and the greater the reduction of the growth rate.

A constant magnetic field perpendicular to the shear flow does not have such a strong influence on the KH instability (Miura & Pritchett 1982), the flow perturbations perpendicular to the shear, i.e. in the y direction, will follow the magnetic field lines, without causing any stretching.

Keppens et al. (1999) numerically studied the KH instability with a magnetic field that was aligned with the shear flow and changed its sign at the shear interface. They found that in such a configuration, the magnetic field can additionally destabilise the system, i.e. increase the KH instability growth rate.

From this brief discussion, we see that the KH instability, which is of hydrodynamical nature, can be affected by a magnetic field in various ways. It is difficult to tell *a priori* its influence on the flow for any field configuration.

So far, we only discussed the KH instability in the frame of ideal (magneto)-hydrodynamics. The studies of Junk et al. (2010) confirm the intuitive presumption that shear viscosity slows down the instability development. For velocity profile (4.26), the instability growth rate is given by (keeping the terms linear in viscosity)

$$\gamma_{\rm kh} = k_{\rm kh} v_0 - \nu \frac{k_{\rm kh}^2}{2}. \tag{4.30}$$

4.3.2 Tearing mode instability

In the previous chapter, we discussed in detail the linear phase of the tearing mode evolution. The instability was studied in a very simple system, so that we could support our investigations

[7] In this chapter, the growth rate and wavevector of the fastest growing KH mode are denoted as $\gamma_{\rm KH}$ and $k_{\rm KH}$, respectively, whereas for all other modes, we use symbols $\gamma_{\rm kh}$ and $k_{\rm kh}$.

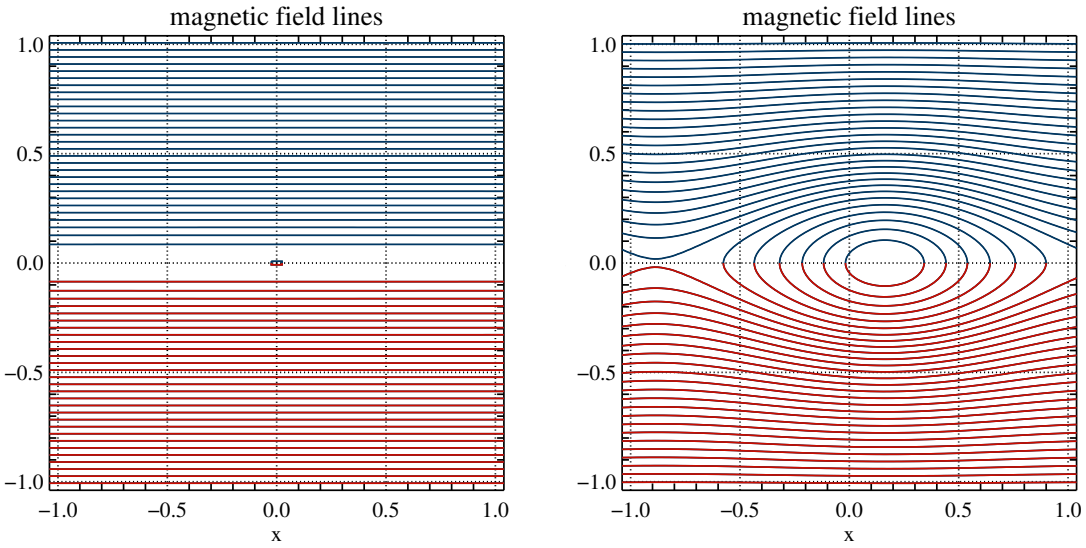

Figure 4.2: Magnetic field reconnection driven by the tearing mode instability. The simulation setup was like the default one in Sec. 3.4.2. The box of size $L_x = L_y = 2\pi/3$ was resolved with 128×128 zones. Resistivity was equal to $\eta = 10^{-4}$. *Left:* Initial magnetic field configuration $b_{0x} = \tanh(\delta y)$. Magnetic field lines with a positive and negative b_x component are blue and red, respectively. *Right:* The tearing mode instability entered the non-linear phase (after 500 dimensionless time units). Around $(x,y) = (-0.8, 0)$, the magnetic field reconnects in a so-called *X point*. In the vicinity of $(x,y) = (0.1, 0)$, a so-called *O point* is visible, where no magnetic field is present. The X and O points are characteristic for the tearing mode instability.

with the analytical theory. We consider the background magnetic field

$$b_{0y} = b_0 \tanh(\delta y), \tag{4.31}$$

where δ^{-1} is proportional to the shear width. In resistive non-viscous MHD, a tearing mode (TM) with a wavevector $k_{\rm tm}$ in the x direction will grow at a rate[8] (see Eq. (3.81)):

$$\gamma_{\rm tm} = (2/2.12)^{4/5} \eta^{3/5} \left(\frac{b_0 k_{\rm tm}}{\sqrt{\rho}}\right)^{2/5} \delta^{6/5} \left(\frac{\delta}{k_{\rm tm}} - \frac{k_{\rm tm}}{\delta}\right)^{4/5}, \tag{4.32}$$

provided $k_{\rm tm} \sim \delta$.

If viscosity is present in the system, it will reduce the TM growth rate. Given $\eta < 0.1\nu$, according to the calculations of Furth et al. (1963) (with our small improvements for this particular field geometry), the instability will develop at the rate (see Eq. (3.90)):

$$\gamma_{\rm tm} = \frac{2}{3} 2^{1/3} \eta^{5/6} \nu^{-1/6} \left(\frac{b_0 k_{\rm tm}}{\sqrt{\rho_0}}\right)^{1/3} \delta^{4/3} \left(\frac{\delta}{k_{\rm tm}} - \frac{k_{\rm tm}}{\delta}\right). \tag{4.33}$$

For the reasons discussed in the previous chapter, we found a discrepancy between the above equation and our simulation results. Therefore, we proposed a semi-analytical formula (see Eq.

[8] Like for the KH instability and MRI, we will denote the growth rate and the wavevectror of the fastest developing TM mode as $\gamma_{\rm TM}$ and $k_{\rm TM}$, respectively, whereas for all other modes, we use symbols $\gamma_{\rm tm}$ and $k_{\rm tm}$.

(3.117) that is only valid for $k_{\rm tm} = 3$ and $\delta = 10$ (but it is possible to generalise it to any combination of δ and $k_{\rm tm}$):

$$\gamma_{\rm tm}(k_{\rm tm} = 3, \delta = 10) = 34.56 \eta^{4/5} \nu^{-1/5} \left(\frac{b_0}{\sqrt{\rho_0}} \right)^{2/5}. \tag{4.34}$$

When tearing modes enter the non-linear phase of their evolution, they significantly change the magnetic field topology. In Fig. 4.2, we can see that initially straight magnetic field lines of opposite polarity start to reconnect at a so called *X point*, which is characteristic for the tearing modes.

4.4 Termination model

In this section, we discuss the GXP MRI termination model. Its key idea is that in the MRI channels, *parasitic instabilities*, i.e. Kelvin-Helmholtz or tearing modes, can develop. Once their growth rate (denoted commonly as $\gamma_{\rm p}$) becomes comparable to the MRI growth rate, $\gamma_{\rm MRI}$, they will start to play a dynamically important role. Eventually, they will destroy the MRI channels and terminate the MRI growth.

The secondary instabilities will develop from perturbations in the system with already well formed MRI channels[9]

$$\mathbf{v} = -q\Omega_0(r - r_0)\hat{\boldsymbol{\phi}} + \tilde{v}_{\rm c}(\hat{\mathbf{r}}\cos\phi_V + \hat{\boldsymbol{\phi}}\sin\phi_v)\sin(k_{\rm MRI}z)e^{\gamma_{\rm MRI}t} + \mathbf{v}_{\rm p}(r,\phi,z,t), \tag{4.35}$$

$$\mathbf{b} = b_{0z}\hat{\mathbf{z}} + \tilde{b}_{\rm c}(\hat{\mathbf{r}}\cos\phi_b + \hat{\boldsymbol{\phi}}\sin\phi_b)\cos(k_{\rm MRI}z)e^{\gamma_{\rm MRI}t} + \mathbf{b}_{\rm p}(r,\phi,z,t), \tag{4.36}$$

where $\mathbf{v}_{\rm p}$ and $\mathbf{b}_{\rm p}$ are the velocity and magnetic field of the parasitic instabilities, respectively. The main challenge of the GXP model is to solve the equations governing their evolution. As we could see in the previous chapter, already computing the tearing mode growth rate with a constant background magnetic field is a difficult task. The MRI channels, which are the background magnetic field and velocity shear for the parasitic instabilities, are time dependent. This leads to additional complications in determining the parasitic growth rate and it is obviously no longer justified to search for solution with a WKB ansatz.

GXP model

To make this task more tractable for analytical studies, Goodman & Xu (1994), Pessah & Goodman (2009) and Pessah (2010) make some arguable[10] simplifications. They compute the parasitic growth rate $\gamma_{\rm p}$ in the shearing box approximation under the assumption that temporal MRI channel variations can be neglected. This is justified only, if the parasitic time scale is much shorter than the MRI time scale, i.e. $\gamma_{\rm MRI} \ll \gamma_{\rm p}$. Moreover, they consider the MRI stage, when the channel amplitude is already much larger than the initial background magnetic field, $b_{\rm c} \gg b_{0z}$. For this reason, they neglect the latter, the Coriolis force and the background shear flow in their calculations. All in all, instead of searching for solutions of perturbations according to Eqs. (4.35) and (4.36), GXP consider a much more simplified system where the velocity and the magnetic field are given by

$$\mathbf{v}(t) = \tilde{v}_{\rm c}(\hat{\mathbf{r}}\cos\phi_V + \hat{\boldsymbol{\phi}}\sin\phi_v)\sin(k_{\rm MRI}z)e^{\gamma_{\rm MRI}t_0} + \mathbf{v}_{\rm p}(r,\phi,z,t), \tag{4.37}$$

$$\mathbf{b}(t) = \tilde{b}_{\rm c}(\hat{\mathbf{r}}\cos\phi_b + \hat{\boldsymbol{\phi}}\sin\phi_b)\cos(k_{\rm MRI}z)e^{\gamma_{\rm MRI}t_0} + \mathbf{b}_{\rm p}(r,\phi,z,t), \tag{4.38}$$

[9] In the equation below, we implicitly assume that the fastest growing MRI mode, with $k_{\rm MRI}$ and $\gamma_{\rm MRI}$, is most likely to emerge from random initial perturbations.

[10] The critics will come later.

where t_0 is the time at which the perturbations are imposed. The evolution equations for this system read (Pessah 2010)

$$\partial_t \mathbf{v}_\mathrm{p} + (\mathbf{v}_\mathrm{c}(t_0)\cdot\nabla)\mathbf{v}_\mathrm{p}(t_0) + (\mathbf{v}_\mathrm{p}\cdot\nabla)\mathbf{v}_\mathrm{c}(t_0) = -\frac{1}{\rho}\Big[\nabla(p_1 + \mathbf{b}_\mathrm{c}(t_0)\cdot\mathbf{b}_\mathrm{p}) + (\mathbf{b}_\mathrm{c}(t_0)\cdot\nabla)\mathbf{b}_\mathrm{p} + (\mathbf{b}_\mathrm{p}\cdot\nabla)\mathbf{b}_\mathrm{p}\Big] + \nu\nabla^2\mathbf{v}_\mathrm{p}, \tag{4.39}$$

$$\partial_t \mathbf{b}_\mathrm{p} + (\mathbf{v}_\mathrm{c}(t_0)\cdot\nabla)\mathbf{b}_\mathrm{p} + (\mathbf{v}_\mathrm{p}\cdot\nabla)\mathbf{b}_\mathrm{c}(t_0) = (\mathbf{b}_\mathrm{c}(t_0)\cdot\nabla)\mathbf{v}_\mathrm{p} + (\mathbf{b}_\mathrm{p}\cdot\nabla)\mathbf{v}_\mathrm{c}(t_0) + \eta\nabla^2\mathbf{b}_\mathrm{p}. \tag{4.40}$$

Pessah (2010) seeks solutions of the form

$$\mathbf{v}_\mathrm{p} = \tilde{v}_\mathrm{p}(z)e^{i\mathbf{k}\cdot\mathbf{x}+\gamma_\mathrm{p}(t-t_0)}, \tag{4.41}$$

$$\mathbf{b}_\mathrm{p} = \tilde{b}_\mathrm{p}(z)e^{i\mathbf{k}\cdot\mathbf{x}+\gamma_\mathrm{p}(t-t_0)}, \tag{4.42}$$

$$\tag{4.43}$$

where $\tilde{v}_\mathrm{p}(z)$ and $\tilde{b}_\mathrm{p}(z)$ are the initial perturbation amplitudes, γ_p is the parasitic instability growth rate and $\mathbf{k} = \mathbf{k}_\mathrm{h} + k_z\hat{\mathbf{z}}$, where $\mathbf{k}_\mathrm{h} \equiv k_r\hat{\mathbf{r}} + k_\phi\hat{\boldsymbol{\phi}}$ is a horizontal wavevector. In the ideal MHD limit, he finds that Kelvin-Helmholtz modes with a wavevector

$$k_\mathrm{KH} \approx 0.59 k_\mathrm{MRI} \tag{4.44}$$

have the highest growth rate given by

$$\gamma_\mathrm{KH} \approx 0.45 k_\mathrm{KH} v_\mathrm{c}(t_0). \tag{4.45}$$

Eq. (4.45), even though only valid in the limit $\gamma_\mathrm{KH} \gg \gamma_\mathrm{MRI}$, gives us an intuitive understanding of the parasitic instability problem. Initially, when the channel amplitudes are small, the KH instability will develop much more slowly than the MRI, i.e. $\gamma_\mathrm{KH} \ll \gamma_\mathrm{MRI}$. Eventually, for a large enough v_c (i.e. for t_0 chosen "late enough") , the secondary instability growth rate will be much larger than the one of the MRI, i.e. $\gamma_\mathrm{KH} \gg \gamma_\mathrm{MRI}$.

Pessah (2010) himself argues whether the condition $\gamma_\mathrm{p} \gg \gamma_\mathrm{MRI}$ can be fulfilled for a simple energetic reason. The parasites could achieve such high growth rates only for very large MRI amplitudes. However, the secondary instabilities constantly drain energy from the channels. Once the former ones have a considerably greater growth rate than the latter ones, the time derivative of the MRI channels' energy will be negative. Hence, the MRI growth cannot continue indefinitely and the channels cannot achieve arbitrarily large amplitudes.

Pessah (2010) puts forward the hypothesis that the MRI exponential growth phase will be terminated by the parasites, when $\gamma_\mathrm{p} \approx \gamma_\mathrm{MRI}$. We denote the channel's magnetic field amplitude for which this condition is met as b^term. Determining b^term in non-ideal MHD is the main goal of Pessah's paper. To compute the MRI termination amplitude, one would need to have an appropriate expression for the parasitic growth rate, $\gamma_\mathrm{p} = \gamma_\mathrm{p}(b_\mathrm{c})$. With the help of that relation, one could obtain b^term from the equation

$$\gamma_\mathrm{p}(b^\mathrm{term}) \equiv \gamma_\mathrm{MRI}. \tag{4.46}$$

Calculating the parasitic instability growth rate in the $\gamma_\mathrm{p} \leq \gamma_\mathrm{MRI}$ regime is a challenging task, because treating MRI channels as time-independent structures, and using Eqs. (4.39) and (4.40) is no longer justified. Nevertheless, Pessah still uses this approximation claiming that "the assumption of stationary background is only marginally satisfied" (quote from Pessah (2010)). According to our understanding, this assumption is clearly violated and therefore Pessah's calculations are inconsistent. To correctly compute the growth rates of parasitic instabilities close to the termination

point, one has to include the temporal variation of the channels, since both timescales are comparable during this phase, i.e. $\gamma_{\rm MRI}^{-1} \approx \gamma_{\rm p}^{-1}$. Before termination, i.e. when $\gamma_{\rm p} < \gamma_{\rm MRI}$, one could rather neglect the secondary instabilities, but for $\gamma_{\rm p} = \gamma_{\rm MRI}$ both instabilities should be taken into account, and for $\gamma_{\rm p} > \gamma_{\rm MRI}$, MRI termination, according to Pessah's hypothesis, has already happened.

Pessah also gives an alternative criterion for MRI termination, namely when the amplitudes of the parasites and MRI channels, $b^{\rm term}$, are comparable. Using the same expressions for $\gamma_{\rm p}$, he estimates that this leads to 3–10 times larger values of $b^{\rm term}$, but this value should once again be questioned. Even if the channels did not change because of the MRI amplification, it would still be wrong to use growth rate expressions derived under the assumption that the perturbations are much smaller than the background velocity and magnetic field, for the case when perturbations and background fields become comparable.

Another point of criticism concerns neglect of the initial background magnetic field. It was argued by Goodman & Xu (1994) and later repeated by Pessah (2010) that at some stage of the MRI evolution, the channel amplitude will be much larger than the initial vertical field, i.e. $b_{\rm c} \gg b_{0z}$ and therefore, the latter one can be neglected. First of all, it was Balbus & Hawley (1991), who in their pioneering paper on the MRI, pointed out that even apparently negligible magnetic field can drastically change the dynamics of the whole system. Second of all, according to Pessah's own estimates (Pessah 2010), $b^{\rm term} \approx 3.8 b_{0z}$ in the ideal MHD limit. Hence, the condition $b_{\rm c} \gg b_{0z}$ is clearly not met around the saturation point.

In the case of the KH instability, a physically better argumentation can be supported by the results of Miura & Pritchett (1982), who studied the instability in 2D[11] for an arbitrary angle between the velocity shear and the constant background magnetic field. They found that a perpendicular field, which in our case is the b_{0z} component, does not change the instability growth rate (it is the same like in pure hydrodynamics). This result could be a hint that the b_{0z} component might be neglected in studies of the KH instability. However, we refrain from drawing too strong conclusions. The magnetic field of the channels (b_r and b_ϕ components), shortly before MRI termination, will be comparable to b_{0z}. This gives rise to non-diagonal components of the Maxwell stress tensor (i.e. $b_r b_{0z}$ and $b_\phi b_{0z}$) which vary in z direction. It would require a careful analysis to determine how these magnetic tension components can affect the KH instability dynamics. In the case of tearing modes, we do not know how the vertical magnetic field component influences their growth rate.

Another dubious step in Pessah's calculations is neglecting the Coriolis force in Eq (4.39) in the regime, where $\gamma_{\rm p} \approx \gamma_{\rm MRI}$. The time derivative of the velocity perturbations and the Coriolis force are of the same order, i.e. $\partial_t \mathbf{v}_{\rm p} = \gamma_{\rm p} \mathbf{v}_{\rm p}$ and $|-\mathbf{v}_{\rm p} \times \mathbf{\Omega}_0| \approx |v_{\rm p} 2\gamma_{\rm MRI}/\alpha| \approx v_{\rm p}\gamma_{\rm p}$ (since $|\alpha|$ is of order 1), respectively.

After these remarks, the results of Pessah (2010) should obviously be taken with some scepticism. As already pointed out, we definitely cannot rely on his parasitic growth rate calculations. However, we should not discard his oversimplified model completely, but rather see which parts of it can be useful in our further analysis.

The MRI termination criterion

Pessah (2010) suggested two termination criteria, either when the parasitic instabilities and the MRI (channels) have comparable growth rates ($\gamma_{\rm p} \approx \gamma_{\rm MRI}$), or amplitudes ($v_{\rm p} \approx v_{\rm c}$ or $b_{\rm p} \approx b_{\rm c}$).

[11] The system was homogeneous in the third direction.

From a mathematical point of view, one can exclude the former criterion. Let us consider a system, where there is no MRI yet. We introduce perturbations in velocity and magnetic field (with amplitudes $\tilde{v}_c$ and $\tilde{b}_c$, respectively) that exactly correspond to the MRI channel solutions (Eqs. (4.18) and (4.19)). Additionally, we add perturbations $v_p(t=0)$ and $b_p(t=0)$, from which the parasitic instabilities will develop. We set the amplitudes of $v_p(t=0)$ and $b_p(t=0)$ to be arbitrarily smaller than $\tilde{v}_c$ and $\tilde{b}_c$, say $\max[v_p(t=0)] = \tilde{v}_c 10^{-10}$ and $\max[b_p(t=0)] = \tilde{b}_c 10^{-10}$. Initially, the secondary instability will develop more slowly than the MRI, because the former's growth rate will be much smaller, i.e. $\gamma_p(t=0) \ll \gamma_{MRI}$. Since γ_{MRI} is constant and $\gamma_p(t)$ increases (approximately exponentially) with time, at some point both growth rates will be equal, i.e. $\gamma_p(t_0) = \gamma_{MRI}$. However, at this time, the parasitic to MRI amplitude ratio ($\max[v_p(t_0)]/\max[v_c(t_0)]$) will be even smaller than initially, because for $t \leq t_0$, $\gamma_p(t) \leq \gamma_{MRI}$. The quantities related to the secondary instabilities would have relative amplitudes smaller than 10^{-10} and can neglected. To play a dynamically important role, the parasites must grow for some time at a higher rate than the MRI, i.e. with $\gamma_p(t) > \gamma_{MRI}$, to catch up with the channel amplitudes. From this simple reasoning, we see that equality of both growth rates, i.e. $\gamma_p = \gamma_{MRI}$, cannot be a good criterion for MRI termination. It has to happen at some later time. Actually, in nature we expect both the MRI and the parasitic instability to be triggered by random perturbations, i.e. both of them should initially have comparable amplitudes. Still, at the time when $\gamma_p(t_0) = \gamma_{MRI}$, the MRI channels will have much higher amplitudes, because they were growing at a higher rate than the parasitic instabilities. Hence, from a physicist's point of view, we could say the condition $\gamma_p(t_0) = \gamma_{MRI}$, does not determine MRI termination, but sets the time after which it will soon[12] happen.

The other MRI termination criterion (Pessah 2010), i.e. comparable amplitudes of the secondary instabilities and the MRI channels, seems to be physically better justified. Certainly, at that stage, the parasitic instabilities must have entered the non-linear phase and modified the MRI channel structure.

The definition of the MRI termination point is also somewhat ambiguous. It could be chosen when the MRI growth rate either starts to decrease, or drops to zero, i.e. when the volume integrated $b_r b_\phi$ component of the Maxwell stress reaches its first maximum (the one, before the turbulent phase sets in). In our simulations, we chose the latter condition, since one can measure it unambiguously and we are interested in how much the MRI can amplify the initial magnetic field.

An alternative formulation

We adopt a different approach than Pessah (2010) and do not try to find approximate equations for the parasitic instabilities at the cost of potentially oversimplifying the problem. Instead, we discuss which features the exact equations for the secondary instability should have. Even though our considerations will have no predictive power by themselves, they will prove to be very useful when extrapolating our simulation results to the parameter regime which is relevant for core-collapse supernovae. We begin the discussion with the Kelvin-Helmholtz instability. Then, we briefly repeat the steps for the tearing modes.

As already mentioned before, even local simulations of the MRI with realistic initial magnetic fields (b_{0z} of order 10^{11}G) are computationally unaffordable. To reduce the simulation's cost, following Obergaulinger et al. (2009), we use initial magnetic fields, which are approximately two orders of magnitude higher, i.e. $b_{0z} \approx 10^{13}$G, than those encountered in the proto-neutron stars.

[12] Obviously *soon* has to be somehow specified. In the MRI case, it should be understood as *withing a few MRI timescales, i.e.* γ_{MRI}^{-1}.

This creates a theoretical problem, however. We need to find a way to extrapolate our simulation results to the parameter regime, which is relevant for core-collapse supernovae. Needless to say, one must always verify whether such an extrapolation is justified. Fortunately, it is the case for simulations in which the MRI is terminated by the KH instability. As we will soon show, in the high plasma β regime (i.e. for $c_s \gg c_A$), which is relevant for our studies, the initial magnetic field can be amplified only by a constant factor in the ideal MHD approximation. This seems to be an intrinsic feature of the MRI.

We do not have an appropriate expression for the growth rate of the fastest developing KH mode in time-dependent MRI channels. However, we can guess some of its features from a simple physical argumentation and dimensional analysis. We start with the expression valid for stationary backgrounds in ideal hydrodynamics, i.e.

$$\gamma_{KH} = f_{KH} v_c k_{KH}, \tag{4.47}$$

where f_{KH} is a dimensionless function. For $f_{KH} = 1$ and $f_{KH} \approx 0.45$, we recover Eqs. (4.28) and (4.45), respectively. For time-dependent channels and background magnetic fields, the above expression must be modified. At first, when writing down all possible variables on which the growth rate of the fastest developing KH mode may depend, the problem seems to be very complicated,

$$\gamma_{KH} = \gamma_{KH}(v_c, v_p, c_{Ap}, c_{Ac}, c_{Az}, c_{ms}, k_{KH}, k_{MRI}, \gamma_{MRI}, \Omega, \alpha). \tag{4.48}$$

It can depend on six speeds (the velocity amplitude of MRI channels v_c, perturbation velocity v_p, three Alfvén speeds related to the magnetic fields of the perturbations c_{Ap}, the magnetic fields of MRI channels c_{Ac} and the constant background magnetic field c_{Az}, and the fast magnetosonic velocity c_{ms}), two lengths (the inverses of the KH instability and the MRI wavevectors k_{KH}^{-1} and k_{MRI}^{-1}, respectively), two timescales (the inverses of the MRI growth rate γ_{MRI}^{-1} and the angular velocity Ω^{-1}), and the dimensionless parameter α determining the rotational profile. However, many of these variables are not independent. We expect that, similarly to Eq. (4.44), the wavevector of the fastest growing KH mode k_{KH} will still be mainly proportional to the wavevector of the fastest growing MRI mode k_{MRI}. The dimensions of any other variables possibly influencing k_{KH} must cancel out:

$$k_{KH} = k_{MRI} h\left(\frac{v_c}{c_{Az}}, \frac{v_p}{c_{Az}}, \frac{c_{Ap}}{c_{Az}}, \frac{c_{ms}}{c_{Az}}, \frac{\Omega}{\gamma_{MRI}}, \frac{k_{MRI} c_{Az}}{\gamma_{MRI}}, \alpha\right), \tag{4.49}$$

where h is a dimensionless function. In general, we can say that with the help of the above equation, the explicit dependence of γ_{KH} on k_{KH} in Eq. (4.48) can be removed, i.e.

$$\gamma_{KH} = \gamma_{KH}(v_c, v_p, c_{Ap}, c_{Ac}, c_{Az}, c_{ms}, k_{MRI}, \gamma_{MRI}, \Omega, \alpha). \tag{4.50}$$

We are interested in the high plasma β regime, in which the fast magnetosonic speed, $c_{ms} \approx c_s \gg c_A$, can be treated as infinite (the fast magnetosonic wave crossing time is much shorter than the MRI timescale, i.e. $\lambda_{MRI}/c_{ms} \ll \gamma_{MRI}^{-1}$). This allows us to use the incompressible flow approximation, i.e. c_{ms} not enter Eq. (4.50). As long as the parasitic perturbations are small (with respect to the other background quantities), they should not influence the secondary instability growth rate either:

$$\gamma_{KH} = \gamma_{KH}(v_c, c_{Ac}, c_{Az}, k_{MRI}, \gamma_{MRI}, \Omega, \alpha). \tag{4.51}$$

With the help of Eq. (4.16), we can eliminate either the angular velocity, or the MRI growth rate, since $\gamma_{MRI} \propto \Omega$. The fastest growing MRI mode is given by Eq. (4.17), hence k_{MRI} is not independent. The channel amplitudes are related by Eq. (4.20), hence $v_c \propto c_{Ac}$ and one of the two

velocities is redundant. In the end, there are only four independent variables in the equation for the KH instability growth rate:

$$\gamma_{\rm KH} = \gamma_{\rm KH}(c_{\rm Ac}, c_{\rm Az}, \Omega, \alpha). \tag{4.52}$$

From dimensional analysis, the above equation must have the form

$$\gamma_{\rm KH} = \Omega f_{\rm KH}\left(\frac{c_{\rm Ac}}{c_{\rm Az}}, \alpha\right), \tag{4.53}$$

where $f_{\rm KH}$ is a dimensionless function which can depend only on two dimensionless variables. We see that the original KH instability growth rate problem (Eq. (4.48)), initially depending on eleven variables, has been greatly simplified. However, we should not forget that the whole complexity of this problem is hidden in the function $f_{\rm KH}(c_{\rm Ac}/c_{\rm Az}, \alpha)$, and determining its form can be extremely complicated. Yet, as long as the amplitude of the secondary instability is small, $f_{\rm KH}$ depends only on one time dependant dimensionless variable, i.e. $c_{\rm Ac}/c_{\rm Az}$.

The KH instability will not affect the MRI until their amplitudes become comparable. As already mentioned before, it is difficult to tell , when this will happen, but for sure not before

$$\gamma_{\rm KH} = \gamma_{\rm MRI}. \tag{4.54}$$

From Eqs. (4.53) and (4.16) we have

$$\Omega f_{\rm KH}\left(\frac{c_{\rm Ac}}{c_{\rm Az}}, \alpha\right) = -\frac{\alpha}{2}\Omega, \tag{4.55}$$

hence

$$f_{\rm KH}\left(\frac{c_{\rm Ac}}{c_{\rm Az}}, \alpha\right) = -\frac{\alpha}{2}. \tag{4.56}$$

This is an interesting result: both growth rates become equal for a constant ratio $c_{\rm Ac}/c_{\rm Az}$. If $\gamma_{\rm KH} = \gamma_{\rm MRI}$ were the termination criterion, the MRI would only amplify the initial magnetic field by a constant factor.

Once the perturbations amplified by the KH instability influence the dynamics of the system, the situation becomes more complicated. The MRI growth rate, will no longer be constant. Moreover, the KH instability will be affected by its own perturbations, i.e.

$$\gamma_{\rm KH} = \gamma_{\rm KH}(c_{\rm Ac}, c_{\rm Az}, c_{\rm Ap}, v_{\rm p}, \Omega, \gamma_{\rm MRI}, \gamma_{\rm KH}, \alpha), \tag{4.57}$$

where $\gamma_{\rm MRI}$ and $\gamma_{\rm KH}$ on the right hand side equation represent the time dependence of the other variables, i.e. if a given quantity is mainly changed by the MRI or the KH instability, its logarithmic time derivative is approximately proportional to $\gamma_{\rm MRI}$ or $\gamma_{\rm KH}$, respectively, e.g. $\partial_t \ln(c_{\rm Ac}) \approx \gamma_{\rm MRI}$. We can rewrite the above equation, bearing in mind the dimensionality of all variables included in the problem,

$$\gamma_{\rm KH} = \Omega g_{\rm KH}\left(\frac{c_{\rm Ac}}{c_{\rm Az}}, \frac{c_{\rm Ap}}{c_{\rm Az}}, \frac{v_{\rm p}}{c_{\rm Az}}, \frac{\gamma_{\rm MRI}}{\Omega}, \frac{\gamma_{\rm KH}}{\Omega}, \alpha\right), \tag{4.58}$$

where $g_{\rm KH}$ is a dimensionless function depending on dimensionless variables. The key point to realise here is that the further evolution of the MRI and KH instability will depend on the parasitic perturbations, which were introduced at $t = 0$. Therefore, it is impossible to formulate a general conditions like Eq. (4.56) for the MRI termination point. However, if we make the physically reasonable assumption that the initial perturbations of both the MRI and the KH instability are proportional to the background magnetic field, i.e. $\tilde{c}_{\rm Ac} \propto c_{\rm Az}$, $\tilde{v}_{\rm c} \propto c_{\rm Az}$, $\max[c_{\rm Ap}(t=0)] \propto c_{\rm Az}$ and

$\max[v_{\rm p}(t=0)] \propto c_{{\rm A}z}$, further progress can be made. If in two systems with different values of the initial vertical magnetic field the corresponding ratios $c_{\rm Ac}/c_{{\rm A}z}$ and $c_{\rm Ap}/c_{{\rm A}z}$ are the same at $t=0$, they will also stay the same later in the evolution. In both systems, the ratios $c_{\rm Ac}/c_{{\rm A}z}$ will equally change with time, i.e. $c_{\rm Ac}/c_{{\rm A}z} \propto \exp(\gamma_{\rm MRI} t)$. The same holds for the ratios $c_{\rm Ap}/c_{{\rm A}z}$, which grow at the same rate, i.e. $\gamma_{\rm KH}(t) = \gamma_{\rm KH}(c_{\rm Ac}/c_{{\rm A}z})$. ratio $c_{\rm Ap}/c_{\rm Ac}$. Consequently, the ratios $c_{\rm Ap}/c_{\rm Ac}$ will also be equal in both systems. Therefore, both systems will enter the non-linear phase of the MRI at the same time and with the same corresponding amplitude ratios. Hence, we can presume that during the further evolution, all ratios will be similar if not the same. Consequently, the MRI termination happens in both systems for the same $c_{\rm Ac}/c_{{\rm A}z}$ ratios. We conclude that the MRI will increase the initial magnetic field by a constant *amplification factor* $\mathcal{A}$, i.e.

$$b^{\rm term} = \mathcal{A} b_{0z}. \tag{4.59}$$

The value of $\mathcal{A}$ needs to be determined from the numerical simulations.

Now, we discuss MRI termination caused by tearing modes. As we will show later, this scenario is not relevant for core-collapse supernovae. The discussion is based on resistive-viscous MHD equations. When, the amplitude of the secondary instability is much smaller than that of the MRI channels, the growth rate of the fastest developing tearing mode can in general depend on the following parameters:

$$\gamma_{\rm TM} = \gamma_{\rm TM}(\eta, \nu, c_{\rm Ac}, v_{\rm c}, c_{{\rm A}z}, k_{\rm TM}, k_{\rm MRI}, \gamma_{\rm MRI}, \Omega, \alpha). \tag{4.60}$$

Once again, we expect the wavevector of that the fastest growing mode, $k_{\rm TM}$, to be a function of the other parameters. Therefore, it can be eliminated from the above equation. For the same reasons like in the case of the KH instability, many of the other quantities are not independent either. In the end, the growth rate equation reduces to

$$\gamma_{\rm TM} = \gamma_{\rm TM}(\eta, \nu, c_{\rm Ac}, c_{{\rm A}z}, \Omega, \alpha). \tag{4.61}$$

With the help of dimensional analysis, the above expression can be rewritten as

$$\gamma_{\rm TM} = \Omega f_{\rm TM}\left(\frac{\eta}{\nu}, \frac{c_{\rm Ac}}{c_{{\rm A}z}}, \frac{\eta\Omega}{c_{{\rm A}z}^2}, \alpha\right), \tag{4.62}$$

where $f_{\rm TM}$ is a dimensionless function which depends on dimensionless variables. Notice the key difference between Eqs. (4.53) and (4.62). The tearing mode growth rate expression contains resistivity η, whose dimension is "compensated" by $\Omega/c_{{\rm A}z}^2$ (or equally well by either $\Omega/c_{\rm Ac}^2$ or $\Omega/(c_{\rm Ac}c_{{\rm A}z})$).[13] Hence, unlike for the KH instability, $c_{\rm Ac}$ and $c_{{\rm A}z}^{-1}$ must enter the growth rate equations with different powers. This means that the ratio $c_{\rm Ac}/c_{{\rm A}z}$ at MRI termination (and therefore the total field amplification) must depend on the initial magnetic field. Therefore, one cannot simply extrapolate results within the parameter regime, in which tearing modes are the dominant secondary instability. Fortunately, this is not the case in proto-neutron stars.

Finally, we mention that also the termination caused by the KH instability becomes more complicated in non-ideal MHD. Since at least the viscosity, ν, has to enter the KH growth rate equation, it can no longer have such a simple form like (4.53). Repeating the discussion for the tearing

[13] The dimension of resistivity cannot be "compensated" only by viscosity for the simple reason that tearing modes are present in resistive-non-viscous MHD.

modes, we find that the KH instability in resistive-viscous MHD must have the following dependence

$$\gamma_{\mathrm{KH}} = \Omega \tilde{f}_{\mathrm{KH}} \left(\frac{\nu}{\eta}, \frac{c_{\mathrm{Ac}}}{c_{\mathrm{A}z}}, \frac{\nu\Omega}{c_{\mathrm{A}z}^2}, \alpha \right). \tag{4.63}$$

There is still a big difference between Eqs. (4.63) and (4.62), however. Because the KH instability is an ideal (magneto-)hydrodynamical instability, viscous and resistive terms will enter the growth rate equation as corrections. However, for sufficiently high hydrodynamic and magnetic Reynolds numbers, i.e. $R_{\mathrm{e}}, R_{\mathrm{m}} \gg 1$, these corrections can possibly be neglected. We could express this fact symbolically as

$$\gamma_{\mathrm{KH}} = \Omega f_{\mathrm{KH}} \left(\frac{c_{\mathrm{Ac}}}{c_{\mathrm{A}z}}, \alpha, \right) - \Omega g_{\mathrm{KH}} \left(\frac{\nu}{\eta}, \frac{c_{\mathrm{Ac}}}{c_{\mathrm{A}z}}, \frac{\nu\Omega}{c_{\mathrm{A}z}^2}, \alpha \right). \tag{4.64}$$

where $g_{\mathrm{KH}} \ll f_{\mathrm{KH}}$ for $R_{\mathrm{e}}, Rm \gg 1$. Hence, using ideal MHD equations for $R_{\mathrm{e}}, Rm > 100$ should still be a reasonable approximation. The tearing modes are a resistive MHD instability and a split like the one in Eq. (4.64) is not possible. The resistivity must enter the main term in Eq. (4.62) and can never be neglected.

Some simple estimations

So far our discussion of the MRI termination was quite formal. Even though our reasoning was mathematically correct, it is hard to gain a simple physical understanding of the problem, when looking at Eqs. like (4.53) and (4.62). At this point we shift focus to a less rigorous approach. We will support our arguments by equations, whose usage is not always well justified. Some of them may be even incorrect and oversimplify the problem. However, these equations will have one big advantage, namely simplicity. To summarise, we go back to Pessah's approach (Pessah 2010), but this time fully aware of its limitations. One point has be made clear. We will not treat the following results as a physically well justified approximate solution of the MRI termination problem and we will not use them to analyse and interpret our numerical simulations. The sole purpose of the following discussion is to gain some intuitive understanding of the phenomenon. As we will see, Eqs. (4.53) and (4.62))encompass the results of Pessah's toy model.

Pessah (2010) considered parasitic instabilities developing in time-independent MRI channels, i.e. Eqs. (4.39) and (4.40). He seeks solutions using the WKB ansatz (Eqs. (4.41) and (4.42)) of the form

$$\mathbf{v}_{\mathrm{p}} = \tilde{v}_{\mathrm{p}}(z) e^{i\mathbf{k}\cdot\mathbf{x} + \gamma_{\mathrm{p}}(t-t_0)},$$
$$\mathbf{b}_{\mathrm{p}} = \tilde{b}_{\mathrm{p}}(z) e^{i\mathbf{k}\cdot\mathbf{x} + \gamma_{\mathrm{p}}(t-t_0)}.$$

The main difficulty consists in determining the functions $\tilde{v}_{\mathrm{p}}(z)$ and $\tilde{b}_{\mathrm{p}}(z)$, which Pessah expands these functions in Fourier series ($\tilde{v}_{\mathrm{p}}(z)$ and $\tilde{b}_{\mathrm{p}}(z)$ must be $2\pi/k_{\mathrm{MRI}}$ periodic in z)

$$\tilde{v}_{\mathrm{p}}(z) = \sum_{n=-\infty}^{\infty} \alpha_n \exp(ink_{\mathrm{MRI}} z), \tag{4.65}$$

$$\tilde{b}_{\mathrm{p}}(z) = \sum_{n=-\infty}^{\infty} \beta_n \exp(ink_{\mathrm{MRI}} z). \tag{4.66}$$

He finds recursion relations for the coefficients α_n and β_n (for the details see Pessah (2010)), and solves those relations numerically. Obviously, the sums in Eqs. (4.65) and (4.66) have to

be truncated in numerical calculations. Pessah (2010) reports that for $|n| \leq 30$ he achieved a convergence to "the desired accuracy" (he did not specify this statement, however). This is a very important point, to which we will come back later.

In the ideal MHD limit, Pessah (2010) finds that the KH mode with the wavevector

$$k_{\rm KH} \approx 0.59 k_{\rm MRI} \tag{4.67}$$

has the highest growth rate given by

$$\gamma_{\rm KH} \approx 0.45 k_{\rm KH} v_{\rm c}(t_0). \tag{4.68}$$

With the help of Eqs. (4.44), (4.17), and (4.20), we rewrite the above equation as

$$\gamma_{\rm KH} \approx -0.13 \alpha \Omega \frac{c_{\rm Ac}}{c_{{\rm A}z}}, \tag{4.69}$$

and note that its form is in accordance with Eq. (4.53).

If we assume that MRI termination happens, when the condition

$$\gamma_{\rm KH} = \gamma_{\rm MRI} \tag{4.70}$$

is met, then by comparing Eqs. (4.69) with (4.16), we would obtain

$$-0.13 \alpha \Omega \frac{c_{\rm Ac}}{c_{{\rm A}z}} = -\frac{\alpha}{2}\Omega, \tag{4.71}$$

and hence

$$\frac{c_{\rm Ac}}{c_{{\rm A}z}} = \frac{b_{\rm c}}{b_{0z}} \approx 3.8. \tag{4.72}$$

The initial magnetic field is amplified by a constant factor (≈ 3.8) before the MRI is terminated. Pessah (2010) reported this result for Keplerian rotational profiles, but the generalisation to any rotational profile given by Eq. (4.1) (i.e. for any α) is straightforward. Eq. (4.72) agrees with our prediction (see Eq. (4.56) and the discussion below) that MRI termination given Eq. (4.70)should happen for a constant ratio $c_{\rm Ac}/c_{{\rm A}z}$. With our method, however, we cannot determine whether this ratio is independent of α.

As we already mentioned before, Eq. (4.70) is not a condition for MRI termination. It should rather happen when the amplitudes of the parasitic instabilities become comparable to those of the MRI channels, for i.e. $\max[b_{\rm p}] \approx b_{\rm c}$. If we assumed that MRI channels grew completely undisturbed until the termination time, $t^{\rm term}$, and then their destruction would instantaneously happen at $t = t^{\rm term}$, we would still be allowed to use Eqs. (4.16), (4.18) and (4.19) to describe their evolution for $t < t^{\rm term}$ (this assumption obviously is not met in reality). Under the same assumption, the KH instability growth rate would be l given by Eq. (4.69), i.e. shortly before MRI termination, the KH instability would achieve its highest growth rate

$$\gamma_{\rm KH}^{\rm max} \approx -0.13 \alpha \Omega \frac{c_{\rm Ac}(t^{\rm term})}{c_{{\rm A}z}}. \tag{4.73}$$

For physically plausible initial conditions (random perturbations from which both the MRI and parasitic instabilities will develop), the time interval between when condition (4.70) is met ($t = t_0$) and the MRI is terminated ($t = t^{\rm term}$), should be independent of the initial magnetic field. Hence, the channel amplitude $c_{\rm Ac}(t_0)$ would be amplified during this time interval by a constant factor

$$c_{\rm Ac}(t^{\rm term}) = c_{\rm Ac}(t_0) e^{\gamma_{\rm MRI}(t^{\rm term} - t_0)}. \tag{4.74}$$

Combining Eqs. (4.70), (4.73) and (4.74), we notice that at the MRI termination point the following condition would be met

$$\gamma_{\rm KH} = \sigma \gamma_{\rm MRI}, \tag{4.75}$$

where

$$\sigma \equiv e^{\gamma_{\rm MRI}(t^{\rm term}-t_0)}. \tag{4.76}$$

The time $t^{\rm term}$ is unknown and it would need to be determined by numerical simulations. We do not expect Eqs. (4.74) and (4.76) to have such a simple form in reality. However, we can still postulate that relation (4.75), with a constant factor $\sigma > 1$, should hold at MRI termination. Once the value of σ is determined with the help of numerical simulations, we can use it to calculate the MRI termination amplitude for any initial magnetic field. Combining Eqs. (4.72), (4.73) and (4.75), we have

$$c_{\rm Ac}(t^{\rm term}) \approx 3.8\sigma c_{\rm Az}. \tag{4.77}$$

A final comment has to be made concerning condition (4.75). It should not be understood that $\sigma\gamma_{\rm KH}$ is a sort of threshold for MRI termination. MRI channels would be destroyed for any $\gamma_{\rm KH} > \gamma_{\rm MRI}$, if the secondary instability were given sufficient time. Eq. (4.75) and the factor σ appear as a result of a particular interplay between the instability growth rates and their initial perturbations.

Pessah (2010) reports that the MRI is terminated by tearing modes (before the KH instability would do the job) for magnetic Reynolds numbers $R_{\rm m} < 1$, i.e. for

$$\frac{c_{\rm Az}^2}{\eta\Omega} < 1. \tag{4.78}$$

Therefore, tearing modes should not play any role in the MRI termination problem, given the conditions relevant for core-collapse supernovae ($R_{\rm m} \gg 1$). At this point, we could finish the discussion of tearing modes, since from our point of view they seem to be unimportant. However, there are two good reasons to pay some attention to this secondary instability. Firstly, tearing modes can be also driven by numerical resistivity (see the discussion in the previous chapter). Obergaulinger et al. (2009) observed them in ideal MHD simulations of MRI in core-collapse supernovae. Therefore, it is important to understand how the (undesired) appearance of this secondary instability can affect simulation results. Secondly, we would like to point out the differences between MRI termination caused by the KH instability and by tearing modes.

The problems with tearing modes result from the form of their growth rate given by Eq. (4.62). Already at the stage, when they grow at the MRI rate, i.e. when $\gamma_{\rm TM} = \gamma_{\rm MRI}$, the ratio $c_{\rm Ac}/c_{\rm Az}$ must depend on the initial magnetic field. This means that also in the subsequent MRI termination phase, this ratio will not be constant either. Thus, many simulations would be needed to investigate the dependence of $b^{\rm term}/b_{0z}$ on the initial magnetic field and resistivity. In addition, even if we found such scaling relations, we could not use them to extrapolate the simulation results to an unknown parameter regime. To do that, we would need to have a sound theoretical justification that this is allowed. All in all, this means that much more work would be required to understand MRI termination caused by tearing modes.

No, we show how the MRI itself is affected by a large value of the resistivity. Then, we discuss tearing modes.

For very low magnetic Reynolds numbers, i.e. $R_{\rm m} < 1$, the fastest developing MRI mode will no longer have the growth rate and wavevector given by Eqs. (4.16) and (4.17), respectively, which are valid in ideal MHD. Calculations of MRI growth rates in non-ideal MHD were done by Pessah & Chan (2008). Needless to say, resistive and viscous terms in the dispersion relation lead to

additional complications. For our purposes, we will use a more heuristic approach, yet giving correct qualitative results. We begin with Eqs. (4.16) and (4.17), which are valid for ideal MHD, i.e.

$$\gamma_{\rm MRI} = -\frac{\alpha}{2}\Omega, \tag{4.79}$$

$$k_{\rm MRI} = \sqrt{1-\frac{(2+\alpha)^2}{4}}\Omega\frac{\sqrt{\rho}}{b_{0z}} = \sqrt{1-\frac{(2+\alpha)^2}{4}}\frac{\Omega}{c_{{\rm A}z}}. \tag{4.80}$$

The width of the MRI channel is $2\pi/k_{\rm MRI}$ and its amplitude grows according to

$$b_{\rm c}(t) = \tilde{b}_{\rm c}e^{\gamma_{\rm MRI}t}. \tag{4.81}$$

Imagine that at some point, say at the time t_0, we turn on resistivity. For the time being, we can forget about any MRI activity and just calculate at what rate the resistivity would diffuse the magnetic field of the channel[14]

$$b_{\rm c}(z,t_0) = b_{\rm c}(t_0)\sin(k_{\rm MRI}z). \tag{4.82}$$

For this magnetic field configuration, solving the diffusion equation,

$$\partial_t\mathbf{b} = \nabla^2\mathbf{b}, \tag{4.83}$$

is trivial, since the sine is its eigenfunction. If the MRI were absent, the magnetic field would decrease according to

$$b_{\rm c}(z,t) = b_{\rm c}(t_0)\sin(k_{\rm MRI}z)e^{-\gamma_{\rm D}t}, \tag{4.84}$$

where

$$\gamma_{\rm D} = \eta k_{\rm MRI}^2. \tag{4.85}$$

Plugging (4.17) into the above equation, we obtain

$$\gamma_{\rm D} = \eta\frac{\Omega^2}{c_{{\rm A}z}^2}. \tag{4.86}$$

In the parameter regime, in which tearing modes are relevant for MRI termination, we can estimate with the help of Eq. (4.78) that

$$\gamma_{\rm D} > \Omega. \tag{4.87}$$

On the other hand, from Eq. (4.16), we have

$$\gamma_{\rm MRI} = -\frac{\alpha}{2}\Omega \approx \Omega, \tag{4.88}$$

and hence

$$\gamma_{\rm D} \gtrsim \gamma_{\rm MRI}. \tag{4.89}$$

For the mode $k_{\rm MRI}$, which is the fastest growing one in ideal MHD, the resistivity would diffuse the magnetic field faster than the MRI is able to amplify it. This does not mean, the MRI is completely suppressed by the dissipative effects that in this parameter regime. Modes with $k_{\rm mri} < k_{\rm MRI}$ have smaller growth rates, $\gamma_{\rm mri}$, than $\gamma_{\rm MRI}$ (the maximum growth rate given by Eq. (4.16)) in ideal MHD.

[14] To make the key point, we only analyse the channels' dependence in z direction. In a proper analysis of this problem, Pessah & Chan (2008) show that the MRI channel orientation in the horizontal plane depends on resistivity and viscosity.

However, from Eq. (4.85), which is valid for any wavevector, we see that their magnetic field would be diffused at a lower rate in resistive MHD. Therefore, there could be some modes whose MRI growth rate $\gamma_{\rm mri}$ in ideal MHD exceeds their dissipation rate in resistive MHD for $R_{\rm m} < 1$, i.e.

$$\gamma_{\rm mri} > \gamma_{\rm D}. \tag{4.90}$$

We would expect that such modes would still be MRI unstable for $R_{\rm m} < 1$, and their growth rate could be roughly estimated as

$$\tilde{\gamma}_{\rm mri} \approx \gamma_{\rm mri} - \gamma_{\rm D}. \tag{4.91}$$

In general, we could presume from this very simplified analysis that the fastest developing MRI modes in non-ideal MHD have smaller growth rates, $\tilde{\gamma}_{\rm MRI}$, and longer wavelengths than in ideal MHD. Moreover, the smaller the magnetic Reynolds number, the lower the maximum MRI growth rate. The rigorous calculations of Pessah & Chan (2008) confirm our heuristic considerations. For $R_{\rm m} = 1$, the maximum growth rate is one order of magnitude lower than in ideal MHD.

Pessah & Chan (2008) analytically studied the MRI in resistive-viscous MHD. We summarise the results relevant for us in Appendix B. These authors numerically solved the dispersion relation to find the fastest growing-modes for arbitrary hydrodynamic and magnetic Reynolds numbers. Pessah & Chan managed to find analytical expressions for $\tilde{\gamma}_{\rm MRI}$ only in limiting cases, usually when the Reynolds numbers were either very large or very small, e.g. for $R_{\rm m} \gg 1$ and $R_{\rm e} \ll 1$, or for $R_{\rm e} = R_{\rm m} \ll 1$. Already for $R_{\rm e} = R_{\rm m} = 10$, using expressions derived in ideal MHD to determine the fastest growing mode (Eqs. (4.16) and (4.17)) leads to errors of order $\approx 10\%$. For the MRI in core-collapse supernovae,where $R_{\rm e}, R_{\rm m} \gg 10$, we can safely use Eqs. (4.16) and (4.17) (see the discussion in Appendix B).

We come back now to the main discussion of MRI termination caused by tearing modes. We will consider a physically unrealistic scenario. We assume that the MRI can be described by Eqs. (4.16) and (4.17), whereas for tearing modes, we use resistive-viscous MHD equations. This scenario would be only justified if the KH instability could not develop in the system for some reason. Only then for $R_{\rm m} > 1$, the tearing modes could play any role. At first, this scenario may seem to be not worth our time, but it is quite important from a numerical point of view. In 2D MRI simulations assuming axial symmetry, the KH instability is suppressed and therefore the MRI can be terminated only by tearing modes. As we will soon see, exactly this happens in our 2D simulations.

We start the analysis of this termination scenario by first considering its precondition, i.e. when tearing modes grow at the rate of the fastest developing MRI ($\gamma_{\rm TM} = \gamma_{\rm MRI}$). In resistive MHD, we could estimate $\gamma_{\rm TM}$ with Eq. (4.32). When additionally viscosity is present in the system, we could use either Eq. (4.33) or Eq. (4.34). The careful reader could point out that all three equations were derived for magnetic field profile $b_{0z} \propto \tanh(\delta z)$ instead of $b_{0z} \propto \sin(\delta z)$), and without any background velocity. However, for the current discussion, these are irrelevant details.[15] We choose Eq. (4.33) for our further analysis (this equation is the most relevant for core-collapse supernova conditions), but it is easy to repeat it with the other equations. We first express Eq. (4.33) using the notation from the previous chapter. For the background magnetic field given

$$b_z(z) = b_0 \tanh(\delta z), \tag{4.92}$$

where b_0 is a constant amplitude and δ^{-1} defines the magnetic shear length, tearing modes with

[15] The tearing mode growth rate for a background magnetic field $b_{0z} \propto \sin(\delta z)$ is given by Eq. (3.85).

wavevectors $k_{\rm tm} \sim \delta$ growth a rate

$$\gamma_{\rm tm} = \frac{2}{3} 2^{1/3} \eta^{5/6} \nu^{-1/6} \left(\frac{b_0 k_{\rm tm}}{\sqrt{\rho_0}} \right)^{1/3} \delta^{4/3} \left(\frac{\delta}{k_{\rm tm}} - \frac{k_{\rm tm}}{\delta} \right). \tag{4.93}$$

The above equation cannot be used to determine the fastest growing tearing mode, i.e. $\gamma_{\rm TM}(k_{\rm TM})$, (see Chapter 3 for an explanation). However, in general $\gamma_{\rm tm} = \gamma_{\rm tm}(\eta, \nu,\ b_0, \rho_0, \delta, k_{\rm tm})$, and for given $\eta,\ \nu,\ b_0$ and ρ_0, a tearing mode growth rate can be treated as a function of two variables, i.e. $\gamma_{\rm tm} = \gamma_{\rm tm}(\delta, k_{\rm tm})$. Even thought we do not know the explicit form of $\gamma_{\rm tm}(\delta, k_{\rm tm})$, it is obvious from a physical point of view that for every δ, there must be a wavevector ($k_{\rm TM}(\delta)$) for which the growth rate is highest ($\gamma_{\rm TM}$).[16] Hence, $k_{\rm TM} = f\delta$, where f is a dimensionless function. Therefore, we can expect that the growth rate of the fastest developing tearing mode scales like[17]

$$\gamma_{\rm TM} \propto \eta^{5/6} \nu^{-1/6} \left(\frac{b_0}{\sqrt{\rho_0}} \right)^{1/3} \delta^{5/3}. \tag{4.94}$$

Now, we adopt the above equation to the MRI problem. The background magnetic field amplitude b_0 is replaced with $b_{\rm c}$, and δ with $k_{\rm MRI}$

$$\gamma_{\rm TM} \propto \eta^{5/6} \nu^{-1/6} c_{\rm Ac}^{1/3} k_{\rm MRI}^{5/3}. \tag{4.95}$$

The only missing part in this proportionality is a constant factor, which we denote as w, i.e.

$$\gamma_{\rm TM} = w \eta^{5/6} \nu^{-1/6} c_{\rm Ac}^{1/3} k_{\rm MRI}^{5/3}. \tag{4.96}$$

The wavevector of the fastest growing MRI mode is given by Eq. (4.17), hence

$$\gamma_{\rm TM} = w \left(1 - \frac{(2+\alpha)^2}{4} \right)^{5/6} \eta^{5/6} \nu^{-1/6} c_{\rm Ac}^{1/3} c_{{\rm A}z}^{-5/3} \Omega^{5/3}. \tag{4.97}$$

Now, we can compute for what value of $c_{\rm Ac}$ the tearing modes grow at the MRI rate. Comparing the above equation with the MRI growth rate equation (4.16) we have

$$w \left(1 - \frac{(2+\alpha)^2}{4} \right)^{5/6} \eta^{5/6} \nu^{-1/6} c_{\rm Ac}^{1/3} c_{{\rm A}z}^{-5/3} \Omega^{5/3} = -\frac{\alpha}{2} \Omega, \tag{4.98}$$

and hence

$$c_{\rm Ac} = c_{{\rm A}z}^{5} \nu^{1/2} \eta^{-5/2} \Omega^{-2} w^{-3} \left(1 - \frac{(2+\alpha)^2}{4} \right)^{-5/2} \left(\frac{-\alpha}{2} \right)^{3}, \tag{4.99}$$

i.e. the MRI channel amplitude, $b_{\rm c} = c_{\rm Ac}\sqrt{\rho}$, is not linearly proportional to the initial vertical magnetic field, $b_{0z} = c_{{\rm A}z}\sqrt{\rho}$, when the condition $\gamma_{\rm p} = \gamma_{\rm MRI}$ is met.

If we use Eq. (4.33) instead of Eq. (4.34) to calculate the tearing mode growth rate, we obtain

$$c_{\rm Ac} = c_{{\rm A}z}^{4} \nu^{1/2} \eta^{-2} \Omega^{-3/2} w^{-5/2} \left(1 - \frac{(2+\alpha)^2}{4} \right)^{-2} \left(\frac{-\alpha}{2} \right)^{5/2}, \tag{4.100}$$

[16] Not for every combination of $\eta,\ \nu,\ b_0,\ \rho_0$ and $delta$, tearing modes develop in a given system (see Chapter 3). In this discussion, we implicitly assume that these parameters are chosen such that the system is tearing mode unstable for certain $k_{\rm tm}$.

[17] There is no guarantee that because $\gamma_{\rm tm} \propto \eta^{5/6} \nu^{-1/6} (b_0/\sqrt{\rho_0})^{1/3}$ is valid for $k_{\rm tm} \sim \delta$ (Eq. (4.93)), then also $\gamma_{\rm TM} \propto \eta^{5/6} \nu^{-1/6} (b_0/\sqrt{\rho_0})^{1/3}$ holds for $k_{\rm TM}$. Hence, Eq. (4.94) might be incorrect. However, we only use this equation for "demonstrative purposes" in the discussion and not for rigorous calculations. Moreover, any other plausible form of $\gamma_{\rm TM}$ would not significantly change conclusions that we draw in this section.

where the constant w has a different value. Finally, in resistive-non-viscous MHD, we have from Eq. (4.32)

$$c_{\mathrm{Ac}} = c_{\mathrm{Az}}^4 \eta^{-3/2} \Omega^{-3/2} w^{-5/2} \left(1 - \frac{(2+\alpha)^2}{4}\right)^{-2} \left(\frac{-\alpha}{2}\right)^{5/2}. \tag{4.101}$$

Already at this point, we see how analysing simulations, in which the MRI is terminated by tearing modes, becomes more complicated. We would need to determine numerically the dependence of the amplification factor $\mathcal{A}$ on the initial magnetic field, which would require many more simulations. Even if we succeed, we would still not be sure whether we can extrapolate these results to the core-collapse supernova regime.

4.5 Numerical simulations

As we already discussed in the previous section, the MRI termination is a very complex process, which is too difficult to be fully described analytically. Therefore, numerical simulations are indispensable to study this highly-non linear phenomenon. Already Obergaulinger et al. (2009) numerically investigated this problem and the subsequent MRI driven turbulent phase in core-collapse supernovae. These authors concentrated on exploring a wide range of the parameter space (e.g. different initial magnetic field configurations, entropy and rotational profiles) mostly by means of 2D and also by a few 3D local ideal MHD simulations. For reasons discussed in the next section, Obergaulinger et al. (2009) used artificially enhanced initial magnetic fields to reduce the computational costs. However, these authors did not provide a reliable prescription how to extrapolate their results to realistic initial magnetic field strengths. Moreover, the influence of the numerical resistivity and viscosity on these authors' results remains unknown.

We extend these studies to non-ideal MHD, but our main goals being different. Instead of covering a large subset of the physical parameter space, we focus on one initial model, in which, apart from numerical parameters, we only vary the initial magnetic field, resistivity and viscosity. We address two questions:

1. Is it possible to extrapolate simulation results, which are obtained with artificially enhanced initial magnetic fields, to the regime relevant for core-collapse supernovae?
2. What is the influence of numerical resistivity and viscosity on these results?

In the next section, we describe the initial condition used in all our simulations. Then, we discuss numerical methods applied in our simulations. In Sections 4.5.2 and 4.5.3, we present the results of our 2D and 3D MRI simulations, respectively. In Sec. 4.5.4, we briefly compare these simulations, and finally, in Sec. 4.6, we discuss the implications of our results for core-collapse supernovae.

4.5.1 Initial conditions

Our initial setup is based on the one used by Obergaulinger et al. (2009). The simulation box centre is located in the equatorial plane at a radius $r_0 = 15.5$ km, which is roughly in the middle of a nascent proto-neutron star ($r_{\mathrm{PNS}} \approx 30$ km). In 3D simulations, the default box size is 1 km $\times$ 4 km $\times$ 1 km in r, ϕ and z direction, respectively. The boundary conditions are periodic in ϕ and z, and *shearing-disc* (Klahr & Bodenheimer 2003) in r direction. This choice is natural for

the ϕ direction, whereas some justification is required for the z direction, in which the system is obviously not periodic. However, the gravitational force's vertical component, F_{gz}, is much smaller than the radial one, F_{gr}, near the equatorial plane for $r \in [15,16]$ km and $z \in [-0.5,0.5]$ km, [18] and therefore the former one can be neglected. Under this approximation, one can assume periodicity in the vertical direction. Unlike in accretion disc simulations, we could not use the shearing sheet boundary condition in the radial direction, because they do not allow for global gradients of thermodynamical variables (which are present in core-collapse supernovae) in the simulation domain. Therefore, following Obergaulinger et al. (2009), we use the shearing disc boundary condition, which is able to take these gradients into account. We do not perform a transformation to the frame co-rotating with the fluid and we assume radial periodicity of the perturbations, e.g.

$$\delta\rho(r,t) \equiv \rho(r,t) - \rho(r,0), \tag{4.102}$$

where $\delta\rho(r,t)$ is by definition an L_r-periodic perturbation at time t, and $\rho(r,0)$ is the initial background state. Apart from the angular velocity,[19] these boundary conditions are applied to density, momentum and entropy.

In 2D simulations, axial symmetry is assumed and therefore all quantities are independent of ϕ. The default simulation box size is 1 km $\times$ 1 km in the (r,z) plane.

As an approximate model for neutron star matter, we use the hybrid equation of state (EOS) of Keil et al. (1996). The total gas pressure, p, consists of two parts: baryonic, p_b, and thermal p_{th}. They are respectively given by

$$p_b = \kappa\rho^{\Gamma_b}, \text{ and} \tag{4.103}$$

$$p_{th} = (\Gamma_{th} - 1)e_{th}, \tag{4.104}$$

where κ is the EOS's polytropic constant, Γ_b and Γ_{th} are the barotropic- and thermal- adiabatic index, respectively, and e_{th} is the thermal part of the internal energy e, i.e. $e_{th} = e - p_b/(\Gamma_b - 1)$. We only consider subnuclear densities, $\rho < \rho_{nuc} = 2 \times 10^{14}$ g cm^{-3}, since in our simulations the density never exceeds a few times 10^{13} g cm^{-3}.

The rotational profile is taken from the global MRI simulations of Obergaulinger et al. (2006b):

$$\Omega = \Omega_0 \left(\frac{r}{r_0}\right)^{\alpha}, \tag{4.105}$$

where $\Omega_0 = 1900$ s^{-1}, $r_0 = 15.5$ km and $\alpha = -1.25$ (for the Keplerian profile, the dimensionless parameter $\alpha = -1.5$). The resulting centrifugal force is insufficient to balance the gravitational attraction. The gas is kept in an initial hydrodynamical equilibrium by an additional pressure gradient, so that

$$\rho\partial_r\varphi - \partial_r p + r\rho\Omega^2 = 0, \tag{4.106}$$

where φ is the gravitational potential. The initial distributions of angular velocity, pressure, density and gravitational potential are depicted in Fig. 4.3.

The choice of the initial magnetic field is a more subtle issue. In all simulations, we used a somewhat idealised initial setup. The magnetic field only has a constant component in the z direction, i.e.

$$\mathbf{b} = b_{0z}\hat{\mathbf{z}}, \tag{4.107}$$

[18] The ratio F_{gz}/F_{gr} is highest at $r = 15$ km and $z = \pm 0.5$ km, yet it is as small as 0.03.

[19] In the shearing sheet method, by construction, angular velocity gradients are not present in the system.

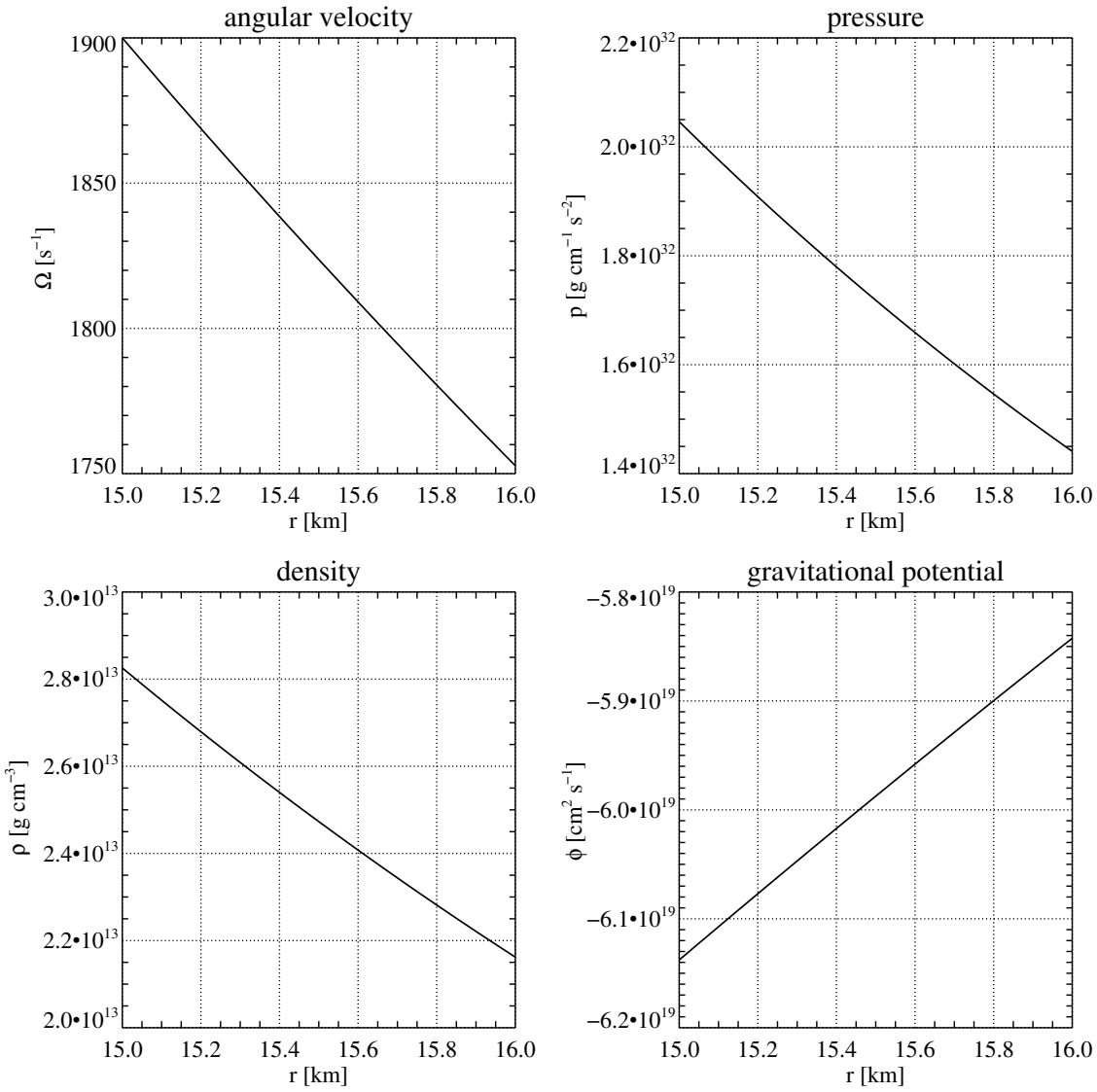

Figure 4.3: Initial conditions used in all our 2D and 3D MRI simulations.

This field geometry is a popular choice in MRI simulations, (see, e.g. Balbus & Hawley (1991); Hawley & Balbus (1991); Sano & Inutsuka (2001); Obergaulinger et al. (2009)), since the vertical component is the most important one for the development of the instability (Balbus & Hawley 1998). Another common choice is a so called *zero net flux* configuration (see, e.g. Fromang et al. (2007); Fromang & Papaloizou (2007); Obergaulinger et al. (2009)), in which the magnetic field has a sinusoidal radial dependence, i.e. $\mathbf{b} \propto \hat{\mathbf{z}} \sin(k_r r)$, where k_r is chosen in such a way that an integer number of wavelengths fits the computational domain ($k_r = 2\pi n / L_r$, L_r being the radial box length and n a natural number).

The initial magnetic field amplitude, b_{0z}, requires some further comments. According to state-of-the-art stellar evolution codes, the pre-collapse magnetic field for the most strongly magnetised progenitors, is less than about 10^9 G. In the initial collapse phase, the magnetic field can be amplified by compression by two orders of magnitude to $\approx 10^{11}$ G (Meier et al. 1976). From Eq. (4.17) we estimate, that given the proto-neutron star conditions, the length of the fastest growing MRI

mode is

$$\lambda_{\rm MRI} \approx 6.9 \text{ cm} \left(\frac{b_{0z}}{10^{11} \text{ G}}\right) \left(\frac{\rho}{2.5\times10^{13} \text{ g cm}^{-3}}\right)^{-1/2} \left(\frac{\Omega}{1900 \text{ s}^{-1}}\right)^{-1}. \quad (4.108)$$

Assuming that approximately 10 zones are required to properly resolve an MRI channel,[20] we would need a resolution of $\approx 10^5$ zones in each direction. Such a high resolution is already unaffordable in 2D simulations, not to mention 3D ones. One could reduce the amount of necessary zones by taking a significantly smaller box of size 100^3 cm^3. Then, only 100^3 zones would be required to resolve the MRI growth. However, this would not solve the problem, because the rotational velocity ($v_\phi \approx 3\times10^9$ cm s^{-1}) would limit the allowed timestep to $\Delta t \approx 3\times10^{-8}$ ms, i.e. almost 10^9 iterations would be required to simulate the MRI until the termination point (≈ 15 ms).

Therefore, Obergaulinger et al. (2009) adopted a different approach to reduce the computational cost. They used initial magnetic fields, which were two orders of magnitude higher ($b_{0z} \approx 10^{13}$ G), to increase the wavelength of fastest growing MRI mode to ≈ 10 m. This reduces the minimum resolution to $\approx 100\times400\times100$ zones in a 1 km $\times$ 4 km $\times$ 1 km box. Because the maximum allowed timestep increases to $\Delta t \approx 3\times10^{-4}$ ms, less than 10^6 iterations are required to simulate 15 ms, which is an affordable number.

In our simulations, we follow Obergaulinger et al. (2009) and also use artificially enhanced initial magnetic field amplitudes. We made sure, however, that for the chosen values, only an integer number of the fastest growing MRI modes fits into the computational domain. Otherwise, they could be suppressed by an unfavourable box size, which is an undesired, yet easy to avoid numerical artefact.[21]

To trigger the MRI, Obergaulinger et al. (2009) added random velocity perturbations of the form

$$\mathbf{v_1} = \Omega r \left[0.1\delta\Re_r(r,\phi,z)\hat{\mathbf{r}} + \delta\Re_\phi(r,\phi,z)\hat{\phi} + \delta\Re_z(r,\phi,z)\hat{\mathbf{z}}\right] \quad (4.109)$$

to the background velocity profile

$$\mathbf{v_0} = \Omega r\hat{\phi}, \quad (4.110)$$

where $\Re_r(r,\phi,z), \Re_\phi(r,\phi,z)$ and $\Re_z(r,\phi,z)$ are random numbers in the range $[-1,1]$, and δ is the perturbation amplitude (of order 10^{-5}). Hence, the initial velocity field is given by

$$\mathbf{v} = \Omega r \left[0.1\delta\Re_r(r,\phi,z)\hat{\mathbf{r}} + \{1+\delta\Re_\phi(r,\phi,z)\}\hat{\phi} + \delta\Re_z(r,\phi,z)\hat{\mathbf{z}}\right]. \quad (4.111)$$

Sometimes these perturbations failed to excite the fastest growing MRI modes (see next section for more detail). To make sure that these modes are triggered in every simulation, we added a sinusoidal perturbation, whose wavelength is equal to $\lambda_{\rm MRI}$, to the radial velocity component. The final form of the initial velocity field reads

$$\mathbf{v} = \Omega r \left[\{0.1\delta\Re_r(r,\phi,z) + \varepsilon\sin(k_z z)\}\hat{\mathbf{r}}\} + \{1+\delta\Re_\phi(r,\phi,z)\}\hat{\phi} + \delta\Re_z(r,\phi,z)\hat{\mathbf{z}}\right], \quad (4.112)$$

where k_z is the radial perturbation wavevector and ε is the amplitude of the sinusoidal perturbation. If not otherwise written, $k_z = k_{\rm MRI}$, $\delta = 10^{-5}$, and $\varepsilon = 2\times10^{-6}$.

[20] We discuss this issue in detail in Section 4.5.2 on 2D simulations. It turns out that 10 zones is a good estimate.

[21] We observed that in simulations with a magnetic field amplitude, for which say 2.5 fastest growing modes would fit in the domain, usually three MRI channels would form. Depending on the initial perturbations, there were two possible scenarios: either all three channels had the same length (hence these modes were shorter than the fastest growing ones), or two channels had the length of the fastest growing one, and one smaller channel which grew considerably more slowly. In both cases, the MRI developed at the rate which was lower than theoretically expected.

Numerical methods

In the previous chapter, we investigated the code's numerical resistivity and viscosity with the help of wave damping and the tearing mode simulations. The numerical dissipation is always an undesirable effect, which can sometimes drastically change the dynamics of the simulated system. Ideally, to minimise the numerical errors, we would like to use an infinitely high resolution with an infinitely small time-step. Because such a simulation would require an infinite amount of computational time, one needs to find an appropriate trade off between the desired accuracy and the computational cost. Based on the results from the previous chapter, we chose a numerical setup for 2D and 3D MRI simulations.

We decided to use the code's best reconstruction scheme (MP9), even though it requires more ghost zones than the other schemes. This aspect is especially important in 3D simulations, in which MPI parallelisation is exploited. The increased number of ghost zones greatly decreases the physical part of the simulated domain. To partially reduce this inevitable computational loss, we used a hybrid code parallelisation, i.e. a combination of OpenMP and MPI techniques.[22] The accuracy offered by the MP9 scheme (very low numerical dissipation in comparison to the other schemes) well justifies this extra computational cost.

When it comes to the time integration, we decided to employ the RK3 scheme. In the tearing mode simulations, the main contribution to the numerical dissipation came form the spatial discretisation errors. We expect this to be also the case in the MRI simulations. Therefore, using the RK4 time integrator, which is computationally one third more expensive, is not justified. The CFL factor was set to $C_{\mathrm{CFL}} = 0.7$ for stability reasons. For higher values, the tearing modes simulations became numerically unstable, and for lower values there was no accuracy gain observed.

In the wave damping simulations, all three Riemann solvers (LF, HLL and HLLD) performed equally well. The teaing mode tests showed that, as expected, the LF solver was inferior to the other ones and introduced much more numerical resistivity to the system. Unfortunately, it was impossible to compare the HLL and HLLD solvers in those tests. We decided to use the HLLD Riemann solver, because it is (theoretically) the most accurate one.

4.5.2 2D simulations

The main advantage of 2D simulations is that they are computationally less expensive, but their practical application is very limited, because the KH instability cannot develop due to axis symmetry constraint (Pessah (2010)) and the MRI can only be terminated by tearing modes. For the hydrodynamic and magnetic Reynolds numbers much larger than one (the parameter regime relevant for the core-collapse supernovae), the KH instability develops much faster than the tearing modes. This means that in 2D simulations, the MRI will reach amplitudes higher than in reality, before the channels are destroyed by tearing modes, which are the only allowed parasitic instability.

Even though 2D simulations overestimate the MRI termination point, they can be used as auxiliary tests for 3D simulations. Firstly, in 2D, we can test whether a chosen resolution is sufficiently high to resolve the fastest growing MRI mode properly . Secondly, 2D simulations can be used to verify the theoretical predictions of Pessah & Chan (2008) for the length and growth rate of fastest growing MRI mode in non-ideal MHD (see Appendix B).

[22] To put it in a nutshell, in this hybrid parallelisation, every MPI process, which solves the MHD equations in a subdomain of the computational domain, can open several OpenMP threads to speed up time consuming loop calculations.

Fastest growing MRI modes

We extended the studies of Obergaulinger et al. (2009) to non-ideal MHD. If not otherwise written, the resistivity and shear viscosity were set to $\nu = \eta = 4.45 \times 10^8$ cm^{2}s^{-1}, which for $b_{0z} = 4.6 \times 10^{13}$ G corresponds to Reynolds numbers (R_e and R_m) equal to 100. Our first goal is to find the magnetic field values, for which an integer number of MRI channels fits into the computational domain. In order to simulate exactly the three, four and five fastest growing MRI modes in the box of the size 1 km, their length has to be equal to $\lambda_\mathrm{MRI} = 0.333$ km, 0.25 km and 0.2 km, respectively.

According to Pessah & Chan (2008) (see Appendix B), the corresponding magnetic fields are $b_{0z} = 4.6 \times 10^{13}$ G, 3.45×10^{13} G and 2.76×10^{13} G, respectively. We verify these predictions with the help of simulations having a resolution of 100^2 zones. For $b_{0z} = 2.76 \times 10^{13}$ G, five MRI channels should be observed. In the first simulation, we triggered the MRI with random perturbations in velocity (see Eq. (4.109)) and only four channels formed (see Fig. 4.4). This could be misinterpreted that the calculations of Pessah & Chan (2008) must be off. However, the correct explanation of this phenomenon is different. The formed channels do not have an equal width (see bottom part of Fig. 4.4). The upper ones are wider and their amplitudes are smaller, hence their growth rates must be lower. In the upper part of the box, the initial random perturbations must have been favourable for more slowly growing MRI modes. Even though their growth rates are lower, they can still dominate the initial evolution, if their amplitudes are considerably higher than those of the fastest growing modes. Once the channel structure is established, the MRI will not change it, but only amplify their amplitudes. The MRI growth rate averaged over the box was equal to, $\gamma_\mathrm{MRI} \approx 1077$ s^{-1}.

In general, such a phenomenon, i.e. the emergence of not identical modes, can possibly be encountered in nature, however, it is undesirable for our purposes. In the end, we want to verify the MRI termination model, which assumes that only the fastest growing modes are present in the system. To avoid the emergence of different modes we used somewhat initial random perturbations, adding a small sinusoidal velocity component $v_r \propto \sin(k_\mathrm{MRI} z)$ (see Eq. (4.112)). With the help of this simple trick, the fastest growing MRI modes formed in all simulations. We point out that we do not use the whole MRI channels as initial conditions, because the velocity components v_ϕ and v_z are only randomly perturbed and the magnetic field components b_r and b_ϕ remain unchanged. Moreover, the amplitudes of the random and sinusoidal perturbations are of the same order (10^{-5}). To test how much the initial perturbations can affect the MRI termination amplitude, we run additional 2D and 3D simulations. We will come back to this issue several times later in the discussion.

In another simulation, in which the modified (i.e. random plus sinusoidal) perturbations from Eq. (4.112) were used, five MRI channels formed (see Fig. 4.5). The instability growth rate was $\gamma_\mathrm{MRI} \approx 1103$ s^{-1}, which is larger than in the previous simulation. However, this is not yet a proof that for $b_{0z} = 2.76 \times 10^{13}$ G, the length of the fastest growing mode is $\lambda_\mathrm{MRI} = 0.2$ km. To test that, we ran four additional simulations with initial magnetic fields in the range 2.6–2.9×10^{13} G and the same type of perturbations. The simulations results are presented in Table 4.1. The MRI growth rates are almost equal, the maximum being observed for $b_{0z} = 2.76 \times 10^{13}$ G. Another question, which needs to be answered is whether using the MP9 reconstruction scheme, 20 zones are sufficient to properly resolve one MRI channel (there were 5 channels in the box, and 100 zones were used in z direction).

One could say, that since the equations of Pessah & Chan (2008) did such a good job at predicting the fastest growing MRI mode, we should just compare now the growth rate measured in the

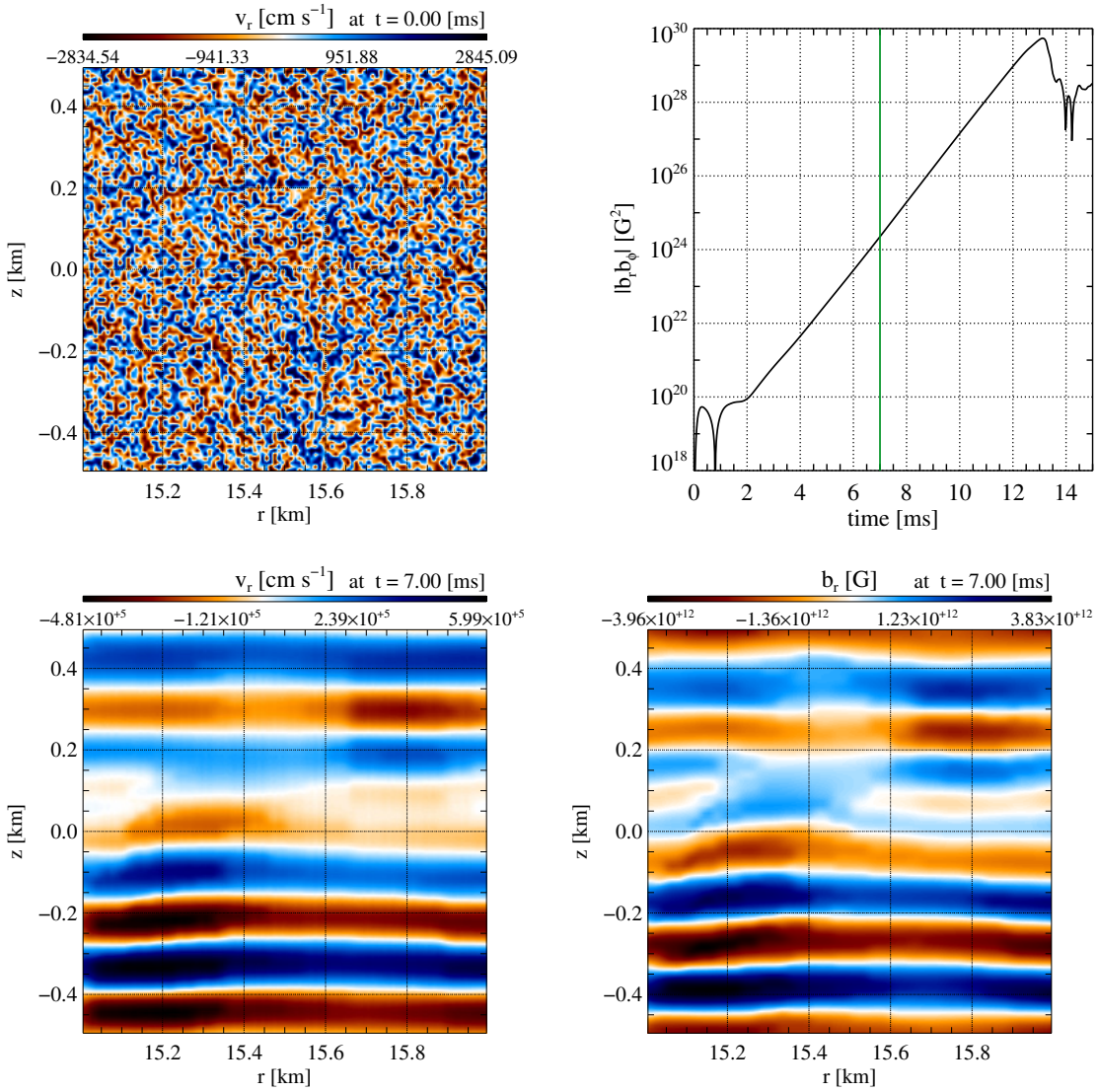

Figure 4.4: 2D MRI simulation with a resolution of 100^2 zones. Given the initial magnetic field $b_{0z} = 2.76 \times 10^{13}$ G (and the other initial conditions described in the main text), the instability would have the highest growth rate for five equally wide MRI channels. The instability was triggered with random velocity perturbations and only four MRI channels formed (compare with Fig. 4.5). *Top left*: initial random perturbations of the radial velocity component v_r. *Top right*: time evolution of the volume averaged Maxwell stress component $|b_r b_\phi|$. From $t \approx 3$ ms to $t \approx 11$ ms, the MRI is fully operational and the magnetic field is exponentially amplified at a constant rate. The green vertical line indicates the time ($t = 7$ ms) at which the snapshots in the bottom panels are taken. *Bottom left*: radial velocity, v_r, at $t = 7$ ms, when four unequal MRI channels are clearly visible. *Bottom right*: radial magnetic field component, b_r, at $t = 7$ ms.

simulations to its theoretically expected value. Well, the problem is that in " numerics" things are not always so straightforward. Given the simulation parameters, the maximum growth rate should read

$$\gamma_{\rm MRI} \approx 1144 \text{ s}^{-1}, \tag{4.113}$$

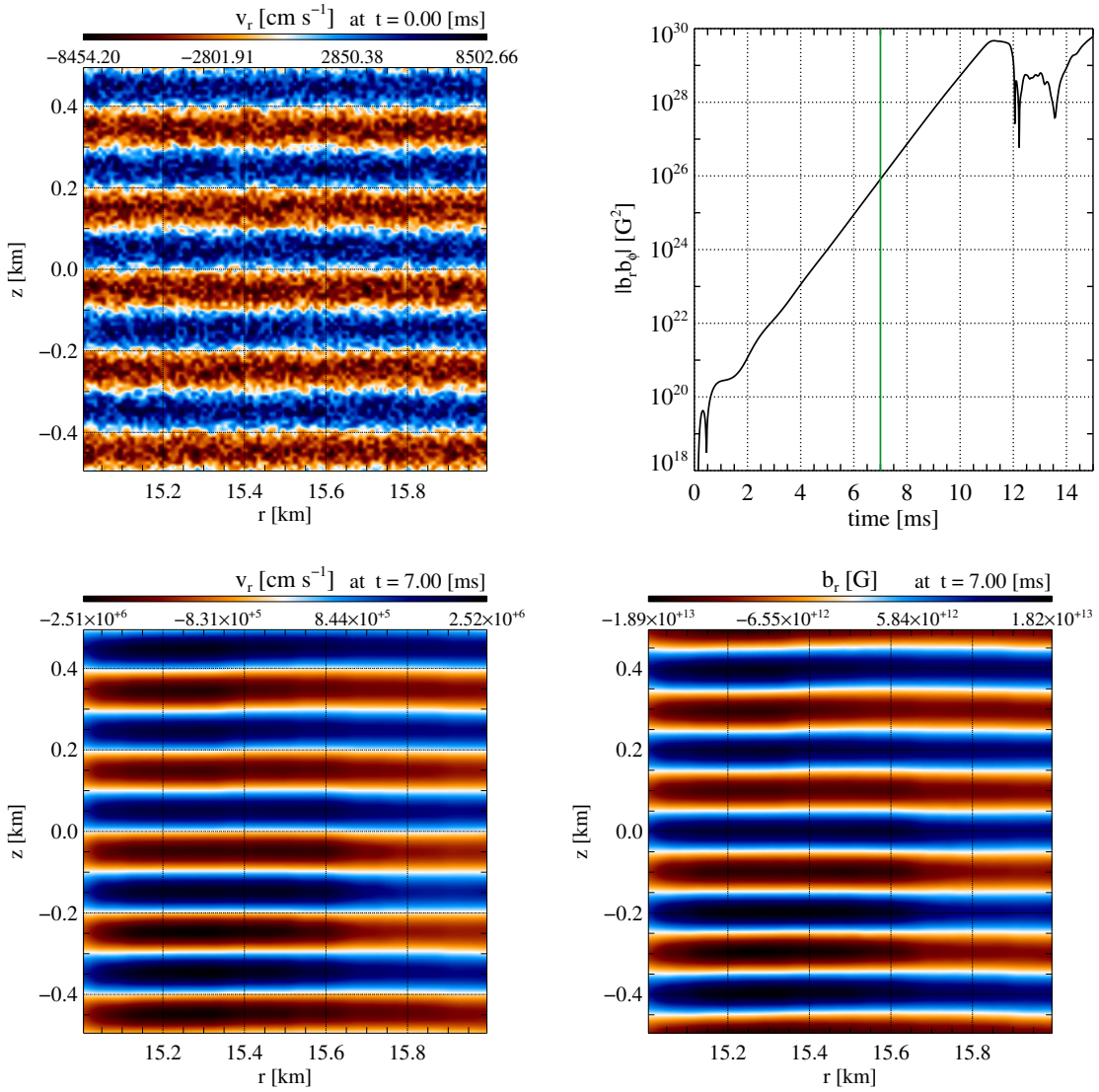

Figure 4.5: Same as Fig. 4.4, but for initial perturbations consisting of two parts: a random one in all three velocity components, and a sinusoidal one (of the wavelength equal to that of the fastest growing MRI mode, $\lambda_{\rm MRI}$) only in the radial component v_r. After approximately two milliseconds, five MRI channels formed (compare with Fig. 4.4). *Bottom left*: radial velocity v_r at $t = 7$ ms. Five equal MRI channels are clearly visible. *Bottom right*: note that the magnetic field channels are shifted in the z direction by $\lambda_{\rm MRI}/4$ with respect to the velocity channels, in accordance with Eqs. (4.18) and (4.19).

but in the simulations we measured $\gamma_{\rm MRI} \approx 1103$ s^{-1} (see Table 4.1). At this point, one could draw premature the conclusion that with 20 zones per MRI channel, the instability must have been underresolved, i.e. the numerical resistivity, η_*, and viscosity, ν_*, must have been higher than $\eta = \nu = 4.45 \times 10^8$ cm^{2}s^{-1}. Therefore, the numerical dissipation reduces the instability growth rate. To test whether this is a plausible explanation, we can use Eqs. (3.1) and (3.5) for the numerical viscosity, ν_*, and resistivity, η_*, respectively, which we proposed and tested in the

b_{0z} [10^{13} G]	$\gamma_{\rm MRI}$ [$\rm s^{-1}$]
2.6	1100.6
2.7	1102.3
2.76	1102.8
2.8	1102.0
2.9	1102.0

Table 4.1: Results of the 2D simulations with a resolution of 100×100 zones. The resistivity and viscosity are set to $\nu = \eta = 4.45 \times 10^8$ $\rm cm^2 s^{-1}$, which corresponds to Reynolds numbers $R_{\rm e} = R_{\rm m} \approx 36$. For an initial magnetic field $b_{0z} = 2.76 \times 10^{13}$ G, the MRI growth rate is highest and $\lambda_{\rm MRI} = 0.2$ km.

previous chapter. For the readers convenience, we write these equations again:

$$\nu_* = \mathfrak{N}_\nu^{\Delta x} \times \mathcal{V} \times \mathcal{L} \times \left(\frac{\Delta x}{\mathcal{L}}\right)^r + \mathfrak{N}_\nu^{\Delta t} \times \mathcal{V} \times \mathcal{L} \times \left(\frac{\mathcal{V}\Delta t}{\mathcal{L}}\right)^q, \tag{4.114}$$

$$\eta_* = \mathfrak{N}_\eta^{\Delta x} \times \mathcal{V} \times \mathcal{L} \times \left(\frac{\Delta x}{\mathcal{L}}\right)^r + \mathfrak{N}_\eta^{\Delta t} \times \mathcal{V} \times \mathcal{L} \times \left(\frac{\mathcal{V}\Delta t}{\mathcal{L}}\right)^q, \tag{4.115}$$

where $\mathfrak{N}_\nu^{\Delta x}$, $\mathfrak{N}_\nu^{\Delta t}$,$\mathfrak{N}_\eta^{\Delta x}$, $\mathfrak{N}_\eta^{\Delta t}$, r, and q depend on the numerical scheme, $\mathcal{L}$ and $\mathcal{V}$ are the characteristic length and speed of the system, respectively. To make use of these equations, we have to specify all these coefficients. The characteristic length of the system must obviously be equal to the MRI channel width, i.e. $\mathcal{L} = \lambda_{\rm MRI}$. As for the characteristic velocity, like in the cases of the wave damping and tearing mode simulations, we should take the fast magnetosonic speed, i.e. $\mathcal{V} = c_{\rm ms}$. When it comes to the coefficients $\mathfrak{N}_\nu^{\Delta x}$, $\mathfrak{N}_\nu^{\Delta t}$,$\mathfrak{N}_\eta^{\Delta x}$, $\mathfrak{N}_\eta^{\Delta t}$, a, and b, we have two possibilities. We could take the values determined in either the wave damping or the tearing mode simulations. We think that the second choice is more reasonable, since we do not want to overestimate the numerical dissipation and the tearing mode simulations were numerically more demanding. It is true that in this case, we did not manage to determine the numerical dissipation coefficients caused by the time integration. However, we presume that also for the MRI and especially for the secondary instabilities, the main contribution to the numerical errors mainly results from the spatial discretisation. In the tearing mode simulations, we did not measure ν_* either. However, it seems reasonable to assume that for the MRI, $\nu_* \approx \eta_*$. Moreover, resistivity influences the MRI more than viscosity does (Pessah & Chan 2008). Finally, we write in a form that is also valid for parasitic instabilities that

$$\nu_* \approx \eta_* = \mathfrak{N}_\eta^{\Delta x} \times \mathcal{V} \times \mathcal{L} \times \left(\frac{\Delta x}{\mathcal{L}}\right)^r, \tag{4.116}$$

and after applying the above equation to the MRI problem

$$\nu_* \approx \eta_* = \mathfrak{N}_\eta^{\Delta x} \times c_{\rm ms} \lambda_{\rm MRI} \left(\frac{\Delta z}{\lambda_{\rm MRI}}\right)^r, \tag{4.117}$$

where for the MP9 reconstruction scheme[23] $\mathfrak{N}_\eta^{\Delta x} = 170 \pm 220$ and $r = 7.56 \pm 0.55$ (see Table 3.12). In Eq. (4.117), we used Δz instead of Δx, because this is the most important dimension for

[23] In the MRI simulations we use the HLLD Riemann solver, whereas $\mathfrak{N}_\eta^{\Delta x} = 170 \pm 220$ was determined for the LF solver (for the former one, $\mathfrak{N}_\eta^{\Delta x}$ was immeasurably smaller). Taking the estimator for $\mathfrak{N}_\eta^{\Delta x}$ of the more dissipative solver, can lead to an overestimation of the numerical resistivity and viscosity. Since we want to estimate the upper limit of the numerical dissipation, this step is acceptable.

resolving the MRI channels. As we can see, the whole effort put in the previous chapter now pays off. We obtain neat expressions, which will allow us to estimate the numerical dissipation for a new problem. Given the initial conditions of the above MRI simulations, $c_{\rm ms} \approx 3.3 \times 10^9$ cms^{-1}, $\lambda_{\rm MRI} = 2 \times 10^4$ cm and $\Delta z = 10^3$ cm, we obtain from Eq. (4.117) that

$$\nu_* \approx \eta_* = 1.5 \times 10^6 \pm 2.8 \times 10^6 \text{ cm}^2\text{s}^{-1}. \tag{4.118}$$

Obviously, we should not conclude that within the errors, there is a chance that $\nu_* \approx \eta_* \approx 0$ cm^{2}s^{-1}, but we can estimate that

$$\nu_* \approx \eta_* < 5 \times 10^6 \text{ cm}^2\text{s}^{-1}. \tag{4.119}$$

When we compare this values to the parameter values from above $\nu = \eta = 4.45 \times 10^8$ cm^{2}s^{-1}, we see that the numerical dissipation, when it comes to MRI channel evolution (this is a very important point), is much smaller than the physical one and should not significantly influence the MRI growth rate. It would be interesting to estimate for what resolution (or equivalently Δz), both types of dissipation (physical and numerical) would become comparable. In a simulation with 10 zones per MRI channel (hence with a twice lower resolution, i.e. 50^2 zones for the box), the numerical resistivity and viscosity should approximately equal

$$\nu_* \approx \eta_* = 1.4 \times 10^6 \pm 2.7 \times 10^8 \text{ cm}^2\text{s}^{-1}. \tag{4.120}$$

One could say that this seems to be a reasonable result, because 10 zones should be more than appropriate for such moderate numerical Reynolds numbers (i.e. $R_{\rm e} = R_{\rm m} \approx 36$) with the MP9 reconstruction scheme. In the end, the MRI channels have exactly the shape of the sine function, and for the wave damping simulations performed with the MP9 schemes, we achieved numerical Reynolds numbers, which are lower than 10^{-4} (see e.g. Figs. 3.2, 3.7 and 3.14). However, there is one very important point, which must not be overlooked, when estimating the numerical dissipation. The numerical resistivity and viscosity do linearly depend on the characteristic velocity, $c_{\rm ms}$. Therefore,

$$\text{for } c_{\rm ms} \to \infty, \qquad \nu_*, \eta_* \to \infty! \tag{4.121}$$

At first, this results may seem to be unintuitive. It is not only the number of zones, which we use to resolve a given phenomenon, that matters.

If we claim, that this is not insufficient resolution causing the discrepancy between the theoretical prediction ($\gamma_{\rm MRI} \approx 1144$) and the measured in simulation MRI growth rate ($\gamma_{\rm MRI} \approx 1103$) , we should give a better explanation. The sceptical reader may say that it is our estimate of the numerical dissipation (Eq. (4.119)), which is off. However, tt is not difficult to explain this discrepancy. We used the equations of Pessah & Chan (2008) to determine the fastest growing mode, given $r = r_0 = 15.5$ km and therefore $\Omega_0 = \Omega(r_0) = 1900$ s^{-1}, and $c_{{\rm A}z} = c_{{\rm A}z}(r_0) \approx 5.52 \times 10^6$ cm s^{-1}. However, the box extends from $r = 15$ km to $r = 16$ km, and both Ω and $c_{{\rm A}z}$ depend on r. Ω is given by Eq. (4.1) and $c_{{\rm A}z}$ changes, because the density is not constant (see Fig. 4.3 and Eq. (4.13)). In Appendix B, we show that for $R_{\rm e} = R_{\rm m} \approx 36$ (the Reynolds numbers of the simulations), the growth rate and wavelength of the fastest developing mode are given by

$$\gamma_{\rm MRI} = \tilde{\gamma}\Omega, \qquad \text{and} \tag{4.122}$$

$$\lambda_{\rm MRI} = \frac{2\pi}{\tilde{k}} \frac{c_{{\rm A}z}}{\Omega}, \tag{4.123}$$

where the dimensionless growth rate $\tilde{\gamma} \approx 0.602$ and the dimensionless wavevector $\tilde{k} \approx 0.891$. At $r = 15$ km, $\Omega \approx 1826$ s^{-1} and $c_{\mathrm{A}z} \approx 5.20 \times 10^6$ cm s^{-1}, while at $r = 15$ km, $\Omega \approx 1970$ s^{-1} and $c_{\mathrm{A}z} \approx 5.94 \times 10^6$ cm s^{-1}. This implies

$$\gamma_{\mathrm{MRI}}(r = 15 \text{ km}) = 1207 \text{ s}^{-1}, \tag{4.124}$$

$$\lambda_{\mathrm{MRI}}(r = 15 \text{ km}) = 0.189 \text{ km}, \tag{4.125}$$

and

$$\gamma_{\mathrm{MRI}}(r = 16 \text{ km}) = 1099 \text{ s}^{-1}, \tag{4.126}$$

$$\lambda_{\mathrm{MRI}}(r = 16 \text{ km}) = 0.233 \text{ km}. \tag{4.127}$$

Moreover, the maximum growth rates given in Eqs. (4.124) and (4.126) hold for modes with wavelengths given by Eqs. (4.125) and (4.127), respectively. However, in the simulations, the channels have a length $\lambda_{\mathrm{MRI}} = 0.2$ km everywhere in the box, i.e. at $r = 15$ km and $r = 16$ km, they will grow at rates lower than those given by Eqs. (4.124) and (4.126), respectively. Finally, Eqs. (4.124)-(4.127) are not entirely correct, because we neglected that at the edges of the box, i.e. for $r = 15$ km or $r = 16$ km, the Reynolds numbers slightly differ from those in the middle of the box, i.e. at $r_0 = 15.5$ km. Thus, also the dimensionless $\tilde{\gamma}$ and $\tilde{k}$ appearing in Eqs. (4.122) and (4.123), respectively, have slightly different values.

All in all, is just a "lucky coincidence" that for the same wavevector (predicted with the help of the equations from Pessah & Chan (2008)), both the MRI grow rate in the middle of the box and the box integrated growth rate of the MRI are the highest.

Armed with this knowledge, we once again have a look at the bottom panels of Fig. 4.4, where we presented the results of the simulation with initial random perturbations in velocity. The magnetic field and the velocity in the uppermost channel that is wider than $\lambda_{\mathrm{MRI}} = 0.2$ km, are amplified at a lower rate than in the two bottom channels whose widths ≈ 0.2 km. Furthermore, the amplitudes of the bottom channels are larger at smaller radii ($r < r_0$), because $\gamma_{\mathrm{MRI}}(r = 15 \text{ km}) > \gamma_{\mathrm{MRI}}(r = 16 \text{ km})$ (compare Eqs. (4.124) and (4.126)). For the upper channels, the situation is opposite. The amplitudes are higher for $r > r_0$, because the channel width is closer to the "optimum value", for which the MRI grows fastest (see Eq. (4.127)). As we can see, this simulation is a very good illustration of the above discussed theory, i.e. Eqs. (4.124)-(4.127).

Our discussion has shown that even such an apparently trivial problem, like the MRI growth rate in a numerical simulation, becomes quite complex when investigated in more detail. To see whether the numerical dissipation significantly affected the simulation results, we have to perform convergence tests. they are usually only done in 1D and 2D simulations, because 3D simulations are not only more expensive, but also their computational cost increases with the 4-th power of the (linear) resolution.

To test whether in the simulations with $b_{0z} = 2.76 \times 10^{13}$G and a resolution of 100^2 zones, the numerical dissipation played an important role, we performed a simulations with twice that resolution, i.e. with 200^2 zones. The MRI growth rate was $\gamma_{\mathrm{MRI}} = 1102.3$ s^{-1}. Hence, the MRI channels were not underresolved in the previous simulations (if that were the case the MRI growth rate would be lower than theoretically expected). Thus , we conclude that 20 zones are sufficient to resolve one MRI channel with the MP9 scheme. However, as we will discuss it later, resolving the MRI channel does not imply that we resolve the complete MRI physics. To simulate properly the parasitic instabilities developing on top of the MRI channels, a much higher resolution is required.

We performed analogous tests for a magnetic field $b_{0z} = 3.45 \times 10^{13}$G. In the simulation with random initial perturbations (Eq. (4.111)), four MRI channels of unequal length formed and

b_{0z} [10^{13} G]	$\gamma_{\rm MRI}$ [$\rm s^{-1}$]
3.3	1111.8
3.4	1111.9
3.45	1112.8
3.5	1110.5
3.6	1107.0

Table 4.2: Results of 2D simulations with a resolution of 100×100 zones. The resistivity and viscosity were set to $\nu = \eta = 4.45 \times 10^8$ $\rm cm^2 s^{-1}$, which corresponds to Reynolds numbers $R_{\rm e} = R_{\rm m} \approx 56$. For the initial magnetic field $b_{0z} = 3.45 \times 10^{13}$G, the MRI growth rate is highest and $\lambda_{\rm MRI} = 0.25$ km.

$\gamma_{\rm MRI} \approx 1063.7$ $\rm s^{-1}$. In the simulation with additional sinusoidal v_r perturbations, four equally wide channels formed and $\gamma_{\rm MRI} \approx 1112.8$ $\rm s^{-1}$. We ran four additional simulations with initial magnetic fields varying from $b_{0z} = 3.3 \times 10^{13}$ G to $b_{0z} = 3.6 \times 10^{13}$ G. The measured growth rates are presented in Table 4.2. They confirm that the fastest growing mode has a wavelength $\lambda_{\rm MRI} = 0.25$ km, for $b_{0z} = 3.45 \times 10^{13}$ G. We also performed a convergence test, i.e. we ran a simulation with twice the resolution (200^2 zones) and a magnetic field $b_{0z} = 3.45 \times 10^{13}$ G. The MRI growth rate was $\gamma_{\rm MRI} \approx 1111.7$ $\rm s^{-1}$.

In an analogous way, we verified that the equations of Pessah & Chan (2008) give correct predictions that for $b_{0z} = 4.6 \times 10^{13}$ G, the fastest growing MRI mode has a wavelength $\lambda_{\rm MRI} = 0.333$ km, i.e. exactly three modes fit into the computational domain.

MRI termination

After these auxiliary simulations concentrating on the MRI growth rate and channel structure, we investigated the MRI termination problem. We set the initial magnetic field to $b_{0z} = 4.6 \times 10^{13}$ G and ran a simulations with a resolution of 100^2 zones. The results are presented in Fig. 4.6. From the initial perturbations given by Eq. (4.112), after ≈ 3 ms, three coherent MRI channels emerged (see the upper right panel of the figure) and the instability was amplifying the magnetic field at a constant rate until $t \approx 11$ ms (see the upper left panel). At $t = 11.86$ ms, the box-integrated Maxwell stress component $|b_r b_\phi|$ reached a maximum. According to our definition, this means that the MRI reached its termination point. In the rest of this chapter, we will refer to $|b_r b_\phi|$ at MRI termination as "the MRI termination amplitude". For $t > 11.86$ ms, tearing modes are clearly visible in the system (bottom panels of the figure). Based on these results, we conclude that the MRI in 2D is indeed terminated by tearing modes. This was already noted by Obergaulinger et al. (2009) in their ideal MHD simulations (in their case, the tearing modes must have been triggered by numerical resistivity, which was reported by these authors).

To investigate the dependence of the MRI termination point on the initial perturbations we ran five more simulations with the same prescription for the initial velocity (Eq. (4.111)). Obviously, in each simulation, random perturbations were distinct, because each time different sets of random numbers $\mathfrak{R}_r(r,\phi,z), \mathfrak{R}_\phi(r,\phi,z)$ and $\mathfrak{R}_z(r,\phi,z)$ were generated. The MRI termination amplitudes[24] vary within a factor of 2 (see Table 4.3). Note that there is a clear correlation between the MRI termination time and amplitude. If the initial perturbations, from which the secondary instability

[24] I.e. the volume averaged Maxwell stress component $|b_r b_\phi|$ at MRI termination.

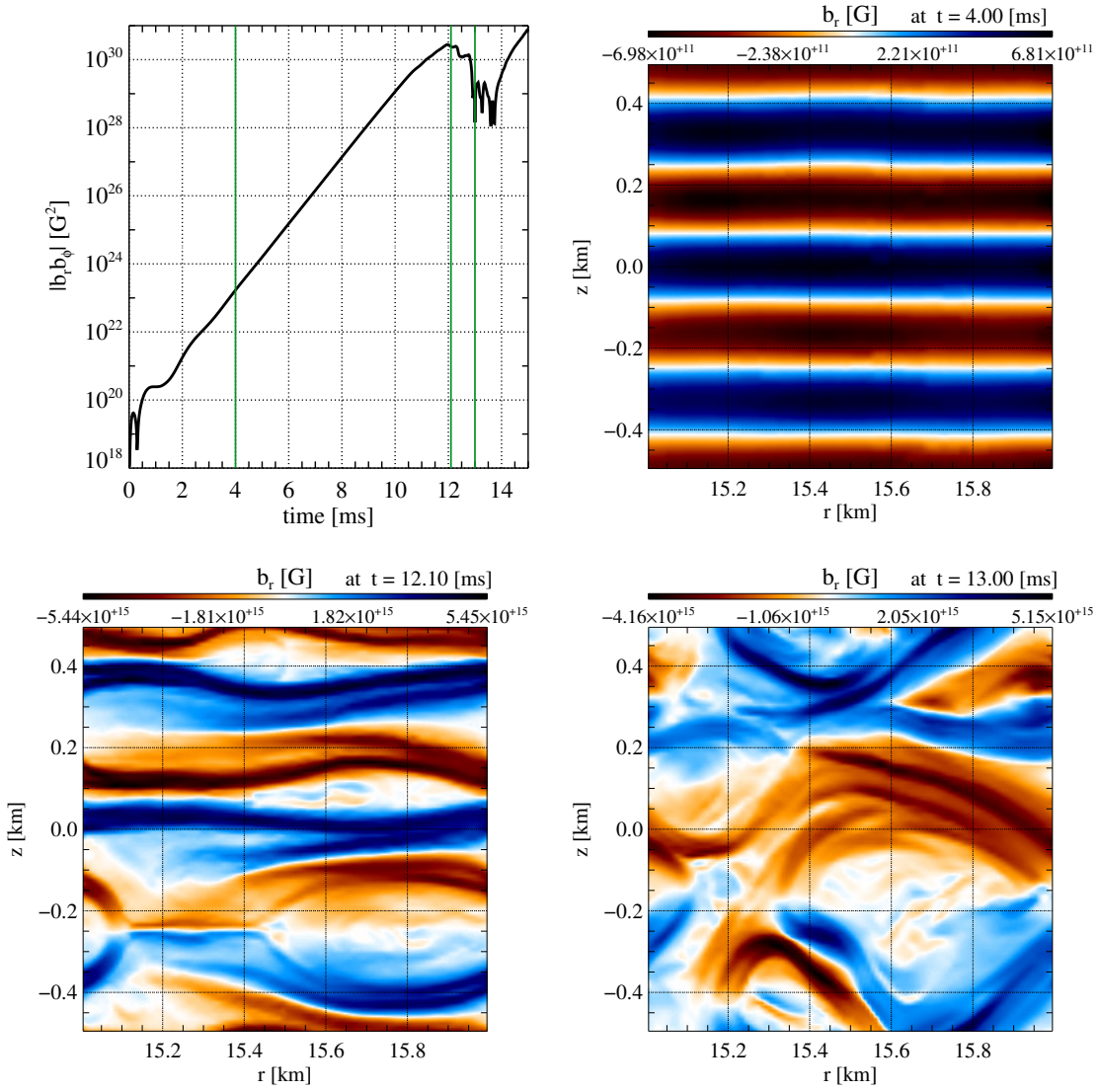

Figure 4.6: An exemplary 2D MRI simulation, in which the instability is terminated by tearing modes. The resolution, the initial magnetic field, the viscosity and the resistivity were set to 100×100 zones, $b_{0z} = 4.6 \times 10^{13}$ G, and $\nu = \eta = 4.45 \times 10^8$ cm^{2}s^{-1}, respectively. *Top left*: Time evolution of the volume averaged Maxwell stress component $|b_r b_\phi|$. From $t \approx 3$ ms to $t \approx 11$ ms, the MRI is fully operational and the channel modes are well developed. At $t \approx 12$ ms the MRI was terminated. Afterwards, a turbulent phase sets in. The green vertical lines mark three times ($t = 7, 12.1$ and 13 ms) at which the structure of the radial magnetic field is presented in the other panels. *Top right*: Three MRI channels. *Bottom left*: Tearing modes, developing on top of the MRI channels, are clearly visible. The X points characteristic for the tearing modes (where magnetic field lines reconnect), are located at $(r = 15.2, z = 0.4)$ km, $(16, 0.1)$ km and $(15.2, -0.3)$ km, and the O points (where magnetic field lines are absent) at $(15.5, 0.4)$ km, $(15.7, 0.1)$ km and $(15.8, -0.3)$ km. *Bottom right*: The MRI channels are disrupted by tearing modes. Shortly afterwards, MHD turbulence sets in and the residues of the channels are no longer visible.

run #	$\lvert b_r b_\phi \rvert$ [10^{30} G^2] at termination	termination time [ms]
1	4.69	12.44
2	2.54	11.88
3	2.52	11.88
4	4.30	12.40
5	2.19	11.82
6	3.24	12.14

Table 4.3: Volume averaged Maxwell stress component $|b_r b_\phi|$ at the termination time for six 2D simulations (*runs*) with initial magnetic field $b_{0z} = 4.6 \times 10^{13}$ G and a resolution of 100×100 zones. The resistivity and viscosity are $\nu = \eta = 4.45 \times 10^8$ cm^{2}s^{-1}, corresponding to Reynolds numbers $R_\mathrm{e} = R_\mathrm{m} = 100$. The different values of the termination amplitude (within a factor of 2) result from different random initial velocity perturbations. Note that there is a clear correlation between the Maxwell stress component $|b_r b_\phi|$ termination value and the time it occurs at.

run #	$\lvert b_r b_\phi \rvert$ [10^{30} G^2] at termination	termination time [ms]
1	2.27	11.72
2	2.20	11.72
3	3.14	11.98
4	2.49	11.74
5	2.32	11.80
6	2.40	11.76

Table 4.4: Same as Table 4.3, but twice higher resolution (200×200 zones).

developed, are smaller, they need to be amplified for a longer time before they become comparable to the MRI channels. In that extra time, the MRI manages to amplify the strength of the channel magnetic fields to higher values, before it was finally terminated.

This explanation can be supported with a Fourier analysis of the initial velocity perturbations. Before we compare the spectra of different simulations, we briefly explain the used technique on an exemplary simulation (presented in Fig. 4.6 and denoted as *run 1* in Table 4.3). We used the standard IDL fast Fourier transform (FFT) of the v_r and v_z velocity components in the z direction defined as:

$$\hat{v}_r(r_j, \bar{k}_z) = \frac{1}{N_z} \sum_{n=0}^{N_z-1} v_r(r_j, z_n) e^{-i2\pi n \bar{k}_z / N_z}, \tag{4.128}$$

$$\hat{v}_z(r_j, \bar{k}_z) = \frac{1}{N_z} \sum_{n=0}^{N_z-1} v_z(r_j, z_n) e^{-i2\pi n \bar{k}_z / N_z}, \tag{4.129}$$

where $j = 1, \ldots, N_r$, N_r and N_z are the numbers of zones in the r and z direction, respectively, and $\bar{k}_z = 0, \ldots, N_z/2$ is a box normalised wavevector (for $\bar{k}_z$ = 1, one sine wave fits in the computational

run #	$\lvert b_r b_\phi \rvert$ [10^{30} G^2] at termination	termination time [ms]
1	2.54	11.86
2	2.53	11.82
3	2.44	11.76
4	2.44	11.74
5	2.48	11.82
6	2.44	11.74

Table 4.5: Same as Table 4.3, but four times higher resolution (400×400 zones). Note that $|b_r b_\phi|$ varies much less than in the simulations with lower resolutions.

domain). The coefficients $\hat{v}_r$ and $\hat{v}_z$ form complex matrices of the dimension $N_r \times (N_z/2+1)$.[25] For the following discussion, we were only interested in "box averaged" (or "spatially averaged") moduli of these coefficients. The averaging is done in all directions orthogonal to z (because, e.g. $\hat{v}_r(r_j, \bar{k}_z)$ are by construction z independent), which in 2D simulations corresponds to only the radial direction, i.e.

$$|\tilde{v}_r(\bar{k}_z)| \equiv \frac{2}{N_r} \sum_{j=1}^{N_r} \sqrt{\hat{v}_r(r_j, \bar{k}_z) \hat{v}_r^*(r_j, \bar{k}_z)}, \tag{4.130}$$

$$|\tilde{v}_z(\bar{k}_z)| \equiv \frac{2}{N_r} \sum_{j=1}^{N_r} \sqrt{\hat{v}_z(r_j, \bar{k}_z) \hat{v}_z^*(r_j, \bar{k}_z)}, \tag{4.131}$$

where j enumerates the radial zones and the asterisk denotes complex conjugation. The factor 2 appears on the right hand side of the above equations, because we discarded the negative frequencies resulting from the IDL FFT (see also Footnote 25) and it is necessary for the correct normalisation. $|\tilde{v}_r(\bar{k}_z)|$ and $|\tilde{v}_z(\bar{k}_z)|$ form $(N_z/2+1)$-dimensional vectors. These coefficients indicate how strongly modes with a given wavevector were on average excited in the box, i.e. for 2D simulations – the more radii r_j at which the modulus of $|\hat{v}_r(r_j, \bar{k}_z)|$ was large, the larger $|\tilde{v}_r(\bar{k}_z)|$. Fig. 4.7 illustrates these concepts. The upper left panel depicts the initial radial velocity v_r given by Eq. (4.112) . Three channels and some random perturbations on the top of them are clearly visible. The right upper panel is a graphical presentation of the spatial averaged Fourier coefficients $|\tilde{v}_r(\bar{k}_z)|$ (Eq. 4.130). Note that $|\tilde{v}_r(\bar{k}_z = 3)|$ is much greater than any other coefficient, because the radial velocity has a corresponding sinusoidal component (see Eq. (4.112)), i.e.

$$v_r(r, \phi, z) = 0.1 \delta \Re_r(r, \phi, z) + \varepsilon \sin\left(3 \frac{2\pi}{L_z} z\right). \tag{4.132}$$

In the bottom panels, the corresponding plots for the vertical velocity are presented. The averaged Fourier coefficients seem to have a larger scatter than in the case of the radial velocity (upper right). This is just a graphical illusion caused by different scales in the ordinate axes. In Fig. 4.8, we compare the coefficients $|\tilde{v}_r(\bar{k}_z)|$ form three simulations, which are denoted as *run 1* (the highest MRI termination amplitude), *run 5* (the lowest termination amplitude) and *run 6* (an average

[25] The IDL FFT routine creates $N_r \times N_z$ matrices with negative wavevectors, i.e. $\bar{k}_z < 0$, stored in rows $N/2+1, \ldots, N-1$. They would be important to properly perform the inverse Fourier transformation. However, for our purposed, these parts of the matrices can simply be discarded.

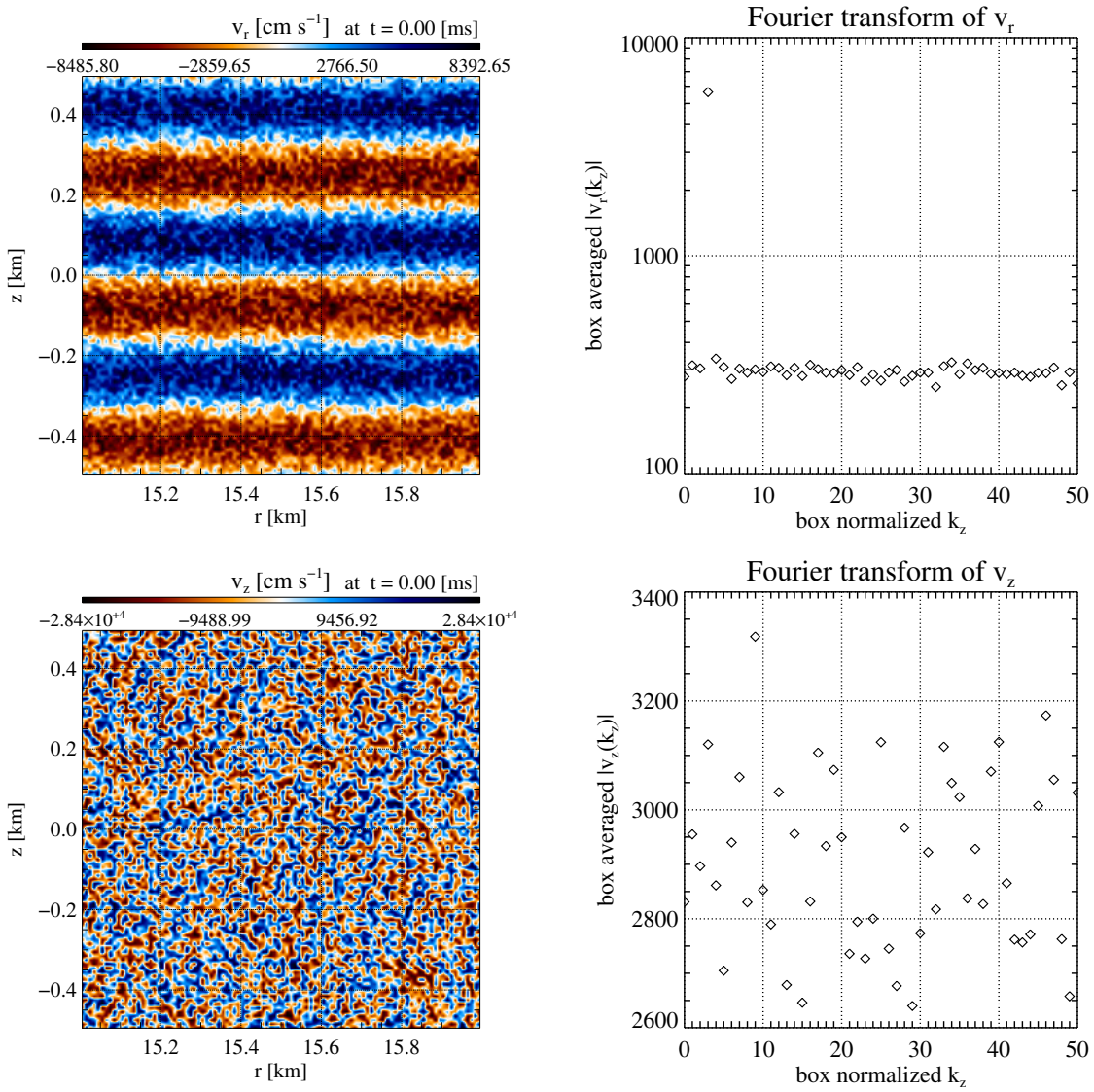

Figure 4.7: Initial velocity, given by Eq. (4.112), and its Fourier transform from a simulation with a resolution, initial magnetic field, viscosity and resistivity of 100×100 zones, $b_{0z} = 4.6 \times 10^{13}$ G, and $\nu = \eta = 4.45 \times 10^8$ cm^{2}s^{-1}, respectively. *Top left*: Radial velocity showing three sinusoidal channels plus some random perturbations. *Top right*: Spatially averaged Fourier transform coefficients, $|\tilde{v}_r(\bar{k}_z)|$, of the radial velocity (see Eq. (4.130)). The clear peak at the box normalised $\bar{k}_z = 3$ results from the sinusoidal component added to the random perturbations (see Eq. (4.112)). *Bottom left*: Z-velocity resulting from random initial perturbations. *Bottom right*: Same as upper right panel, but for $|\tilde{v}_z(\bar{k}_z)|$. Since the initial perturbations are purely random, there is no clear maximum. The larger scatter in the averaged Fourier components (in comparison with $|\tilde{v}_r(\bar{k}_z)|$), is caused by using different scales in the ordinate axis in both right panels.

termination amplitude) in Table 4.3. In the first simulation, the random perturbations were the most successful at exciting the parasitic instability (the tearing modes). However, it is impossible to tell from this figure, which Fourier modes are preferred by the secondary instability, because we only considered averaged Fourier coefficients and we only compared the components of the vertical

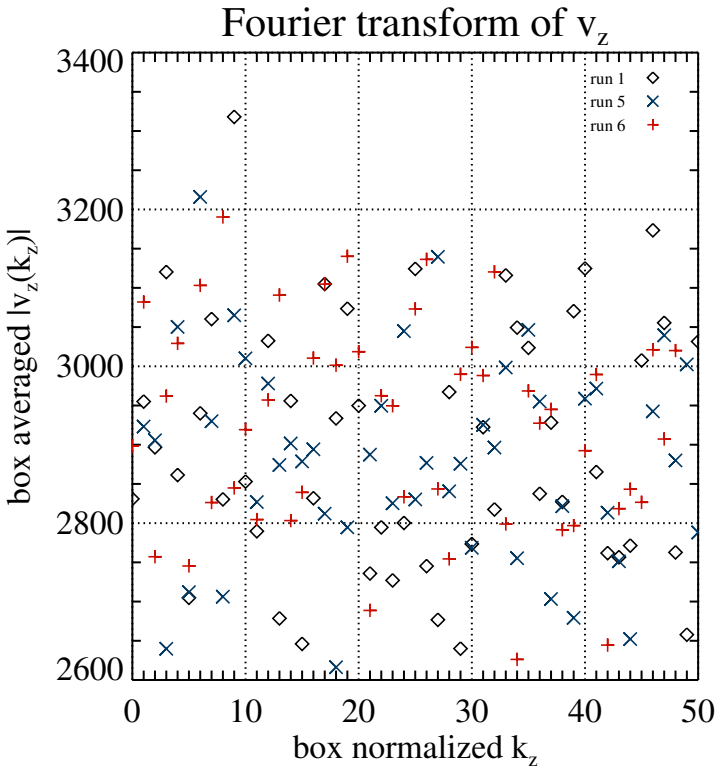

Figure 4.8: Comparison of the spatially averaged Fourier transform coefficients $|\tilde{v}_r(\bar{k}_z)|$ (see Eq. (4.131)) of the initial vertical velocity from three simulations denoted as *run1* (black diamonds), *run 5* (blue crosses) and *run 6* (red pluses) in Table 4.3.

velocity, v_z. However, the other components, v_r and v_ϕ, are also important for the development of the parasitic instability. Since we do not know the eigenfunctions of the tearing modes for this setup, it is impossible to perform a more in-depth analysis. We conclude that for 2D simulations with resolution of 100×100 zones, initial perturbations can change the MRI termination amplitude within a factor 2. The coefficients $|\tilde{v}_z(\bar{k}_z)|$ are in the range

$$|\tilde{v}_r(\bar{k}_z)| = 2900 \pm 400. \tag{4.133}$$

Even though we ran the simulations with resistivity and viscosity $\nu = \eta = 4.45 \times 10^8$ cm^{2}s^{-1}, it is not clear how large they are in comparison to their numerical counterparts. To test this, we ran another six simulations with the same initial conditions but twice the resolution, i.e. with 200^2 zones (see Table 4.4). We can notice two differences in comparison with simulations ran at the lower resolution – the MRI termination amplitudes vary less (factor 1.5) and they are lower on average. These differences can be explained by the fact that in the simulations with the higher resolution, the initial random perturbations are more likely to trigger efficiently parasitic instabilities for two reasons. Firstly, the perturbations have "more variety" in Fourier space, i.e. because the allowed wavevectors can be twice as large and therefore twice as many modes could be excited (the maximum wavevector is given by $\bar{k}_z = N_z/2$). Secondly, there are twice more zones in the radial direction. This means that there will be roughly twice as many r_j, for which the random perturbations will be similar to the tearing mode eigenfunction.

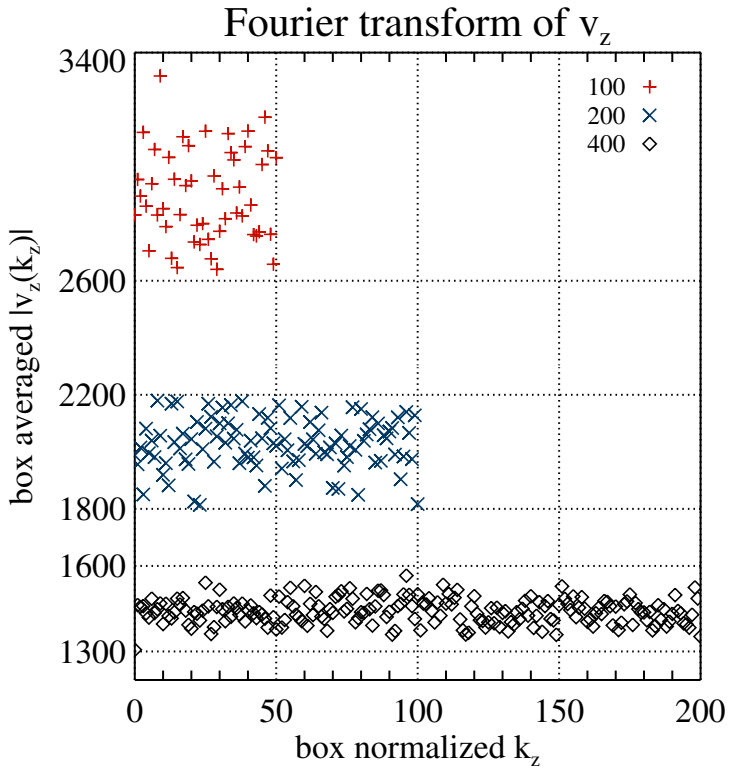

Figure 4.9: Comparison of the spatially averaged Fourier transform coefficients $|\tilde{v}_r(\bar{k}_z)|$ (see Eq. (4.131)) of the initial vertical velocity from three simulations with different resolutions: 100×100 (red pluses) , 200×200 (blue crosses) and 400×400 (black diamonds). The simulations are denoted as *run 1* in Tables 4.3, 4.4 and 4.5, respectively.

Finally, we ran six simulations with the same physical setup ($b_{0z} = 4.6 \times 10^{13}$ G and $\nu = \eta = 4.45 \times 10^8$ cm^{2}s^{-1}), but a resolution of 400×400 zones (see Table 4.5). The MRI termination amplitude has almost the same value in all six simulations, because there are even more zones, and therefore the probability that in some part of the box, the random perturbations will be similar to the tearing mode eigenfunctions is higher.

In Fig. 4.9, we compare the averaged Fourier transform coefficients $|\tilde{v}_r(\bar{k}_z)|$ from three simulations (*run 1* in the corresponding tables) with resolution of 100×100, 200×200 and 400×400 zones. The higher the resolution, the lower the scatter in $|\tilde{v}_r(\bar{k}_z)|$. Intuitively, this can be connected with the scatter of the Maxwell stress component $|b_r b_\phi|$ at the MRI termination: the more variety in the perturbations, the higher the chance that the parasitic instability will be efficiently triggered.

According to the GXP model (see Section 4.4), the MRI should be terminated shortly after the parasitic instabilities start to grow faster than the MRI itself. So far, we only measured the MRI growth rate and termination amplitude. However, apart from a graphical identification (see Fig. 4.6), we have not investigated the secondary instability in sufficient detail. The key information, which we would like to extract from the simulations, is the parasitic growth rate. It would facilitate the studies for several reasons. Firstly, it could be possibly used to formulate some semi-analytical expressions for the secondary instability growth. Secondly, we could verify the GXP model by a direct comparison of the MRI and the parasitic growth rates. Unfortunately, for the reasons

which we discuss in the next section on 3D simulations, we were unable to measure the secondary instability growth rate.

4.5.3 3D simulations

The main objectives

According to our rough estimates based on the GXP model (see Section 4.4), given conditions in the core-collapse supernovae, the MRI should be terminated by the KH instability. However, it could not develop in the 2D simulations because of the assumed axial symmetry, and the MRI was terminated by tearing modes, instead. Therefore, the MRI termination problem can be properly investigated only in 3D simulations, whose main drawback, however, is a much higher computational cost. For the resolutions used by us, the 3D simulations were more expensive than the 2D ones by a factor of 250 to 1000.[26] Covering the whole parameter space relevant for the core-collapse supernovae would require too many simulations (of the order of hundred). Obergaulinger et al. (2009) performed such investigations with the help of 2D simulations. However, apart from the MRI growth rates, one should not trust their results, because the MRI was terminated there by tearing modes irrelevant in supernovae. The scope of our study is seemingly much more modest. We only focus on one initial model, in which besides numerical parameters, only the resistivity, the viscosity and the magnetic field amplitude will be changed. We will try to answer the following questions:

1. Is the Kelvin-Helmholtz instability responsible for MRI termination?
2. What is the influence of the numerical viscosity and resistivity on the termination amplitude?
3. Can we verify the GXP model (with our modifications)?
4. Can we extrapolate the results to the conditions relevant for core-collapse supernovae (i.e. lower initial magnetic fields)?

The resolution requirements

The initial conditions for the 3D simulations were already described in Sec. 4.5.1. Following Obergaulinger et al. (2009), we used a simulation box of size $L_r \times L_\phi \times L_z = 1$ km $\times$ 4 km $\times$ 1 km as the default one. These authors also studied the post-termination phase, and in particular, the possible appearance of second MRI growth phase, which they often observed in their 2D simulations. Obergaulinger et al. (2009) found that for $L_\phi / L_z \geq 2$, parasitic instabilities could effectively prevent another MRI channel formation (and the subsequent second MRI onset) in the (post-termination) turbulent phase. Initially, we also intended to investigate the post-termination

[26] To run a 2D MRI simulation with a resolution of 100×100 zones for 15 ms, $\approx$ 20 CPUhs are needed on the SuperMUC. For a 3D simulation with $100 \times 100 \times 100$ zones, the computational time amounts to $\approx$ 5 000 CPUhs. Doubling the resolution in a 2D and 3D simulation increases the computational time by a factor of 8 and 16, respectively (because of scaling problems, which usually arise when a simulation is run on many processors, these factors are in practice somewhat higher). The computational cost of a 2D and 3D simulation with 400 zones in each dimension (these are highest resolutions that we used in our studies), increases to $\approx$ 1 280 and $\approx$ 1 280 000 CPUhs, respectively. The 3D simulation is by factor $\approx$ 1000 more expensive.

stage in detail. However, because of limited computational resources, we had to restrict these studies. [27]

A very important issue, which needs to be discussed first, is the required resolution to study the MRI termination problem. As a starting point in our considerations, we take a simulation with the default resolution of $100 \times 400 \times 100$ zones for the a of size 1 km $\times$ 4 km $\times$ 1 km. Approximately $\approx$ 20 000 CPUhs on the SuperMUC are needed to run such a simulation for 15 ms (i.e. until MRI termination). For an initial magnetic field $b_{0z} = 4.6 \times 10^{13}$ G, viscosity and resistivity $\nu = \eta = 4.45 \times 10^8$ cm^{2}s^{-1}, three MRI channels form will in the computational domain (because $\lambda_{\rm MRI} = 0.333$ km). This gives ≈ 33 zones (in the vertical direction) per MRI channel. As we already know from the 2D simulations, 20 zones are sufficient to resolve fully an MRI channel with the MP9 reconstruction scheme. However, the problem arises, when parasitic instabilities are taken into account. In Section 4.4, we criticised the assumptions, which Pessah (2010) made to calculate secondary instabilities, yet some of his results are useful for our current considerations. He found approximate parasitic eigenfunctions with the help of the Fourier series expansion (see Eqs. (4.65) and (4.66) and the discussion below). Pessah (2010) reported that it is sufficient to consider modes with wavevectors $k \leq 30 k_{\rm MRI}$ to achieve a convergence to the desired accuracy.[28] Hence, to resolve the secondary instabilities with the same precision, we would need to use 30 times more zones than were needed per MRI channel. A simulation with the 30 times higher resolution, would require at least 30^4 more computational time, i.e. $30^4 \times 20\,000 \approx 10^{10}$ CPUhs, which is beyond the reach of any supercomputer in the predictable future.[29]

In a simulation with the standard resolution (i.e. 100 zones in the z direction), ≈ 33 zones are used per MRI channel. However, in Sec. 4.5.2, we showed that 20 zones are sufficient to resolve one channel and also estimated that maybe even ≈ 10 zones would do. Hence, we could reduce the resolution in each dimension by a factor of ≈ 3, decreases the computational cost ≈ 81 times. In addition, maybe a lower accuracy than the one which Pessah (2010) reached in his calculations, would be sufficient for our purposes. Thus, resolving only modes with wavevectors $k \leq 10 k_{\rm MRI}$, and not $k \leq 30 k_{\rm MRI}$, might be fine , as well. This would reduce the computational time by another factor of 81. From this rough estimate, we obtain that we may need ≈ 100 zones per MRI channels in the z direction, hence $300 \times 1200 \times 300$ zones for the whole box (given the above mentioned initial conditions), and the total simulation cost would "only" amount to 2 500 000 CPUhs.

Parasitic instabilities require a high resolution only in the z direction (see Eqs. (4.65) and (4.66) and the discussion below), whereas in the horizontal plane, only a modest number of zones is needed, because the moduli of the horizontal part of the secondary instability wavevector (i.e. components k_r and k_ϕ) and the fastest growing MRI mode wavevector ($k_{\rm MRI}$) are comparable, i.e. $k_{\rm KH} \approx 0.59 k_{\rm MRI}$ (see (4.44)). In other words, $\lambda_{\rm KH} \approx 2\lambda_{\rm MRI}$, and only 30–60 (120–240) zones [30] would be necessary in the radial (azimuthal) direction to resolve the parasitic instability during its linear

[27] Bodo et al. (2008) performed a part of their studies in a box of size $L_r \times L_\phi \times L_z = (aL_z) \times (aL_z) \times L_z$, where $a > 1$. This choice is better justified. In ideal MHD, the KH instability grows fastest (on the top of the MRI channels), when its horizontal wavevector forms an angle $\phi = \pi/4$ with the radial axis (Goodman & Xu 1994). Hence, simulation boxes with $L_r = L_\phi$ are optimal for the development of this parasitic instability. One should also make sure that at least one KH mode fits into the computational domain.

[28] That author did not exactly specify what he meant by "the desired accuracy". However, in (semi-)analytical calculations one can usually achieve high accuracy more easily than in purely numerical studies. Therefore, we can presume that we would be satisfied with the same level of precision (probably the relative errors not greater than 10^{-2} or maybe even much smaller) in our simulations.

[29] If we were given all $\approx$ 155000 cores of the SuperMUC (which in June 2013 still was among the top 10 Supercomputers in the world; see www.top500.org), we would need to run one simulation for at least 12 years.

[30] The lower limit assumes a resolution of 10 zones in the horizontal direction per MRI channel.

phase (i.e. when the perturbation amplitudes are much smaller than the MRI channels). Hence, in the most optimistic scenario, a resolution of $30 \times 120 \times 300$ zones would be sufficient to capture the evolution of both the MRI and the secondary instability in the pre-termination phase. The corresponding computational time of 25 000 CPUhs would be affordable. However, we do not think that studying MRI termination in a simulation with such different resolutions in the spatial directions is adequate. In this highly non-linear process, phenomena taking place at much smaller scales in the horizontal plane may eventually become very important. The subsequent MRI driven turbulent phase would be affected by the non-equidistant grid as well.

Before running any simulation, we can predict some general features of the MRI termination amplitude dependence on resolution. In 3D simulations, the KH instability can develop and eventually disrupt the MRI channels before tearing modes would do it. Hence, the MRI will be active for a shorter time and we expect the termination amplitude to be lower in 3D than in 2D. We also know that the resolutions, which we are going to use, are sufficient to capture the MRI channel evolution, but the KH instability may be underresolved. Hence, there will be some numerical viscosity, ν_*, decreasing the growth rate of this secondary instability. By combining Eqs. (4.30) and (4.45), we roughly estimate that

$$\gamma_{\mathrm{KH}} \approx 0.45 k_{\mathrm{KH}} v_{\mathrm{c}} - \nu_* \frac{k_{\mathrm{KH}}^2}{2}, \tag{4.134}$$

where v_c is the (velocity) channel amplitude.[31] The termination will happen not before the growth rates of the MRI and the KH instability become comparable, i.e.

$$\gamma_{\mathrm{KH}} = \gamma_{\mathrm{MRI}}. \tag{4.135}$$

Substituting γ_{KH} with the estimate from Eq. (4.134), we write this precondition as

$$0.45 k_{\mathrm{KH}} v_{\mathrm{c}} \approx \gamma_{\mathrm{MRI}} + \nu_* \frac{k_{\mathrm{KH}}^2}{2}. \tag{4.136}$$

Hence, at lower resolutions, because of the numerical viscosity, MRI channels will reach higher amplitudes before the KH instability becomes important. Consequently, in simulations with lower resolutions, the MRI termination amplitude will be higher. At first, this statement sounds counterintuitive. Usually, when something is insufficiently resolved, it develops more slowly or reaches smaller values. In this case, however, it is not the MRI itself, but the secondary instability, which is underresolved. Looking at Eq. (4.136), we can predict the general behaviour of the MRI termination amplitude with increasing resolution. The amplitude should decrease, until the term containing ν_* becomes insignificant. When, a further increase of the resolution does not lead to any reduction of the termination amplitude, convergence has been reached.

Parasitic instability identification

We started the 3D studies, with a simulation in a box of size $1\ \mathrm{km} \times 4\ \mathrm{km} \times 1\ \mathrm{km}$ and a resolution of $100 \times 400 \times 100$ zones. The initial magnetic field, the viscosity and the resistivity were set to $b_{0_z} = 4.6 \times 10^{13}$ G, and $\nu = \eta = 4.45 \times 10^8\ \mathrm{cm^2 s^{-1}}$, respectively. We triggered the instability with the perturbations defined in Eq. (4.112). Like in the 2D simulations, MRI channels formed after $\approx$ 3 ms (upper right panel of Fig. 4.10) and the instability was fully operational. The Maxwell stress

[31] Combining these two equations for KH growth rates for different velocity profile is an oversimplification, but it should correctly capture the general features of the instability growth rate.

component $|b_r b_\phi|$ is exponentially amplified until ≈ 11 ms (upper left panel). At $t = 10.9$ ms some disturbances of the MRI channels are visible (bottom left panel). One tenth of the millisecond later, at $t = 11$ ms, we can clearly recognise the patterns of the KH instability, which is developing on top of the MRI channels (bottom right panel). Eventually, this secondary instability disrupts the channels and terminates the MRI at $t = 11.2$ ms (see Fig. 4.11). The box averaged Maxwell stress component $|b_r b_\phi|$ is equal to 9.33×10^{29} G^2 (Table 4.6). 0.3 ms after the termination, at $t = 11.5$ ms, the residues of the channels are still visible. At $t = 12$ ms, MRI-driven turbulence sets in (bottom panels of Fig. 4.11). We did not observe any second MRI growth phase during the later stages of the evolution (see Fig. 4.12), which is in accordance with Obergaulinger et al. (2009) and Bodo et al. (2008).

These results confirm the hypothesis put forward in the GXP model, that it is the KH instability, which is responsible for the MRI termination in 3D simulations (and nature). Knowing the time evolution of the growth rate would be very helpful for a further verification of the GXP model (with our modifications). Unfortunately, we were unable to measure the parasitic growth rate in both 2D and 3D simulations. We discuss this issue in more detail below.

Measuring the parasitic instability growth rate

Obergaulinger et al. (2009) used $E^z_{\rm mag} \equiv \int b_z^2/2 \, {\rm d}V$, to trace the evolution of the secondary instabilities. The idea behind this is that since the MRI does not affect the initial vertical magnetic field component during the exponential growth phase, all changes in b_z should be caused by the parasitic instability ($b_{\rm pz}(t)$). These authors claimed that $\dot{E}^z_{\rm mag}/(2E^z_{\rm mag})$, where $\dot{E}^z_{\rm mag} \equiv \partial_t E^z_{\rm mag}$, should be proportional to the parasitic growth rate, $\gamma_{\rm p}$. However, because the initial background magnetic field, b_{0z}, also contributes to $E^z_{\rm mag}$, i.e.

$$E^z_{\rm mag}(t) = \int \frac{(b_{0z} + b_{\rm pz}(r,\phi,z,t))^2}{2} {\rm d}V, \tag{4.137}$$

$\dot{E}^z_{\rm mag}/(2E^z_{\rm mag})$ does not have an easy physical interpretation. It is approximately equal to the parasitic growth rate, only if $b_{\rm pz} \gg b_{0z}$, which is never the case before MRI termination. To trace the evolution of the parasites it is better to use the quantity

$$E^{\rm pz}_{\rm mag}(t) \equiv \int \frac{(b_z - b_{0z})^2}{2} {\rm d}V = \int \frac{(b_{\rm pz}(r,\phi,z,t))^2}{2} {\rm d}V, \tag{4.138}$$

because $\dot{E}^{\rm pz}_{\rm mag}/(2E^{\rm pz}_{\rm mag})$ provides a better estimate of the growth rate of the secondary instabilities. Computing $E^{\rm pz}_{\rm mag}$ would require some minor modification of the code and repeating the simulations. However, we found an alternative, equally good method of dealing with this problem. We traced the contribution of the motions in the z direction to the kinetic energy:

$$E^z_{\rm kin}(t) = \int \frac{\rho(r,\phi,z,t)(v_{\rm pz}(r,\phi,z,t))^2}{2} {\rm d}V. \tag{4.139}$$

Because the MRI should not excite any motion in this direction, any increase of $E^z_{\rm kin}$ indicates activity of the parasites. Although $v_{\rm pz}(r,\phi,z,t)$ is unknown, we can make some estimates. In the GXP model

$$v_{\rm pz}(t) = v_{\rm pz}(t_0) e^{\gamma_{\rm p}(t-t_0)}, \tag{4.140}$$

where $v_{\rm pz}(t_0)$ is the parasitic velocity at time t_0, i.e. during the time interval $t - t_0$, the velocity would grow with (an approximately) constant rate $\gamma_{\rm p}$. Hence,

$$\frac{\dot{v}_{\rm pz}(t)}{v_{\rm pz}(t)} = \gamma_{\rm p}, \tag{4.141}$$

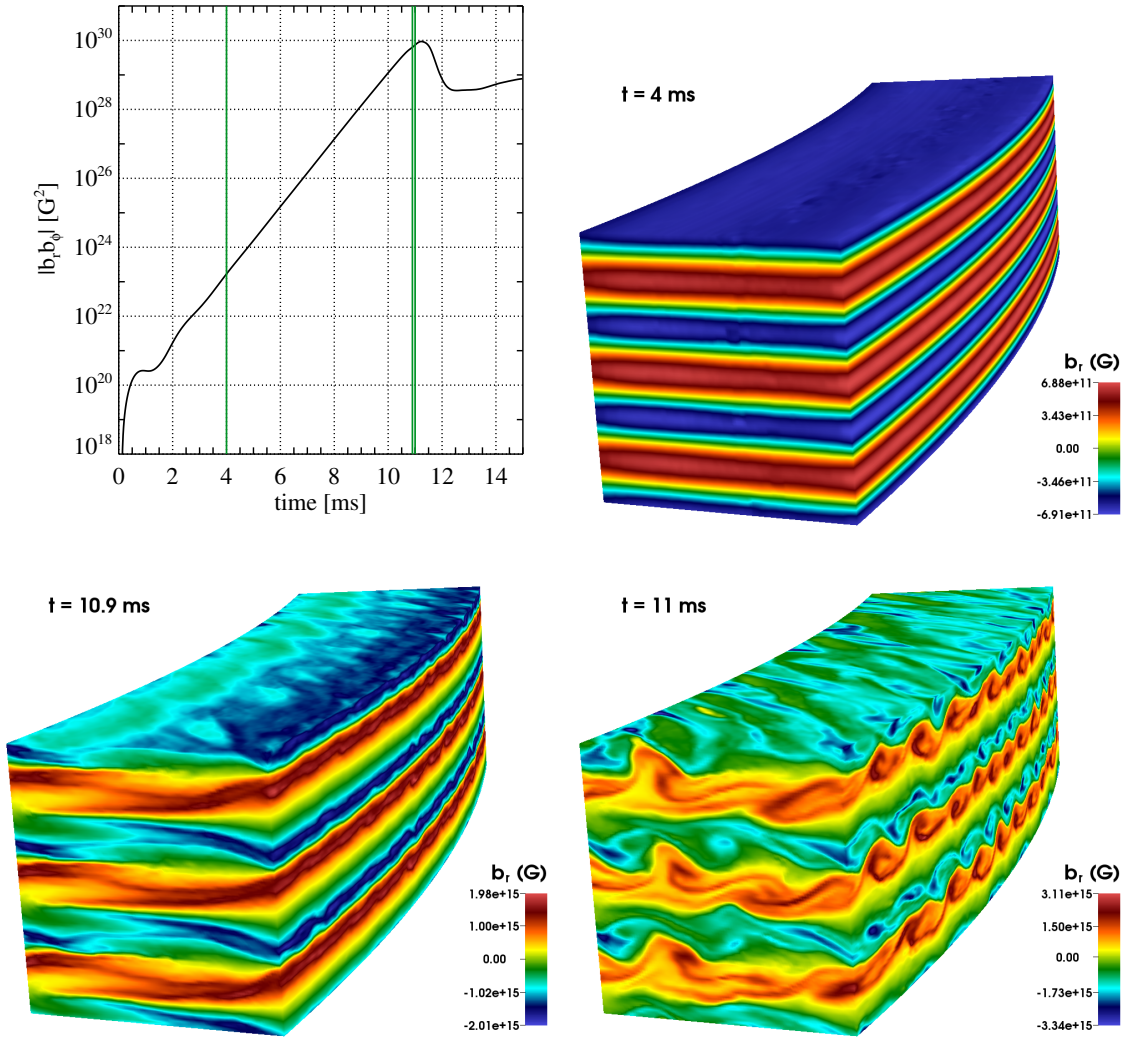

Figure 4.10: 3D MRI simulation, in which the instability is terminated by the Kelvin-Helmholtz instability. The simulation box has a size of 1 km $\times$ 4 km $\times$ 1 km in the r, ϕ and z directions, respectively, and is resolved with $100 \times 400 \times 100$ zones. The initial magnetic field, the viscosity and the resistivity are $b_{0z} = 4.6 \times 10^{13}$ G, and $\nu = \eta = 4.45 \times 10^8$ cm^{2}s^{-1}, respectively. *Top left*: time evolution of the volume averaged Maxwell stress component $|b_r b_\phi|$. From $t \approx 3$ ms to $t \approx 10$ ms, the MRI is fully operational and the channel modes are well developed. At $t \approx 11$ ms, the MRI was terminated and a turbulent phase sets in. The green vertical lines mark the three times ($t = 4, 10.9$ and 11 ms) at which the radial magnetic field strength at the simulation box surface is presented in the other three panels. In all 3D plots, the following axis orientation is used: the z direction is up, the r direction – right, and the ϕ direction – "diagonal". *Top right*: The radial magnetic field at $t = 4$ ms forms three MRI channels. *Bottom left*: The radial magnetic field shortly before MRI termination, at $t = 10.9$ ms. Some perturbations in the MRI channels are visible. *Bottom right*: From the perturbation pattern at $t = 11$ ms, we can identify the Kelvin-Helmholtz instability.

or equivalently

$$\frac{\dot{E}^z_{\rm kin}}{2E^z_{\rm kin}} \approx \gamma_{\rm p}. \tag{4.142}$$

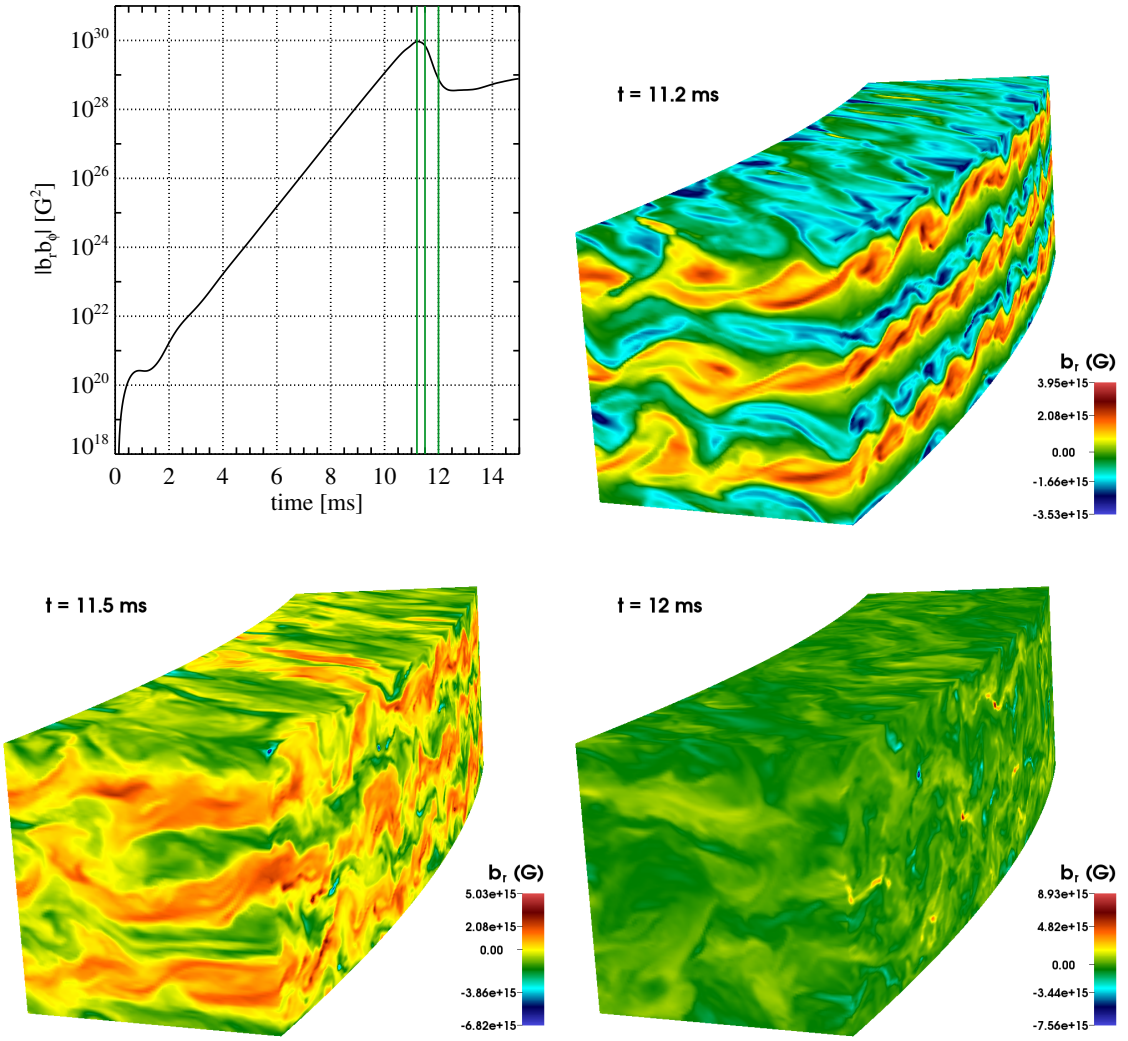

Figure 4.11: Later evolution of the simulation presented in Fig. 4.10. *Top left*: time evolution of the volume averaged Maxwell stress component $|b_r b_\phi|$. The green vertical lines mark the three times ($t = 11.2, 11.5$ and 12 ms) at which the radial magnetic field at the simulation box surface is presented in the other three panels. In all 3D plots, the following axis orientation is used: the z direction is up, the r direction – right, and the ϕ direction – "diagonal". *Top right*: The radial magnetic field at $t = 11.2$ ms, when the Kelvin-Helmholtz instability develops on top of the MRI channels. *Bottom left*: The MRI channels are being disrupted by the KH instability. *Bottom right*: MHD turbulence sets in and the MRI channels are no longer visible.

However, because MRI channels, which are the background field for the parasites, are time dependent, Eq. (4.140) is incorrect for two reasons. The growth rate of the parasites is also time dependent, i.e. $\gamma_p = \gamma_p(t)$, and we cannot simply use an WKB ansatz ($v_{pz}(t) \propto e^{\gamma_p t}$) for the perturbations without further complications, as we will see next.

If we assume

$$\gamma_p(t) = \gamma_p(t_0) e^{\gamma_{MRI}(t-t_0)}, \tag{4.143}$$

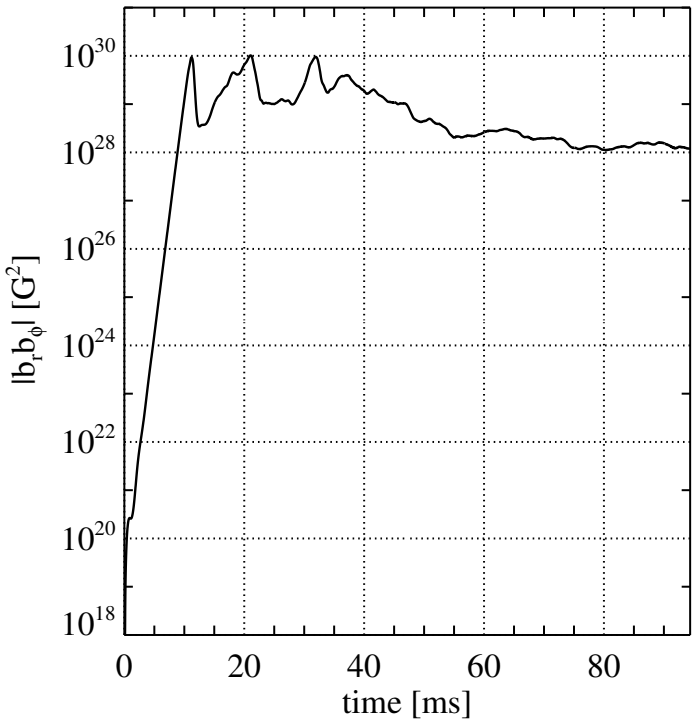

Figure 4.12: Time evolution of the volume averaged Maxwell stress component $|b_r b_\phi|$ for a 3D MRI simulation in a box of size 1 km $\times$ 4 km $\times$ 1 km in the r, ϕ and z direction, respectively. The initial magnetic field, the viscosity and the resistivity are $b_{0z} = 4.6 \times 10^{13}$G, and $\nu = \eta = 4.45 \times 10^8$ cm^{2}s^{-1}, respectively. From $t \approx 3$ ms to $t \approx 10$ ms, the MRI is fully operational. At $t \approx 11$ km, the instability is terminated by the Kelvin-Helmholtz instability and shortly afterwards a turbulent phase sets in.

where $\gamma_{\rm p}(t_0)$ is the parasitic growth rate at time $t_0 < t$, obviously, we cannot simply write

$$v_{{\rm p}z}(t) = v_{{\rm p}z}(t_0) e^{\gamma_{\rm p}(t)(t-t_0)} = v_{{\rm p}z}(t_0) e^{\gamma_{\rm p}(t_0)\exp(\gamma_{\rm MRI}(t-t_0))(t-t_0)}, \tag{4.144}$$

because it overestimates the perturbations' growth. We can only estimate that

$$v_{{\rm p}z}(t_0) e^{\gamma_{\rm p}(t_0)(t-t_0)} \leq v_{{\rm p}z}(t) \leq v_{{\rm p}z}(t_0) e^{\gamma_{\rm p}(t)(t-t_0)}, \tag{4.145}$$

where $\gamma_{\rm p}(t)$ is given by Eq. (4.143). But then

$$\frac{\dot{v}_{{\rm p}z}(t)}{v_{{\rm p}z}(t)} \neq \gamma_{\rm p}(t) \tag{4.146}$$

and $\gamma_{\rm p}(t)$ loses its growth rate interpretation.

Instead, we could first define the parasitic growth rate as

$$\tilde{\gamma}_{\rm p}(t) \equiv \frac{\dot{v}_{{\rm p}z}(t)}{v_{{\rm p}z}(t)}, \tag{4.147}$$

and then try to find how it is related to $\gamma_{\rm p}(t)$ given by Eq. (4.143). However, the solutions of both the tearing mode and KH instability are based on the assumption that $\dot{v}_{\rm pz}(t)/v_{\rm pz}(t) = {\rm const.}$, which is not the case in our situation. As a result, perturbations evolving on top of time-dependent background fields would not only grow at a different rate, but would also have different eigenfunctions. Moreover, it is arguable if these perturbations would evolve according to Eq. (4.147) at all.

We measured the quantity $\dot{E}^z_{\rm kin}/(2E^z_{\rm kin})$ in our 2D and 3D simulations. In all cases, shortly after the MRI channels form it was approximately equal to the MRI growth rate, $\gamma_{\rm MRI}$ (see Fig. 4.13).

If $E^z_{\rm kin}$ increases because of parasitic instabilities, we would expect that $\dot{E}^z_{\rm kin}/(2E^z_{\rm kin}) \ll \gamma_{\rm MRI}$ until shortly before the MRI termination . Since it was not the case, the increase of the kinetic energy must be related to the MRI itself. Because the analytical MRI theory does not predict such a phenomenon, it must be of a numerical origin. We came up with one hypothesis to explain it. The MRI growth rate is given by (see Eqs. (4.16) and (4.1)),

$$\gamma_{\rm MRI} = -\frac{\alpha}{2}\Omega = -\frac{\alpha}{2}\Omega_0 \left(\frac{r}{r_0}\right)^{\alpha}, \tag{4.148}$$

where $r_0 = 15.5$ km. The simulation domain extends from $r_{\rm min} = 15.0$ km to $r_{\rm max} = 16.0$ km, i.e. the maximum and the minimum of the MRI growth rate differ by $\approx 8\%$. This leads to a radial shear in the MRI channel amplitudes located at the radial boundaries, which is not compensated for by the shearing box boundary conditions (see e.g. bottom panels of Fig. 4.5), which only work properly when the MRI growth rate is almost constant in the whole domain (i.e., when $(r_{\rm max} - r_{\rm min})/r_0 \ll 1$). The shear can generate some motions (kinetic energy) and magnetic field in the z direction (see Fig. 4.14). Unfortunately, because of this non-physical phenomenon we cannot use $\dot{E}^z_{\rm kin}/(2E^z_{\rm kin})$ to diagnose the parasitic growth rate.

Convergence

As we already discussed, we expect that the simulation with $100 \times 400 \times 100$ zones will not fully resolve the evolution of the parasitic (i.e. KH) instability. This statement can be supported with the numerical viscosity estimate (see Eq. (4.116). The numerical dissipation depends on the characteristic length of the simulated phenomenon, $\mathcal{L}$. We estimated that for the MRI channels ($\mathcal{L} = \lambda_{\rm MRI}$; see Eq. (4.118)):

$$\nu_* \approx \eta_* = (1.5 \pm 2.8) \times 10^6 \ {\rm cm^2 s^{-1}}. \tag{4.149}$$

The simulation was run with $\nu = \eta = 4.45 \times 10^8$ cm^{2}s^{-1}. Hence, when resolving the MRI channels, the numerical resistivity and viscosity (ν_* and η_*, respectively) are much smaller than their physical counterparts (ν and η, respectively). The situation is very different, however, when it comes to the secondary instability. We do not know exactly the characteristic length of the KH instability developing on top of the channels. We can only roughly estimate its lower limit. Pessah (2010) in his approximate calculations of parasitic instabilities used Fourier modes with wavevectors up to $k \leq 30 k_{\rm MRI}$ (see Eqs. (4.65) and (4.66) and the discussion below). If we wanted to resolve the secondary instabilities with the same accuracy as Pessah, we should use $\mathcal{L} = \lambda_{\rm MRI}/30$ as the characteristic length of the problem. In that case, the numerical resistivity and viscosity resulting from the KH instability can be estimated as

$$\nu_* \approx \eta_* = (2.6 \pm 4.9) \times 10^{14} \ {\rm cm^2 s^{-1}}, \tag{4.150}$$

which corresponds to numerical Reynolds numbers of order $R_{\rm e} \approx R_{\rm m} \approx 10^{-4}$. Hence, because of the very strong numerical damping, modes with such short wavelengths could not properly evolve

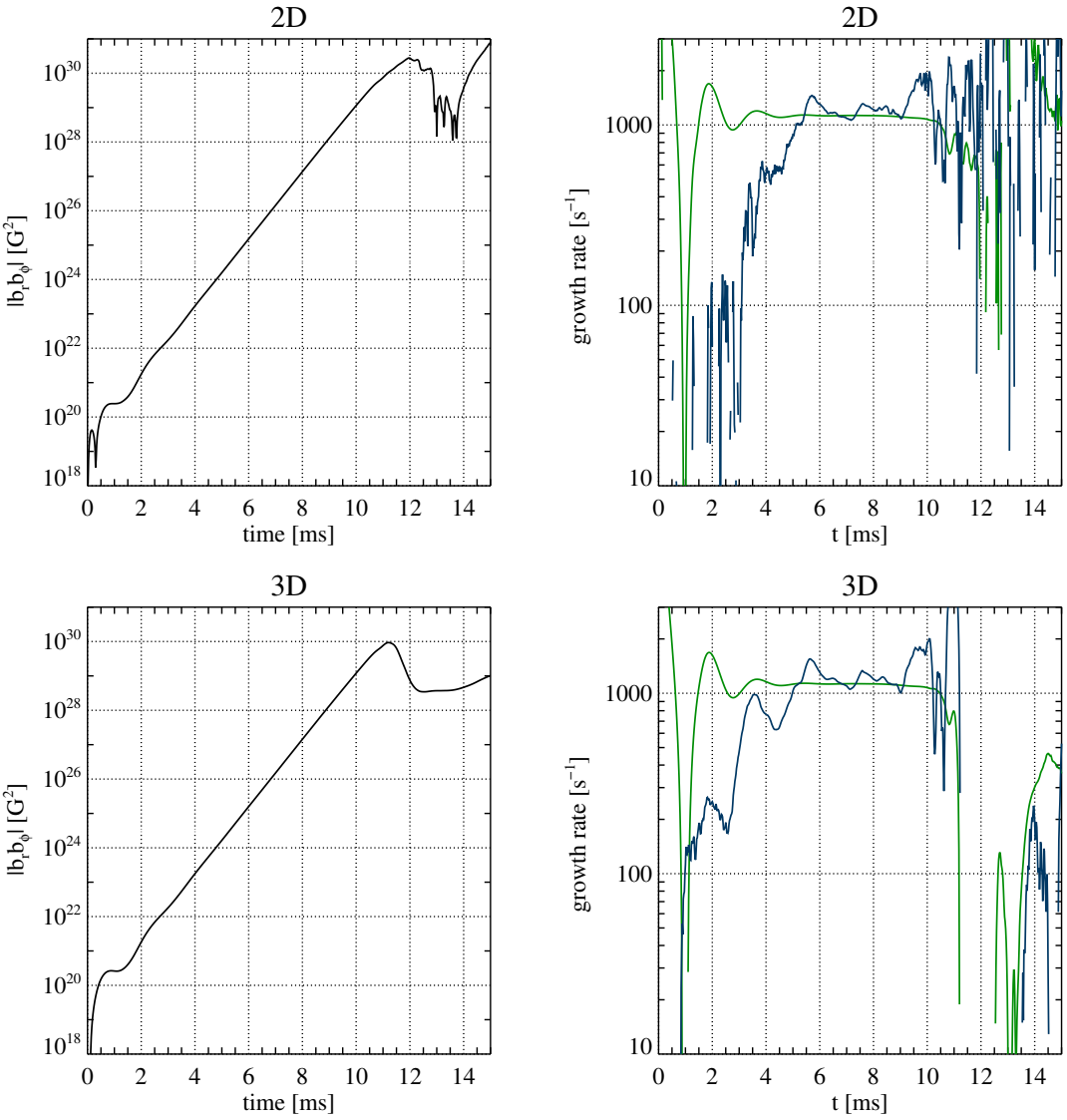

Figure 4.13: An attempt to measure the parasitic instability growth rate in a 2D and 3D MRI simulations with $b_{0z} = 4.6 \times 10^{13}$ G in a box of the size 1 km $\times$ (4 km$\times$)1 km in $r,(\phi,)z$ directions, respectively, and the resolution set to $100 \times (400\times)100$ zones. *Top left*: time evolution of the volume averaged Maxwell stress component $|b_r b_\phi|$ in the 2D simulation. From $t \approx 3$ ms to $t \approx 11$ ms, the MRI is fully operational, and for $t \approx 12$ ms, it is terminated by tearing modes. *Top right*: the green curve depicts the growth rate of the Maxwell stress component $|b_r b_\phi|$, i.e. $\partial_t(|b_r b_\phi|)/(2|b_r b_\phi|)$, which from $t \approx 4$ to $t \approx 10$ is approximately constant and equals $\gamma_{\rm MRI}$. The blue curve depicts $\dot{E}^z_{\rm kin}/(2E^z_{\rm kin})$, which should be equal to the growth rate of the parasitic instability (in this case, the tearing mode). Already at $t \approx 5$ ms, $\dot{E}^z_{\rm kin}/(2E^z_{\rm kin})$ exceeds $\gamma_{\rm MRI}$, however the MRI is not terminated shortly afterwards. *Bottom left*: the time evolution of the volume averaged $|b_r b_\phi|$ Maxwell stress component in the 3D simulation. For $t \approx 11$ms, the MRI terminated by the Kelvin-Helmholtz instability. *Bottom right*: analogous plot to the upper right one, but for the 3D simulation. $\dot{E}^z_{\rm kin}/(2E^z_{\rm kin})$ exceeds $\gamma_{\rm MRI}$ at $t \approx .5$ ms. Moreover, from $t \approx 4$ ms to $t \approx 10$ ms, the blue curves look very similar in the upper and lower left panels, even thought they should indicate the growth rates of different parasitic instabilities. This suggests that for $t \leq 10$ ms, the growth of $E^z_{\rm kin}$ is caused by some other (non 3D-)phenomenon.

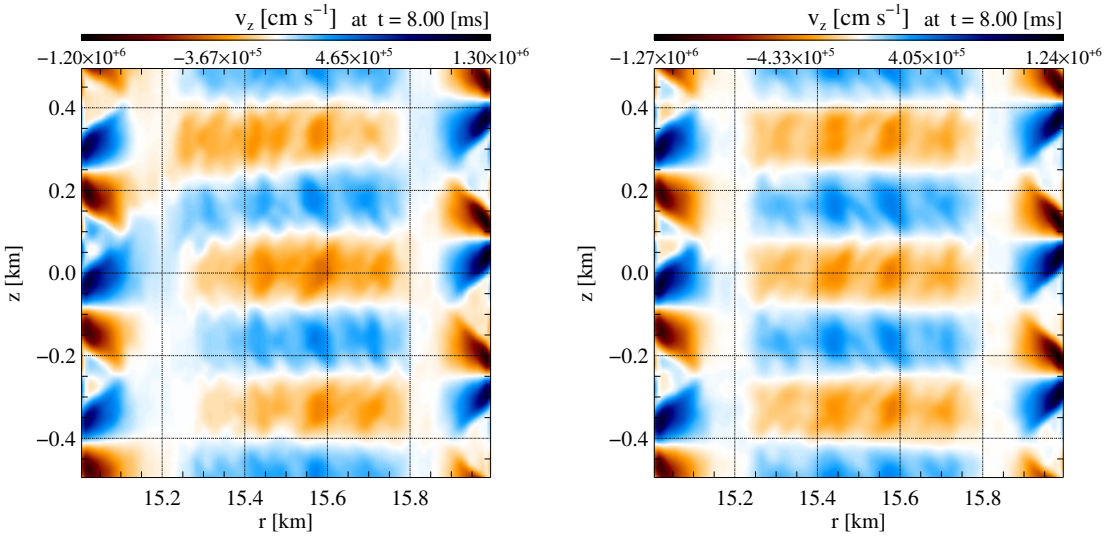

Figure 4.14: Vertical velocity, v_z, at $t = 8$ ms in the 2D (left) and 3D simulations (right) shown in Fig. 4.13. The MRI should not induce any vertical motions, therefore one could presume that they are indicators of the parasitic instabilities. However, we already know that in 2D and 3D simulations, there are different dominant secondary instabilities (tearing modes and KH instability), yet these two velocity profiles are very alike. Moreover, they have extrema close to the radial boundaries.

in the simulation.[32] We are faced with a numerical viscosity and resistivity, which are many orders of magnitude higher than desired (or better to say: tolerable). However, maybe longer modes (with, e.g. $k \approx k_{\rm MRI}/10$ and not with $k \approx k_{\rm MRI}/10$) are the most important for resolving the KH instability, and for these, the numerical dissipation is obviously smaller (because then $\mathcal{L} \approx \lambda_{\rm MRI}/10$). Moreover, simulations with higher resolutions will further decrease the numerical viscosity and resistivity.

This observation draws our attention to a very important general problem. In simulations of two (or more) phenomena, which have very different characteristic lengths, numerical resistivity and viscosity cannot be treated like scalars (even up to first order approximation). This adds additional complications, when comparing simulation results with theoretical predictions. The scale dependent numerical dissipation has to be somehow properly included in the (semi-)analytical description of the simulated problem. It would also be a mistake, however, to use the highest possible values of the numerical resistivity and viscosity for both phenomena. Some sort of a hybrid approach may be necessary, e.g. in our case, we could in principle use the ideal MHD equations for the MRI, and the non-ideal MHD equations (with scalar resistivity and viscosity) to describe the parasitic instability. [33] In many other situations, the choice may be less obvious, however. After these remarks, we come back to the main discussion.

In the simulation with a resolution of $100 \times 400 \times 100$ zones, the box averaged Maxwell stress component $|b_r b_\phi|$ at the MRI termination point was equal to 9.33×10^{29} G^2. This means that the

[32] We could simply notice that, in the given simulation, ≈ 33 zones are used per MRI channels. This only gives approximately one zone to resolve the characteristic length $\mathcal{L} = \lambda_{\rm MRI}/30$, which is obviously bound to fail.

[33] We wrote "in principle", because we did not even try to solve the secondary instability evolution equations, since it is a highly non-linear problem.

amplification factor $\mathcal{A}$ defined in Eq. (4.59) was equal to

$$\mathcal{A} \equiv \frac{b^{\text{term}}}{b_{0z}} = \frac{\sqrt{|b_r b_\phi|}}{b_{0z}} = 21.0. \tag{4.151}$$

To test how much the value depends on the initial perturbations, we run two additional simulations with the same initial conditions (obviously the random perturbations were unique in each case). The results of all three simulations are presented in Table 4.8 (first three rows). The differences among the termination amplitudes (and hence the amplification factors) are marginal. We explain this issue in the next section.

To test whether the termination amplitude was affected by numerical viscosity, we run a simulation with the very same physical and numerical setup, but a twice higher resolution, i.e. with $200 \times 800 \times 200$ zones. The MRI was terminated earlier and the box averaged Maxwell stress component was smaller and equal to $|b_r b_\phi| = 7.34 \times 10^{29}$ G^2 (see Table 4.6). This result can be easily understood in the light of the previous discussions. Increasing the resolution, lowered the numerical viscosity for the KH instability and therefore it developed faster and disrupted the MRI channels earlier.

So far, we can conclude that at least in the simulations with a resolution of $100 \times 400 \times 100$ zones, the numerical viscosity, ν_*, for the KH instability must have been (at least comparable to or) higher than $\nu = 4.45 \times 10^8$ cm^{2}s^{-1}. Otherwise, their MRI termination amplitudes would converge to those of the simulation with twice higher resolution ($200 \times 800 \times 200$ zones). We do not know however, if the numerical viscosity played a non-negligible role also in the latter simulation. The only way to check this is by running another simulation, with an even higher resolution and then comparing the results. However, because the computational cost of the simulation with $200 \times 800 \times 200$ zones was $\approx 250\,000$ CPUhs, a simulation with a twice higher resolution would need at least 4 000 000 CPUhs, which were not at our disposal. Hence, we ran the simulation with the highest resolution in a smaller box, that did not affect the MRI termination, but would have affected the subsequent turbulent phase. From Eq. (4.44), we estimate that the fastest growing KH mode

$$\lambda_{\text{KH}} \approx 1.7 \lambda_{\text{MRI}} \approx 0.56 \text{ km}. \tag{4.152}$$

Because the KH wavevector should form an angle $\pi/4$ with the r axis, the KH instability should be able to develop in a box, whose minimum size in the horizontal direction is $L_r \times L_\phi = 0.5$ km $\times$ 0.5 km.[34] As we discussed in Sec. 4.5.2, the MRI growth rate does depend on the radius. Therefore, changing the radial box size could possibly influence the box averaged MRI growth rate and termination amplitude. Reducing the box size by a factor of four in the azimuthal direction (from $L_\phi = 4$ km to $L_\phi = 1$ km), however, should not change the MRI termination amplitude. To test this hypothesis, we ran a simulation of box size 1 km $\times$ 1 km $\times$ 1 km with resolution $100 \times 100 \times 100$ zones (run 5 in Table 4.6). The MRI termination amplitude was the same as in the simulation run with the standard box size (see Table 4.6).

For the given initial magnetic field, i.e. $b_{0z} = 4.6 \times 10^{13}$ G, three MRI channels form in the z direction. It is tempting to reduce the vertical box size by a factor of three, so that only one channel forms in the computational domain. However, we must test, whether this step will not influence the MRI termination amplitude, e.g. in a box with three MRI modes, some inter-channel interactions

[34] The diagonal of a box as small as $L_r \times L_\phi = 0.4$ km $\times$ 0.4 km is greater than 0.56 km. However, in such a small box, the mode could develop only along the diagonal. On the other hand, the modes developing close to the edges would be affected by the boundary conditions in any box. It would be better to study the parasitic instability in a box rotated by 45° around the z axis. This box orientation, however, would be sub-optimal for the MRI channels.

run #	box size $(r \times \phi \times z)$ [km]	resolution $(r \times \phi \times z)$	zones per channel	$\lvert b_r b_\phi \rvert$ [10^{30} G^2] at termination	termination time [ms]	amplification factor $\mathcal{A}$
1	$1 \times 4 \times 1$	$60 \times 240 \times 60$	20	1.11	11.36	22.9
2	$1 \times 4 \times 0.333$	$60 \times 240 \times 34$	34	0.977	11.22	21.5
3	$1 \times 4 \times 1$	$76 \times 304 \times 76$	≈ 25	1.04	11.28	22.2
4	$1 \times 4 \times 1$	$100 \times 400 \times 100$	≈ 33	0.933	11.20	21.0
5	$1 \times 1 \times 1$	$100 \times 100 \times 100$	≈ 33	0.930	11.18	21.0
6	$1 \times 1 \times 0.333$	$100 \times 100 \times 34$	34	0.929	11.20	21.0
7	$1 \times 4 \times 1$	$200 \times 800 \times 200$	≈ 67	0.734	11.10	18.6
8	$1 \times 1 \times 0.333$	$400 \times 400 \times 134$	134	0.731	11.12	18.6

Table 4.6: The results of 3D MRI simulations with initial magnetic field, viscosity and resistivity of $b_{0z} = 4.6 \times 10^{13}$ G, and $\nu = \eta = 4.45 \times 10^8$ cm^{2}s^{-1}, respectively. In the simulations, different resolutions and box sizes were used. Comparing runs 4–6, we conclude that the box size within the explored range does not have any influence on the MRI termination amplitude and therefore on the amplification factor.

could be possible, or the channels could be disrupted at slightly different times. To test this, we ran a simulation in a box of size 1 km $\times$ 1 km $\times$ 0.333 km with a resolution of $100 \times 100 \times 34$ zones (run 6 in Table 4.6), which gave the same MRI termination amplitude.

After making sure that a simulation run in a box, whose volume is 12 times smaller (in comparison to the standard box), gives the same predictions for the MRI termination amplitude, we ran a simulation in a box of size 1 km $\times$ 1 km $\times$ 0.333 km with a resolution $400 \times 400 \times 134$ zones (run 8 in Table 4.6).[35] The MRI termination amplitude was the same as in the simulation run with the standard box size of $200 \times 800 \times 200$ zones (run 7 in Table 4.6). This shows that the influence of the numerical viscosity in the simulation with $200 \times 800 \times 200$ zones was negligible. Hence, we can draw the conclusion that for Reynolds numbers $R_\mathrm{e} = R_\mathrm{m} = 100$, the amplification factor is $\mathcal{A} = 18.6$ (see Table 4.6), which also gives an upper limit for supernova conditions (e.g. for even larger Reynolds numbers: $R_\mathrm{e}, R_\mathrm{m} \gg 100$).

For reasons, discussed in the next section, we ran two more simulations in the standard box (1 km $\times$ 4 km $\times$ 1 km), with much lower resolutions of $60 \times 240 \times 60$ and $76 \times 304 \times 76$ zones (runs 1 and 3 in Table 4.6). The results show a clear correlation between the MRI termination amplitude and time. The lower the resolution, the later the termination time and hence the higher the termination amplitude (and by definition, the amplification factor). Fig. 4.15 depicts the time evolution of the volume averaged Maxwell stress component $\lvert b_r b_\phi \rvert$ from simulations presented in Table 4.6. During the first $\approx$ 10.7ms, the time evolution of the $\lvert b_r b_\phi \rvert$ is indistinguishable in all simulations. Differences appear once the parasitic instabilities start to play a role in the system.

So far, we have used an initial magnetic field strength, which is approximately two orders of magnitude higher than the upper limit expected in core-collapse supernovae (at the stage when the proto-neutron star forms). Hence, without giving any prescription how to extrapolate our results, our simulations cannot be used to draw any conclusions, given supernova conditions.

[35] This simulation required $\approx$ 460 000 CPUhs.

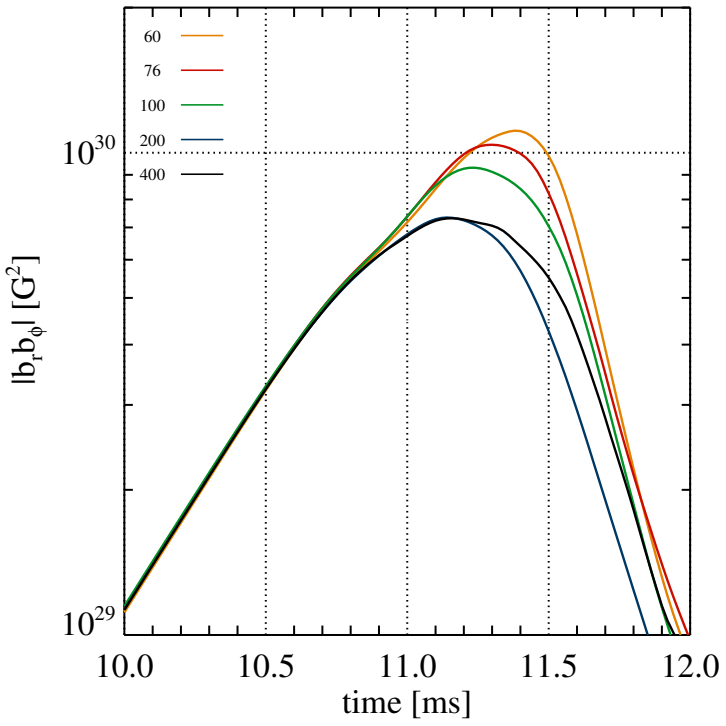

Figure 4.15: Time evolution of the volume averaged Maxwell stress component $|b_r b_\phi|$ from 3D MRI simulations with different resolutions and with the magnetic field, the viscosity and the resistivity set to $b_{0z} = 4.6 \times 10^{13}$ G, and $\nu = \eta = 4.45 \times 10^8$ cm^{2}s^{-1}, respectively. All simulations, but the one with the highest resolution, were run in a box of size 1 km $\times$ 4 km $\times$ 1 km in the r, ϕ and z directions, respectively. The simulation with the highest resolution was run in a smaller box, i.e. of 1 km $\times$ 1 km $\times$ 0.333 km, to reduce the computational cost. The list of the simulations is presented in Table 4.6. The evolution of $|b_r b_\phi|$ is almost identical in all simulations, i.e. with: 60 (orange), 76 (red), 100 (green), 200 (blue) and 400 (black) radial zones, until $t \approx 10.7$ ms. After this time, the differences start to be visible. In general, the lower the resolution, the higher the termination amplitude. Only the simulations with the two highest resolutions converge to the same value. Note that there is a clear correlation between the MRI termination time and termination amplitude.

The influence of the initial magnetic field

In Sec. 4.4, we argued that the amplification factor $\mathcal{A}$ should be independent of the initial magnetic field strength. To test whether this statement holds, we ran three additional simulations with two different initial field values. We used the standard simulation box size (1 km $\times$ 4 km $\times$ 1 km), and viscosity and resistivity set to $\nu = \eta = 4.45 \times 10^8$ cm^{2}s^{-1}. In the first two simulations with resolution of $100 \times 400 \times 100$ zones, we set the initial magnetic field to $b_{0z} = 2.76 \times 10^{13}$ G and 3.45×10^{13} G, for which respectively five and four MRI channels formed in the computational domain. In the former and the latter simulation, the amplification factor was $\mathcal{A} = 23.4$ and $\mathcal{A} = 21.6$, respectively (run 1 and 3 in Table 4.7). In a corresponding simulation with an initial magnetic field $b_{0z} = 4.6 \times 10^{13}$ G, the amplification factor was $\mathcal{A} = 21.0$ (see run 5 in Table 4.7). These

run #	b_{0z} [10^{13} G]	resolution ($r \times \phi \times z$)	zones per channel	$\gamma_{\rm MRI}$ [s^{-1}]	$\lvert b_r b_\phi \rvert$ [10^{30} G^2] at termination	termination time [ms]	amplification factor $\mathcal{A}$
1	2.76	$100 \times 400 \times 100$	20	1108	0.416	10.86	23.4
2	2.76	$168 \times 672 \times 168$	≈ 34	1109	0.366	10.84	21.9
3	3.45	$100 \times 400 \times 100$	25	1119	0.555	11.06	21.6
4	4.6	$60 \times 240 \times 60$	20	1126	1.11	11.36	22.9
5	4.6	$76 \times 304 \times 76$	≈ 25	1127	1.04	11.28	22.2
6	4.6	$100 \times 400 \times 100$	≈ 33	1127	0.929	11.20	21.0

Table 4.7: The results of 3D MRI simulation run in a box of the size 1 km $\times$ 4 km $\times$ 1 km in the r, ϕ and z directions, respectively. In all simulations, the viscosity and the resistivity were set to $\nu = \eta = 4.45 \times 10^8$ $cm^2 s^{-1}$. For the initial magnetic field $b_{0z} = 2.76 \times 10^{13}$ G, 3.45×10^{13} G and 4.6×10^{13} G, respectively, five, four and three MRI channels formed in the computational domain.

results suggest that $\mathcal{A}$ does depend on the initial magnetic field. We must not forget, however, that because in the simulations with $b_{0z} = 2.76 \times 10^{13}$ G and 3.45×10^{13} G, five and four MRI channels formed, respectively, a smaller number of zones was available to resolve one channel: 20 and 25, respectively. This means, that because of the higher numerical viscosity, the KH instability developed more slowly and therefore, the MRI could amplify the magnetic field for a longer time (to higher amplitudes).

We ran three more simulations, to support this argument. In the first simulation with an initial magnetic field $b_{0z} = 2.76 \times 10^{13}$ G, we used a higher resolution of $168 \times 672 \times 168$ zones (run 2 in Table 4.7), which corresponds to a resolution of ≈ 33 zones per MRI channel. The amplification factor dropped to $\mathcal{A} = 21.9$, which is closer to the value obtained in the simulation with $b_{0z} = 4.6 \times 10^{13}$ G (Table 4.7). In two other simulations with magnetic field $b_{0z} = 4.6 \times 10^{13}$ G, we used lower resolutions of $60 \times 240 \times 60$ and $76 \times 304 \times 76$ zones (run 3 and 4 in Table 4.7). This approximately gives the same number of zones per MRI channel as in the simulations with $b_{0z} = 2.76 \times 10^{13}$ G and 3.45×10^{13} G, respectively, and $100 \times 400 \times 100$ zones. In both cases, in the simulations with $b_{0z} = 2.76 \times 10^{13}$ G the amplification factor was somewhat higher than in the corresponding simulations with $b_{0z} = 4.6 \times 10^{13}$ G (in the simulations with the lower resolutions $\mathcal{A} = 23.4$ and $\mathcal{A} = 22.9$, respectively for the smaller and bigger initial field, and in the simulations with the higher resolutions $\mathcal{A} = 21.9$ and $\mathcal{A} = 21.0$, respectively). This could still suggest some weak dependence of $\mathcal{A}$ on the initial magnetic field strength. However, in the simulation with $b_{0z} = 3.45 \times 10^{13}$ G, the amplification factor $\mathcal{A} = 21.6$ is lower than in the corresponding simulation with $b_{0z} = 4.6 \times 10^{13}$ G, i.e. $\mathcal{A} = 22.2$. This clearly shows, that these small differences are of a numerical origin.

First of all, we made sure that an integer number of the MRI channels would fit into the computational domain. However, we could not do the same for the KH modes, which develop in diagonal direction (in the horizontal plane) in the box. Moreover, the fastest growing KH mode length depends on the channel width – for a different initial magnetic field strength, a different non-integer number of the KH modes will fit in the computational domain. This can clearly affect the MRI termination process. Second of all, in all simulations we used the same values of the viscosity and resistivity. This means that simulations with different initial magnetic fields had somewhat different Reynolds numbers, which could affect the system dynamics (see e.g. the MRI growth rates in Table 4.7). All in all, we can conclude that the amplification factor $\mathcal{A}$ does not depend on the initial magnetic field strength.

Influence of initial perturbations

In the 2D simulations, we learnt that the MRI termination amplitude can be significantly (for the current discussion by a factor of two) affected by the initial velocity perturbations (see e.g. Table 4.3). Therefore, it is necessary to investigate this issue also with 3D simulations. We ran for this purpose three simulations with the standard initial magnetic field, box size and resolution, i.e. $b_{0z} = 4.6 \times 10^{13}$ G, $L_r \times L_\phi \times L_z = 1$ km $\times$ 4 km $\times$ 1 km and $100 \times 400 \times 100$ zones, respectively. The initial velocity was given by Eq. (4.112):

$$\mathbf{v} = \Omega r \left[\{0.1\delta\Re_r(r,\phi,z) + \varepsilon \sin(k_z z)\}\hat{\mathbf{r}} \right] + \{1 + \delta\Re_\phi(r,\phi,z)\}\hat{\boldsymbol{\phi}} + \delta\Re_z(r,\phi,z)\hat{\mathbf{z}} \Big],$$

where $k_z = k_{\mathrm{MRI}}$ is the radial perturbation wavevector, $\delta = 10^{-5}$ and $\varepsilon = 2 \times 10^{-6}$ are the random and the sinusoidal perturbation amplitudes, respectively. In all three simulations, the differences between the MRI termination amplitudes were marginal (see Table 4.8), in strong contrast to the results of the 2D simulations with the same resolution in the (r,z) plane (see Table 4.3). In 3D simulations, the initial random perturbations are introduced not only in one (r,z) slice, i.e. for constant ϕ, but throughout the box. Hence, the likelihood that in some part of the box, random perturbations will effectively trigger parasitic instability is much higher. This can be illustrated with the Fourier transforms of the radial and vertical velocity in the z direction, analogous to Eqs. (4.128) and (4.129), respectively:

$$\hat{v}_r(r,\phi,\bar{k}_z) = \frac{1}{N_z} \sum_{n=0}^{N_z-1} v_r(r,\phi,z) e^{-i2\pi n \bar{k}_z / N_z}, \tag{4.153}$$

$$\hat{v}_z(r,\phi,\bar{k}_z) = \frac{1}{N_z} \sum_{n=0}^{N_z-1} v_z(r,\phi,z) e^{-i2\pi n \bar{k}_z / N_z}. \tag{4.154}$$

This time, the spatial averaging of the coefficients $\hat{v}_r(r,\phi,\bar{k}_z)$ and $\hat{v}_r(r,\bar{k}_z)$ is performed in two orthogonal directions: r and ϕ, i.e.

$$|\tilde{v}_r(\bar{k}_z)| \equiv \frac{2}{N_r N_\phi} \sum_{j=1}^{N_r} \sum_{k=1}^{N_\phi} \sqrt{\hat{v}_r(r_j,\phi_k,\bar{k}_z)\hat{v}_r^*(r_j,\phi_k,\bar{k}_z)}, \tag{4.155}$$

$$|\tilde{v}_z(\bar{k}_z)| \equiv \frac{2}{N_r N_\phi} \sum_{j=1}^{N_r} \sum_{k=1}^{N_\phi} \sqrt{\hat{v}_z(r_j,\phi_k,\bar{k}_z)\hat{v}_z^*(r_j,\phi_k,\bar{k}_z)}, \tag{4.156}$$

where j and k enumerate the zone numbers in the radial and azimuthal directions, respectively. The outcome of this procedure is presented in Fig. 4.16. For comparison, we also included there the 2D simulation results, which were already presented in Figs. 4.7 and 4.8. As we can see, the coefficients $|\tilde{v}_r(\bar{k}_z)|$ and $|\tilde{v}_r(\bar{k}_z)|$ have a much smaller scatter in the 3D simulations, because the random perturbations had much more variety. Fig. 4.16 can by no means be taken as a rigorous proof of our claim, but it strongly supports our argumentation.

So far, we only showed, that for one particular combination of δ and ε in Eq. (4.112), the MRI termination amplitude is constant. An important question to ask is, whether it is also the case for different perturbation amplitudes. On the one hand, one could intuitively guess that for higher values of ε (the amplitude of the sine perturbations in v_r), the MRI might be able to form the channels faster and amplify the magnetic field to higher values. On the other hand, random perturbations with higher amplitudes, δ, would be better seeds for the parasitic instabilities. They could develop faster and terminate the MRI earlier. To test this, we run one simulation with the

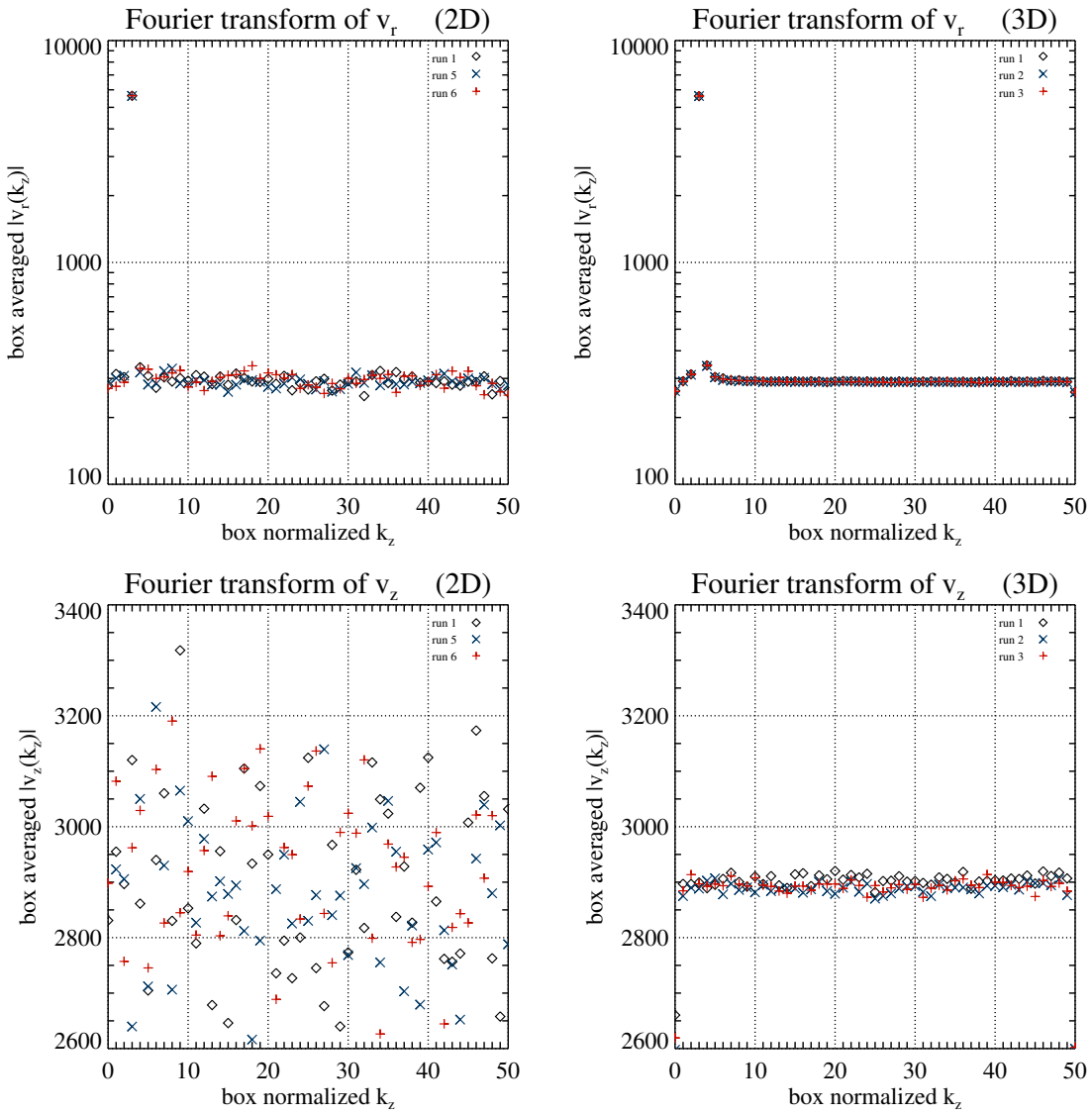

Figure 4.16: Comparison of the spatially averaged Fourier transform coefficients $|\tilde{v}_z(\bar{k}_z)|$ and $|\tilde{v}_z(\bar{k}_z)|$ (see Eqs. (4.130), (4.131), and Eqs. (4.155), (4.156)) of the initial radial and vertical velocity for the 2D (left panels) and 3D (right panels) simulations. Similar plots for a 2D simulation are presented in Fig. 4.7. *Top left*: The coefficients $|\tilde{v}_r(\bar{k}_z)|$ from three 2D simulations denoted as *run 1* (black diamonds), *run 5* (blue crosses) and *run 6* (red pluses) in Table 4.3. The peak corresponding to the sine perturbation (see Eq. (4.112)) at $\bar{k}_z = 3$ is clearly visible. The other coefficients have some random scatter. *Top right*: The coefficients $|\tilde{v}_r(\bar{k}_z)|$ of 3D simulations denoted as *run 1* (black diamonds), *run 2* (blue crosses) and *run 3* in Table 4.8. The values of the corresponding coefficients $|\tilde{v}_r(\bar{k}_z)|$ are similar in all three simulations. *Bottom left*: The coefficients $|\tilde{v}_z(\bar{k}_z)|$ from the three 2D simulations. Since the perturbations of v_z were purely random, there is no distinct maximum in $|\tilde{v}_z(\bar{k}_z)|$, but some scatter. *Bottom right*: The coefficients $|\tilde{v}_z(\bar{k}_z)|$ from the three 3D simulations. The scatter is much smaller than for the 2D simulations.

run #	$\delta[10^{-5}]$	$\varepsilon[10^{-6}]$	k_z	box size $(r\times\phi\times z)$ [km]	resolution $(r\times\phi\times z)$	$\lvert b_r b_\phi\rvert$ $[10^{30}\mathrm{G}^2]$ at termination	termination time [ms]	amplification factor $\mathcal{A}$
1	1	2	$k_{\rm MRI}$	$1\times4\times1$	$100\times400\times100$	0.933	11.20	21.0
2	1	2	$k_{\rm MRI}$	$1\times4\times1$	$100\times400\times100$	0.931	11.20	21.0
3	1	2	$k_{\rm MRI}$	$1\times4\times1$	$100\times400\times100$	0.943	11.21	21.1
4	2	2	$k_{\rm MRI}$	$1\times4\times1$	$100\times400\times100$	0.949	11.22	21.2
5	1	2	$k_{\rm MRI}$	$1\times1\times0.333$	$100\times100\times34$	0.929	11.20	21.0
6	1	2	$3k_{\rm MRI}$	$1\times1\times0.333$	$100\times100\times34$	0.851	14.40	20.0

Table 4.8: The results of 3D simulations designed to investigate the dependence of the MRI termination amplitude on the initial velocity perturbations (given by Eq. 4.112)). The initial magnetic field, the viscosity and the resistivity set to $b_{0z}=4.6\times10^{13}$ G, and $\nu=\eta=4.45\times10^{8}$ cm^{2}s^{-1}, respectively. The amplitudes: δ of the sine radial velocity perturbations, and ε of the random velocity perturbations were defined in Eq. (4.112). $k_{\rm MRI}$ is the wavevector of the MRI fastest growing mode, i.e., $k_{\rm MRI}\equiv2\pi/\lambda_{\rm MRI}$. Given the initial conditions, $k_{\rm MRI}=2\pi/0.333$ km^{-1}. In the first three simulations, the same prescription for the initial velocity was used (obviously, the random part of the perturbations was unique in every simulation). In the last simulation, the radial velocity perturbations formed channels, which were three times shorter, than the MRI fastest growing mode (see also Fig. 4.17). In general, we can conclude that the MRI termination amplitude very weakly depends on the initial perturbations.

very same initial conditions (i.e. $b_{0z}=4.6\times10^{13}$ G, $L_r\times L_\phi\times L_z=1$ km $\times4$ km $\times1$ km and $100\times400\times100$ zones) but a twice higher random perturbation amplitude, i.e. $\delta=2\times10^{-5}$ instead of $\delta=10^{-5}$. The simulation results are presented in Table 4.8. The amplification factor was even slightly larger than in the previous simulations, i.e. $\mathcal{A}=21.2$. This disproves our hypothesis.

The final issue, which needs to be discussed, is the sinusoidal component (proportional to ε) of the radial velocity perturbations in Eq. (4.112), which we introduced to guarantee a certain number of equally wide MRI channels. However, it is highly doubtful, whether such perturbations would be encountered in nature. To test how much these sinusoidal perturbations affect the MRI termination amplitude, we performed another simulation. In the box of the size $L_r\times L_\phi\times L_z=1$ km $\times1$ km $\times0.333$ km, resolved with $100\times100\times34$ zones, we set the initial magnetic field set $b_{0z}=4.6\times10^{13}$ G (run 6 in Table 4.8). For these initial conditions, exactly one fastest growing MRI mode would fit into the computational domain. Once again we used Eq. (4.112), however this time we set $k_z=3k_{\rm MRI}$, i.e. the radial velocity formed three channels, which were three times smaller than the fastest growing MRI mode (see the upper left panel of Fig. 4.17). The other velocity components were, as usually, randomly perturbed. It is hard to imagine more unfavourable initial conditions for the MRI fastest growing mode. Still, after ≈3 ms (later than usually), the instability managed to form one channel (see the bottom left panel of the figure).[36]

[36]This simulation is a very good illustration of two aspects. Firstly, the MRI is a powerful instability, which does not need any specially fine tuned initial conditions to start growing. Secondly, that the simulated physics can be sometimes (strongly) affected by boundary conditions, which facilitated the formation of exactly one channel from unfavourable initial conditions for the following reason. Three channels were not growing fast enough, to dominate the initial stage of the evolution. For the formation of either two or one MRI channels, these perturbations were as good as random ones. Only one channels formed, because it had a much higher growth rate. However, all other possibilities like , e.g. formation of 1.5 channels were forbidden by the periodic vertical boundary conditions. It is not clear, whether in a much larger box, exactly one channel would emerge from these initial conditions. See e.g. Fig 4.4, where four instead

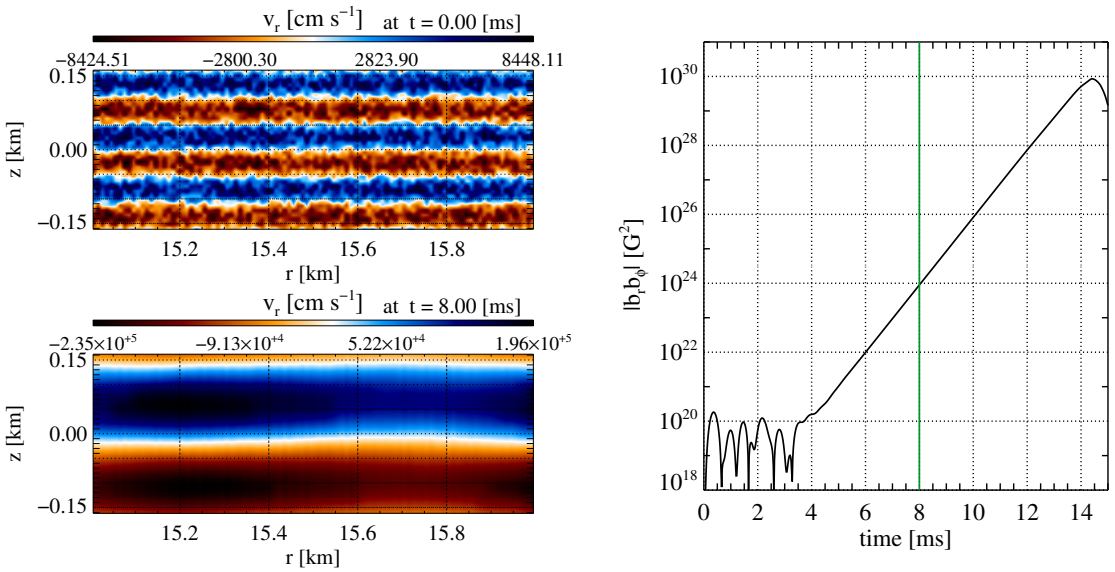

Figure 4.17: The influence of the initial velocity perturbations on MRI channel formation in a 3D simulation (run 6 in Table 4.6). The magnetic field, the viscosity and the resistivity were set to $b_{0z} = 4.6 \times 10^{13}$ G, and $\nu = \eta = 4.45 \times 10^8$ cm^{2}s^{-1}, respectively. The simulation box size 1 km $\times$ 1 km $\times$ 0.333 km in the r, ϕ and z directions, respectively, was resolved with $100 \times 100 \times 34$ zones. The initial velocity is given by Eq. (4.112). However, this time, the wavelength of the sinusoidal radial velocity perturbations was equal to $\lambda = 0.111$ km (see *upper left* panel), instead of to $\lambda_{\rm MRI} = 0.333$ km – the wavelength of the fastest growing MRI mode. In spite of these unfavourable initial conditions, after $\approx$ 4ms, one fastest growing MRI channel was formed (see *bottom left* panel). *Right:* time evolution of the volume averaged Maxwell stress component $|b_r b_\phi|$. Because of the unfavourable initial conditions, the MRI starts to be fully operational only after ≈ 4 ms, and not as usually after ≈ 2 ms (compare e.g. with Fig. 4.10). The termination amplitude $|b_r b_\phi|$ (achieved at a later time) is almost the same as in the other comparable simulations (see Table 4.6). The green vertical like marks the time $t = 8$ ms at which the radial velocity is shown in the bottom left panel.

What is more important, the amplification factor $\mathcal{A} = 20.0$ was only 5% smaller than in the other simulations (see Table 4.8). From this result, we can conclude that the amplification factor very weakly depends on the initial conditions.

Final conclusions

We have shown that in the 3D MRI simulations with Reynolds numbers $R_{\rm e} = R_{\rm m} = 100$, the MRI amplifies the initial magnetic field by a constant factor $\mathcal{A} = 18.6$, independent of the initial magnetic field strength and very weakly depending on the initial perturbations.[37] This result provides us with an upper limit for the magnetic field amplification by the MRI at even higher Reynolds numbers, for which $\mathcal{A}$ can be even smaller. We conclude that theoretically expected magnetic fields encountered in core-collapse supernovae (in the nascent proto-neutron star in the post-bounce phase) of order 10^{11} G cannot be amplified by the MRI to dynamically significant amplitudes of order 10^{15} G.

of the theoretically expected five MRI channels formed from random perturbations.

[37] Provided they do not have a special form, e.g. of the exact MRI channel solutions.

viscosity ν [cm^2 s^{-1}]	resistivity η [cm^2 s^{-1}]	box size $(r \times \phi \times z)$ [km]	resolution $(r \times \phi \times z)$	$\gamma_{\rm MRI}$ [s^{-1}]	$\lvert b_r b_\phi \rvert$ [10^{30} G^2] at termination	termin. time [ms]	amp. factor $\mathcal{A}$
0	0	$1 \times 4 \times 1$	$100 \times 400 \times 100$	1137	0.960	11.10	21.3
4.45×10^8	4.45×10^8	$1 \times 4 \times 1$	$100 \times 400 \times 100$	1127	0.933	11.20	21.0
4.45×10^9	4.45×10^8	$1 \times 4 \times 1.05$	$100 \times 400 \times 106$	1128	1.02	11.26	22.0
4.45×10^8	4.45×10^9	$1 \times 4 \times 1.08$	$100 \times 400 \times 108$	1042	0.926	12.32	20.9
4.45×10^9	4.45×10^9	$1 \times 4 \times 1.13$	$100 \times 100 \times 114$	1043	1.09	12.36	22.7
4.45×10^{10}	4.45×10^{10}	$1 \times 4 \times 1.95$	$100 \times 100 \times 200$	566	0.536	22.76	15.9

Table 4.9: Results of the simulations with the initial magnetic field set to $b_{0z} = 4.6 \times 10^{13}$ G and different values of viscosity and resistivity. $\nu = 4.45 \times 10^8, 4.45 \times 10^9$ and 4.45×10^{10} cm^{2}s^{-1} corresponds to $R_{\rm e} = 100, 10$ and 1, respectively. The box size in the z direction is chosen so that three fastest growing MRI modes fit into the computational domain.

Other Reynolds numbers

Additionally, we run a few simulations with the initial magnetic field set to $b_{0z} = 4.6 \times 10^{13}$ G and with different Reynolds numbers in the standard box size 1 $km \times 4$ km $\times L_z$ with a resolution of $100 \times 400 \times N_z$ zones. The resistivity and viscosity were independently set to $4.45 \times 10^8, 4.45 \times 10^9$ or 4.45×10^{10} cm^{2}s^{-1}, which corresponds to Reynolds numbers $100, 10$ and 1, respectively. The vertical box length, L_z, and the resolution, N_z, were chosen so that exactly three fastest growing MRI modes fit into the computational domain, and ≈ 33 zones were used per channel. We also run one simulation without physical viscosity and resistivity, i.e. $\nu = \eta = 0$ cm^{2}s^{-1}, which corresponds to infinite Reynolds numbers, i.e. the ideal MHD limit. Obviously, numerical dissipation was present in that simulations. The details of the initial setups and simulation results can be found in Table 4.9. Since (apart from the ideal MHD limit) such low Reynolds numbers, i.e. $R_{\rm e}, R_{\rm m} \leq 100$, are not encountered in core-collapse supernovae, we did not spend too much time analysing these simulations. The MRI channels are well resolved in all simulations and the measured instability growth rate values are reliable. Note that only for $R_{\rm e} = R_{\rm m} = 1$, the MRI growth rate is significantly affected by resistivity and viscosity. The growth rate in the ideal MHD limit is very close to the one obtained for $R_{\rm e} = R_{\rm m} = 100$, which were the default Reynolds numbers in our simulations. As for the amplification factor, it is clear that in all simulations it must have been affected by numerical dissipation. Therefore, we cannot draw any reasonable conclusions on the dependence of the amplification factor on hydrodynamic and magnetic Reynolds numbers.

4.5.4 Comparison of 2D and 3D simulations

In this section, we present a brief comparison between the 2D and 3D MRI simulations. The first stages of the instability, i.e. MRI channel formation and exponential magnetic field amplification, look the same in both type of simulations. Differences become visible during the phase, when the MRI is terminated by parasitic instabilities developing on top of its channels. In the 2D simulations, the KH instability is suppressed because of the assumed axial symmetry, and these are only tearing modes, which can terminate the MRI growth. In the 3D simulations, the faster developing KH instability is responsible for the disruption of the MRI channels. In Fig. 4.18, we compare the radial magnetic field at MRI termination in a 2D and 3D simulation. The differences in the field structure are obvious.

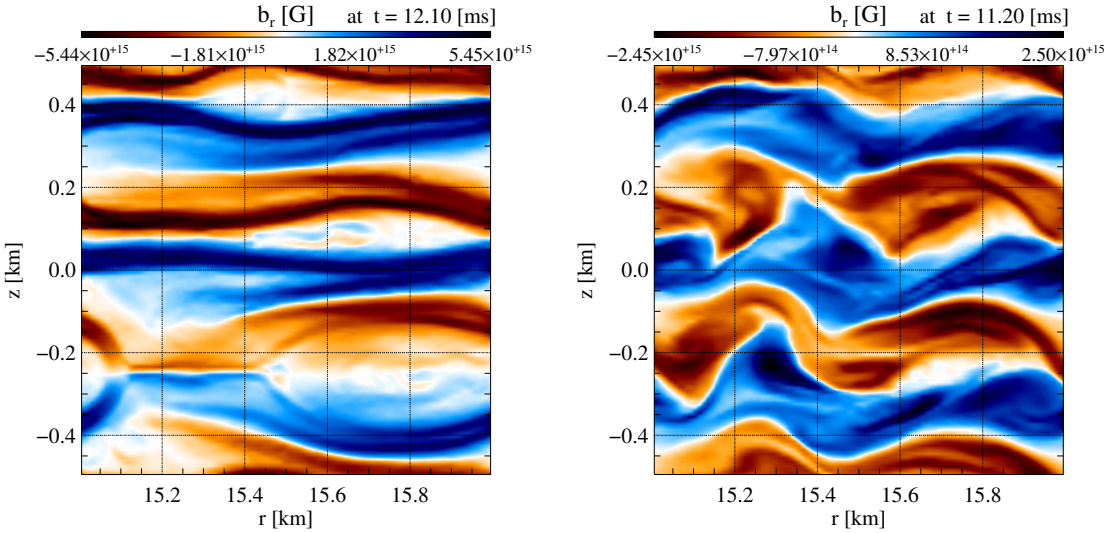

Figure 4.18: Comparison of the radial magnetic field at MRI termination in a 2D (left) and 3D (right) simulation with the initial magnetic field, the viscosity and the resistivity set to $b_{0z} = 4.6 \times 10^{13}$ G, and $\nu = \eta = 4.45 \times 10^8$ cm^{2}s^{-1}, respectively. The results of the 2D and 3D simulation were already presented in Fig. 4.6, and Figs. 4.10 and 4.11, respectively. In the left panel, the X and O points characteristic for the tearing modes are clearly visible. From the field pattern in the right plot, we can identify the Kelvin-Helmholtz instability. The two panels clearly demonstrate that the MRI termination mechanism is different in 2D and 3D simulations.

Because the MRI is terminated faster in 3D simulations, it can amplify the initial magnetic field less. In Fig. 4.19, we present the MRI termination amplitude as a function of resolution for the 2D and 3D simulations.

Another difference, which can be observed in Fig. 4.19, is that in the 2D simulations (especially at lower resolution), the MRI termination amplitude depends on the initial random velocity perturbations. We explained this phenomenon by the fact that in 3D simulations, where many more zones were used, the random perturbations had a higher chance to trigger parasitic instabilities effectively in some part of the simulation domain.

4.6 Summary

In accordance with Obergaulinger et al. (2009), by means of numerical simulations, we showed that the MRI can develop in core-collapse supernovae. Moreover, we have confirmed the theoretical hypothesis (Goodman & Xu (1994), Pessah & Goodman (2009), Pessah (2010)) that the MRI can be terminated by parasitic instabilities, i.e. the Kelvin-Helmholtz or tearing mode instability. We pointed out some inconsistencies in Pessah's calculations of the MRI termination amplitudes and proposed an alternative description of this highly non-linear phenomenon. Combining this theoretical, somewhat phenomenological, approach with our simulation results, we conclude that for the conditions encountered during a core-collapse supernova explosion, the MRI can amplify the initial magnetic field only by a constant factor (≈ 20). Therefore, the progenitor's magnetic field (of order 10^9 G), first amplified by compression (up to $\approx 10^{11}$G) in the pre-bounce phase and later by the MRI in the post-bounce phase (up to $\approx 10^{12}$ G), cannot reach dynamically important

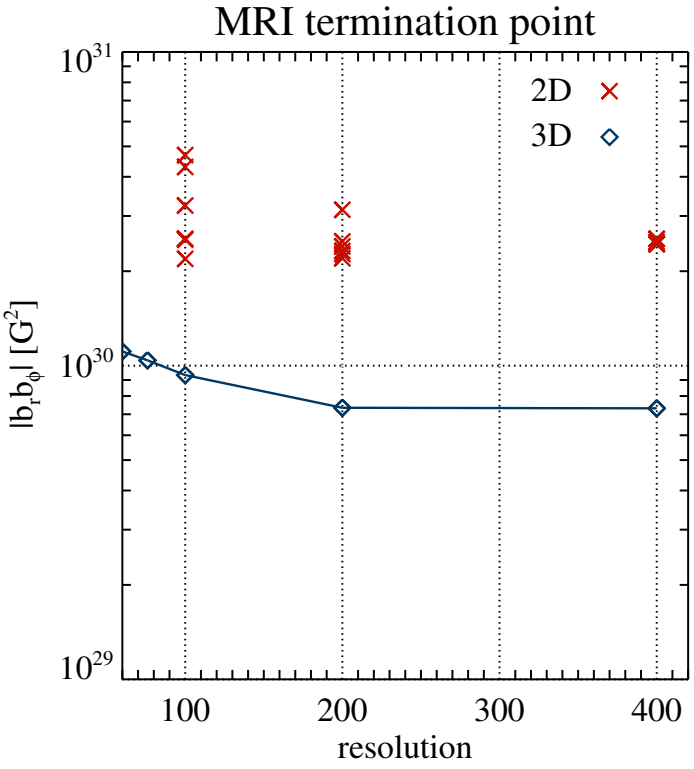

Figure 4.19: Comparison of the MRI termination amplitude in 2D (red crosses) and 3D (blue diamonds) simulations with the initial magnetic field, the viscosity and the resistivity set to $b_{0z} = 4.6 \times 10^{13}$ G, and $\nu = \eta = 4.45 \times 10^8$ cm^{2}s^{-1}, respectively. The results were presented in Tables 4.3, 4.4 and 4.5 for the 2D and in Table 4.6 for the 3D simulations. The abscissa gives the number of zones used to resolve the radial direction, r. Since the Kelvin-Helmholtz instability cannot develop in 2D, the magnetic field is amplified to higher amplitudes (in comparison with the 3D simulations) by the MRI before it is terminated by tearing modes. In 3D simulations, the MRI is terminated by the faster developing KH instability and therefore the magnetic field reaches lower values. In the 2D simulations with lower resolutions, the MRI termination amplitude depends on the random initial velocity perturbations (see Eq. (4.112)). In 3D simulations, there is no such dependence observed. For the resolution "100", the results from three different simulations are plotted. However, the differences between the amplitudes are indistinguishable in the plot (see Table 4.8). The simulations with resolutions "200" and "400" converge to the same value (see Table 4.6).

amplitudes (of order 10^{15} G). However, it is known from astronomical observations that magnetars have magnetic fields of order 10^{15} G (Kouveliotou et al. 1998). Thus, the question of magnetic field amplification remains open. Some new mechanism has to be proposed. The MRI could still be an important but not the sole amplifying agent.

Another important lesson that we learnt is that for MRI studies, 3D simulations are a must. In 2D simulations, because of the assumed axial symmetry, the KH instability is suppressed and the MRI can only be terminated by the tearing modes. This undesirable and unphysical phenomenon will lead to too high MRI termination amplitudes. Hence, only the exponential growth phase of the MRI can be correctly captured in 2D numerical simulations. However, there is no need for such simulations, since analytical equations describing this stage of the MRI evolution are known even in non-ideal MHD (Pessah & Chan 2008).

The idea of taking magnetic fields, which have amplitudes much higher than expected in nature, as initial conditions and then trying to extrapolate the simulation results to the parameter regime of interest seems to be questionable. It is true that we successfully did it in the local MRI simulations, however, we do not think that this will always be possible. The problem, which we considered was relatively simple (in comparison with the core-collapse mechanism) and we knew what physical phenomena can be expected. Moreover, because of many symmetries in the system, we managed to find appropriate scaling relations.

Without an appropriate (semi-)analytical model, it would be very difficult to interpret our results (and similarly, the results of Obergaulinger et al. (2009)). One might wonder whether the initial magnetic field was amplified to 10^{15} G because for this value the magnetic field energy became comparable to the kinetic or rotational energy (in this case one might expect also much smaller initial fields to be amplified to this value), or because the system would amplify any field only by a constant factor (which was the case in the MRI simulations). In the latter case, much weaker initial magnetic fields (of order 10^{11} G) could not reach values of 10^{15} G. Obviously, one could not exclude more complicated scenarios.

This leads us to the final conclusion. Any reliable simulation of the magnetic field amplification hast to be done in 3D. Moreover, the initial amplitudes must not be artificially enhanced. Such simulations inevitably demand very high resolutions. Whereas it should be computationally feasible to study locally the magnetic field amplification problem in core-collapse supernovae in the foreseeable future, we do not think that it will ever be possible in global simulations.

Chapter 5

Summary and outlook

Magnetic field amplification in core-collapse supernovae

The main goal of this thesis was to investigate whether magnetic fields can be amplified to dynamically important strengths (of order 10^{15} G) within a few hundreds of milliseconds in the post-bounce phase of a core-collapse supernova (CC-SN).

According to state-of-the-art stellar evolution theory, magnetic fields in CC-SN progenitors are unlikely to exceed 10^9 G (Heger et al. 2005). In the initial (pre-bounce) core-collapse phase, a magnetic field can be amplified by compression by roughly two orders of magnitude. In the post-bounce phase, further amplification can be caused by convection or the standing accretion shock instability. However, recent numerical studies of Obergaulinger & Janka (2011) show that magnetic field strengths of order of 10^{15} G cannot be reached in CC-SNe of non-rotating progenitors, unless unrealistically high initial magnetic field strengths are used. For rotating cores, there are additional ways in which magnetic field can be amplified. One of them is linear winding, which is, however, too slow to increase the magnetic field strength to dynamically relevant values on the supernova timescale (i.e. in less than a second; see, e.g. an estimate by Spruit (2008)). Akiyama et al. (2003) pointed out that matter in rotating proto-neutron stars can be unstable against the magnetorotational instability (MRI; Balbus & Hawley (1991)). Independently of the initial magnetic field strength, the MRI increases the magnetic field exponentially with time, which makes this instability the most promising amplifying agent in CC-SNe. Obergaulinger et al. (2009) confirmed by means of local numerical ideal MHD simulations that the instability growth-rate is sufficient to increase the magnetic field strength by several orders of magnitude in the post-bounce phase. However, because of computational constraints, these authors used initial magnetic fields which were two orders of magnitude higher than theoretically expected. Moreover, the influence of numerical dissipation on these authors' simulation results is unknown. Furthermore, because of a general lack of understanding of the MRI termination process, Obergaulinger et al. (2009) were unable to answer the question whether given realistic initial magnetic fields, the MRI would be able to amplify magnetic fields to dynamically relevant field strengths.

Our main goal was to extend the numerical studies of Obergaulinger et al. (2009) to non-ideal MHD simulations, investigate the influence of numerical dissipation and extrapolate the results to a parameter regime relevant for CC-SNe. Such an extrapolation requires an appropriate (physically justified) prescription. Goodman, Xu and Pessah (later denoted as GXP) in a series of papers (Goodman & Xu (1994), Pessah & Goodman (2009), Pessah (2010)) proposed and developed an MRI termination model. Its key idea is that the initial exponential growth-phase of the MRI, dur-

ing which coherent velocity and magnetic field channels form, can be terminated by secondary instabilities, i.e. the Kelvin-Helmholtz or the tearing mode instability. Based on these assumptions, Pessah (2010) (almost) analytically calculated MRI termination amplitudes (i.e. magnetic field strength at termination) for different hydrodynamical and magnetic Reynolds numbers (denoted as R_e and R_m, respectively). We planned to verify these predictions with the help of 2D and 3D resistive-viscous MHD simulations. However, a closer look at Pessah's assumptions and simplifications revealed that his calculations (i.e. the GXP model) are mathematically inconsistent and therefore unreliable. Consequently, we proposed an alternative, free of the GXP model's flaws, prescription for extrapolating our simulation results to the CC-SN regime. In deriving our somewhat implicit formulae, we did not neglect physical effects which could possibly play an important role in the MRI termination process and we did not use results of linearised MHD equations to study nonlinear phenomena. We verified this prescription with the help of numerical simulations, which confirmed its predictive power. This allowed us to conclude that, for sufficiently high Reynolds numbers, i.e. $R_\mathrm{e}, R_\mathrm{m} \gg 10$, independently of the initial magnetic field strength, the MRI is able to amplify a magnetic field by a constant factor $\mathcal{A}$. This result is relevant not only for CC-SNe, but also for other astrophysical systems, especially accretion discs. For the rotational profile used in our simulations, the amplification factor, $\mathcal{A}$, was of order of 20. This leads us to the final conclusion concerning CC-SNe. Given that the magnetic field of the most strongly magnetised progenitors can be pre-amplified from $\approx 10^9$ G to $\approx 10^{11}$ G by compression during the collapse phase, the MRI is unable to amplify the magnetic field in the post-bounce phase to dynamically relevant strengths (of order 10^{15} G), but only to roughly 10^{12} G.

In accretion discs, gas rotates according to a Keplerian profile, which could lead to a slightly different (but still constant) value of the amplification factor, $\mathcal{A}$ (given $R_\mathrm{e}, R_\mathrm{m} \gg 10$, which is the case in all but proto-planetary discs). We presume that this variation should not be larger than a factor of a few. However, this statement should be verified with numerical simulations. Our study sheds some light on the nature of the MRI. The instability can be ubiquitous in accretion discs, may be able to amplify even very weak initial magnetic fields, yet not by many orders of magnitude, but only by a moderate factor. Numerical simulations with insufficient resolution per MRI channel are misleading and suggest that much stronger amplification would be possible However, as we could see in our resolution studies performed in Chapter 4, this artificial boost of the amplification factor $\mathcal{A}$ is caused by numerical viscosity. Even though we used a monotonicity preserving scheme of 9th order (MP9) and 33 zones per MRI channel (which are more than used in most MRI studies), thiw was still insufficient to resolve fully the secondary Kelvin-Helmholtz instability which was responsible for MRI termination in 3D simulations. Simulations with more than 66 zones per channel converged to the same MRI termination amplitude (in other words, to the same amplification factor, $\mathcal{A}$). This shows that high resolutions are required to study the process of MRI termination, not to mention the subsequent turbulent phase. This is a very important lesson for the whole MRI community.

Even though we managed to answer the main question concerning the MRI-driven magnetic field amplification in CC-SNe, we still see room for further research and improvements. Firstly, from the numerical point of view, it would be interesting to investigate how the MRI termination amplitude depends on resolution for lower order reconstruction schemes, i.e. MP5 and MP7. Obviously, this dependence would not be physical, but it would rather show how much numerical viscosity is present in a given simulation. Answering this question would be very valuable for users of other MHD codes, in which often only even lower order reconstruction schemes are implemented.

Secondly, we showed in our simulations that the amplification factor, $\mathcal{A}$, does not depend on the

initial magnetic field strength. However, because of limited computational time, we managed to show numerical convergence only for one initial magnetic field amplitude. We have demonstrated that in simulations with other initial field strengths, numerical viscosity played an non-negligible role. Still, we managed to estimate its effect and conclude that the amplification factor, $\mathcal{A}$, is indeed independent of the initial magnetic field. However, we think that it would be worthwhile to show numerical convergence for at least two more initial magnetic field amplitudes. Such studies would definitely show whether the amplification factor, $\mathcal{A}$, is constant for a given rotational profile without the need of making additional assumptions regarding numerical viscosity.

Thirdly, it would be undoubtedly beneficial to study the evolution of the parasitic instabilities in more detail. This could be very helpful in formulating a consistent semi-analytical MRI termination model. As a first step in this direction, we tried to measure the growth rate of the secondary instabilities with the help of $E^z_{\rm kin}$, i.e. the contribution of the fluid motions in the z direction to the kinetic energy . The idea behind this procedure is quite simple. Since the MRI does not induce any motion in the vertical direction, any change in $E^z_{\rm kin}$ should be caused by parasitic instabilities. Unfortunately, because of the chosen radial *shearing-disc* boundary condition (Klahr & Bodenheimer 2003), and because of the fact that the MRI growth rate depends on (local) angular velocity (shear), we observed that the MRI channels developed faster (and therefore had higher amplitudes) for smaller radii. This would lead to a (radius dependent) shear (gradient) in the perturbations of both the velocity and magnetic field at the radial boundaries, which is not properly taken into account (compensated) by the imposed boundary conditions. The shear would consequently lead to some spurious fluid motions in the vertical direction, making it impossible to measure the activity (growth rate) of the secondary instabilities with the help of $E^z_{\rm kin}$. We can think of two solutions how to reduce or eliminate this problem.

1. The simulation box could be moved further away from the proto-neutron star centre. For larger radii, the relative MRI growth-rate difference at the boundaries (proportional to $(r_2 - r_1)/r_0$, where r_1 and r_2 are the box boundaries and r_0 is the box centre), would be smaller, which would consequently reduce spurious vertical fluid motions. However, we cannot choose r_0 to be arbitrarily large, because the radius of a proto-neutron star is approximately $r_{\rm PNS} \approx 30$ km.

2. Alternatively, we could use the *shearing sheet* technique, which consists in transforming to the frame co-rotating with a fiducial fluid element at a radius r_0 and linearising the rotational profile around r_0. The main advantage of this approximation is that the local angular velocity shear and therefore also the MRI growth-rate, which is directly proportional to it, are constant in the whole simulation domain. This should eliminate unphysical and undesired vertical motions related to the shear in the perturbation amplitudes at the radial boundaries. However, since the shearing sheet approximation does not allow for global gradients, it is not suitable for studying the MRI in CC-SNe, where at least pressure gradients are necessary to provide the initial magnetohydrodynamical equilibrium. Therefore, results of such simulations could not be easily extrapolated to the parameter regime of interest here, but would rather serve as an auxiliary input for creating a consistent semi-analytical theory of the MRI termination process.

Numerical resistivity and viscosity

Another very important aspect, which was frequently discussed in this thesis are numerical errors. In Chapter 2, we argued that they can be very often interpreted as (numerical) viscosity

and resistivity. Chapter 3 was devoted to verifying this claim. Moreover, we proposed some simple ansatzes for estimating numerical dissipation. Next, we tested these prescriptions with the help of (sound, Alfvén, and fast magnetosonic) wave damping and tearing mode simulations. We demonstrated that after some calibration (tests), our ansatzes can be used for estimating the numerical dissipation of any grid based MHD code. This is probably the most interesting result for the numerical MHD community. In Chapter 4, we used these prescriptions to assess numerical viscosity and resistivity in the simulations of the MRI in CC-SNe.

Verifying our ansatzes with the help of the wave damping simulations was rather straightforward. Initial conditions were easy to implement and simulations were computationally inexpensive. The results confirmed our hypothesis that numerical dissipation depends on the characteristic velocity and length of the simulated system. Moreover, we confirmed that the employed (spatial) reconstruction and time integration schemes had their theoretical order of accuracy within the measurement errors. We recommend users of other MHD codes interested in applying ansatzes for estimating the numerical viscosity and resistivity to perform a suitable calibration with the help of wave damping simulations. The main advantages of this procedure are simplicity and low costs (in terms of both computational- and human work-time).

We also tested our ansatz for numerical resistivity (and the concepts of the characteristic velocity and length) with the help of tearing mode simulations. This instability was interesting to study for several reasons. Firstly, tearing modes can develop on the top of the MRI channels and subsequently terminate its further growth. As we have shown in Chapter 4, we observed this phenomenon in 2D MRI simulations. Therefore, we decided to investigate this parasitic instability in a much simpler system, i.e. with a constant background magnetic field and no velocity shear. Secondly, resistivity manifest itself in the tearing mode instability in a somewhat unusual way. It does not only simply dissipate magnetic field energy (into thermal and kinetic energy), but also converts one magnetic field component into another one. It could be imagined that resistivity not only "destroys" but also "creates" something in the system. Therefore, we also investigated whether numerical resistivity (which is, in the end, just a sum of numerical errors) would exhibit similar properties. Our simulations showed that indeed this was the case. Tearing modes driven by numerical and physical resistivity were in many aspects alike. Thirdly, velocity perturbations in the tearing mode instability experience a very strong variation around the magnetic field shear. Moreover, they become singular for vanishing resistivity, and consequently tearing modes not valid solutions in the ideal MHD limit. Therefore, it was very important to run some ideal MHD simulations to see how the code would behave in the vicinity of potentially singular points. The used high-order reconstruction schemes, i.e. MP5, MP7 and MP9, managed to "regularise" the singular points (by introducing some numerical resistivity), which prevented the code from suffering any unphysical instability (apart from the numerically driven tearing modes). For the reasons explained in Chapter 3, MP7 and MP9 reconstruction schemes experienced a (slight) reduction of their accuracy order. However, they still performed much better than any other lower order reconstruction scheme. For MP3 or the piece-wise linear scheme, the code would often crash or produce completely unreliable results. These observations convinced us to use the highest order reconstruction scheme, i.e. MP9, in the 3D MRI simulations, where such singular points could naturally occur (during the exponential growth phase - around the shear of magnetic field channels, and after MRI termination - literally everywhere).

We think that it would be worth conducting similar studies for the Kelvin-Helmholtz instability, which is responsible for MRI termination in 3D simulations (and nature). Firstly, we could test our ansatz for the numerical viscosity on another two dimensional hydrodynamical instability. Secondly, such a detailed investigation of the Kelvin-Helmholtz instability dependence on

numerical viscosity could be very helpful in further MRI studies. A better understanding how this parasitic instability develops in systems with non-negligible numerical viscosity could greatly facilitate and improve an analysis of 3D MRI simulation results.

Appendix A

Semi-analytical theory of the tearing mode instability

In Sec. 3.4.2, we wanted to verify the theoretical prediction (3.90) for the growth rate of the tearing mode in resistive-viscous MHD with the help of numerical simulations. However, we observed discrepancies between theory and simulation results (see Eqs. (3.105)–(3.109) and discussion after). Therefore, we postulated the "semi-analytical" ansatz (3.110) for the instability growth rate

$$\gamma \stackrel{?}{=} n_0 \eta^{n_1} \nu^{n_2} \left(\frac{b_0}{\sqrt{\rho_0}} \right)^{n_3} k^{n_4} \delta^{n_5} \left(\frac{\delta}{k} - \frac{k}{\delta} \right)^{n_6}, \tag{A.1}$$

where n_0 is a constant and $n_1, \ldots, n_6$ are fractionals, which need to be determined by numerical simulations. The dimension of the growth rate is $[s^{-1}]$, which we will write shortly as $\dim(\gamma) = [\mathrm{s}^{-1}]$, and it has to be "constructed" from the other physical quantities. Since $\dim(\eta) = \dim(\nu) = [\mathrm{cm}^2\ \mathrm{s}^{-1}]$, $\dim(c_\mathrm{A}) = [\mathrm{cm\ s}^{-1}]$ and $\dim(k) = \dim(\delta) = [\mathrm{cm}^{-1}]$, we obtain from dimensional analysis that the following conditions must hold

$$n_1 + n_2 + n_3 = 1, \quad \text{and} \tag{A.2}$$

$$\frac{n_1 + n_2}{2} + n_3 - n_4 - n_5 = 0. \tag{A.3}$$

The analytical expression (3.90) for tearing mode growth rate in resistive-viscous MHD does not agree with our simulation results either. Therefore, there is no reason to trust Eq. (3.88) for ε_RV, which is proportional to resistive-viscous layer width. However, we can formulate a similar (to Eq. (A.1)) ansatz for ε_RV, i.e.

$$\varepsilon_\mathrm{RV} \stackrel{?}{=} \eta^{m_1} \nu^{m_2} \left(\frac{b_0}{\sqrt{\rho_0}} \right)^{m_3} k^{m_4} \delta^{m_5}, \tag{A.4}$$

where $m_1, \ldots, m_6$ are fractional numbers and

$$m_1 + m_2 + m_3 = 0, \quad \text{and} \tag{A.5}$$

$$\frac{m_1 + m_2}{2} + m_3 - m_4 - m_5 = 1. \tag{A.6}$$

This time we did not introduce a constant m_0, since ε_RV cannot be measured directly from simulations. It should just be thought as a prescription to transform y in ODE (3.68) to a dimensionless

variable $\tilde{s} \equiv y/\varepsilon_{\mathrm{RV}}$. What we can expect however, is that the characteristic velocity peak, v_y, (which according to our convention defines the width of the resistive-viscous layer) should be present at the same value of $\tilde{s}$ (i.e. the function $\tilde{\Phi}(\tilde{s})$ has a maximum at a certain constant $\tilde{s}$). In other words, the distance of the velocity peak from the centre, which we will denote with the symbol $L_{\varepsilon_{\mathrm{RV}}}$, should be proportional to $\varepsilon_{\mathrm{RV}}$. Therefore, the resistive-viscous layer width should be equal to

$$L_{\varepsilon_{\mathrm{RV}}} \stackrel{?}{=} m_0 \varepsilon_{\mathrm{RV}} \stackrel{?}{=} m_0 \eta^{m_1} \nu^{m_2} \left(\frac{b_0}{\sqrt{\rho_0}} \right)^{m_3} k^{m_4} \delta^{m_5}, \tag{A.7}$$

where m_0 is a constant to be determined from simulations.

In Sec. 3.4.2, we numerically investigated the dependence of the tearing mode growth rate as a function of resistivity (see Fig. 3.27). We fitted the simulation results with the function

$$\ln(\gamma) = a \ln(\eta) + c. \tag{A.8}$$

obtaining $a = 0.7994 \pm 0.0012$ (see Eqs. (3.107) and (3.108)), which seems to indicate that $n_1 = 4/5$. Then, ansatz (A.1) would read

$$\gamma \stackrel{?}{=} n_0 \eta^{4/5} \nu^{n_2} \left(\frac{b_0}{\sqrt{\rho_0}} \right)^{n_3} k^{n_4} \delta^{n_5} \left(\frac{\delta}{k} - \frac{k}{\delta} \right)^{n_6}. \tag{A.9}$$

To verify this guess and also to investigate the dependence of the tearing mode growth rate on viscosity, we ran another set of simulations with the same numerical setup like in those presented in see Fig. 3.27 (i.e. resolution of 2048×2048 zones, $\delta = 10, k = 3, b_0 = \rho_0 = 1$), but the viscosity set to $\nu = 10^{-4}$ and resistivity in the range $\eta = 10^{-6}$–10^{-5}. The measured growth rates (see Fig. A.1), we once again fitted by the function

$$\ln(\gamma) = a \ln(\eta) + c \tag{A.10}$$

obtaining the following results

$$a = 0.801 \pm 0.004, \tag{A.11}$$
$$c = 5.838 \pm 0.051. \tag{A.12}$$

The estimator of a reconfirms our assumption that $n_1 = 4/5$.

Now, we can reinterpret the simulation results and extract information on the influence of the viscosity in the following somewhat indirect way. We fit the functions

$$\ln(\gamma) = 0.8 \ln(\eta) + c_1, \quad \text{and} \tag{A.13}$$
$$\ln(\gamma) = 0.8 \ln(\eta) + c_2 \tag{A.14}$$

to the simulation results with $\nu = 10^{-4}$ and $\nu = 10^{-5}$, respectively. If ansatz (A.9) holds, the difference between c_1 and c_2 should be

$$c_1 - c_2 = \ln(10^{-4 n_2}) - \ln(10^{-5 n_2}) = n_2 \ln(10) \tag{A.15}$$

From the linear regression we obtained the following estimators

$$c_1 = 5.385 \pm 0.001, \tag{A.16}$$
$$c_2 = 5.826 \pm 0.003, \tag{A.17}$$

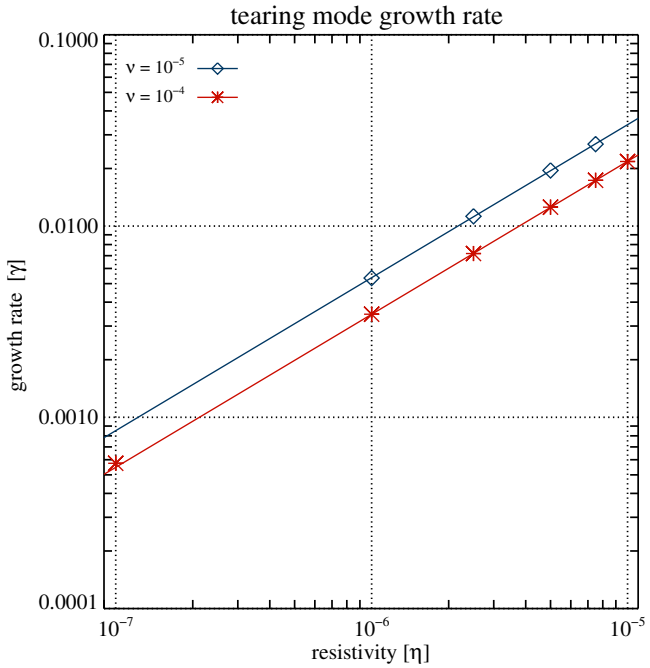

Figure A.1: Tearing mode growth rate as a function of resistivity. Blue diamonds and red asterisks denote results of simulations run with constant viscosity set to $\nu = 10^{-5}$ and $\nu = 10^{-4}$, respectively, the HLL Riemann solver, the MP reconstruction scheme and the resolution of 2048×2048 zones. The solid lines of the corresponding colours result from linear fits to the logarithms of the measured growth rates.

hence $c_1 - c_2 = -0.441 \pm 0.004$, from which we can infer $n_2 = -1/5$, since $(-1/5)\ln(10) \approx -0.461$. If γ were proportional to $\nu^{-1/6}$ or $\nu^{-1/4}$, $c_1 - c_2$ should be equal to $-(1/6)\ln(10) \approx -0.384$ or $-(1/4)\ln(10) \approx -0.576$, respectively. Therefore, we conclude that $n_2 = -1/5$.

We can also determined the values of m_1 and m_2 in Eq. (A.7) for $L_{\varepsilon_{\mathrm{RV}}}$, i.e. the width of the resistive-viscous layer. For every simulation after 30 time units, we plotted $v_y(x = 0, y)$ and measured the positions of the velocity peaks $L^+_{\varepsilon_{\mathrm{RV}}}$ (for $y > 0$) and $L^-_{\varepsilon_{\mathrm{RV}}}$ (for $y < 0$; see bottom right panel of Fig. 3.26, where these peaks are marked with green vertical lines). To reduce the measurement error, we can estimate that

$$L_{\varepsilon_{\mathrm{RV}}} = \frac{L^+_{\varepsilon_{\mathrm{RV}}} - L^-_{\varepsilon_{\mathrm{RV}}}}{2} \pm \frac{\Delta y}{2}, \tag{A.18}$$

where Δy is the width of one zone.[1] To the measured widths of the resistive-viscous layer (see Fig. A.2) in simulations with $\nu = 10^{-4}$ and $\nu = 10^{-5}$, we fitted the functions

$$\ln(L_{\varepsilon_{\mathrm{RV}}}) = a_1 \ln(\eta) + c_1, \quad \text{and} \tag{A.19}$$

$$\ln(L_{\varepsilon_{\mathrm{RV}}}) = a_2 \ln(\eta) + c_2, \tag{A.20}$$

[1] A more conservative approach would require to take Δy as a measurement error . One can make the following observation, however. For the sake of simplicity let us assume that index i numerates zone interfaces and $y(i = 0) = 0$. There are two possibilities: either we see a clear local maximum, i.e. $v_y(0, y(i_M - 1)) < v_y(0, y(i_M)) > v_y(0, y(i_M + 1))$, or the maximum is "smeared" across two zones, i.e. $v_y(0, y(i_M - 1)) < v_y(0, y(i_M)) \approx v_y(0, y(i_M + 1)) > v_y(0, y(i_M + 2))$. In the first case we would conclude, that the exact (mathematical) value of $L^+_{\varepsilon_{\mathrm{RV}}}$ should be somewhere in the range $[y(i_M) - \Delta y/2, y(i_M) + \Delta y/2]$. In the other case, the exact maximum is more likely to lie between the two interfaces, hence $L^+_{\varepsilon_{\mathrm{RV}}} \in [(y(i_M) + y(i_{M+1})/2 - \Delta y/2, (y(i_M) + y(i_{M+1})/2 + \Delta y/2]$.

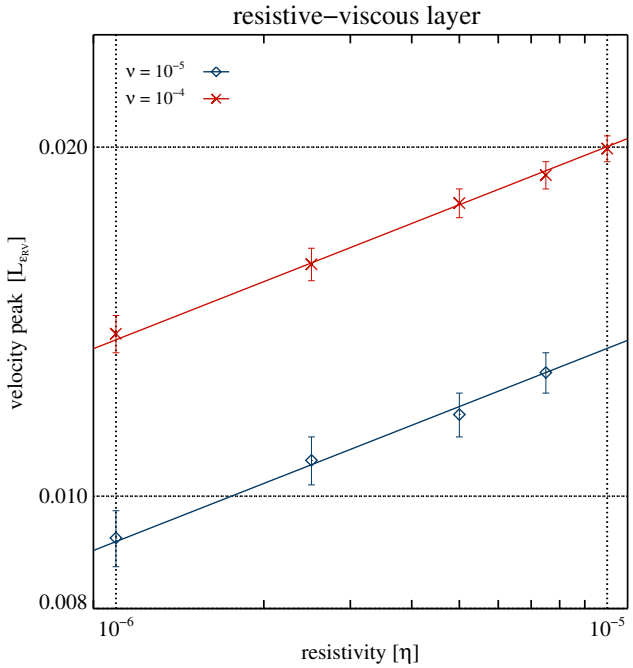

Figure A.2: Resistive-viscous layer width as a function of resistivity. Blue diamonds and red asterisks denote results of simulations run with constant viscosity set to $\nu = 10^{-5}$ and $\nu = 10^{-4}$, respectively, the HLL Riemann solver, the MP9 reconstruction scheme and a resolution of 2048×2048 zones. The solid lines of the corresponding colours result from linear fits to the logarithms of the measured resistive-viscous layer widths.

respectively, obtaining

$$a_1 = 0.160 \pm 0.003, \qquad c_1 = -2.079 \pm 0.037 \text{ and} \tag{A.21}$$

$$a_2 = 0.1591 \pm 0.0073, \qquad c_2 = -2.3928 \pm 0.0057. \tag{A.22}$$

The logarithm of Eq. (A.7) reads

$$\ln(L_{\varepsilon_{\mathrm{RV}}}) = m_1 \ln(\eta) + \ln\left[m_0 (\nu)^{m_2} \left(\frac{b_0}{\sqrt{\rho_0}} \right)^{m_3} k^{m_4} \delta^{m_5} \right]. \tag{A.23}$$

The estimators of a_1 and a_2 are equal within the measurement error to $1/6 = 0.1\bar{6}$. We note that $a_1 = a_2 \equiv m_1 = 1/6$ is consistent with the original Eq. (3.88) for $\varepsilon_{\mathrm{RV}}$. Therefore, to check if its other predictions are correct, we refitted the functions

$$\ln(L_{\varepsilon_{\mathrm{RV}}}) = 0.1\bar{6} \ln(\eta) + c_1, \text{ and} \tag{A.24}$$

$$\ln(L_{\varepsilon_{\mathrm{RV}}}) = 0.1\bar{6} \ln(\eta) + c_2, \tag{A.25}$$

expecting that $c_1 - c_2 = (1/6)\ln(10) \approx 0.384$. We obtained the following estimators

$$c_1 = -1.992 \pm 0.004, \text{ and} \tag{A.26}$$

$$c_2 = -2.393 \pm 0.006, \tag{A.27}$$

hence $c_1 - c_2 = 0.40 \pm 0.01$. This result confirms that $m_2 = 1/6$.

So far we know that $n_1 = 4/5$ and $n_2 = -1/5$. From condition (A.2), we obtain that $n_3 = 1-(n_1+n_2) = 2/5$. Hence ansatz (A.9) should read

$$\gamma \stackrel{?}{=} n_0 \eta^{4/5} \nu^{-1/5} \left(\frac{b_0}{\sqrt{\rho_0}}\right)^{2/5} k^{n_4} \delta^{n_5} \left(\frac{\delta}{k} - \frac{k}{\delta}\right)^{n_6}, \tag{A.28}$$

where from condition (A.3), we have $n_4 + n_5 = 8/5$. Analogically, from conditions (A.5) and (A.6), and ansatz (3.112), by putting $m_1 = m_2 = 1/6$, we should have

$$L_{\varepsilon_{\mathrm{RV}}} \stackrel{?}{=} m_0 (\eta\nu)^{1/5} \left(\frac{b_0}{\sqrt{\rho_0}}\right)^{-1/3} k^{m_4} \delta^{m_5}, \tag{A.29}$$

where $m_4 + m_5 = -3/5$.

Another set of simulations enabled us to verify the postulated dependence of the growth rate and the resistive-viscous layer width on background magnetic field (Eqs. (A.28) and (A.29), respectively). The initial parameters were set to either $\delta = 10,\ k = 3,\ \rho_0 = 1,\ \eta = 5\times10^{-5},\ \nu = 10^{-4}$ and b_0 in the range 0.5–10, or $\delta = 20,\ k = 6,\ \rho_0 = 1,\ \eta = 10^{-6},\ \nu = 10^{-5}$ and b_0 in the range 0.5–4. The latter simulations, were run in a twice smaller box, i.e. $L_x = L_y = \pi/6$, and a twice lower number of zones in each direction, i.e. 1024×1024 (the effective resolution being the same). The logarithms of Eqs. (A.28) and (A.29) read

$$\ln(\gamma) = \frac{2}{5} b_0 + \ln\left[n_0 \eta^{4/5} \nu^{-1/5} \rho_0^{-1/5} k^{n_4} \delta^{n_5} \left(\frac{\delta}{k} - \frac{k}{\delta}\right)^{n_6}\right], \quad \text{and} \tag{A.30}$$

$$\ln(L_{\varepsilon_{\mathrm{RV}}}) = -\frac{1}{3} b_0 + \ln\left(m_0 \eta^{1/6} \nu^{1/6} k^{m_4} \delta^{m_5} \rho_0^{1/6}\right) \tag{A.31}$$

respectively. To the simulation results (presented in Fig. A.3) with $\delta = 10,\ k = 3$ and $\delta = 20,\ k = 6$, we fitted the functions

$$\ln(\gamma) = a_1 \ln(b_0) + c_1, \tag{A.32}$$

$$\ln(L_{\varepsilon_{\mathrm{RV}}}) = \alpha_1 \ln(b_0) + \beta_1 \tag{A.33}$$

and

$$\ln(\gamma) = a_2 \ln(b_0) + c_2, \tag{A.34}$$

$$\ln(L_{\varepsilon_{\mathrm{RV}}}) = \alpha_2 \ln(b_0) + \beta_2, \tag{A.35}$$

respectively, obtaining the following estimators

$$a_1 = \ 0.3906 \pm 0.0044, \qquad c_1 = -4.377 \pm 0.006, \tag{A.36}$$

$$a_2 = \ 0.4112 \pm 0.0078, \qquad c_2 = -4.058 \pm 0.005, \tag{A.37}$$

$$\alpha_1 = -0.364 \pm 0.017, \qquad \beta_1 = -4.021 \pm 0.015, \tag{A.38}$$

$$\alpha_2 = -0.329 \pm 0.017, \qquad \beta_2 = -5.17 \pm 0.01. \tag{A.39}$$

They confirm that $a_1 = a_2 \equiv n_3 = 2/5 = 0.4$ and $\alpha_1 = \alpha_2 \equiv m_3 = -1/3 = -0.\bar{3}$ within the measurement error. Please note that we predicted these results beforehand in Eqs. (A.28) and (A.29), respectively. Were there any discrepancies between our semi-analytical theory and these simulation results, we would have to modify or discard the former.

With these simulation results, one more aspect of Eqs. (A.28) and (A.29) can be tested. Even though the powers n_4, n_5, n_6 and m_4, m_5 are undetermined, we expect from dimensional analysis

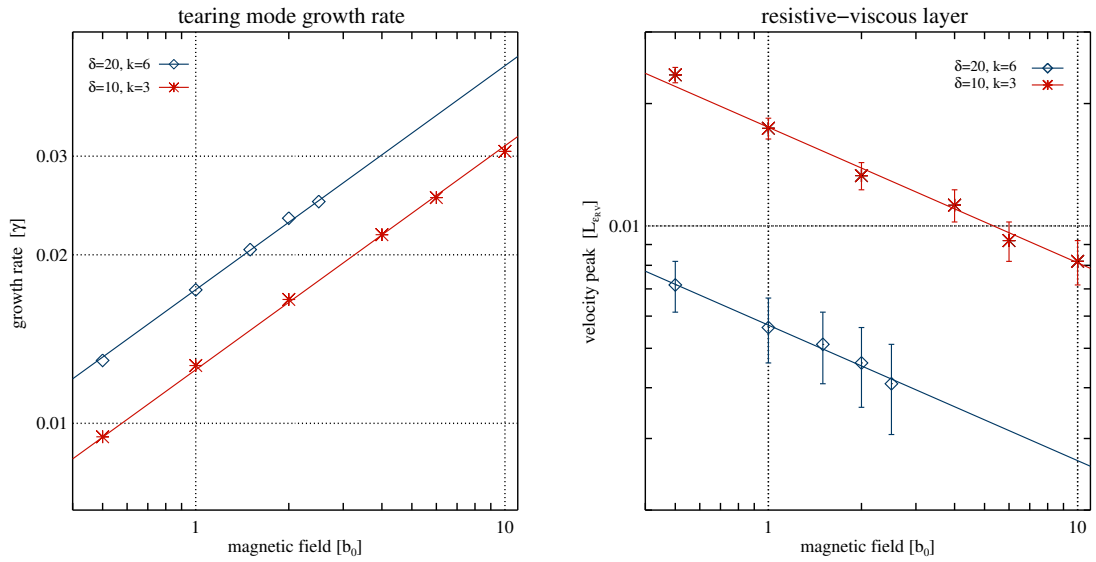

Figure A.3: Tearing mode growth rate (*left*) and resistive-viscous layer width (*right*) as a function of background magnetic field. Results of simulations with $\delta = 20,\ k = 6,\ \rho_0 = 1,\ \eta = 10^{-6},\ \nu = 10^{-5}$ and b_0 ranging from 0.5 to 4 are depicted with blue diamonds. Red asterisks represent result of simulations with $\delta = 10,\ k = 3,\ \rho_0 = 1,\ \eta = 5\times 10^{-5},\ \nu = 10^{-4}$ and b_0 in the range 0.5–10. Straight lines of the corresponding colours result from linear fits to the logarithms of the simulation data.

that $n_4 + n_5 = 8/5$ and $m_3 + m_4 = -2/3$. Therefore, doubling δ and k (from $\delta = 10, k = 3$ to $\delta = 20, k = 6$) should increase the instability growth rate by a factor of $2^{8/5}$ and decrease the resistive-viscous layer width by a factor of $2^{-2/3}$. Since the ratio δ to k is the same, the term $(\delta/k - k/\delta)^{n_6}$ remains constant. Hence, despite not knowing the exact value of n_6, we can still use of Eq. (A.28) for this case. Taking into account the different values of resistivity and viscosity between these two simulation sets, we theoretically expect $\Delta_{c\ \mathrm{theory}} \equiv c_1 - c_2 \approx 0.282$ and $\Delta_{\beta\ \mathrm{theory}} \equiv \beta_1 - \beta_2 \approx 1.11$. To check this hypothesis we fitted the functions

$$\ln(\gamma) = \frac{2}{5}\ln(b_0) + c_1, \tag{A.40}$$

$$\ln(\gamma) = \frac{2}{5}\ln(b_0) + c_2, \tag{A.41}$$

$$\ln(L_{\varepsilon_{\mathrm{RV}}}) = -\frac{1}{3}\ln(b_0) + \beta_1 \tag{A.42}$$

$$\ln(L_{\varepsilon_{\mathrm{RV}}}) = -\frac{1}{3}\ln(b_0) + \beta_2 \tag{A.43}$$

$$\tag{A.44}$$

to the simulation results and obtained

$$c_1 = -4.385 \pm 0.006, \tag{A.45}$$

$$c_2 = -4.055 \pm 0.005, \tag{A.46}$$

$$\beta_1 = -4.03 \pm 0.02, \tag{A.47}$$

$$\beta_2 = -5.17 \pm 0.01. \tag{A.48}$$

Hence $\Delta_{c\ \text{simulation}} \equiv c_1 - c_2 = 0.330 \pm 0.011$ and $\Delta_{\beta\ \text{simulation}} \equiv \beta_1 - \beta_2 = 1.14 \pm 0.03$. The difference between the theory and simulation amounts to

$$\Delta_{c\ \text{theory}} - \Delta_{c\ \text{simulation}} = -0.048 \pm 0.011, \tag{A.49}$$

$$\Delta_{\beta\ \text{theory}} - \Delta_{\beta\ \text{simulation}} = -0.03 \pm 0.03. \tag{A.50}$$

The predictions for the resistive-viscous layer agree within the measurement error. The discrepancy for the growth rate change is ≈ 0.04, i.e. the theory underestimates it by 4% ($1 - e^{0.04} \approx 0.04$). This error is small and could be explained, e.g. by the fact that we underresolved the simulations. Therefore, we conclude that our ansatzes for the instability growth rate and the resistive-viscous layer width (Eqs. (A.28) and (A.29), respectively) are correct.

From the theoretical point of view, tearing modes should not depend on the background pressure p_0. Firstly, because all equations were derived in the incompressible limit, i.e. formally for $c_\mathrm{s} = \sqrt{\Gamma p_0/\rho_0} \to \infty$. Therefore, all terms proportional to pressure should cancel out, otherwise they would dominate the equations. The second argument comes from dimensional analysis. Pressure, via the sound speed, would introduce an extra term of dimension $[\mathrm{cm\ s^{-1}}]$ in the equations for the tearing-mode growth rate and the resistive-viscous layer width. Since there are no other physical quantities from which one could 'construct' $[\mathrm{cm^{-1}\ s}]$ to compensate that term, we conclude that the equations must be pressure independent. To verify our theoretical considerations, rather as a formality, we ran a few simulations with the standard setup (i.e. $\delta = 10,\ k = 3,\ b_0 = \rho_0 = 1$), resistivity and viscosity set to $\eta = 10^{-4}$ and $\nu = 10^{-4}$, respectively, and pressure in the range $p_0 = 1$–100. The resolution was 512×512 zones. The simulation results (presented in Fig. A.4) confirm that tearing mode growth rate is pressure independent in the incompressible limit.

Another quantity that could possibly influence tearing modes, is the bulk viscosity. However in the incompressible limit, i.e. $\nabla \cdot \mathbf{v} = 0$, and all terms containing the bulk viscosity vanish. Therefore, bulk viscosity should not to affect the tearing modes. We ran a few simulations with a non-zero bulk viscosity and indeed it did not change the growth rate.

Let us summarise now our results. The purely analytically derived expression (3.90) for the tearing mode growth rate did not agree with our simulation results. Therefore, we postulated semi-analytical equations, which are a mixture of theoretical insight and simulation results. After some modifications, we obtained equations, which fully agree with the simulations. For the reader's convenience we write them down again in their best known form. The equation for the tearing mode growth rate reads

$$\gamma = n_0 \eta^{4/5} \nu^{-1/5} \left(\frac{b_0}{\sqrt{\rho_0}} \right)^{2/5} k^{n_4} \delta^{n_5} \left(\frac{\delta}{k} - \frac{k}{\delta} \right)^{n_6}, \tag{A.51}$$

where n_0 is a constant, n_4, n_5, n_6 are fractionals and $n_4 + n_5 = 8/5$. The equation for the resistive-viscous layer width reads

$$L_{\varepsilon_\mathrm{RV}} = m_0 (\eta \nu)^{1/6} \left(\frac{b_0}{\sqrt{\rho_0}} \right)^{-1/3} k^{m_4} \delta^{m_5}, \tag{A.52}$$

where m_0 is a constant, m_4, m_5 are fractionals and $m_4 + m_5 = -2/3$. We can calibrate these equations, using the results of the simulations run with the highest resolution. From estimators the (A.16) and (A.26), we obtain[2]

$$\gamma(k = 3, \delta = 10) = 34.56 \eta^{4/5} \nu^{-1/5} \left(\frac{b_0}{\sqrt{\rho_0}} \right)^{2/5} \tag{A.53}$$

[2]In these two equations we decided not to include the measurement errors, since in the applications discussed in Sec. 3.4.2, they would be negligible anyway.

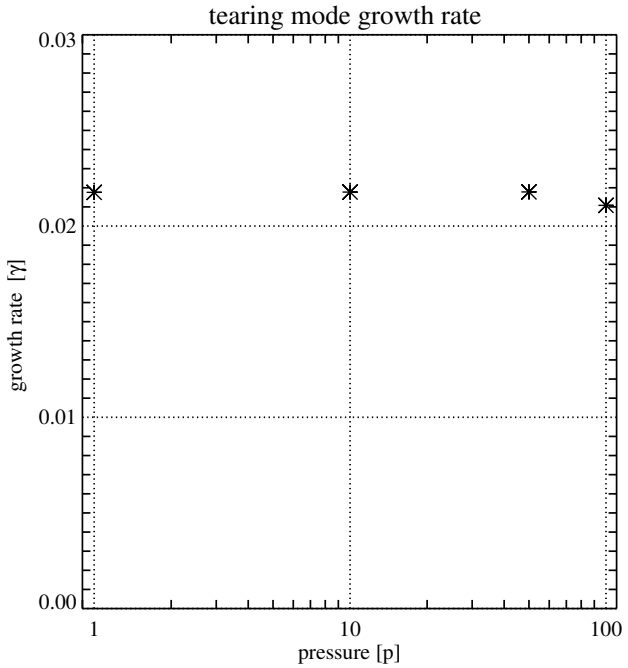

Figure A.4: Tearing mode growth rate as a function of background pressure in simulations with resistivity and viscosity set to $\eta = 10^{-4}$ and $\nu = 10^{-4}$, respectively, and pressure in the range $p_0 = 1$–100. The simulation domain was resolved with 512×512 zones. In accordance with theoretical predictions, tearing mode growth rate is pressure independent in the incompressible limit.

and

$$L_{\varepsilon_{\mathrm{RV}}}(k = 3, \delta = 10) = 0.634(\eta\nu)^{1/6} \left(\frac{b_0}{\sqrt{\rho_0}} \right)^{-1/3}, \tag{A.54}$$

where these equations are only valid for $k = 3$ and $\delta = 10$.

Finally, we would like to comment on possible reasons of the discrepancy between the theoretical prediction for the tearing mode growth rate (Eq. (3.90)) and the simulation results. Firstly, this equation was derived the under assumption (see Eq. (3.98) for the non-viscous case)

$$\varepsilon_{\mathrm{RV}} \ll y_{\mathrm{m}} \ll \delta^{-1}, \tag{A.55}$$

whereas in the simulations, only a much weaker condition (see Eq. (3.102))

$$\varepsilon_{\mathrm{RV}} < 0.1\delta^{-1}, \tag{A.56}$$

was met.[3] As a consequence, maybe in this regime the dominant terms in ODE (3.68) are those containing the fifth (or even lower) and not the sixth order derivative of v_y. Another possible explanation is that the constant ψ approximation does not hold, either just in the simulated regime or in general. Or maybe it is a combination of both reasons.

[3] However, when the latter condition was violated, the simulations did not agree with the semi-analytical theory.

Appendix B

Magnetorotational-instability growth-rate in non-ideal MHD

In this appendix, we briefly summarise the results of Pessah & Chan (2008) relevant for us. In the following equations, all physical quantities are transformed into dimensionless variables with the help of the characteristic time Ω_0^{-1} (the angular velocity Ω_0 was defined in Eq. (4.1)) and length $c_{\mathrm{A}z}\Omega_0$ (the Alfvén speed was defined in Eq. (4.13)). As an example, let us consider the dimensionless viscosity $\tilde{\nu}$. To recover its physical dimension it has to be multiplied by $c_{\mathrm{A}z}^2\Omega_0^{-1}$, i.e.

$$\nu = \frac{\tilde{\nu} c_{\mathrm{A}z}^2}{\Omega_0}. \tag{B.1}$$

From now on, we will drop the tilde symbol over the dimensionless variables, which should not lead to any confusion. In this convention, the hydrodynamical and magnetic Reynolds numbers simply read

$$R_{\mathrm{e}} = \frac{1}{\nu} \tag{B.2}$$

and

$$R_{\mathrm{m}} = \frac{1}{\mu}, \tag{B.3}$$

respectively. The notation of the variables used in this appendix follows the convention chosen by Pessah & Chan (2008). Hence, two variables, which are denoted by the same letter in Chapter 4 and in this appendix, may represent two distinct quantities.

Pessah & Chan (2008) find from the dispersion relation that the growth rate of the MRI unstable modes in resistive-viscous MHD is given by

$$\gamma = (\sqrt{\Delta} - \Lambda)^{1/2} - \frac{\nu}{2}k^2\left(1 - \frac{\kappa^2}{2\sqrt{\Delta}}\right) - \frac{\eta}{2}k^2\left(1 + \frac{\kappa^2}{2\sqrt{\Delta}}\right), \tag{B.4}$$

where k is the wavevector, κ is the epicyclic frequency (defined in Eq. (4.7)) and

$$\Lambda = \frac{3\alpha}{4} + \frac{y}{2}, \tag{B.5}$$

$$\Delta = (y+\alpha)^2 - \lambda, \tag{B.6}$$

where

$$\alpha = 2(k^2 - \mu^2) + \kappa^2, \tag{B.7}$$

$$\lambda = (k^2 - \mu^2)^2 + \kappa^2(k^2 + \mu^2) - 4k^2, \tag{B.8}$$

$$y = -\frac{5}{6}\alpha + \frac{1}{3}\frac{P}{U} - U, \tag{B.9}$$

where

$$\mu = \frac{1}{2}(\nu - \eta)k^2, \tag{B.10}$$

$$P = -\frac{\alpha^2}{12} - \lambda, \tag{B.11}$$

$$Q = -\frac{\alpha^3}{108} + \frac{\alpha\lambda}{3} - \frac{\beta^2}{8}, \tag{B.12}$$

$$U = \left(\frac{Q}{2} \pm \sqrt{\frac{Q^2}{4} + \frac{P^3}{27}}\right)^{1/3} \tag{B.13}$$

(the choice of either sign Eq. (B.13) is unimportant, see Pessah & Chan (2008) for a discussion), where finally

$$\beta = -2\mu\kappa^2. \tag{B.14}$$

As we can see, this dispersion relation is a quite complex expression (the interested reader will find its derivation in Pessah & Chan (2008)). We decided not to introduce it into the main text, but to present some simple heuristic arguments how dissipative effects influence the MRI, instead (see the discussion in Section 4.4, *Some simple estimates*). The growth rate γ defined by Eq. (B.4) must be real and positive, i.e. $\gamma > 0$ (we do not consider here the other three possible modes: two oscillatory and one damped). However, not for all combinations of k, ν and η, this will be the case. Pessah & Chan (2008) investigated for which parameters, the condition $\gamma > 0$ is met. These authors also derived some approximate analytical expressions for the maximum growth rate, given certain limits of the Reynolds numbers (e.g. for $\eta \gg 1$ and either $\nu \ll 1$ or $\nu \gg 1$, etc.).

For our purposes, we adopted a very straightforward approach. We simply plotted γ, in *Mathematica 8*, as a function of k for given ν and η. Then, we could easily find by eye for which k, γ had a maximum. With this method, we could achieve any desired accuracy. Given $\eta = \nu = 0.01$ (which corresponds to $R_\mathrm{e} = R_\mathrm{m} = 100$, the default Reynolds numbers, which we used in the simulations) and rotational profile (4.1), the maximum growth rate $\gamma \approx 0.615$ is achieved for $k \approx 0.914$. For comparison, in ideal MHD, the maximum $\gamma = 0.625$ for $k \approx 0.927$. As we can see, the difference is very small.

In some simulations, we changed the amplitude of the initial magnetic field (instead of $b_{0z} = 4.6 \times 10^{13}$ G, we used either $b_{0z} = 3.45 \times 10^{13}$ G or $b_{0z} = 2.76 \times 10^{13}$ G), but we kept the values of the physical viscosity and resistivity constant. This obviously affects the Reynolds numbers. The simulations with $b_{0z} = 3.45 \times 10^{13}$ G, had Reynolds numbers $R_\mathrm{e} = R_\mathrm{m} \approx 56$, corresponding to $\eta = \nu \approx 0.018$ in dimensionless units. For these values, the maximum growth rate $\gamma \approx 0.610$ is given for $k \approx 0.904$. For $b_{0z} = 3.45 \times 10^{13}$ G, the dimensionless $\eta = \nu \approx 0.018$, for which the maximum $\gamma \approx 0.602$ is at $k \approx 0.891$.

Acknowledgments

I have never liked it, when in a single author publication, “we”, instead of “I”, is used. Yet, I used the same style in my own thesis. There is a good reason for this, however. Writing this dissertation would not be possible without three people: Ewald Müller (my supervisor), Martin Obergaulinger and Pablo Cerdá-Durán (my co-supervisors). I would like to thank them for their support, interesting scientific discussions during these four years, and proofreading and improving the final form of this thesis. I thank Ewald for attracting my interest to core-collapse supernovae and offering an interesting PhD project. I would like to thank Martin for providing me with everything “computer-related” that was necessary for writing this thesis, from his numerical code to LaTeX templates.

There are so many different people whom I would like to thank for so many different things that even now, at the end of writing this thesis, I still have problems with organising its content.

For proofreading parts of the thesis, I thank Margi, Rob, Laura and Kate.

For constant improvement of my language skills – the thanks go to Rob, Philipp and Pedro, and computer skills – to Martin and Philipp.

I feel obliged to thank the “car rescue team” here, i.e. Rob, Pedro, Bruno, Michael and Philipp.

I thank all my MPA friends for the fantastic atmosphere at the institute, among others: Rob, Sandra, Irina, Jonas, Maxime, Chervin, Bruno, Sotiria, David, Gilles, Felicia, Pedro, Michael, Philipp, Christina, Janina, Lorenz, Ivo, Ashley, Hätschi, Rüdiger, Roderik, Caroline, Wenting, Akila, Andressa, Celeste, Zaz, Isa, Tom, Payel, and all others whom I forgot to mention and who should be on this list.

I also thank my flatmates: Schomi, Tobi, Silvia and Michael.

I would like to thank my parents Elżbieta and Krzysztof, and brother Krzysztof for helping me to move to Munich and their support during these years.

Finally, I would like to thank Margi for everything, and for her constant support and incredible patience in the final years of the PhD.

Bibliography

Akiyama, S., Wheeler, J. C., Meier, D. L., & Lichtenstadt, I. 2003, ApJ, 584, 954

Ardeljan, N. V., Bisnovatyi-Kogan, G. S., & Moiseenko, S. G. 2005, MNRAS, 359, 333

Arlt, R. & Rüdiger, G. 2001, A&A, 374, 1035

Balbus, S. A. 1995, ApJ, 453, 380

Balbus, S. A. & Hawley, J. F. 1991, ApJ, 376, 214

Balbus, S. A. & Hawley, J. F. 1998, Reviews of Modern Physics, 70, 1

Bethe, H. A. 1990, Reviews of Modern Physics, 62, 801

Biskamp, D. 1997, Nonlinear Magnetohydrodynamics (Cambridge University Press)

Biskamp, D. 2005, Magnetic Reconnection in Plasmas (Cambridge University Press)

Bisnovatyi-Kogan, G. S., Popov, I. P., & Samokhin, A. A. 1976, Ap&SS, 41, 287

Blondin, J. M., Mezzacappa, A., & DeMarino, C. 2003, ApJ, 584, 971

Bodo, G., Mignone, A., Cattaneo, F., Rossi, P., & Ferrari, A. 2008, A&A, 487, 1

Brandenburg, A., Nordlund, A., Stein, R. F., & Torkelsson, U. 1995, ApJ, 446, 741

Burrows, A. 2013, Reviews of Modern Physics, 85, 245

Burrows, A., Dessart, L., Livne, E., Ott, C. D., & Murphy, J. 2007, ApJ, 664, 416

Campos, L. M. B. C. 1999, Physics of Plasmas, 6, 57

Cerdá-Durán, P., Font, J. A., & Dimmelmeier, H. 2007, A&A, 474, 169

Chandrasekhar, S. 1960, Proceedings of the National Academy of Science, 46, 253

Chandrasekhar, S. 1961, Hydrodynamic and hydromagnetic stability (International Series of Monographs on Physics, Oxford: Clarendon, 1961)

Colgate, S. A. & White, R. H. 1966, ApJ, 143, 626

Evans, C. R. & Hawley, J. F. 1988, ApJ, 332, 659

Fromang, S. & Papaloizou, J. 2007, ArXiv e-prints, 705

Fromang, S., Papaloizou, J., Lesur, G., & Heinemann, T. 2007, ArXiv e-prints, 705

Furth, H. P., Killeen, J., & Rosenbluth, M. N. 1963, Physics of Fluids, 6, 459

Goedbloed, J. P., Keppens, R., & Poedts, S. 2010, Advanced Magnetohydrodynamics (Cambridge University Press)

Goedbloed, J. P. H. & Poedts, S. 2004, Principles of Magnetohydrodynamics (Cambridge University Press)

Goodman, J. & Xu, G. 1994, ApJ, 432, 213

Hanke, F., Müller, B., Wongwathanarat, A., Marek, A., & Janka, H.-T. 2013, ApJ, 770, 66

Hawley, J. F. 2000, ApJ, 528, 462

Hawley, J. F. & Balbus, S. A. 1991, ApJ, 376, 223

Hawley, J. F. & Balbus, S. A. 1992, ApJ, 400, 595

Hawley, J. F. & Balbus, S. A. 2002, ApJ, 573, 738

Hawley, J. F., Balbus, S. A., & Stone, J. M. 2001, ApJL, 554, L49

Hawley, J. F., Gammie, C. F., & Balbus, S. A. 1995, ApJ, 440, 742

Hawley, J. F., Gammie, C. F., & Balbus, S. A. 1996, ApJ, 464, 690

Heger, A., Woosley, S. E., & Spruit, H. C. 2005, ApJ, 626, 350

Hou, T. Y. & Le Floch, P. G. 1994, Math. of Computation, 62, 497

Jackson, J. D. 1998, Classical Electrodynamics, 3rd Edition (Wiley-VCH)

Janka, H.-T. 2012, Annual Review of Nuclear and Particle Science, 62, 407

Janka, H.-T., Hanke, F., Hüdepohl, L., et al. 2012, Progress of Theoretical and Experimental Physics, 2012, 010000

Janka, H.-T., Langanke, K., Marek, A., Martínez-Pinedo, G., & Müller, B. 2007, Physics Reports, 442, 38

Junk, V., Walch, S., Heitsch, F., et al. 2010, MNRAS, 407, 1933

Keil, W., Janka, H.-T., & Müller, E. 1996, ApJL, 473, L111+

Keppens, R., Tóth, G., Westermann, R. H. J., & Goedbloed, J. P. 1999, Journal of Plasma Physics, 61, 1

Klahr, H. H. & Bodenheimer, P. 2003, ApJ, 582, 869

Kotake, K., Yamada, S., Sato, K., et al. 2004, Phys. Rev. D, 69, 124004

Kouveliotou, C., Dieters, S., Strohmayer, T., et al. 1998, Nature, 393, 235

Landi, S., Londrillo, P., Velli, M., & Bettarini, L. 2008, Physics of Plasmas, 15, 012302

Laney, C. 1998, Computational Gasdynamics (Cambridge University Press)

Lazarian, A. & Vishniac, E. T. 1999, ApJ, 517, 700

LeVeque, R. J. 2002, Finite Volume Methods for Hyperbolic Problems (Cambridge University Press)

Masada, Y., Takiwaki, T., Kotake, K., & Sano, T. 2012, ApJ, 759, 110

Meier, D. L., Epstein, R. I., Arnett, W. D., & Schramm, D. N. 1976, ApJ, 204, 869

Menou, K., Balbus, S. A., & Spruit, H. C. 2004, ApJ, 607, 564

Miura, A. & Pritchett, P. L. 1982, J. Geophys. Res., 87, 7431

Miyoshi, T. & Kusano, K. 2005, Journal of Computational Physics, 208, 315

Müller, E. & Hillebrandt, W. 1979, A&A, 80, 147

Obergaulinger, M. 2008, PhD thesis, Max-Planck-Institut für Astrophysik, Garching bei München

Obergaulinger, M., Aloy, M. A., Dimmelmeier, H., & Müller, E. 2006a, A&A, 457, 209

Obergaulinger, M., Aloy, M. A., & Müller, E. 2006b, A&A, 450, 1107

Obergaulinger, M., Cerdá-Durán, P., Müller, E., & Aloy, M. A. 2009, A&A, 498, 241

Obergaulinger, M. & Janka, H.-T. 2011, ArXiv e-prints

Pessah, M. E. 2010, ApJ, 716, 1012

Pessah, M. E. & Chan, C.-k. 2008, ApJ, 684, 498

Pessah, M. E. & Goodman, J. 2009, ApJL, 698, L72

Roediger, E., Brüggen, M., Simionescu, A., et al. 2011, MNRAS, 413, 2057

Sano, T. & Inutsuka, S.-i. 2001, ApJL, 561, L179

Sano, T., Inutsuka, S.-i., Turner, N. J., & Stone, J. M. 2004, ApJ, 605, 321

Sawai, H., Yamada, S., & Suzuki, H. 2013, ApJL, 770, L19

Schnack, D. D. 2009, Lectures in Magnetohydrodynamics (Springer)

Shakura, N. I. & Syunyaev, R. A. 1973, A&A, 24, 337

Shore, S. N. 2007, Astrophysical Hydrodynamics: An Introduction (Wiley-VCH)

Shu, C.-W. 1997, ICASE Report No.97-65

Spitzer, L. & Härm, R. 1953, Physical Review, 89, 977

Spruit, H. C. 2008, in American Institute of Physics Conference Series, Vol. 983, 40 Years of Pulsars: Millisecond Pulsars, Magnetars and More, ed. C. Bassa, Z. Wang, A. Cumming, & V. M. Kaspi, 391–398

Stone, J. M., Hawley, J. F., Gammie, C. F., & Balbus, S. A. 1996, ApJ, 463, 656

Stone, J. M. & Pringle, J. E. 2001, MNRAS, 322, 461

Suresh, A. & Huynh, H. 1997, J. Comput. Phys., 136, 83

Symbalisty, E. M. D. 1984, ApJ, 285, 729

Toro, E. 1997, Riemann Solvers and Numerical Methods for Fluid Dynamics (Berlin: Springer)

Ugliano, M., Janka, H.-T., Marek, A., & Arcones, A. 2012, ApJ, 757, 69

Velikhov, E. 1959, Sov. Phys. JETP, 36, 995

Woosley, S. E., Heger, A., & Weaver, T. A. 2002, Reviews of Modern Physics, 74, 1015

Woosley, S. E., Langer, N., & Weaver, T. A. 1993, ApJ, 411, 823

Yamada, S. & Sawai, H. 2004, ApJ, 608, 907